Structure-Function Relationships in Cellular Copper Control

A Thesis

Submitted to the College of Graduate Studies and Research

in Partial Fulfillment of the Requirements

for the Degree of Doctor of Philosophy

in the

Department of Geological Sciences

University of Saskatchewan, Saskatoon, SK, Canada

By

Limei Zhang

Spring 2009

PERMISSION TO USE

In presenting this thesis in partial fulfillment of the requirements for a Postgraduate degree from the University of Saskatchewan, I agree that the Libraries of this University may make it freely available for inspection. I further agree that permission for copying of this thesis in any manner, in whole or in part, for scholarly purposes may be granted by the professor or professors who supervised my thesis work or, in their absence, by the Head of the Department or the Dean of the College in which my thesis work was done. It is understood that any copying or publication or use of this thesis or parts thereof for financial gain shall not be allowed without my written permission. It is also understood that due recognition shall be given to me and to the University of Saskatchewan in any scholarly use which may be made of any material in my thesis.

Requests for permission to copy or to make other use of material in this thesis in whole or part should be addressed to:

Head of the Department of Geological Sciences

University of Saskatchewan

114 Science Place

Saskatoon, Saskatchewan

Canada

S7N 5E2

ABSTRACT

X-ray absorption spectroscopy and computational chemistry have been used to probe the structure of biomolecules involved in cellular copper homeostasis. X-ray absorption spectroscopy shows that copper chaperones involved in cytochrome c oxidase assembly bind Cu(I) with trigonal coordination environments in poly-copper thiolate clusters, but the number of coppers in these clusters remains unclear. X-ray absorption spectroscopy of the metal-sensing transcription factor-1 from *Drosophila melanogaster* and metallothionein from *Saccharomyces cerevisiae* with stoichiometries of four or less shows a tetracopper cluster in an all-or-none manner in these molecules. These results suggest that cooperative binding of copper to form tetracopper clusters may be a common mechanism employed by copper control molecules. The active site structure of the novel copper-sensitive repressor CsoR in *Mycobacterium tuberculosis* binds copper in a trigonal coordination geometry with two sulfur and one nitrogen donors according to X-ray absorption spectroscopy results. Molecular dynamics simulations of both apo- and Cu-bound CsoR reveal local conformational changes in CsoR upon copper binding, which suggests multiple possible mechanisms of Cu-dependent transcriptional regulation by CsoR. Finally, X-ray absorption spectroscopy and X-ray fluorescence imaging have been used to understand the molecular basis of a promisng new treatment for Wilson's disease (a genetic disorder of Cu homeostasis) using tetrathiomolybdate. Overall, the results presented provide an essential structural basis for understanding copper homeostasis in living cells.

ACKNOWLEDGEMENTS

The thanks I give here go beyond my appreciation for support in advising and editing this research project. A great many faculty and family members, colleagues and friends have supported me throughout my studies.

I would like to express my deepest appreciation to my PhD supervisor Dr. Graham George and my committee member Dr. Ingrid Pickering for their invaluable support, guidance and encouragement throughout my research and training, and for walking me through the most difficult period during my study. I also thank all other advising committee members Dr. Helen Nichol, Dr. Tom Ellis and my external examiner Dr. Ninian Blackburn for their insightful comments and words of encouragements. My thanks also go to Dr. Dennis Winge, Dr. David Giedroc and Dr. Karl Summer and their group members for the collaboration with my PhD research.

I am indebted to Dr. De-Tong Jiang and Dr. Ning Chen for the opportunities of the hand-on experience at HXMA beamline, Canadian Light Source and for the extensive beamline knowledge and experience they have taught me during my volunteer work.

I owe a great deal of thanks to all our group members for the help in data collection and intriguing discussion in data analysis. I feel lucky to have an opportunity to work with all of them. Especially I would like to thank Dr. Jake Pushie in our group for the great help with my molecular dynamics simulation work and insightful comments on my thesis.

My heartfelt thanks go to my previous graduate supervisor Dr. Edward Ishiguro. I would have not reached this point without his encouragements and advices.

DEDICATION

I would like to dedicate this dissertation to the very special people in my life:

To my grandfather who has passed away when I was 10. I wish that he knew I have made one of our dreams to be true, and I will keep going as time goes by.

To my parents who have given me the freedom to chase my dream and their full-hearted support for whatever and whenever I need.

To my brother and sister, my sister-in-law, and my lovely niece and nephew for their love and support.

TABLE OF CONTENTS

LIST OF TABLES

LIST OF FIGURES

LIST OF ABBREVIATIONS

AST	aspartate aminotransferase
CcO	cytochrome c oxidase
CsoR	copper-sensitive operon repressor
DCY	deprotonated cysteine
DFT	density functional theory
dMTF-1	*Drosophila melanogaster* metal-responsive transcription factor-1
DTDP	2,2'-dithiodipyridine
DTT	dithiothreitol
EPR	electron paramagnetic resonance
EXAFS	extended X-ray absorption fine structure
GGA	generalized gradient approximation
HPLC	high pressure liquid chromatography
IMS	intermembrane space
LDA	local-density approximation
LEC rat	Long Evans cinnamon rat
LPP rat	Rat with defection in PINA/Atp7b locus
MD	molecular dynamics
MM	molecular mechanics
MRE	metal responsive element
MS	mass spectroscopy
MT	metallothionein
MTF-1	metal-responsive transcriptional factor-1
NLS	nuclear localization signal
NMR	nuclear magnetic resonance
OPLS	optimized potential for liquid simulations
OPLS-AA	optimized liquid simulation for all-atoms force field
QM	quantum mechanics

PINA	Pineal Night-specific ATPase
RMSD	root mean square deviation
RMSF	root mean square fluctuation
SOD	superoxide dismutase
TTM	tetrathiomolybdate
XAS	X-ray absorption spectroscopy
XFI	X-ray fluorescence imaging

Amino acid code

A	Ala	Alanine
R	Arg	Arginine
N	Asn	Asparagine
D	Asp	Aspartic acid
C	Cys	Cysteine
E	Glu	Glutamic acid
Q	Gln	Glutamine
G	Gly	Glycine
H	His	Histidine
I	Ile	Isoleucine
L	Leu	Leucine
K	Lys	Lysine
M	Met	Methionine
F	Phe	Phenylalanine
P	Pro	Proline
S	Ser	Serine
T	Thr	Threonine
W	Trp	Tryptophan
Y	Tyr	Tyrosine
V	Val	Valine

CHAPTER 1

COPPER HOMEOSTASIS IN LIVING ORGANISMS

1.1 Cellular Copper Control

Copper is an essential trace element required by most living organisms (Bertinato and L'Abbe, 2004). It is involved in a large variety of biological processes, including energy production (cytochrome c oxidase), connective tissue formation (lysyl oxidase), iron metabolism (ferroxidase), neurotransmitter synthesis (dopamine-β-monooxygenase), metabolism of neurotransmitters peptide histidine-methionine (monoamine oxidase), melanin formation (tyrosinase), and antioxidant functions (superoxide dismutase and ceruloplasmin) (Tapiero et al., 2003). In these processes, copper plays a number of roles, which include being an active site component in metalloenzymes and a component of electron-transfer processes, or a combination of these. Copper deficiency can cause anemia, neutropenia, osteoporosis and other abnormalities of bone development, and may also lead to loss of pigmentation, neurological symptoms and impaired growth (Tapiero et al., 2003).

Regardless of the importance of copper to the organism, excess copper is toxic to all cells. Free copper ions can generate free radicals via the so-called Fenton-type reactions, and cause oxidation damage to functional molecules such as proteins, lipids and nucleic acids in living organisms (Halliwell and Gutteridge, 1992; Valko et al.,

2005). Copper also can bind non-specifically to other essential proteins, and thus disturb their normal functions (Valko et al., 2005). Because of its toxicity, copper is very tightly regulated with an effective copper level that corresponds to less than one free copper ion per cell (Rae et al., 1999). Organisms from bacteria to human beings achieve this via elaborate molecular machinery composed of a number of copper control molecules which regulate copper uptake and excretion, distribution within the cell, storage and detoxification. All the copper control molecules in this molecular machinery function cooperatively in the cell. If any of these copper control mechanisms malfunctions, it will cause abnormal cellular copper homeostasis, and result in serious health problems or even death. The best characterized human diseases associated with dysfunction of copper homeostasis are Menkes disease and Wilson's disease, both of which are due to mutations in P-type ATPase copper transporters (see Section 1.3.4) (Harrison and Dameron, 1999; Mercer, 2001). In addition, evidence is accumulating that abnormal copper homeostasis is linked to Alzheimer's disease, and other neurological diseases. Identification of these copper control molecules and understanding their mechanisms is required for prevention and cure of these health problems. Undoubtedly, studies on structures of these molecules, particularly on the structures around copper binding sites in the molecules provide critical information for understanding molecular mechanisms. Extensive research has been carried out on this over the past few decades (Camakaris et al., 1999; Solioz and Stoyanov, 2003; Balamurugan and Schaffner, 2006; Grotz and Guerinot, 2006). In this chapter, current progress in understanding copper homeostasis in both prokaryotic and eukaryotic organisms will be briefly reviewed, with a focus on structural studies using yeast as a eukaryotic model and *E. coli* as a prokaryotic model.

1.2 Copper Homeostasis in Eukaryotes

1.2.1 Copper Uptake

In eukaryotes, copper is delivered into cells from the surrounding environment by a family of small, membrane-associated, Cu(I)-specific transporters, known as the Ctr family (Dumay et al., 2006; De Feo et al., 2007). Multiple Ctr members have been

found in certain eukaryotic organisms for copper uptake under different conditions. For example, three copper transporters have been identified in yeast, namely yCtr1, yCtr2 and yCtr3 (Figure 1-1). Both yCtr1 and yCtr3 are high Cu(I) affinity transporters and are integrated with the plasma membrane (Van Ho et al., 2002; Rees and Thiele, 2004). Before binding by yCtr1 or yCtr3, extracellular Cu(II) is reduced to Cu(I) by plasma membrane associated reductases such as Fre1 and Fre2 (Hassett and Kosman, 1995; Georgatsou et al., 1997). Excess copper is sequestered in the cellular vacuole, and can be subsequently imported into cytoplasm upon copper deficiency by the low affinity copper transporter yCtr2 which is located in the vacuolar membrane (Portnoy et al., 2001; Rees et al., 2004). Among all the Ctr members, Ctr1 is the most extensively studied and is found in many eukaryotic systems (Dumay et al., 2006). Ctr1 contains three putative transmembrane domains and forms a trimeric complex within the plasma membrane (Lee et al., 2002a; Petris, 2004; Lee et al., 2007; De Feo et al., 2009). One or more Met-rich metal binding motifs are conserved in the N-terminal extracellular domain of Ctr1 and these motifs have been proposed to be important in copper acquisition (Lee et al., 2002a; Puig et al., 2002; Petris et al., 2003). Cu(I) is bound at the cytosolic C-terminal domain of yCtr1 as four Cu(I) ions in a cuprous thiolate polynuclear cluster Cu_4S_6 (Xiao et al., 2004). This has been proposed to be involved in copper delivery to cellular copper chaperones (Xiao and Wedd, 2002). Ctr proteins import Cu(I) ion in an ATP-independent fashion, and the transporting ability is stimulated by extracellular acidic pH and high K^+ concentrations (Lee et al., 2002a). It is proposed that Cu(I) import by Ctr1 may be facilitated by the high ratio of environmental copper level to cellular copper level, arising from the fact that intracellular copper concentrations are extremely low (Rae et al., 1999; Lee et al., 2002a; Petris, 2004).

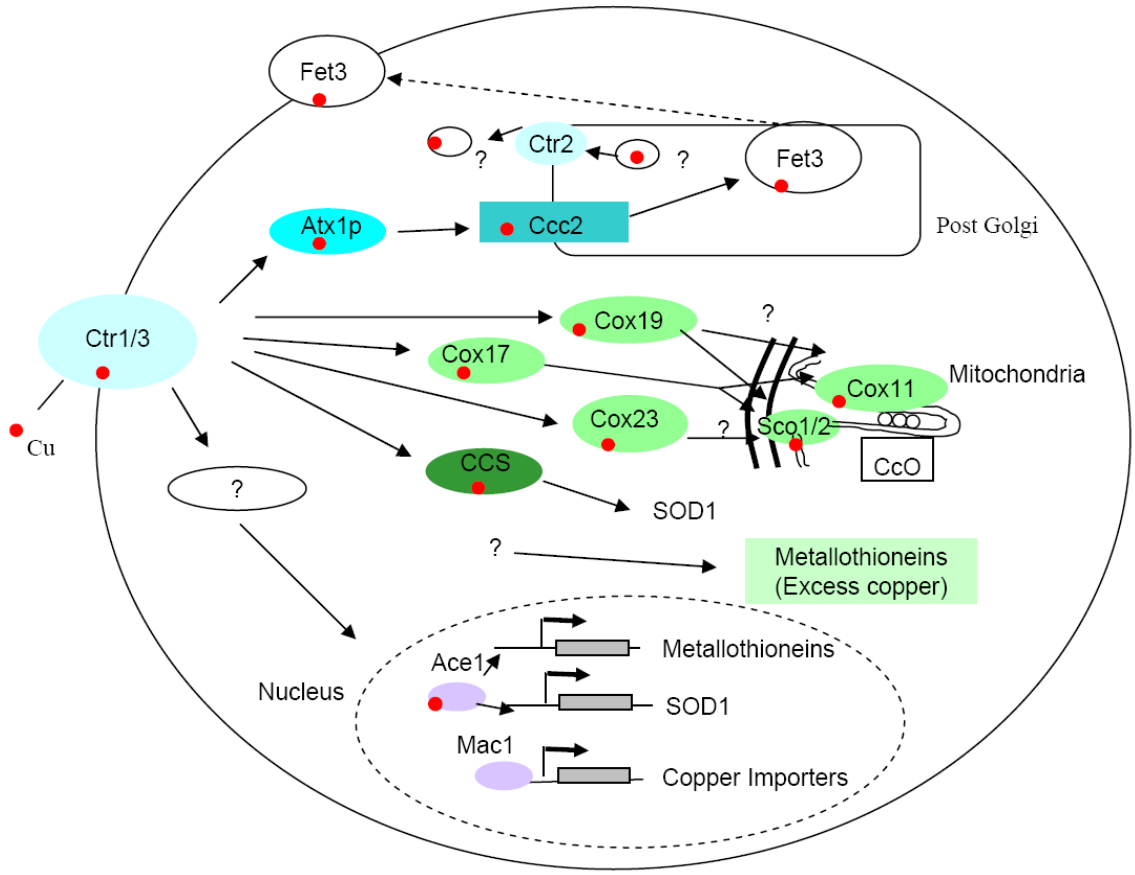

Figure 1-1. Schematic illustration of proposed copper homeostasis in yeast. The molecules involved in copper import are highlighted in ; the chaperone for copper secretory pathway is highlighted in ; the molecule involved in copper excretory pathway is highlighted in ; the copper chaperones in cytochrome c oxidase assembly pathway are in ; the copper chaperone for Cu, Zn-superoxide dismutase SOD1 is in ; the molecule involved in copper storage and detoxification is highlighted in ; the copper-dependent regulators are in .

Other copper transporters also exist in the eukaryotes, since deletion of both yCtr1 and yCtr3 in yeast results in 30% of wild-type cellular copper content (Lee et al., 2002b). One divalent metal transporter identified so far is Fet4 in yeast (and its homolog DMT1 in fruit flies and mammals) (Dix et al., 1994; Lee et al., 2002b). Fet4 was first identified as a low-affinity iron transporter. However further studies show that this protein can also transport copper (Hassett et al., 2000). Other copper uptake pathways may also exist, since copper uptake in Ctr1 deletion embryonic cells is not inhibited by Fe^{2+} (Lee et al., 2002b).

How copper is transferred from the importers in the cellular membrane to other copper control molecules in the cell remains unknown. It has been suggested that the transporters are unlikely to interact with intracellular copper chaperones directly since copper transporters located in both the cell surface and intracellular membrane are all capable of contributing copper to the chaperones regardless of their structural divergence (Portnoy et al., 2001). However, such direct transporter-chaparone interactions have been observed *in vitro* for both cyanobacterial proteins (Tottey et al., 2002) and for yeast proteins (Xiao and Wedd, 2002).

1.2.2 Copper Distributions

As mentioned earlier, copper is strictly controlled inside the cell due to its toxicity, and there are virtually no free copper ions in the cell under normal physiological conditions. Therefore copper enzymes cannot acquire copper ions directly from a cytoplasmic pool, and copper ion "taxicabs" are needed to deliver copper to the enzymes that require it. In both eukaryotic and prokaryotic cells, a specialized family of proteins, known as copper chaperones is used for this task (Pufahl et al., 1997). Copper chaperones are small proteins that acquire copper ions from copper transporters either directly or indirectly, and then convey and donate them to specific molecular targets within the cell (O'Halloran and Culotta, 2000). This family of copper proteins possesses special properties both structurally and chemically distinct from other copper-binding proteins. In order to fulfill their task, copper chaperones must bind copper ions with great tenacity during their travels from the transporter to the destination, but they must readily give up their bound copper upon arrival at the target protein, and do so with great specificity. Several copper distribution pathways are conserved between yeast and humans, as shown in Figure 1-1 and described below.

1.2.2.1 Delivery of Copper to the Secretory Pathway

The first copper chaperone identified in yeast was Atx1. It delivers copper to the lumen of the trans-Golgi network via a P-type transport ATPase Ccc2 (Lin and Culotta,

1995). Cu(I) is then loaded into the multicopper-containing protein ferroxidase Fet3 before it is exported out of the cytoplasmic membrane (Pufahl et al., 1997; Arnesano et al., 2001). Similarly, Hah1 (or Atox1), the human homolog of Atx1, delivers copper to P-type ATPase ATP7A and ATP7B in the trans-Golgi network. ATP7A and ATP7B are also known as the Menkes and Wilson's proteins, respectively (Section 1.3.4). ATP7A is involved in copper incorporation into several copper-dependent enzymes such as tyrosinase in the secretory pathway, while ATP7B directs copper insertion into a serum ferroxidase, ceruloplasmin (Prohaska and Gybina, 2004). Extensive work has been carried out to understand the mechanism of copper transfer from Atx1 (or Hah1) to Ccc2 (or ATP7A/B). Current data indicate that Atx1 contains a conserved ferredoxin-like domain with four stranded β sheets and two α helices (Arnesano et al., 2001). Two cysteines in the $MXCX_2C$ motif of this domain bind to a single Cu(I) (Ralle et al., 2003). The copper transfer from Atx1 to Ccc2 is facilitated by Atx1-Ccc2 protein-protein interactions followed by a ligand exchange reaction involving the formation of a transient trigonally coordinated copper centre (Banci et al., 2006; Holt and Merz, 2007). It remains unknown whether other copper chaperones are involved before and during copper incorporation into these Cu-dependent proteins in the trans-Golgi network.

1.2.2.2 Copper Delivery to Cu, Zn-Superoxide Dismutase

CCS (also called Lys7 in yeast) is a copper chaperone which delivers copper to Cu,Zn-superoxide dismutase (SOD) (Schmidt et al., 2000). CCS delivers copper to both cytoplasmic and (at least partially) mitochondrial SOD, and catalyzes the formation of an essential disulfide bridge in SOD (Schmidt et al., 2000; Field et al., 2003). CCS is the largest cellular copper chaperone identified so far, with three conserved domains (Schmidt et al., 2000). The N-terminal Domain I of CCS is a homolog to Atx1 including the familiar $MXCX_2C$ copper-binding site. However, this domain does not appears to directly function in insertion of copper to SOD, and it is not essential unless copper is limited (Schmidt et al., 2000). Instead, copper insertion into SOD appears to be fulfilled via the short unstructured Domain III with a CXC copper binding site (Schmidt et al.,

2000; Stasser et al., 2005; Stasser et al., 2007). The central domain of CCS (Domain II) is homologous to its target enzyme, SOD, and it can form a protein-protein complex with SOD either with or without copper (Schmidt et al., 1999; Lamb et al., 2000). It has been proposed from both solution studies and crystallography that CCS and SOD form a heterodimer or heterotetramer prior to copper transfer (Lamb et al., 2000; Lamb et al., 2001). The detailed mechanism of copper transfer from CCS to SOD remains unclear.

1.2.2.3 Copper Chaperones in Cytochrome C Oxidase Assembly Pathway

Cytochrome c oxidase (CcO) is the last enzyme in the respiratory chain and the ultimate consumer of oxygen. It spans the inner mitochondrial membrane (Capaldi et al., 1983; Capaldi, 1990). Copper is required for CcO activity as an essential component of both the binuclear Cu_A and heme-a_3-Cu_B sites (Beinert, 1995; Tsukihara et al., 1996). To date, a large number of proteins have either been identified as or been proposed to be copper chaperones employed for copper delivery and/or insertion into CcO. These include Cox17, Cox19, Cox23, Cox11, Sco1 and Sco2 (Hamza and Gitlin, 2002; Cobine et al., 2006; Bertini and Cavallaro, 2008). The first three proteins are found both in the cytoplasm and in the inter-membrane space of the mitochondrion, while the last three proteins are incorporated into the inner mitochondrial membrane. A detailed introduction for these copper chaperones is given in Chapter 3, prior to discussing structural studies on the copper binding sites in Cox19 and Cox23. No copper chaperones have yet been identified that deliver copper from the cytoplasm into the mitochondrion. Previous studies have ruled out Cox17 and Cox19 as candidates for this process, since they are still functional when tethered to the inner membrane (Maxfield et al., 2004; Rigby et al., 2007). Thus, either Cox23 or another unknown copper chaperone serves as copper shuttle from cytoplasm to mitochondrion.

1.2.3 Copper Storage and Detoxification

Regardless of the elaborate controls for copper import, export and distribution within the cell, the need of a copper buffer pool still exists for temporary copper storage

and detoxification in the case of a sudden increase in the ambient copper concentration. This task is fulfilled mainly by the metallothioneins and other small Cu-ligand molecules such as glutathione. Metallothioneins are a group of small, Cys-rich proteins with remarkable affinity to metals including but not limited to copper (Kagi, 1991; Palmiter, 1998). In the case of copper, metallothionein is required to bind copper tightly for the purpose of detoxification while it is ready to deliver copper to other copper chaperones for copper export or returning the copper to cytoplasmic pool when the copper level runs low (Hartmann et al., 1983). To fulfil the dual function, metallothionein binds to copper either in a stable trigonal coordination or in an active digonal coordination (See Chapter 4 for details).

In the mitochondrial matrix, a non-proteinaceous pool of soluble, anionic, low molecular weight complexes accounts for about 70% of the total copper content in the mitochondrion in yeast and mammals (Cobine et al., 2004). This copper pool may be stored for CcO and other Cu-dependent proteins in the mitochondrion. The copper pool in the mitochondrial matrix is dynamic in response to cytosolic copper level, and it is accessible to a heterologous cuproenzyme (Cobine et al., 2004). Efforts to identify the matrix copper ligand have, to date, been unfruitful. X-ray absorption spectroscopy of the intact mitochondrion suggests that the majority of copper in the mitochondrion exists as a trigonally coordinated copper with sulfur-like donors (i.e. phosphorus, sulfur or chlorine). However, the ligands of this matrix copper pool changes to oxygen/nitrogen once the mitochondrion is exposed to air (Zhang, Winge et al., unpublished data).

1.2.4 Copper Excretion out of the Cell

The soft metal ion translocating P-type ATPAases (Cu-ATPases), represented by Ccc2 in yeast and its human homologs ATP7A and ATP7B, are used for copper excretion in eukaryotes. This type of P-type ATPases is located in the biological membranes, and typically contain 8 transmembrane domains (Melchers et al., 1996; Rensing et al., 1999). They export metal ions across the membrane using energy from

ATP hydrolysis, which requires metal-specific binding, delivery of metal to the membrane, and release of metal on the other side of the membrane. To meet their functional requirements, the Cu-ATPases show distinct structural features including one to six N-terminal CX_2C sequences and a CPC motif in the sixth transmembrane segment (Lutsenko et al., 1997; DiDonato et al., 2000). The CX_2C sequence binds to soft metal cations with the two cysteines from the motif *in vitro*, and it appears to play a role either in moving the copper ions across the membrane or regulating Cu-ATPase activity, depending on which organism they are in (Lutsenko et al., 2007). The CPC motif in the sixth transmembrane segment may be involved with copper translocation (Lutsenko et al., 2007). ATP hydrolysis is believed to occur at the ATP-binding domain by transferring γ-phosphate from ATP to the invariant Asp residue in the DKTG motif of this domain (Lutsenko et al., 2007).

1.2.5 Regulation of the Copper Control Molecules

The proteins involved in the copper homeostasis are regulated at both transcriptional and post-translational levels in eukaryotes. A number of transcription factors have been identified to date. In the case of copper overload, copper binding to Ace1 in yeast (or MTF-1 in mammals) causes metallothionein and SOD to be up-regulated for detoxification (Thiele, 1988; Gralla et al., 1991; Brugnera et al., 1994). In the case of copper deficiency, Mac1 in yeast increases the expression of copper importers (as described below in Section 1.4.1) (Jensen and Winge, 1998). A human transcription factor corresponding to Mac1 has not yet been found. Interestingly, MTF-1 of fruit flies responds to both copper overload and copper deficiency by activating different proteins (see Chapter 5 for details). Regardless of the apparently opposite functional roles, Ace1, MTF-1 and Mac1 all bind to copper cooperatively to form a four-copper cluster (Brown et al., 2002), and this copper binding property might be related to their function in response to cellular copper level (see Chapter 5 of this thesis for further discussion).

Post-translational regulation of copper control molecules has also been reported in eukaryotes. One example of this is the regulation of the location and stability of Ctr1 in response to cellular copper level. Ctr1 is localized in the cell membrane in copper-deficient cells, and has been found to rapidly relocate to cytoplasmic vesicles upon exposure to high level of copper. Furthermore, high rates of Ctr1 degradation have been reported at high cellular copper concentrations (Ooi et al., 1996; Petris et al., 2003). These results imply that the stability of Ctr1 and a change of its sub-cellular localization have roles in regulating copper uptake by Ctr1 (Petris et al., 2003). Interestingly, Mac1 not only regulates the expression of Ctr1, but also regulates it post-translationally by aiding in its degradation (Yonkovich et al., 2002). Similarly, the P-type ATPases Cu exporters ATP7A/B also re-localize in responsive to cellular copper level. ATP7A and ATP7B are predominantly located in the trans-Golgi network under low copper conditions, and are involved in copper insertion into Cu-enzymes such as ceruplasmin, which then carry Cu out of the cell. Upon copper overload, however, ATP7A relocates from the tran-Golgi network to the cytoplasmic membrane, and it is believed that the relocation is associated with copper export activity (Petris et al., 1996). ATP7B also shows similar Cu-dependent relocation in response to copper overload by translocating from the tran-Golgi network to vesicles near the canalicular membrane, and because of this it is believed to function in biliary copper excretion (Schaefer et al., 1999).

1.2.6 Disease Associated with Disorders in Cu Homeostasis

Due to the two-faced nature of copper (both toxic and beneficial), copper homeostasis is critical to ensure proper function of Cu-dependent enzymes while protecting the cell from toxicity of copper. Serious problems can occur when any components of copper homeostasis are disrupted. Two well-studied human examples where there is dysfunction in copper homeostasis are Menkes and Wilson's diseases (Harrison and Dameron, 1999; Mercer, 2001).

Menkes disease is caused by a mutation in the *Atp7a* gene locus on the X-chromosome (Chelly et al., 1993; Mercer et al., 1993; Vulpe et al., 1993). Defects in

ATP7A cause generalized copper deficiency since it is associated with copper insertion into copper-dependent secretory proteins, as described earlier in this chapter (Section 1.2.2.1 and Section 1.2.5). Thus, patients with Menkes disease show symptoms related to deficiency in Cu-dependent enzymes. Among the most notable features of this disease are severe neurological defects, and it is believed this is mainly due to a reduction in dopamine-β-monooxygenase and cytochrome c oxidase activities in the brain (Chelly et al., 1993). Deficiency in Mo-dependent enzymes in the brain may also be part of the neurological defects, as it has been reported that Cu may play an important role in the synthesis of molybdenum cofactor (Kuper et al., 2004), and deficiency in the molybdenum enzyme sulfite oxidase is known to cause serious neurological defects. Current effective treatments of Menkes disease include intravenous administration of Cu(II)-*bis*-histidine complexes in the early stages of the disease (Christodoulou et al., 1998).

In an opposite effect to the copper deficiencies that occur with Menkes disease, patients with Wilson's disease suffer from copper overload. Wilson's disease is caused by defects in the gene encoding another Cu-transporting ATPase ATP7B (Bull et al., 1993; Petrukhin et al., 1993; Yamaguchi et al., 1993). Without properly functional ATP7B, copper in the liver cannot be excreted into bile and thus it accumulates in the liver and subsequently other organs (Li et al., 1991). Copper accumulation in these organs poses problems due to toxicity when copper levels rise above the detoxification capacity within cells, and results in serious damages to the organs concerned. Treatments for Wilson's disease include using copper chelators (e.g. D-penicillamine) to remove copper accumulated in the liver and using increased dietary Zn^{2+} to effectively compete for copper absorption (Walshe, 2006). A study of tetrathiomolybdate as a potential treatment for Wilson's disease is reported in Chapter 7 of this thesis.

1.3 Cu Homeostasis in Prokaryotes

Compared to eukaryotes, considerably fewer components of copper homeostasis have been reported in prokaryotes, and current knowledge mainly comes from studies of *E. coli* and *Enterococcus hirae* (Rensing and Grass, 2003; Solioz and Stoyanov, 2003). The relative simplicity of prokaryotic copper control may be partially due to a lack of intracellular compartmentalization present in eukaryotes, and thus with no need of organelle-specific copper chaperones. The copper homeostasis mechanisms identified so far in *E. coli* are shown in Figure 1-2, and they will be briefly reviewed below.

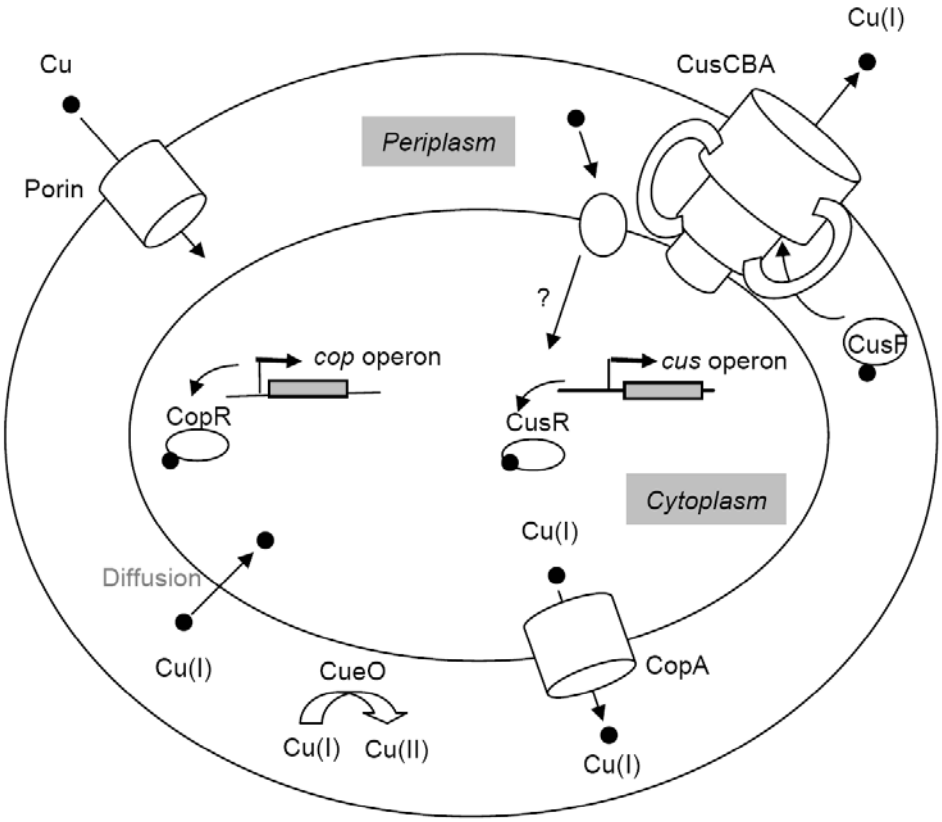

Figure 1-2. Schematic illustration of proposed copper homeostasis in E. coli.

The mechanisms of copper uptake in prokaryotes are not completely understood. It has been inferred that copper can cross the outer membrane into the periplasm through porins, since a copper-resistant, porin-deficient strain has been isolated for *E. coli* (Lutkenhaus, 1977). No specific transporter has yet been reported for carrying copper into the cytoplasm, and it has been proposed that Cu(I) might gain entry into the cytoplasm through simple diffusion (Outten et al., 2001). In contrast, *E. coli* copper efflux systems are better understood. Current work suggests that Cu(I) is pumped out of cell into the periplasm by an inner-membrane ATPase transporter called CopA, as described earlier, followed by oxidation to Cu(II) by the multi-copper oxidase CueO. Periplasmic copper is then pumped out of cell by the CusC(F)BA system (Rensing et al., 2000; Grass and Rensing, 2001; Outten et al., 2001). Exporting Cu by CopA requires the presence of exogenous thiols (e.g. DTT) and ATP (Mandal et al., 2002). Similar to other P-type ATPases, CopA contains two CX_2C motifs in the N-terminal region, which do not seem to be required for function (Fan et al., 2001). No detailed information has been reported concerning the mechanism of copper export by CopA. CueO is a multi-copper oxidase that possesses anti-fungal laccase-like activity. It serves as a safeguard in the periplasm by oxidizing Cu(I) into the less toxic Cu(II). Both CopA and CueO are regulated by a member of the MerR family of metal responsive regulator, CueR (Outten et al., 2000). CueR is extremely sensitive to free Cu(I), which essentially allows no free Cu(I) in the cell (Changela et al., 2003). CueR binds to Cu(I) in a shielded, digonal coordination through two conserved cysteines, as confirmed by crystal structure and X-ray absorption spectroscopy (Changela et al., 2003; Chen et al., 2003). The detailed mechanisms underlying copper-dependent gene regulation by CueR are not yet understood. The CusC(F)BA system forms a membrane-bound, proton-driven transporter complex (Rensing and Grass, 2003). CusA is the centre of the complex and is believed to be responsible for copper transport; CusC is the putative channel-forming protein and CusB is involved in defining the overall structure of the multi-protein complex (Bagai et al., 2007). All three proteins are essential for function (Franke et al., 2003). CusF is a small periplasmic protein which binds to Cu(I) by two methionines and

one histidine (Loftin et al., 2007). It is proposed that CusF delivers copper to the Cus efflux system, and thus facilitates the copper detoxification in the periplasm. Consistent with this, CusF is not essential for the function of the Cus system, but it is required for maximum exporting capacity (Loftin et al., 2007). The CusC(F)BA system is regulated by a two-component regulating system CusRS (Munson et al., 2000; Outten et al., 2001). CusS is a cytoplasmic membrane histidine kinase and may serve as a sensor for copper stress in the periplasm. CusR is a copper-dependent regulator that activates the transcription of *cusCFBA* operon upon copper overload, and also responses to Ag(I) although at a lower sensitivity (Munson et al., 2000; Outten et al., 2001).

Gram-positive bacteria such as *E. hirae* do not have a space equivalent to the periplasmic space of Gram-negative organisms, and the Cus copper control system is thus absent from Gram-positive bacteria (Rensing and Grass, 2003). The P-type transporter ATPase CopA is found in *E. hirae*, but it appears to serve in copper uptake under copper-limiting conditions although evidence for this is indirect (Odermatt et al., 1994). Mutation studies showed that *E. hirae* strains with CopA deletion grow poorly in copper-limited media, and are more resistant to Ag(I), which is assumed to use the same pathway to enter into the cell (Odermatt et al., 1993). A recent structural study on the *E. hirae* CopA by crosslinking and molecular modelling suggest two very unusual copper binding sites in CopA, with Cu coordination by Ser or Asn backbone nitrogen at both sites (Lubben et al., 2009). However, these conclusions seem unlikely as the model of CopA is based on a calcium ATPase (likely to be structurally distinct), and the results are in conflict with NMR data on *E. hirae* CopA homolog in *Bacillus subtillis* (Singleton and Le Brun, 2009). The export of copper in *E. hirae* is achieved by another P-type ATPase which is called CopB (Odermatt et al., 1994; Solioz and Odermatt, 1995). The expression of *cop* operon with *copA* and *copB* genes in *E. hirae* is regulated by CopY. It has been proposed that Zn(II)-bound CopY can bind to the inverted repeat sequence upstream of *cop* operon and thus block the transcription of *cop* operon under normal copper conditions. Upon copper overload, two Cu(I) ions donated by CopZ replace Zn(II) in CopY, and release CopY from the promoter region of cop operon

(Cobine et al., 2002). CopZ is a homologue to Atx1, and it was originally proposed to function as a copper transcription factor. Later studies showed that purified CopZ has the capacity to donate copper to the CopY transcription factor *in vitro* (Harrison et al., 2000). Other targets for CopZ, such as the copper efflux pump, have not yet been excluded.

All the Cu-related transcription factors described above are limited to a subgroup of bacteria. They are the copper-selective orthologs from a multiple-functional protein family that are responsive to a broad range of environmental changes. A widely-distributed Cu-specific regulator was not identified until the discovery of CsoR from *Mycobacterium tuberculosis* (Liu et al., 2007). CsoR is a Cu-dependent regulator in response to copper overload and it has been conserved in most bacteria. Studies on the structure of the Cu-binding site and the functional mechanism of CsoR are described in Chapter 6 of this thesis.

1.4 Restrictions of the Structural Studies on Cellular Cu Control Molecules

Structural studies on the molecules involved in cellular Cu control, particularly on the Cu binding sites, provide essential information for understanding the mechanisms by which copper is transferred between these molecules. To date, and despite significant efforts, only a few crystal structures of these molecules and almost none for copper chaperones, have been reported that include a bound copper ion. Furthermore, Cu(I) ions are silent to other spectroscopic probes such as electron paramagnetic resonance (EPR) spectroscopy and essentially invisible to nuclear magnetic resonance (NMR) spectroscopy due to the quadrupole moment of ^{63}Cu and ^{65}Cu. Thus, most direct information on the binding of copper in copper control molecules has come from X-ray absorption spectroscopy (XAS). In the work comprising this thesis, XAS, complemented by computational chemistry, has been used to probe the structures at Cu binding sites of several components of cellular Cu control, including copper chaperones in the CcO assembly pathway, two Cu-sensitive regulators and Cu-metallothionein.

CHAPTER 2

METHODS AND TECHNIQUES

2.1 Introduction

In this thesis X-ray absorption spectroscopy (XAS) (Sayers et al., 1971; Lee et al., 1981), aided by computational chemistry (Lipkowitz and Boyd, 2000), has been used to study the local structures of the metal centres in Cu control molecules. As a structural tool, XAS has advantages for non-crystalline complex systems because of its element specificity and its sensitivity to the local coordination environment of the element of interest (Teo, 1986). For the systems considered in this thesis, XAS provides detailed local structural information around the copper centres in the proteins with minimum sample preparation. XAS can be divided into two regions: the extended X-ray absorption fine structure (EXAFS) spectrum and the X-ray absorption near-edge spectrum. Analysis of the EXAFS spectrum can yield accurate interatomic distances (within ca. 0.02 Å) between the absorbing atom and the neighbouring atoms, as well as the numbers and types of atoms in the immediate environment (within ~5 Å) of the absorbing atom. Analysis of the near-edge X-ray absorption spectrum can reveal information on the electronic structure of the metal including formal oxidation state, coordination geometry, and the type of ligands around the absorber. The theory and data analysis of X-ray absorption spectroscopy, and in particular for EXAFS, has been

extensively reviewed in the past (Lee et al., 1981; Teo, 1986; Rehr and Albers, 2000). This chapter will provide a brief overview of theory and data analysis aspects of XAS.

X-ray fluorescence imaging (XFI) is a technique for quantitatively determining spatial distribution of element(s) in a sample. It has been an important technique in studying the metal homeostasis and toxicity in the life sciences because of its elemental specificity, good detection limits, its *in situ* and non-destructive nature, and the ability to extract spatial-specific chemical information from complex matrixes (Pickering et al., 2000; Bertsch and Hunter, 2001; Pickering and George, 2007). XFI has been used in this thesis work to trace the distribution of Cu-Mo complexes in biological systems. The experimental setup and data collection procedures pertinent to the work in this thesis will be briefly described later in this chapter.

Although XAS can provide precise local structural information, such as bond lengths, it generally cannot provide three-dimensional (3-D) geometric information. Computational chemistry can potentially predict this information and is thus used as a complementary approach to XAS. In this thesis, quantum mechanics is used to corroborate the structural results from XAS analysis, as well as to postulate possible 3-D structural models near the metal binding site using structural parameters obtained from XAS as a guide. Molecular dynamics (MD) simulations have been used to model the time-dependent behaviour of the solvated protein. Both computational methods will be introduced in more details later in this chapter.

2.2 X-ray Absorption Spectroscopy

2.2.1 X-Ray Absorption

An X-ray beam will lose intensity when passing through matter via various absorption processes, which to a large extent are due to the photoelectric effect. For a monochromatic X-ray beam, the transmitted beam intensity is proportional to the incident beam intensity, and reduces exponentially with the thickness of the given sample. The absorption coefficient (the proportionality constant) is defined by:

$$\mu(E)x = \ln\frac{I_0}{I}, \tag{2.1}$$

where μ is the linear absorption coefficient; I_0 and I are the incident and the transmitted X-ray intensities, respectively; x is the thickness of a homogenous sample. Generally speaking, the absorption decreases with increasing X-ray photon energy. However, when the incident X-ray photon energy matches the core electron binding energy the X-ray photon is absorbed and the core shell electron is ejected out of the atom as a photoelectron (photoionization). The ejection of the core electron results in a core hole in the excited state of the absorbing atom. This photoabsorption process causes an abrupt increase in the absorption coefficient, which is referred to as an absorption edge. The absorption edges are usually named according to the original binding energy level of the core electron ejected by the absorbed photon, as *K*-, *L*-, *M*-edge,…*etc.*, corresponding to the principal quantum number *n* 1, 2, 3, …*etc.*, respectively. Because each element has characteristic binding energy for every core electron, the X-ray photon energy of a given absorption edge is element-specific.

In an XAS experiment the absorption coefficient is measured as a function of the incident X-ray photon energy. The direct absorption process can be difficult to monitor when the sample is dilute such as the case for most biological samples. In such cases, the absorption coefficient of the element of interest can be measured indirectly through products of secondary processes associated with the absorption event. The core hole created by photoabsorption can be filled by a number of mechanisms, and one of these is X-ray fluorescence emission. Here an electron from an outer shell drops down to fill the core hole, with the extra energy released via X-ray fluorescence emission. The energy of the fluorescence photon in this process is simply the difference in the binding energies of the outer and inner electrons (Figure 2-1). The fluorescence yield increases with atomic number, and is larger for K lines than for L lines, or subsequent line emissions (Teo, 1986). Another major mechanism is Auger electron yield. Here the core hole is filled by an outer shell electron which releases energy by ejection of another electron as an Auger electron (Figure 2-1). The kinetic energy of the Auger electron is

equal to the difference between the initial and final state of the atom. Auger emission occurs with higher probability for light elements and at low absorption energies (Teo, 1986). In addition to the two processes described above, emitted Auger electrons or fluorescence photons can eject further electrons from outer shells generating a secondary electron shower, the intensity of which is to a good approximation proportional to the absorption (Stern and Heald, 1983). Therefore, X-ray absorption coefficient can also be obtained by measuring either fluorescence or electron yield:

$$\mu(E)x = C\frac{F}{I_0}, \tag{2.2}$$

where μ is the absorption coefficient; x is the thickness of a homogenous sample; C is a constant; F is the intensity of X-ray fluorescence intensity or electron yield; and I_0 is the incident X-ray intensity. C is normally neglected as it can be eliminated when the EXAFS is extracted.

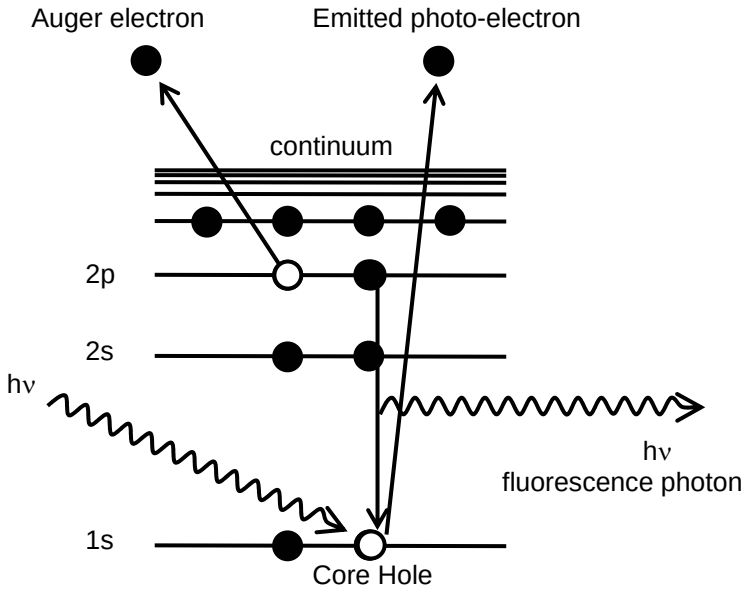

Figure 2-1. Schematic illustration of the fluorescence radiation and Auger electron emission concomitant with X-ray absorption.

2.2.2 Theory of X-ray Absorption Spectroscopy

In XAS, the X-ray absorption coefficient of the element of interest is measured as a function of incident X-ray photon energy. Figure 2-2 shows an example of the Cu K-edge absorption spectrum of copper metal. XAS is usually divided into two spectral regions. That adjacent to the absorption edge is referred as X-ray absorption near edge spectrum, which includes pre-edge features before the absorption edge jump and up to around 50 eV above the absorption edge. The features before the absorption edge in the near edge spectrum reflect the excitation of the core electrons to various bound states, while the near edge features above the absorption edge arise from the effects including many-body interactions, multiple scattering, and bond structure (Lang and Williams, 1978). The near edge features contain important structural information such as oxidation state, the nature of the ligands and coordination state. However, the fundamental theory of the near edge spectroscopy has not yet attained the level in which

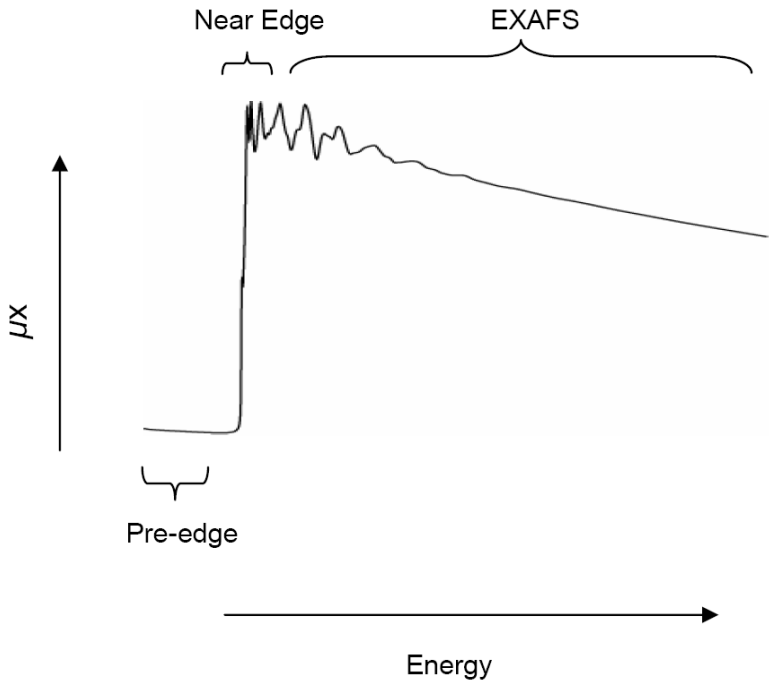

Figure 2-2. Copper K-edge X-ray absorption spectrum of the standard Cu foil.

it can be reliably used as a quantitative structural tool, although most recent improvements in EXAFS theory by Rehr, et al. have shown promise (Rehr and Albers, 2000). Currently the quantification of near edge spectra is largely dependant on comparisons with the spectra of known standards.

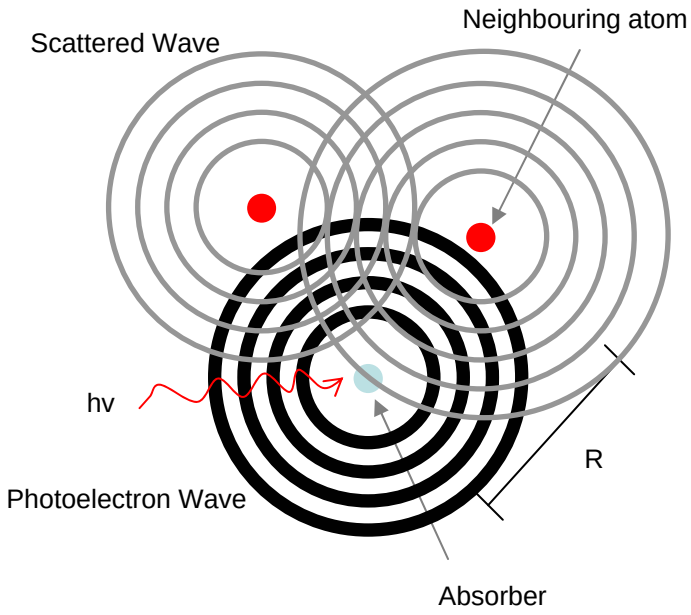

Figure 2-3. Schematic illustration of interaction between the outgoing photoelectron wave of S symmetry emitted by an X-ray photon and the electron wave backscattered from the neighbouring atoms.

The extended X-ray absorption fine structure (EXAFS) refers to the oscillatory modulation of the X-ray absorption coefficient on the high-energy side of an absorption edge, and can extend up to 1000 eV or more above the edge (Lee et al., 1981). The EXAFS phenomenon can be graphically illustrated as in Figure 2-3: the ejected photoelectron traverses away from the absorber, and it can be backscattered by the surrounding atoms when it propagates from the absorber. At the absorber quantum interference between outgoing photoelectron and backscattered photoelectron de Broglie waves modulates the absorption coefficient, which leads to the absorption fine

structure as a function of the incident X-ray photon energy. The EXAFS (χ) is defined as the dimensionless quantity:

$$\chi(E) = \frac{\mu(E) - \mu_0(E)}{\mu_0(E)}, \tag{2.3}$$

where μ_0 is the background absorption coefficient and μ is the observed absorption coefficient. Because the photoelectron interference depends upon how far away the scattering atoms are from the absorbing atom, and upon how many and what types of scattering atoms there are around the absorbing atom, analysis of χ can provide structural information around the absorber.

The theory of the EXAFS has been investigated as early as the 1930's. However, the structural content was not fully understood until a modern theoretical description of EXAFS was developed in the early 1970's (Sayers et al., 1971). In the modern theory of EXAFS, χ is the sum of the interference effects of all the backscatters, as shown in the following equation (Rehr and Albers, 2000):

$$\chi(k) = \sum_i \underbrace{\frac{N_i S_0^2 S_i(k) |f_i(k)|}{kR_i^2} e^{-2R_i/\lambda_i(k)} e^{-2\sigma_i^2 k^2}}_{\text{Amplitude Component}} \underbrace{\sin\left[2kR_i + \varphi_i(k) + 2\delta_c(k)\right]}_{\text{Phase component}}, \tag{2.4}$$

where $|f_i(k)|$ is the EXAFS amplitude function of each of N_i atoms from the i^{th} backscatter shell at the distance R_i from the absorber; S_0^2 is the constant total amplitude reduction factor due to many-body effects at the absorber; $S_i(k)$ is the amplitude reduction factor which is weakly dependent on energy and scattering path of the backscatter type i, and it is a refinement to S_0^2 (Rehr and Albers, 2000); the amplitude reduction term $e^{-2R_i/\lambda_i(k)}$ represents the inelastic losses in the scattering process, where $\lambda_i(k)$ is the energy-dependent photoelectron mean free path function for the atom type i; $e^{-2\sigma_i^2 k^2}$ is a Debye-Waller factor (σ_i^2)-dependent amplitude reduction term, which includes both thermal vibration and static disorder; the frequency of the EXAFS

oscillations is determined by R_i in k space; $\varphi_i(k)$ is the EXAFS backscatter phase shift function for the atom type i; and $\delta_c(k)$ is the EXAFS central atom (absorber) phase shift function (Rehr and Albers, 2000). In the Eq. 2.4, the EXAFS χ is expressed as a function of photoelectron wave vector k which simplifies the relationship with respect to structural parameters. k is defined as:

$$k = \left(\frac{2\pi}{\lambda_e} \right) = \sqrt{\frac{2m_e}{\hbar^2}(E - E_0)} \,, \tag{2.5}$$

where λ_e is the de Broglie wavelength; m_e is the electron rest mass, E is the incident X-ray energy, E_0 is the X-ray threshold energy of the absorption edge.

The equation 2.4 describes EXAFS (χ) in two separable terms: amplitude and phase. In a simplified description, for a given type of backscatter, the larger the distance R_i is, the smaller the amplitude of EXAFS signal will be. The $\sin[2kR_i]$ term describes the phase function of the EXAFS component, with approximately a frequency of $2R_i$ in k space: the larger the distance R_i is, the more the EXAFS signal will oscillate. The R_i defined here specifically refers to single scattering path length between the absorber and one backscatter only. In multiple scattering theory, the photoelectron wave may be scattered from a number of atoms. In such case, the effective R_i is equal to half of the total path length.

EXAFS spectrum in k space can be Fourier transformed to an effective radial distribution function using the following function (Teo, 1986):

$$\rho(R) = \frac{1}{(2\pi)^{1/2}} \int_{k_{\min}}^{k_{\max}} w(k)\chi(k)k^n e^{i2kR} dk \,, \tag{2.6}$$

where n is k-weighting factor, and w is the window function. The use of Fourier transforms with EXAFS spectra was a key step in the development of modern EXAFS theory (Sayers et al., 1971). The Fourier transform describes the local structure in a more visual fashion, with the centre of peaks position close to the distance of

backscatters to the absorber, while the phase shift correction is needed for the real distance (Lee and Beni, 1977):

$$\rho(R) = \frac{1}{(2\pi)^{1/2}} \int_{k_{\min}}^{k_{\max}} w(k)\chi(k)k^n e^{i(2kR+\varphi(k))} dk \,, \tag{2.7}$$

where $\varphi(k)$ is the total phase factor of a particular scattering path of interest which equals the sum of the phase shifts at the central absorbing atom and the neighbouring backscatterer involved in the path.

2.2.3 Data Collection

XAS data acquisition requires an intense tunable source of X-rays. For dilute samples such as those to be studied in this thesis work, the technique can only be done using synchrotron light sources. Synchrotron radiation was first observed accidentally in 1946 during attempts to improve the efficiency of producing high-energy electrons with a betatron (Elder et al., 1947). Synchrotron radiation at modern light sources is often generated by modulating the trajectory of the ultra-relativistic electrons (or positrons) using an array of alternating magnets such as a wiggler located in a straight section of the so-called storage ring where the electrons or positrons circulate (Figure 2-4) (Jiang et al., 2007). Photons are emitted along tangents to the trajectory of the electrons and are polarized in the plane of the storage ring.

Figure 2-4 shows the optical layout of a typical hard X-ray XAS beamline. Radiation exiting the front end region is commonly referred to as “white beam”, as it has a very wide range of photon energies from infrared to γ rays. A vertically collimating mirror is positioned following the front end upstream of monochromator, which serves to collimate the X-ray beam and as a power filter. Following this is the X-ray monochromator which is used to select the desired photon energy from the white beam. Typically the X-ray monochromator uses two vertically arranged Si crystals that are parallel with each other and cut along a lattice plane (Figure 2-4). When the white

X-ray beam passes through the crystals with an incident angle of θ, only photons satisfying the Bragg condition (Eq. 2.8) pass through the monochromator:

$$n\lambda = 2d\sin\theta, \text{ n= 1, 2, 3…..,} \qquad (2.8)$$

where d is the spacing between the lattice planes at the working temperature, and θ is the incident angle of the X-ray beam with respect to the lattice plane. As indicated by Eq. 2.8, the reflected X-rays are not truly monochromatic, since they also contain higher energy harmonics (n>1). The undesired higher energy harmonics can be rejected by detuning the monochromator crystals, that is, setting the second set of crystal off maximum intensity angle position. Harmonic rejection by detuning the monochromater utilizes the fact that the rocking curves of the higher harmonics are much narrower than those of the fundamental (n=1). The second mirror (toroidal mirror) in Figure 2-4 is used to focus beam both vertically and horizontally. The collimating mirror and toroidal mirror can also be used for harmonic rejection by setting them to an angle of incidence that is less than the critical angle for the fundamental but greater than the critical angle for harmonics, so that the latter are not reflected.

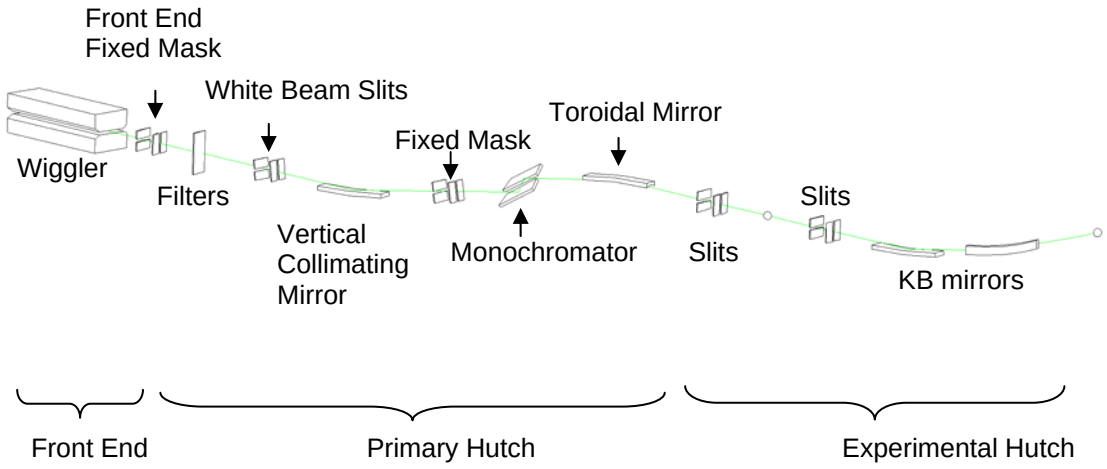

Figure 2-4. Schematic optical layout of the HXMA beam line at the Canadian Light Source.

As mentioned in Section 2.2.1, the X-ray absorption spectrum can be recorded either by measuring the loss of the photon intensity after passing through the sample (transmission), or by measuring the fluorescence or electron yield accompanying the X-ray absorption process. As the Auger effects are significant in the case of light elements, electron yield is normally used when measuring soft X-ray absorption (≤5 keV). In the hard X-ray energy region, X-ray absorption is typically measured either by transmission or by fluorescence yield. X-ray transmission is appropriate for concentrated samples, whereas X-ray fluorescence yield is typically used with dilute samples. The application of XAS to dilute, biological systems typically relies on the state-of-art energy-dispersive semiconductor detector, such as silicon or germanium array detectors. 32-element solid state germanium array detectors have been used for XAS collection of all the protein samples in this thesis work. The experimental setup for fluorescence XAS measurement at the CLS HXMA beamline is shown in Figure 2-5. The sample is set at 45˚ to the incident beam, while the fluorescence detector (a Ge array detector is shown) is set at 90˚ to the incident beam and 45˚ to the sample plane, to minimize the interference from Compton scattering. In most cases, the sample is kept at a temperature of 10 K during data collection using a liquid He cryostat to both reduce the EXAFS amplitude losses due to molecular vibration and to help protect the sample from X-ray beam damage. The spectrum of a standard foil of the element of interest is also collected simultaneously for the purpose of energy calibration. The setup for transmission XAS measurement is similar to fluorescence XAS measurement, but the fluorescence detector is not needed and only the ion chambers are used to measure the transmitted beam intensity. In this case the sample is usually set at 90˚ to the incident beam. The X-ray absorption spectra can be generated using the Eq. 2.1 and 2.2 for transmission and fluorescence XAS, respectively. The thickness of the sample x in Eq. 2.1, and the constant C in Eq. 2.2 will be eliminated when EXAFS is extracted (see Section 2.3.4).

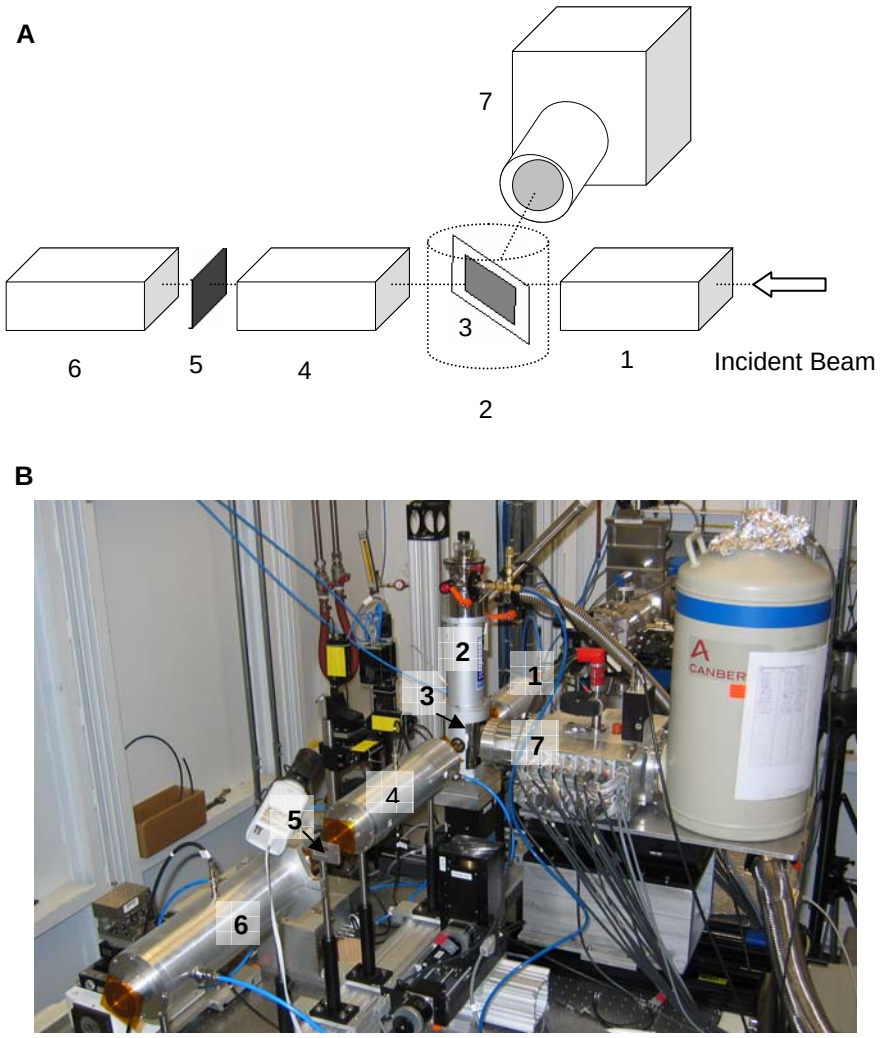

Figure 2-5. A typical experimental setup for a fluorescence XAS experiment. A). schematic drawing of the experimental setup. B) photograph of a fluorescence XAS experiment setup at HXMA beamline of Canadian Light Source. 1, ion chamber I_0; 2, ion chamber I_1; 3, Sample; 4, Liquid-He Cryostat; 5, standard foil; 6, ion chamber I_2; 7, fluorescence detector.

2.2.4 Data Analysis

In order to obtain structural information, the EXAFS data needs to be extracted from the raw absorption data. This extraction process involves energy calibration, data averaging, background removal, conversion of E to k, normalization and μ_0 correction. After the extraction, the amplitude and phase function from each backscatter is typically

calculated using FEFF (Rehr and Albers, 2000), and the structural information is obtained by least-squares non-linear curve-fitting adjusting refinable parameters to obtain best fits.

The XAS data analysis was done using EXAFSPAK throughout this thesis project work (http://ssrl.slac.stanford.edu/~george/exafspak/exafs.htm). Only the general principles are covered in this section. For detailed procedures, please check EXAFSPAK manual (www-ssrl.slac.stanford.edu/~george/exafspak/manual.pdf).

2.2.4.1 Data Reduction

All the Cu data were calibrated with reference to the lowest energy inflection of the absorption spectrum of a standard Cu foil collected simultaneously with the XAS data of the sample (assumed to be 8980.3 eV). The EXAFS $\chi(E)$ is extracted using Eq. 2.3. The experimentally measured total absorption of the sample includes but is not limited to the absorption due to the particular edge of element of interest. The signal below the edge jump is considered as background, which can be fitted with either a polynomial or Gaussian function and then extrapolated beyond the edge and subtracted from the total absorption data. Since the absorption coefficient of the elemental $\mu_0(E)$ is generally unknown, it can be assumed that the smooth part of the measured $\mu(E)$ approximates $\mu_0(E)$. In this thesis work, $\mu_0(E)$ is estimated by fitting a spline function using the least squares procedures to the absorption spectrum above the X-ray threshold energy E_0. A spline function is a function defined over a series of intervals with each interval containing a polynomial of a defined order n; at the knots between adjacent intervals the polynomials share the same derivative values from the zero order up to n-1, i.e. ensuring the n^{th} spline function is continuous across the knots to the order of n-1.

According to Eq. 2.3, to extract the EXAFS, the difference between experimentally obtained absorption and the spline curve needs to be normalized with respect to $\mu_0(E)$, the absorption with absence of neighbouring atoms. However, the experimental background $\mu_0(E)$ obtained by spine fitting is complicated by many factors, such as spectrometer baseline, residual absorption by other elements in the measured

sample, beam harmonics (Teo, 1986). In this thesis work, a theoretical $\mu_0{}^{th}(E)$ is used instead for normalization:

$$\chi(E) = \frac{\mu(E) - \mu_0(E)}{\mu_0^{th}(E)}, \tag{2.3.1}$$

where $\mu_0{}^{th}(E)$ is obtained in the following way: an edge jump value is obtained from the experimental data (e.g. reading the jump size directly from the experimental $\mu(E)$ at a selected energy E', or, reading it from a linear fit to the $\mu(E)$ near the edge at the selected energy), and then the approximation of the function $\mu_0{}^{th}(E)$ is obtained by multiplying this jump value with an energy dependent function estimated by the victoreen equation:

$$\mu_0^{th}(E) = C\lambda^3 - D\lambda^4, \tag{2.9}$$

where λ is the X-ray wavelength; C and D are the Victoreen's absorption coefficients (Macgillavry and Rieck, 1962) and they were scaled to normalize the Victoreen at E' to unity.

The EXAFS $\chi(E)$ is converted to k space using Eq. 2.5. E_0 is chosen with certain liberty here, since it will be readjusted as a fitting parameter when modeled with theoretical scattering amplitude and phase function. In this thesis, E_0 for Cu data has been set to 9000 eV. The EXAFS $\chi(k)$ is multiplied by a certain power of k to compensate for the attenuation of the EXAFS amplitude at high k range. A k^3-weighting has been used in the thesis work unless it is specified otherwise. The k^3-weighting usually leads to a relatively uniform distribution of the weighted-EXAFS amplitude over the typical data ranges used in this thesis (Teo, 1986).

2.2.4.2 Data Fitting

The structural information around the absorber can be extracted from the EXAFS spectrum by fitting the experimental data with theoretical EXAFS calculated based on selected models. There are typically two methods of the EXAFS calculation: one way is to extract amplitude and phase function from the experimental EXAFS of a

known model compound; the other way is to use *ab initio* EXAFS programs such as FEFF (Rehr and Albers, 2000). The parameter variables for the curve fitting are usually the number of atoms N_i, the backscatter–absorber distance R_i, the Debye-Waller factor σ^2_i, and ΔE_{0i}, the shift of X-ray threshold E_0 for the *ith* scattering shell, respectively. In each curve fitting of the Cu EXAFS in this thesis, a common value for ΔE_0 has been assumed for all the different scattering paths involved. The total amplitude reduction factor S_0^2 has been set to 1 for all the Cu data except for the high resolution EXAFS spectra (with $k_{max} > 15$ Å^{-1}). The refinement of the structural parameters is achieved by iteratively nonlinear least-squares searching for the minimum of the sum of the squares of the residuals:

$$F = \frac{\sum k^6 (\chi_{\exp tl} - \chi_{calcd})^2}{\sum k^6 \chi_{\exp tl}{}^2}. \qquad (2.10)$$

Among the structural parameters to be refined in the curve fitting, N and σ^2 are highly correlated with each other, and because of this, these two parameters can only be determined with an accuracy of around ±25% without another source of structural information. Similarly R and ΔE_0 are also correlated with each other. To a first approximation increasing ΔE_0 by *ca.* 3 eV will cause an increase in R of *ca.* 0.01 Å (Teo, 1986). Therefore, it is a common practice to use ΔE_0 and σ^2 values from known model compounds as a guide for determining the chemically best fit, other than solely depending on the numerically best fit defined in Eq. 2.10.

2.2.5 Strengths and Limitations of the EXAFS Technique

The major strength of EXAFS lies in its accuracy in determining the inter-atomic distance R between the absorber and a neighbour atom. The accuracy in determining interatomic distance R by EXAFS is expected to be approximately ±0.02 Å, and thus EXAFS can provide accurate local interatomic distances. Another unique strength of EXAFS lies in its capability of probing local structural information in complex systems without knowledge of long range atomic arrangement. For systems

where a reliable characterization by crystallography becomes difficult, such as the copper chaperones as discussed in Chapter 1, EXAFS might be "the only game in town" for directly probing the structure of the copper binding sites.

Some limitations of EXAFS technique are inherently obvious: it is a local atomic probe by definition and scatterers outside the nearest or the second nearest coordination shells provide EXAFS that is too weak to be reliably analyzed. Therefore the structural information detected by EXAFS is usually limited to within 5-6 Å from the absorber of interest. Additionally, EXAFS alone cannot distinguish backscatters that have similar atomic numbers because the amplitude and phase functions are too similar. When multiple coordination shells overlap because of similar bond lengths, the analysis of the EXAFS can become difficult. The ability of EXAFS to distinguish different components in such cases can be quantized by the resolution of EXAFS ΔR, which is the minimum distance between similar ligands that can be distinguished. ΔR can be approximately estimated by $\pi/2\Delta k$, where Δk is the usable range of the data in k space. For a typical data range, ΔR is around 0.10 - 0.15 Å (George, 1997; Harris et al., 2006). So for backscatterers separated by less than ΔR, the analysis will be model-dependent. Cancellation between the EXAFS of scatterers can also pose problems. This cancellation refers to the destructive effects in the sum of EXAFS signal when two EXAFS components are partially or completely out of phase. As shown in Figure 2-6, the FEFF-calculated EXAFS spectrum of the Cu···Cu interaction at 2.75 Å is partially out of phase with that of Cu···Cu interaction at 2.90 Å in the low energy region and is nearly completely out of phase in the high energy region ($k > 7$ Å^{-1}), and due to this the amplitude of the sum of EXAFS for these two interactions are reduced, especially at the high energy end. The EXAFS cancellation effects are more obvious in the Fourier transform spectra, where the peak for the Cu···Cu interaction at 2.90 Å is reduced to a shoulder of the Cu···Cu interaction at 2.75 Å. Cancellation effects can often be misleading and can pose significant challenges in determining the structure around the metal centre, as further discussed in relevant chapters of this thesis.

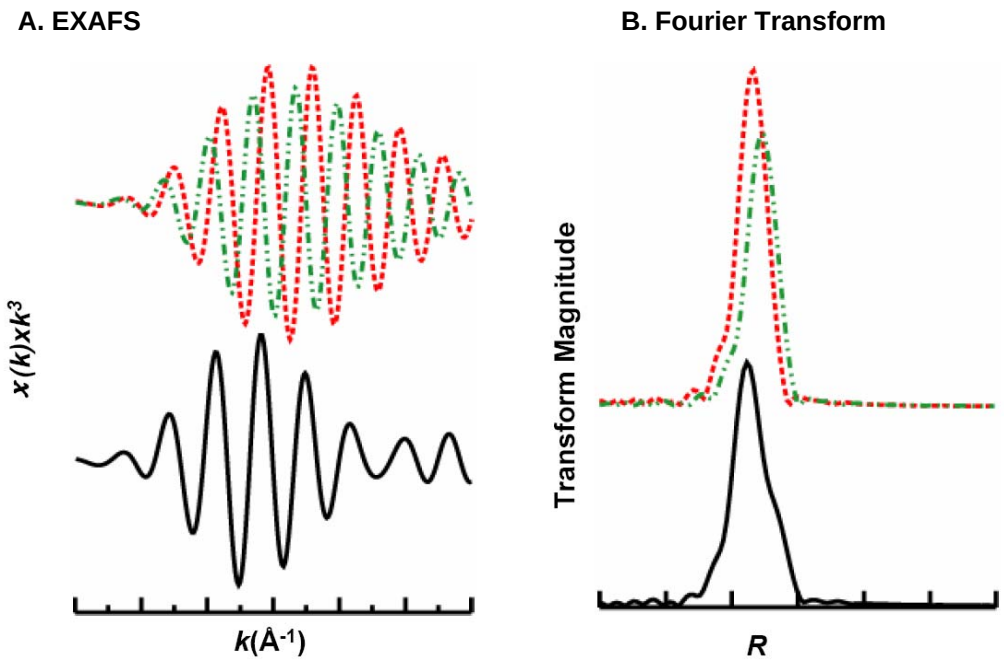

Figure 2-6. Illustration of the cancellation between calculated EXAFS oscillations of two different Cu···Cu interactions. On the top of Panel A are the FEFF-calculated EXAFS spectra for Cu···Cu interactions at 2.75 Å (red dash line) and 2.90 Å (green broken line), respectively, and the bottom is the sum of the two EXAFS components; Panel B show the corresponding Fourier transform spectra.

2.3 X-ray Fluorescence Imaging

As described in Section 2.2.1, an element can absorb incident X-ray photons and release the extra energy in the form of an element-specific fluorescence photon. Therefore, the spatial distribution of the element(s) of interest in the sample matrix can be detected simultaneously by monitoring the element-specific fluorescence signals while raster-scanning the sample matrix with the incident X-ray photon energy above the absorption edge(s) of element(s) of interest. This technique is called X-ray fluorescence imaging (XFI). XFI has several advantages over the more widely employed electron microprobe techniques, including superior sensitivity (below 1 ppm) for most elements with atomic number > 20; the ability to detect non-conductive materials *in situ*; no requirement for ultra-high vacuum sample environment; non-

destructive nature of the measurement (Bertsch and Hunter, 2001). With combination of μ-XAS, XFI can be used for visualizing the spatial location of metals with chemical information (Pickering and George, 2007) and the measurement of metal level can be quantitative (Pickering et al., 2000). The strength and limitations of XFI has been reviewed previously (Bertsch and Hunter, 2001). Here the experimental setup and data processing is briefly described.

The schematic diagram and photograph of a basic XFI setup is shown in Figure 2-7 A and B, respectively. The micro-sized beam can be delivered with a range of beam size from sub-micron level up to a few hundred microns by a variety of optics, including pin hole, capillary, Kirkpatrick-Baez mirrors and Fresnel zone plate depending upon the nature of the question to be addressed. The sample is mounted on a motorized stage and can be raster-scanned in horizontal and vertical directions across the beam path. The scan can be either continuously moving with data taken on the fly, or point by point, depending on the degree of imaging quality required. Typically the sample surface is mounted at 45º to the incident beam, to both minimize X-ray scattering and to facilitate both the positioning of an X-ray fluorescence detector and an optical microscope for sample alignment and monitoring. The optical microscope is focussed on the sample surface, and is typically used to locate features of interest on the sample surface and to monitor the scanning process. The X-ray fluorescence detector is typically placed in the plane defined by the beam path and the beam polarization at 90º to the incident beam to minimize the interference from scattering. Generally an energy-dispersive detector, such as a Si-drift or Ge detector, is used to provide full spectral determination of the fluorescence X-ray signals with low background (Figure 2-7C). The two-dimensional distribution map of element(s) of interest on the sample is obtained by collecting the total counts of element-specific fluorescence in the spectra, as highlighted in the Figure 2-7C, at each pixel of the image as the sample is raster-scanned across the beam path. Ion chambers may also be placed before and after the sample to monitor the flux of X-ray photons used to normalize the fluorescence signal(s) of interest.

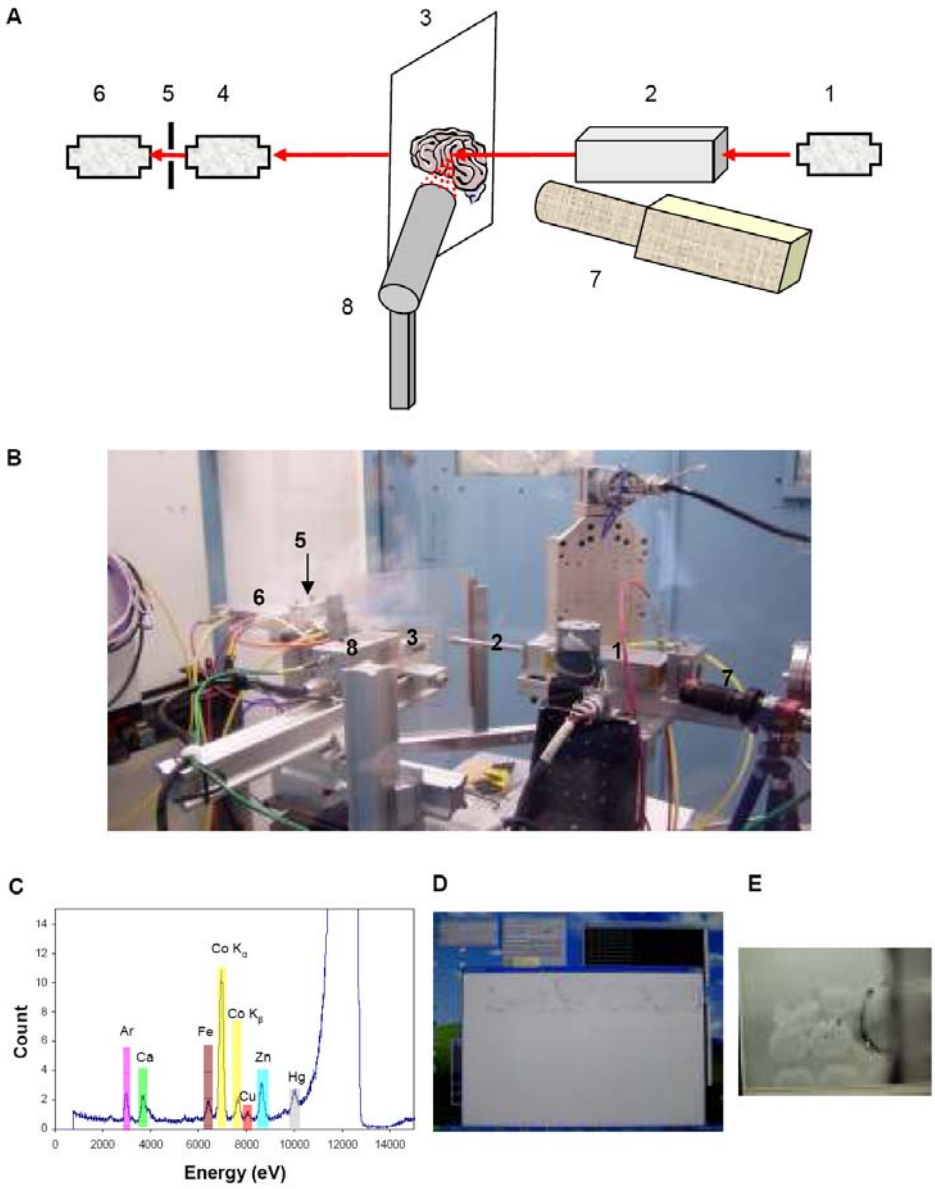

Figure 2-7. Demonstration of basic experimental setup for hard X-ray fluorescence imaging. A) schematic drawing of the basic experimental setup and B) photograph of X-ray fluorescence imaging setup at Beamline 6-2 of Stanford Synchrotron Radiation Laboratory. In both A and B: 1, ion chamber I_0; 2, pinhole or optics for focusing beam (pin hole for B); 3, sample stage; 4, ion chamber I_1 (this is blocked by the sample stage in B); 5, Huber slits; 6, ion chamber I_3; 7, microscope; 8, fluorescence detector. C) spectrum output from the fluorescence detector with of X-ray fluorescence signals from the elements of interest highlighted by colors. D) a fluorescence image as it was being acquired and E) image from the optical microscope during the image scan.

2.4 Computational Chemistry

As a branch of chemistry, computational chemistry incorporates the results from both theoretical and experimental chemistry into efficient computer programs to calculate the structures and properties of molecules, and to predict their chemical reactions (Sax, 2008). Computational chemistry is commonly used to provide complementary information to experimental chemistry. In some cases, the information from experimental chemistry is too expensive to obtain or even not possible from experimental methods, such as the structure of intermediates from chemical reactions. In such cases, the computational chemistry becomes a powerful tool to provide valuable insights into the system that is otherwise unavailable from direct experimentation.

Currently, there are typically two ways to approach chemical problems by computation: quantum mechanical methods and molecular mechanical methods. These terms are used throughout this thesis to be consistent with past literatures. Quantum mechanical methods use *ab initio* (from Latin, meaning "from first principles") or semi-empirical approaches to describe the system with account of the complex motion of all electrons. Quantum mechanical methods provide a high level of detail and subtle information on the electrons of the system, at the expense of computational time which is often considerable. Molecular mechanical methods are based on classical physics, and use force fields with embedded empirical parameters to describe atomic or molecular behaviours of the system. Molecular mechanical methods cannot provide such a complete description as quantum mechanical methods do, but they are orders of magnitude faster to compute and can therefore handle much larger systems such as whole proteins which are not realistically possible using quantum mechanical methods. Both quantum mechanics (QM), specifically density functional theory (DFT), and the molecular mechanics (MM) have been used in this thesis work to provide information that is complementary to that available from EXAFS and to simulate the solution molecular dynamics of the protein. The theories of DFT and molecular dynamics (MD) are briefly described below.

2.4.1 Density Functional Theory

In principle, the quantum mechanical behaviour of electrons in a multiple-electron system can be described by the many-body wavefunction for the system using the time-dependent Schrödinger equation. However, in practice, it is not possible to solve the many-body wave function as the potential of the system not only includes the interactions between electrons and nuclei, but also all the interactions among the electrons themselves. According to the Pauli exclusion principle, no multiple electrons with the exactly same quantum number exist in one atom. An electron in a certain orbital will repel electrons with the same spin state by creating an exclusion area around the electron. This exclusion zone is referred to as the exchange-correlation hole and the potential due to exchange-correlation effects is referred to as exchange-correlation energy (McWeeny, 1960).

DFT bypasses the difficulty in solving many-body wavefunction for N-electron system $\psi(r_1, s_1; ....r_N, s_N)$ by treating electron density $\rho(r)$ as the central variable rather than many-body wavefunction. By doing so, DFT reduces the number of variables in an *N*-electron system from 3*N* to 3, *i.e.* three Cartesian directions. DFT theory is based on Hohenberg-Kohn theorems and Kohn-Sham equation (Hohenberg and Kohn, 1964; Kohn and Sham, 1965). The Hohenberg-Kohn theorems stated that: (1) The external potential is a unique functional of the electron density only. Thus the Hamiltonian, and hence all ground state properties, can be determined solely by the computed electron density. (2) The ground state energy may be obtained variationally, and the density that minimizes the total energy is the exact ground state density. Therefore the total energy of an N-electron system as a function of electron density can be expressed in Kohn-Sham equations as shown below:

$$E[\rho(r)] = T_k[\rho(r)] + \int V_{ext}(r)[\rho(r)]dr + V_H[\rho(r)] + E_{xc}[\rho(r)]. \qquad (2.11)$$

The Kohn-Sham equations decompose a system with *N* interacting electrons into *N* sets of single-electron systems with several energy terms: T_k is the kinetic energy of an *N*

non-interacting electron system with the same electron density in the real system; the external potential V_{ext} is due to Coulomb interactions between electrons and nuclei; V_H is the Hartree potential due to the interaction between the electron at position r and the rest of electrons in the system; and the exchange-correlation potential E_{xc} as described above. Many approximate exchange-correlation functionals have been proposed, including local-density approximation (LDA) and generalized gradient approximation (GGA). LDA approximates the exchange-correlation energy for an electron at position *r* as a function of the local electron density at position *r*, assuming a slowly changing electron density of the system (Gunnarsson and Lundqvist, 1976). Regardless of its extreme simplicity, LDA works accurately for many applied systems, and even works reasonably well in systems where the electron density does change rapidly. However, LDA tends to under-estimate atomic ground state energies and ionization energies, while over-estimating binding energies (Becke, 1989). The GGA uses the gradient of the charge density to correct for deviations in electron density. For systems where the electron density is slowly varying, the GGA is an improvement over LDA (Becke, 1988; Perdew and Wang, 1992).

There are several modern DFT-based software packages available. Regardless of the varied appearances, all DFT-based software packages solve the Kohn-Sham equation iteratively using a user-specified functional until self-consistency is achieved. The most common convergence criteria are that the difference of total energy and density between successive iterations is smaller than a user-defined tolerance.

2.4.2 Theory of Molecular Dynamics Simulations

It has been more than three decades since the first MD simulation on a biological molecule was reported (McCammon et al., 1977). Now MD simulations are one of the most popular tools available for theoretical studies of biological molecules (Karplus and McCammon, 2002). This computational method calculates the time-dependent behaviour and provides detailed information on the dynamics of biological

molecules, which includes protein stability; conformational changes; protein folding; molecular recognition between proteins and between proteins and nucleic acids or membrane complexes; and ion transport in biological systems (Cheatham and Young, 2000; Karplus and McCammon, 2002; Warshel, 2002; Banci, 2003). Molecular dynamics simulations have also been used in structural refinements employing X-ray crystallography and NMR experiments, as well as in rational drug design (Palmer, 2001; Somogyi and Greller, 2001; Brunger and Adams, 2002). Several previous studies have used MD to develop an understanding of the mechanisms of Cu homeostasis (Poger et al., 2005; Holt and Merz, 2007; Rodriguez-Granillo and Wittung-Stafshede, 2009). The results from MD are fully consistent with the structural data that are available. As with DFT, a number of software packages are available for MD simulations. In the work described in this thesis, GROMACS is predominantly used (Berendsen et al., 1995; Lindahl et al., 2001; Van der Spoel et al., 2005).

The MD simulation methods are based on a classical mechanics representation of interacting particles (in this case the particles are atoms within molecules). Newton's equations of motion are solved for a system of N interacting atoms is employed to describe how the particles in the system evolve with time:

$$F_i = m_i \frac{\partial^2 r_i}{\partial^2 t}, \; i = 1,..,N, \tag{2.12}$$

where m_i is the mass, r_i is the trajectory at time t, and F_i is the force applied to the *ith* atom, respectively. F_i is defined by the negative derivatives of a potential function V:

$$F_i = -\frac{\partial V}{\partial r_i}. \tag{2.13}$$

The equation is solved at a small time interval (sub pico-second level), and the coordinates of atoms in the system are recorded as a function of time to represent the trajectory of the system. A force field is needed to generate the potential energies and

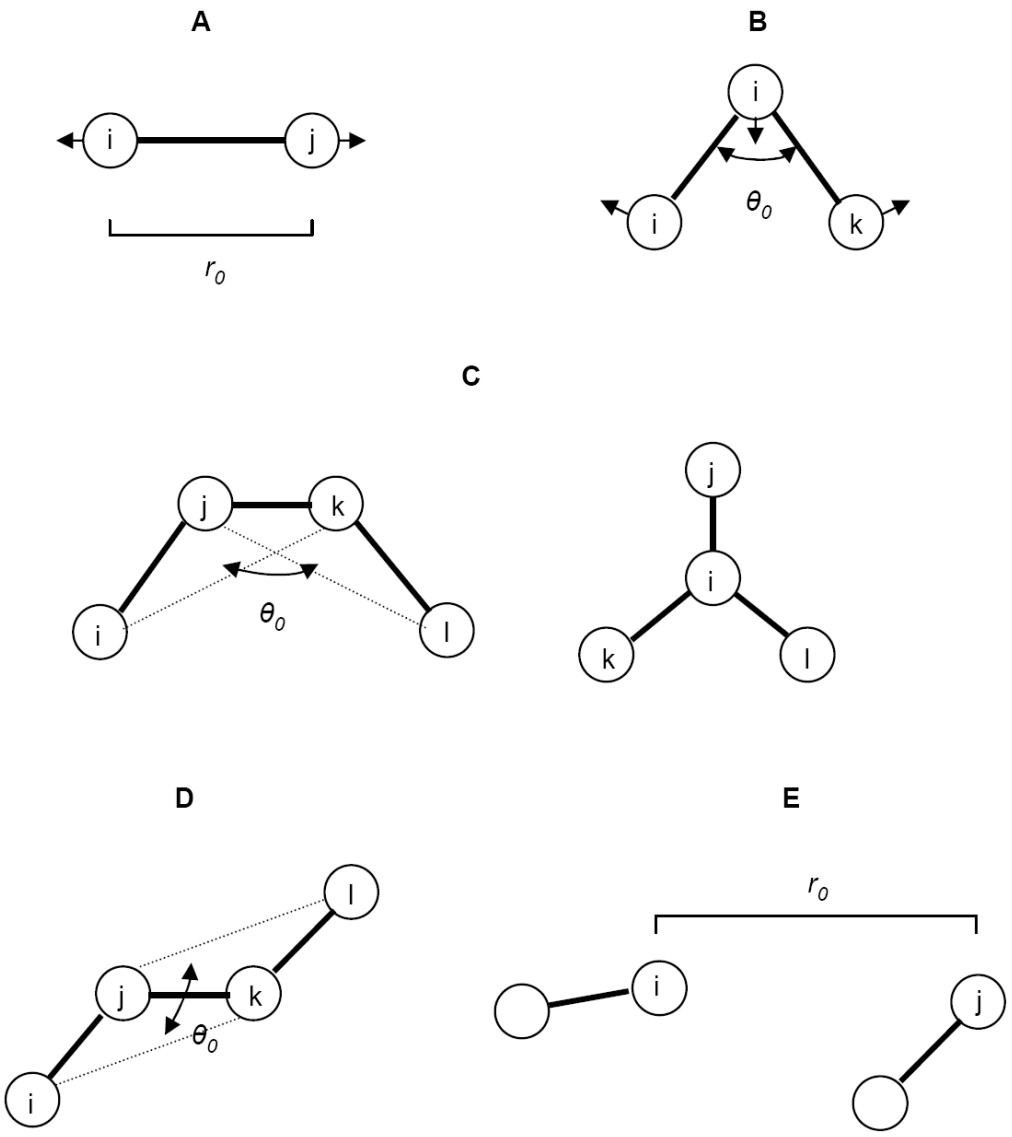

Figure 2-8. Schematic illustration of the atomic interactions in the force fields. A, bond stretching; B, angle bending; C, improper dihedral angle; D, proper dihedral angle; E, non-bonded interactions.

the forces for the interacting particles. The so-called force field here is consisted of a set of equations that define the potential functions and the parameters used in this set of equations. The potential energies can be divided into three categories: bonded interactions, non-bonded interactions and restraints. Force fields can either be selected

from the available choices in the software packages for the simulation or be defined by users. The optimized potential for liquid simulations all-atom force field (OPLS-AA) (Kaminski et al., 1994; Jorgensen et al., 1996) with self-defined restraints is briefly described as below.

a. *Bonded interactions*. Bonded interactions are based on a fixed list of atoms, and they include bond stretching (2-atom interactions), bond angle (3-atom interactions) and dihedral angle (4-atom interactions) (Figure 2.8 A-D). The bond stretching between the covalently-bonded atoms is represented by a harmonic potential which approximates to the potential energy for the vicinity of the equilibrium bond distance r_0:

$$V_{bond}(r) = \frac{1}{2} k_{bond} (r - r_0)^2, \tag{2.14}$$

where k_{bond} is the harmonic force constant in units of $kJ \cdot mol^{-1} \cdot Å^{-2}$. The bond angle vibration in a three-atom system is also represented by a harmonic potential on the bond angle θ:

$$V_{angle}(\theta) = \frac{1}{2} k_{angle} (\theta - \theta_0)^2, \tag{2.15}$$

where the harmonic force constant k_{angle} in units of units of $kJ \cdot mol^{-1} \cdot rad^{-2}$. The dihedral angle ξ in the four-atom system defines the angle between the plane (*i, j, k*) and (*j, k, l*). Improper dihedral potentials are included in the force field to restrict the geometry or conformation, such as planarity or chirality, of the atoms in the system. The improper dihedral potential is also approximated by a harmonic potential:

$$V_{id}(\xi) = \frac{1}{2} k_{id} (\xi - \xi_0)^2. \tag{2.16}$$

For the cases that atoms are allowed to rotate fully about a chemical bond, a proper dihedral potential is used instead of improper dihedral. Due to the requirement of periodicity for complete rotation about a bond, a harmonic potential is not adequate to

describe this type of motion. Instead, a Ryckaert-Bellemans-type potential function is used to define the proper dihedral potential, $V_{pd}(\phi_i)$ (Van der Spoel et al., 1996):

$$V_{pd}(\phi_i) = \frac{1}{2}V_1(1+\cos(\phi+f_1)) + \frac{1}{2}V_2(1-\cos(2\phi+f_2)) + \frac{1}{2}V_3(1+\cos(3\phi+f_3)), \quad (2.17)$$

where V_1, V_2, and V_3 are the barrier height constants; and f_1, f_2, and f_3 are the phase angles which are set to zero for most systems. In this function, the 1-4 interactions between atoms *i* and *l* (shown in Figure 2-8 D) are also been taken into account.

b. *Non-bonded interactions*. The non-bonded interactions refer to the interactions between atoms not included in any of the bonded interactions as described above (Figure 2.8 E). The non-bonded interactions include a repulsion term, a dispersion term and a Coulomb term. The dispersion and repulsion terms are collectively referred as van der Waals interactions, and are described by a Lennard-Jones potential function (Jorgensen et al., 1996):

$$V_{LJ}(r_{ij}) = 4\varepsilon_{ij}[(\frac{\sigma_{ij}}{r_{ij}})^{12} - (\frac{\sigma_{ij}}{r_{ij}})^{6}], \quad (2.18)$$

where σ_{ij} is the mean of the collision diameters (defined as the distance where the inter-particle potential is zero) and ε_{ij} is the mean of the depths of potential well for the atoms *i* and *j*, respectively; r_{ij} is the distance between the two atoms *i* and *j*. In this function, the first component ~ $1/r_{ij}^{12}$, dominating at short distance, describes the repulsion of the two atoms when getting close to each other; and the second component ~ $-1/r_{ij}^{6}$, dominates at long distances and represents the dispersion between two atoms when moving away from each other. The Coulomb potential between two charged (or partially charged) atoms *i* and *j* is given by:

$$V_c(r_{ij}) = \frac{q_i q_j}{4\pi\varepsilon r_{ij}}, \quad (2.19)$$

where q_i and q_j are the charges on the atoms *i* and *j*; ε is the dielectric constant of the medium; r_{ij} is the distance between the two atoms *i* and *j*. Theoretically the number of

such interactions can be huge in most defined systems because each atom may interact with all other atoms in the system. Practically, a spatial cutoff is applied to reduce the number of non-bonded interactions within a reasonable range for the efficiency of the simulation. In this thesis work, a 10-Å cutoff is applied for all non-bonded interactions, since the interactions between atoms beyond this distance are negligible to the total energy in the system.

c. *Restraints*. Special potentials can be used to restrict the motion of the system within a reasonable range or to be consistent with experimental data. Such restraints can be applied to position of the atom(s), distances, bond angles, dihedral angles, or upon the orientation of the vectors. Restraints applied in the MD simulations in this thesis work will be described in more details in Chapter 6.

CHAPTER 3

CU(I) CLUSTERS IN THE COPPER CHAPERONES FOR CYTOCHROME C OXIDASE ASSEMBLY

3.1 Abstract

A number of proteins have been found to be involved in delivering Cu to cytochrome c oxidase, the terminal enzyme of the respiratory chain in the mitochondrion: they are Sco1, Sco2, Cox11, Cox17, Cox19 and Cox23. Important questions concern the molecular mechanisms underlying target protein recognition and Cu delivery, and structural studies on both the proteins and metal binding sites are essential in developing mechanistic understanding. In this project, X-ray absorption spectroscopy and computational chemistry were used to study the metal centres in Cox19 and Cox23. X-ray absorption spectroscopy results show that Cox19 and Cox23 resemble Cox17 in forming a trigonal Cu(I)-thiolate poly-copper cluster, but the nuclearity of the cluster is unclear. Mutagenesis and X-ray absorption spectroscopy were used in combination to understand the role of the cysteinyl residue Cys30 which is critical for Cu(I) binding and for in vivo function of Cox19. The effects of protein concentration and dithiothreitol were also investigated by X-ray absorption spectroscopy.

3.2 Introduction

Cytochrome c oaxidase (CcO) is a multiple-subunit enzyme that is located in the inner mitochondrial membrane (Ferguson-Miller and Babcock, 1996). It is the terminal enzyme in the respiratory chain, catalyzing electron transfer from cytochrome c to dioxygen (Kadenbach and Merle, 1981; Capaldi et al., 1983). CcO contains between 7 and 13 subunits, depending on the organism, among which 3 subunits (Cox1, Cox2 and Cox3) are mitochondrially expressed, while the remainder are encoded by nuclear genes (Carr and Winge, 2003; Stiburek et al., 2006). Proper assembly of all the subunits in the mitochondrion and insertion of essential cofactors such as copper, heme, magnesium and zinc into their designated sites is required for fully functional CcO (Hamza and Gitlin, 2002). There are two copper binding sites in CcO designated as Cu_A and Cu_B, respectively. Cu_A is located in the carboxyl domain of Cox2 in the intermembrane space (IMS), and contains a mixed-valence, binuclear-Cu cluster. This copper binding site serves as the primary electron acceptor from cytochrome c. Cu_B site in the Cox1 unit contains a single Cu ion centre which associates with heme a_3 (Beinert, 1995; Tsukihara et al., 1995). This heme-copper binuclear centre receives electrons transferred from Cu_A site via heme a and it is the active site of O_2 reduction to H_2O (Tsukihara et al., 1995; Tsukihara et al., 1996).

The fact that both Cox1 and Cox2 are expressed in the mitochondrion suggests that copper ions are transferred from the cytoplasm into the mitochondrion and then inserted into these sites (Hamza and Gitlin, 2002). A series of proteins, which include Cox11, Cox17, Cox19, Cox23, Sco1 and Sco2, are believed to be involved in the delivery of copper into the mitochondrion and/or the insertion of copper into Cox1 and Cox2, respectively (Hamza and Gitlin, 2002; Carr and Winge, 2003; Cobine et al., 2006) (Figure 3-1). Sco1 is an inner mitochondrial membrane protein with the single transmembrane helix and a globular domain protruding into IMS (Balatri et al., 2003). It has been suggested that Sco1 is involved in copper insertion into the Cu_A site in Cox2

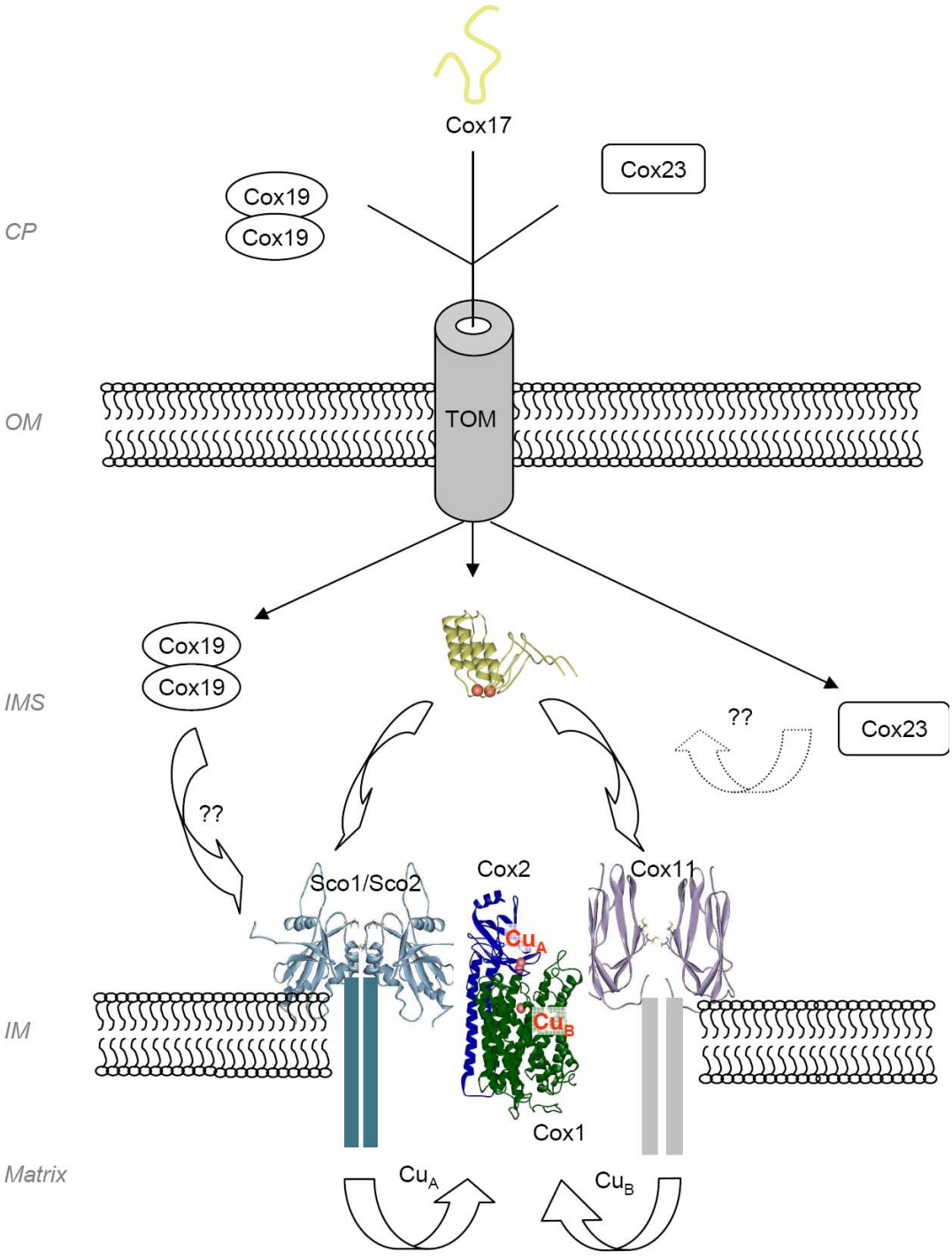

Figure 3-1. The schematic view of proposed Cu delivery pathway in cytochrome c oxidase assembly. CP, cytoplasm; OM, mitochondrial outer membrane; IMS, mitochondrial inner membrane space; IM, mitochondrial inner membrane; Matrix, mitochondrial matrix; TOM, mitochondrial protein transport machinery of outer membrane.

and that the single transmembrane helix is required for functional Sco1 (Chinenov, 2000; Dickinson et al., 2000; Beers et al., 2002). Sco1 contains a conserved potential metal-binding motif CX_3C (where X denotes non-cysteine residues) and can bind to both Cu(I) and Cu(II). Reported evidence implies that both Cu(I) and Cu(II) binding is required for normal function of Sco1 (Rentzsch et al., 1999; Nittis et al., 2001; Horng et al., 2005). Structural rearrangement has also been observed in the a protruding loop (designated Loop 8) of Sco1 upon Cu binding (Banci et al., 2006a). The conserved residues in the sequence motif ^{217}KKYRVYF^{223} on the leading edge of this loop are thought to be involved in the interaction between Sco1 and Cox2 (Rigby et al., 2008). Sco2 is a homolog of Sco1, but it may play a different role in the CcO assembly. Sco1 but not Sco2 is essential for CcO activity in yeast, and deficiency of Sco1 cannot be completely relieved by overexpression of Sco2 (Glerum et al., 1996b). In humans, however, Sco1 and Sco2 may play independent, cooperative roles in the Cu insertion into the Cu_A site (Leary et al., 2004). The maturation of Cu_B site in Cox1 of CcO requires the activity of Cox11 (Tzagoloff et al., 1993; Hiser et al., 2000). Cox11 forms a dimer in the inner mitochondrial membrane and binds to Cu(I). Like Sco1, Cox11 has a single transmembrane helix in the N-terminal domain and a soluble domain in the C-terminal domain extended to the IMS (Banci et al., 2004). X-ray absorption spectra suggest that the Cox11 dimer contains a binuclear-Cu(I) cluster with each Cu(I) ligated to sulfur from three conserved cysteines, Cys111, 208 and 210 (Carr et al., 2002). The mechanism of how Cu(I) is inserted into the Cu_B site by Cox11 remains unclear. Functional studies show that Cox11 from *S. pombe* exists as a natural fusion protein with the partner protein homolog to a component in the small subunit of mitochondrial ribosome in *S. cerevisiae* (Saveanu et al., 2001). In addition, an N-terminal portion of Cox11 has showed weak interaction with a mitochondrial ribosomal component (Khalimonchuk et al., 2005). Based on these observations, it has been proposed that Cu(I) insertion into nascent Cox1 by Cox11 may occur co-translationally or in the assembly of Cox1, Cox4 and Cox5A subcomplex (Khalimonchuk et al., 2005).

Cox17 is a small, Cys-rich, Cu-binding protein, conserved in all the eukaryotes sequenced so far (Arnesano et al., 2005b). It exists both in cytoplasm and in IMS of the mitochondrion. Cox17 is proposed to deliver copper to both the Cu_A site via Sco1 and to the Cu_B site via Cox11, although no stable interactions between Cox17 and Sco1 or Cox11 have been observed (Horng et al., 2004). The function of Cox17 in CcO assembly is unlikely to be associated with shuttling Cu ions from cytoplasm into the mitochondrion, since engineered Cox17 tethered to the inner membrane of mitochondrion is still fully functional (Maxfield et al., 2004). Cox17 deletion mutations can be overcome either by addition of Cu to the medium or by over-expression of Sco1 or Sco2 (Glerum et al., 1996b; Glerum et al., 1996a). Fully reduced Cox17 can bind up to three Cu per protein, while partially oxidized Cox17 containing two disulfide bridges binds to single Cu per protein (Arnesano et al., 2005a). Mutagenesis studies show that three of six conserved cysteines in the CCX_9C motif, Cys23, 24 and 26, are essential for functional Cox17 *in vivo,* and are predicted to be directly involved in Cu-binding (Heaton et al., 2000). In addition Cys57 is also essential for Cox17 activity and this residue may be involved in Cu transfer to Sco1, rather than in directly binding to the Cu ion (Horng et al., 2004). Different Cox17 conformers have been reported in structural studies. Size exclusion chromatography experiments suggest that Cox17 isolated from bacterial sources is in equilibrium between dimer-monomer ($K_D \sim 5\mu$M) and tetramer-dimer ($K_D \sim 20\mu$M), and that the tetramer is more efficient than the dimer in transferring Cu to Sco1 *in vitro* (Horng et al., 2004). The UV-visible electronic spectra of Cox17 suggest trigonal coordination of Cu(I) in a solvent-shielded environment (Srinivasan et al., 1998). In agreement with this, Extended X-ray absorption fine structure (EXAFS) spectroscopy of Cu-loaded Cox17 demonstrates the presence of a poly-copper cluster, with each Cu ion being ligated by three thiolates sulfur (Srinivasan et al., 1998). In contrast, only monomeric species have been identified by nuclear magnetic resonance (NMR) spectra and by mass spectroscopy (MS) (Abajian et al., 2004; Palumaa et al., 2004; Arnesano et al., 2005a; Banci et al., 2008). The NMR data also suggest that Cu(I) is bound by Cys23 and Cys26, and that there is a disulfide bond

switch from Cys26-Cys57 to Cys24-Cys57 prior to Cu binding. It remains a mystery which Cox17 conformer is physiologically relevant.

Cox19 and Cox23 resemble Cox17 in many aspects (Nobrega et al., 2002; Barros et al., 2004; Rigby et al., 2007). Firstly, they are all members in a family of small, soluble, Cu-binding proteins. Secondly, they are all widely distributed among different species, from fungi to plants and animals. Thirdly, a twin CX_9C structural motif is conserved among these proteins, and this motif forms a helical hairpin conformation in Cox17. Fourthly, they are all present both in cytoplasm and in the IMS of the mitochondrion. Fifthly, deletion mutation of any of these proteins results in loss of CcO activity, suggesting they are involved in the Cu delivery/insertion pathways during CcO assembly considering their Cu-binding properties. Regardless of these similarities, differences have been found among these proteins, implying they are playing different roles in the CcO assembly pathway. Unlike Cox17, Cox19 mutant cannot be suppressed by increasing copper concentration in the medium (Nobrega et al., 2002). Preliminary studies show that Cox19 can partially transfer copper to Sco1 in the absence of Cox17, but Cox19 cannot relieve the loss of CcO activity caused by Cox17 deletion (*Winge et al.*, personal communication) (Rigby et al., 2007). Yeast with Cox19 tethering to the inner membrane of mitochondrion can still grow with glycerol as carbon source, although the CcO activity reduces to 50% of the wild type. Structures and metal binding properties of Cox19 have been previously characterized (Rigby et al., 2007). According to this study, size exclusion chromatography experiments show that Cox19 exists as a dimer at low protein concentration (<100 μM). Metal analyses indicate Cox19 binds to one Cu(I) per monomer of protein (as purified from *E. coli* with supplemental Cu in the medium in the presence of 1 mM DTT during purification). Cox19 starts to form higher order of oligomers when it is concentrated to more than 300 μM. Like Cox17, the UV-visible spectra suggest Cu(I) in a solvent-shielded environment. Sequence alignment analysis shows that Cox19 contains four cysteines, namely Cys30, 40, 52 and 62, widely conserved among species from yeast to mammals, as well as in Cox17. Cys30, but not Cys40, 52 and 62, is critical for the functional

Cox19 according to site-directed mutagenesis results. The absence of Cys30 results in severe deficiency in Cox19 activity, and the double mutation of Cys30 and Cys62 completely abolishes the activity of the protein. Correlated with this, the Cox19 mutant with substitution of both Cys30 and Cys62 with alanine shows much lower Cu(I) binding than wild type protein. The exact role of Cox19 in the CcO assembly pathway remains unclear. Cox23 deletion mutants can be rescued by overexpression of Cox17 together with a increased medium copper, but not vice versa. This may imply that Cox23 may function upstream of Cox17 in the same pathway (Barros et al., 2004).

While extensive studies of both biochemical and structural properties of Sco1, Sco2, Cox11 and Cox17 have been reported as described above, little is known about the nature of copper binding of Cox19 and Cox23. In order to approach an understanding of the mechanisms of Cu transfer from Cox19 and Cox23 to their targets, X-ray absorption spectroscopy (XAS) and computational chemistry have been used to study the metal binding properties of yeast Cox19. The Cu centre of Cox23 was also briefly explored and compared to other CcO-related copper chaperones in this study.

3.3 Material and Methods

3.3.1 Sample Preparations

Samples were prepared either by the candidate or by members of *Dr. Dennis R Winge*'s group at University of Utah. The expression vectors containing *cox19*-Strep or cox23-Strep alleles were transformed into competent BL21 (pLysS) *E. coli*. Transformants were grown at 37°C to an O.D.600 = 0.6 (AU), induced by the addition of 0.45 mM isopropyl 1-thio-β-D-galactopyranoside, and incubated for an additional 4 h at 30°C. For purification of copper-loaded protein, $CuSO_4$ was added to the culture medium, to a final concentration of 1 mM, just prior to induction. Cells were then washed and resuspended in 50 mM Tris, 100 mM NaCl, pH 8.0 buffer. Cells were lysed by freeze-thawing followed by repeated sonication in buffer either with or without 1 mM dithiothreitol (DTT) added. Lysate was cleared by centrifugation at 50,000g for 30

min at 4°C and the supernatant was saved for protein purification. The following purification procedures were performed either at 4°C, aerobic condition or at room temperature under anaerobic condition for purification with DTT or without DTT, respectively. Supernatant was loaded onto a 10 ml Strep-Tactin column (Qiagen), pre-equilibrated in 50 mM Tris, 100 mM NaCl, pH 8.0 buffer either with or without 1 mM DTT. The column was then washed 3 times; once with 40 ml of wash buffer (50 mM Tris, 100 mM NaCl, pH 8.0), once with 40 ml of high salt buffer (50 mM Tris, 500 mM NaCl, pH 8.0), and again with 40 ml of original wash buffer. Purified protein was then eluted off with 40 ml of buffer (50 mM Tris, 100 mM NaCl, pH 8.0, 1 mM desthiobiotin). The purified protein was concentrated to the desired volume in a 5000 Da-cutoff Vivaspin 20 (VivaScience) spin column. Flow through, washes 1-3, and elution fractions were analyzed by SDS-PAGE on a 15% polyacrylamide gel and visualized by Coomassie staining. Protein was quantified by UV absorption at 280 nm after acidification and then confirmed by amino acid analysis on a Hitachi L-8800 analyzer after hydrolysis in 5.7 N HCl containing 0.1% phenol *in vacuo* at 110°C. Copper concentrations were determined for the same fractions by using a Perkin-Elmer AAnalyst 100 atomic absorption spectrophotometer. In some cases as specified later, pure, concentrated protein was subjected to 12 h dialysis in wash buffer either with or without 1 mM DTT at 4°C using a Slide-A-Lyzer dialysis cassette with a 3500 Da-cutoff membrane (Pierce).

For reconstitution studies, apo-Cox19-Strep was denatured and reduced in 6 M guanidinium HCl, 100 mM DTT for 1 h at room temperature. The protein was desalted into 50 mM Tris, 100 mM NaCl, pH 7.4 buffer using Bio-Gel P-6 resin (Bio-Rad). Cysteine reduction was verified by quantifying reduced thiols by the 2,2'-dithiodipyridine (DTDP) assay described previously (Grassetti and Murray, 1967). Cu(I)-acetonitrile was added to apo-Cox19-Strep with a ratio of Cu:protein around 5:1. The unbound Cu(I)-acetonitrile was removed using Bio-Gel P-6 resin. The samples used in this study are listed in Table 3-1.

Table 3-1. List of samples.

Sample	Specification
Cox19-1mMDTT	Cox19, wild type, 1.33 mM Cu-equivalent protein with 1mM DTT in the buffer
Cox19-mut	Cox19 mutant with Cys30 and Cys62 substituted by Ala, 0.5 mM Cu-equivalent protein, in the presence of 1mM DTT in the buffer
Cox19-500μMDTT	Cox19, wild type, 1.04 mM Cu-equivalent protein, with 500 μM DTT in the buffer
Cox19-dim	Cox19 dimer, isolated from Cox19-500μMDTT by gel filtration, 908 μM Cu-equivalent protein, 500 μM DTT in the buffer
Cox19-tet	Cox19 tetramer, isolated from Cox19-500μMDTT by gel filtration, 415 μM Cu-equivalent protein, 500 μM DTT in the buffer
Cox19-0DTT	Cox19, wild type, 1.12 mM Cu-equivalent protein, purified with 0.75 mM DTT in the buffer, and then DTT was removed by dialysis
Cox23	Cox23 wild type, 1,5 mM Cu-equivalent protein, purified with 1mM DTT in the buffer

3.3.2 Size Exclusion Chromatography

Analytical size exclusion chromatography was utilized to evaluate the quaternary state of apo- and Cu-Cox19-Strep using an S-75 column equilibrated with 50 mM Tris, 100 mM NaCl, pH 8.0, either with or without 1 mM DTT. Data were recorded using Unicorn^{TM} (GE Healthcare) software and an AKTA Fast Protein Liquid Chromatography unit (Amersham Pharmacia). 0.1 ml of metal-free or Cu-bound protein was loaded on the column and eluted over 1.5 column-volumes fractionated into 1ml fractions. Elution profiles were monitored by absorbance at 280 nm and fractions were assessed for copper by atomic absorption spectroscopy. Higher protein concentrations were also analyzed. Low molecular weight size standards from Amersham Pharmacia were used for column calibration.

3.3.3 X-ray Absorption Spectroscopy Data Collection

X-ray absorption spectroscopy measurements were conducted at the Stanford Synchrotron Radiation Lightsource with the SPEAR 3 storage ring containing 80-100mA at 3.0 GeV. Copper K-edge data were collected using beamline 9-3 with a wiggler field of 2 Tesla and employing a Si(220) double-crystal monochromator. Beamline 9-3 is equipped with a rhodium-coated vertical collimating mirror upstream of the monochromator and a bent cylindrical focusing mirror (also rhodium-coated) downstream of the monochromator. Harmonic rejection was accomplished by setting the energy cut-off angle of the mirrors to 12 keV. The incident and transmitted x-ray intensities were monitored using nitrogen-filled ionization chambers, and x-ray absorption was measured as the copper Kα fluorescence excitation spectrum using an array of 30 germanium detectors (Cramer et al., 1988). During data collection, samples were maintained at a temperature of approximately 10 K using an Oxford instruments liquid helium flow cryostat. For each sample, four 35-min scans were accumulated, and the energy was calibrated by reference to the absorption of a standard copper metal foil measured simultaneously with each scan, assuming a lowest energy inflection point of the copper foil to be 8980.3 eV.

3.3.4 X-ray Absorption Spectroscopy Data Analysis

The extended x-ray absorption fine structure (EXAFS) oscillations $\chi(k)$ were quantitatively analyzed by curve fitting using the EXAFSPAK suite of computer programs (http://ssrl.slac.stanford.edu/exafspak.html). *Ab initio* theoretical phase and amplitude functions were calculated using the program FEFF version 8.25 (Rehr et al., 1991). No smoothing, filtering, or related operations were performed on the data.

3.3.5 Computational Chemistry

The initial structural model for computational chemistry of the copper centre in Cox19 was based on EXAFS curve fitting results. Geometry optimization of the model structure was initially performed using the semi-empirical code MOPAC, employing the PM5 Hamiltonian (Fujitsu Cache WorkSystem Pro Version 6.1) and then further

refined by density functional theory (DFT) (Accelrys 3.2 DMol^3). The Becke exchange (Becke, 1988b) and Perdew correlation (Perdew and Wang, 1992) functionals were used in the DFT calculations; calculations were spin-unrestricted, and convergence tolerance criteria were set as medium with energy change at less than 2.0 x 10^{-5} Hartree. Convergence was achieved within the maximum iterations of 50. Optimization on the refined metal centre tethered with short peptides was executed by molecular mechanics (Fujitsu Cache WorkSystem Pro Version 6.1) using Augmented MM3 parameters.

3.4 Results

3.4.1 Structural Study on the Copper Centre of Cox19

3.4.1.1 XAS of the Copper-Binding Sites in Cox19 and its Non-Functional Mutant

Cu K-edge X-ray absorption data were collected for Cu-loaded wild type Cox19 (CuCox19) to probe the structure around the copper-binding centre. The non-functional mutant Cox19-C3062A, with both Cys30 and Cys62 replaced by Ala, was also studied using XAS to test whether the copper binding is modified in the mutant. Both the wild type and the mutant were prepared at 4°C under the aerobic conditions, in presence of 1 mM DTT.

The Cu K-edge near-edge spectrum of CuCox19 showed a feature at 8983 eV diagnostic of a 1s $\rightarrow$ 4p Cu(I) transition (Kau et al., 1987) (Figure 3-2). Quaternary Cu(I) complexes have near edge features above 8985 eV, and thus the presence of quaternary Cu(I) coordination in CuCox19 is ruled out (Kau et al., 1987). The X-ray absorption near edge spectra for $[Cu_4(SPh)_6]^{4-}$, containing a trigonal Cu(I) coordination, and $[Cu(SC_{10}H_{12})_2]^{2-}$ with a digonal Cu(I) coordination are also included in Figure 3-2 for comparison (Bowmaker et al., 1984; Dance, 1986). No low molecular weight Cu(I) compounds that are four-coordinate with thiolate donors have been reported. The energy and intensity of the near-edge features shown in CuCox19 are similar to those seen in the trigonal Cu(I)-thiolate cluster, suggesting trigonal Cu(I) thiolate coordination in CuCox19. The near edge features in the Cox19-C3062A double mutant

are essentially the same as the wild type (Figure 3-2), suggesting same/similar copper binding sites in both proteins.

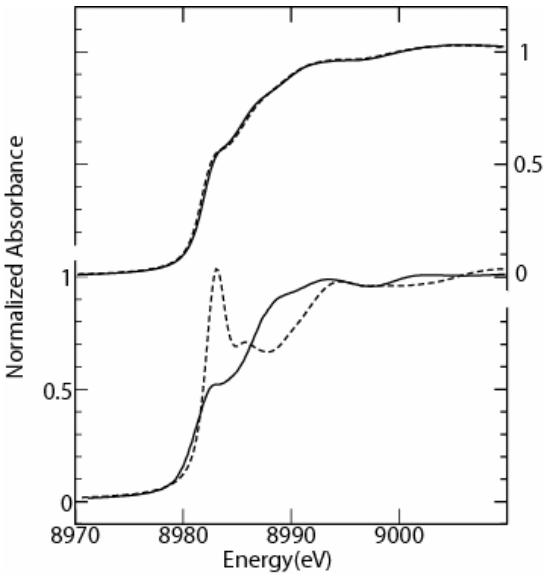

Figure 3-2. Comparison of Cu K-edge X-ray absorption near-edge spectra Cox19 wild type, non-functional mutant Cox19-C3062A with Cu(I)-thiolate model compounds. On the top are the Cox19 wild type (solid line); Cox19-C3062A, the mutant with both Cys30 and Cys62 substituted by Ala (dash line). On the bottom are the two model Cu(I) thiolate compounds – a trigonal Cu(I) complex, $[Cu_4(SR)_6]^{4-}$ ($[Cu_4(SPh)_6]^{4-}$) (solid line), and a digonal Cu(I) complex, $[Cu(SR)_2]^{2-}$ ($[Cu(SC_{10}H_{12})_2]^{2-}$) (dash line).

The Cu K-edge EXAFS and Fourier transform for CuCox19 is shown in Figure 3-3A and B, respectively. Two main peaks are seen in the Fourier transform, indicating prominent backscattering from two shells of neighbouring atoms. The transform peak at around 2.3 Å was best fit with three sulfur ligands at 2.26 Å (Table 3-2). This Cu—S distance is typical of trigonal Cu(I) coordination, and excludes digonal Cu(I) coordination, for which shorter Cu—S bond lengths (2.17 ± 0.01 Å) are expected (Bowmaker et al., 1984; Dance, 1986). Trigonal coordination here refers to the coordination environment with 3 ligands, which are not necessarily coplanar, and digonal coordination refers to a linear or nearly linear 2-coordinate environment. These definitions will be used throughout this thesis unless otherwise specified. Fits of the EXAFS data were attempted using nitrogen/oxygen ligands but in all cases these were

inadequate. The Fourier transform peak at about 2.7 Å is well reproduced by copper backscattering, which confirms the presence of a polycopper cluster in Cox19. The nuclearity of the polycopper centre in Cox19 is unclear. The best fit is achieved by including 3 Cu atoms with two shorter Cu···Cu interactions at 2.66 Å and one longer Cu···Cu interaction at 2.86 Å (Table 3-2). It is noted that this fit leads to a significantly larger Debye-Waller factor for both Cu···Cu interactions compared to that of tetranuclear Cu thiolate clusters in other reported Cu-binding proteins (Brown et al., 2002; Xiao et al., 2004). A fit with only one Cu in the scattering shell arising from a binuclear site increased the fit error from 13.9% to 16.9%. However, the differences in the fit error between two fitting models are not sufficiently significant to determine the nuclearity for polycopper cluster in Cox19. Based on the dimer conformation and the 1:1 ratio of copper to protein, the two-copper cluster model as described earlier (Srinivasan et al., 1998), has been used in the fitting by including one Cu···Cu interaction in the second scattering shell.

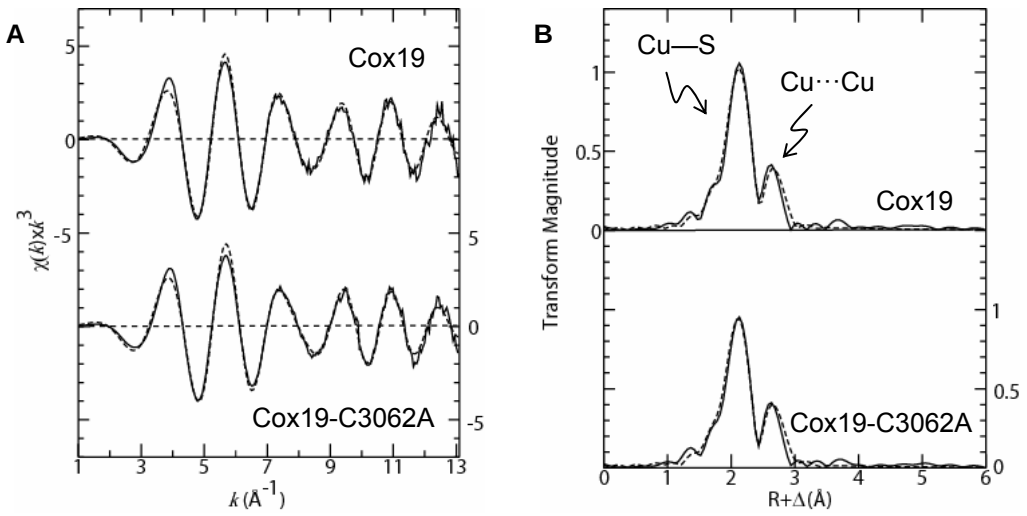

Figure 3-3. A) EXAFS and B) Fourier transforms of Cu loaded Cox19 wild type and Cys30Ala and Cys62Ala double mutant (Cox19-C3062A). Solid lines indicate experimental data and broken lines are the best fits obtained with parameters given in Table 1. All Fourier transforms are phase-corrected for Cu-S backscattering. Both Cox19 wild type and the C30,62 double mutant protein were purified with 1mM DTT.

Table 3-2. Cu K-edge EXAFS curve-fitting parameters of Cox19 wild type and the non-functional mutant[a].

Sample	Cu—S			Cu—Cu			
	N	*R* (Å)	*σ2* (Å^2)	*N*	*R* (Å)	*σ2* (Å^2)	*F*
Cox19	3	2.261(1)	0.0077(1)	2	2.664(2)	0.0103(2)	0.139
				1	2.861(5)	0.0112(1)	
	3	**2.257(2)**	**0.0079(1)**	**1**	**2.655(3)**	**0.0082(2)**	**0.169**
Cox19-C3062A	3	2.255(1)	0.0080(2)	2	2.659(3)	0.0103(2)	0.13
				1	2.862(5)	0.0107(5)	
	3	**2.250(1)**	**0.0083(2)**	**1**	**2.659(3)**	**0.0083(2)**	**0.163**

a. *N* represents for coordination number, *R* for interatomic distance, σ^2, the Debye-Waller factor for mean-square deviation in *R*. The fit error *F* is defined as $(\sum k^6(\chi_{exptl} - \chi_{calcd})^2/\sum k^6\chi_{exptl}^2)^{1/2}$. The values in parentheses are the estimated standard deviations (precisions) obtained from the diagonal elements of the covariance matrix. Fits shown in boldface represent the best fits obtained for the samples.

The EXAFS and the corresponding Fourier transform of Cox19-C3062A strongly resemble those of the wild type. This correspondence has been further confirmed by the curve fitting results as shown in Table 3-2. The similarity in the XAS spectra of the Cox19 wild type and Cys30, Cys62 double mutant strongly suggest that they both have essentially the same local structure around the Cu-binding site. This observation may rule out the possibility that Cox19 dimer forms a tetracopper cluster unless another source of thiol donors (such as those from exogenous DTT) is involved in the Cu binding site of Cox19-C3062A mutant.

3.4.1.2 Probing of the Nuclearity of Cox19 Cu Centre by Computational Chemistry

Based on the EXAFS curve fitting results, models for two-copper and four-copper cluster have been constructed, respectively (Figure 3-4 A and B). The initial structures were first optimized by MOPAC employing PM5 Hamiltonian, and then subsequently refined by DFT. As expected there are some differences between inter-

atomic separations from DFT energy minimization and experimental observations by EXAFS. DFT optimization using the LDA functional gives good Cu—S bond lengths but Cu···Cu separations that are about 0.15 Å shorter than those determined by EXAFS. Conversely, the GGA functional over-estimates Cu—S bond lengths by ~0.1 Å with Cu···Cu separations that agree with those determined by EXAFS. Whereas the overall structure of crystallographically known clusters are well reproduced by DFT, an improved functional is clearly needed to quantitatively describe Cu(I) thiolate clusters.

Both DFT-refined structures were computed with cysteine-tethered Cu-S core structures. Following local refinement by MOPAC/DFT the core structure of the two-copper cluster was locked and tethered with short peptides C30-X_9-C40 from Cox19. The resulting structure was successfully optimized by Molecular Mechanics using Augmented MM3 parameters, and the final structure is shown in Figure 3-4 C. Similar calculations were also performed using the four-copper cluster model in a Cox19 dimer

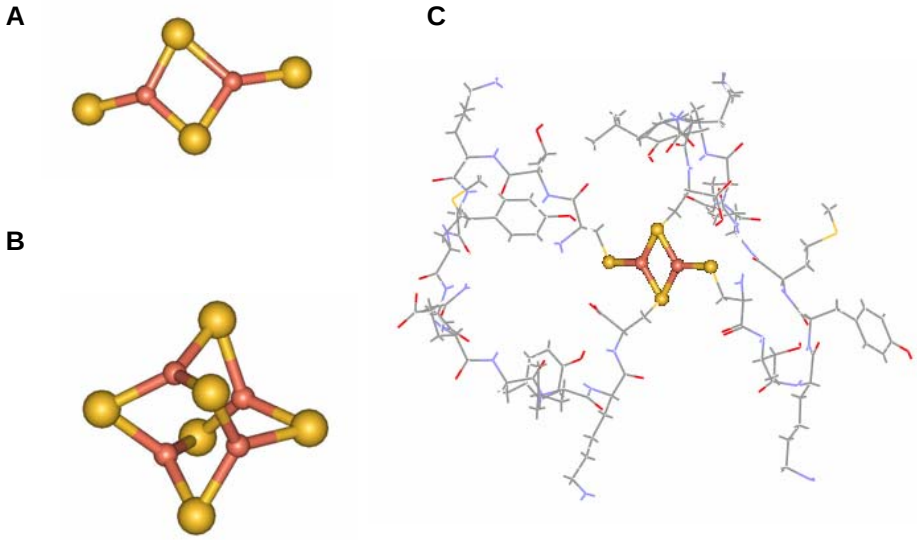

Figure 3-4. Computational modeling for the structure of the copper centre in Cox19 from yeast. The initial models were constructed based on the EXAFS curve fitting results, followed by geometry optimization with MOPAC and DFT. A, the two-Cu cluster model; B, the four-Cu cluster model, and C, two-copper cluster structure tethered by two 11-aa peptides Cys30-X9-Cys40. The orange spheres represent copper atoms, gold for sulfur, red for oxygen, blue for nitrogen, grey for carbon and white for hydrogen.

to test its chemical feasibility in theory. The initial structure was constructed with two 23-aa peptides C30-X_9-C40-X_{11}-C52 from Cox19, with all the available cysteines bound to copper. The calculation failed to converge in the iterative solution of the Kohn-Sham equations self-consistent field. One possible explanation could be that, since little is known about the apo-Cox19 folding structure, the initial structure of the peptide used in the optimization could be far from the actual folding favoured for the convergence. A second attempt was started with the following initial structure: four 11-aa peptides Cys30-X_9-Cys40 from Cox19 were added to the four-copper cluster, with four Cys30 and two Cys40 tethered to the cluster. The calculation successfully converged (data were not shown here). However, the two peptides with only Cys30 binding to the copper centre were remained in the linear structure. Such computations on the potential models of CuCox19 will process much more effectively once approximate Cox19 structure is obtained from other techniques such as crystallography or NMR.

3.4.2 Investigation of Factors Affecting the Metal Centre of Cox19

Previous size exclusion chromatography studies in *Winge*'s lab showed that both CuCox19 and apoCox19 exist as a stable dimeric species at the physiologically relevant concentration (< 100 μM) in the presence of 1 mM DTT. A mixture of tetramers and dimers are found in solution at protein concentrations of 300 μM. At higher concentrations (above 500 μM) the protein shows tetrameric and higher order oligomeric species (Rigby et al., 2007). This apparent concentration-dependent oligomerization becomes complicated when other factors are considered including oxidation due to air exposure and the ratio of DTT to the protein. Oxidation is a common problem for proteins with thiol group(s) suffering from oxidation by the oxygen in the air. Oxidation of the thiol groups between the monomers of Cox19 would cause oligomerization of the protein. DTT is commonly used in the biological system as a reductant to protect thiol groups in solubilized proteins (Cleland, 1964), and it was added during Cox19 sample preparations to prevent the oxidation of the thiol groups.

However, the presence of DTT in the protein samples arouses serious concerns, since it has been pointed out that DTT might interfere with the metal binding by providing thiol donors directly to the metal(s) (Cornell and Crivaro, 1972; Po et al., 1973; Gnonlonfoun et al., 1991; Krezel et al., 2001). X-ray absorption spectroscopy was used to examine the metal centre of a number of Cox19 samples under different preparation conditions. These include Cox19 in the presence of 1 mM DTT (as in Section 3.5.1), Cox19 in the presence of 500 μM DTT (Cox19-500μMDTT) and Cox19 initially prepared with 0.75 mM DTT and then dialyzed overnight against DTT-free buffer in an attempt to remove most of the DTT (Cox19-0DTT). Tetrameric (Cox19-tet) and dimeric (Cox19-dim) present in the Cox19-500μMDTT sample were chomatographically separated and XAS spectra were collected to test if the oligomerization state change causes any structural changes in the copper centre. All the above samples were at a concentration of around 1 mM Cu-equivalent protein, except for Cox19-tet which was about 0.5 mM.

As discussed above, the Cu K-edge near edge spectra of all the Cox19 samples shows typical features of a trigonally coordinated Cu(I) (Figure 3-5A). An approximately 0.4 eV energy shift to higher energy is found for the near edge spectrum of Cox19-1mMDTT, when compared to that of Cox19-500μMDTT or Cox19-0DTT. The EXAFS and corresponding Fourier transforms (Figure 3-5B and C) reveal structural differences between Cox19 with 1mM DTT and those with 0.5 mM or less DTT clearly showing that high levels of this compound perturb the Cu binding site. In particular, the high-*k* region (k>7 Å^{-1}) of the EXAFS spectrum of Cox19-1mMDTT, where Cu···Cu interactions are more pronounced, is significantly different from the corresponding region of the EXAFS of Cox19-500μMDTT and Cox19-0DTT. The intensity of the peaks at 2.2 Å and 2.7 Å in the Fourier transform of Cox19-1mMDTT are only 66% and 53%, respectively, of that observed in Cox19-500μMDTT. In addition, the 2.7 Å transform peak of Cox19-1mMDTT is shifted slightly to lower R, when compared to those of Cox19 with less DTT. These observations are quantitatively confirmed by curve fitting shown in Figure 3-5 C and D and summarized in Table 3-3. The peak at ~2.3 Å in the Fourier transform is best fitted when including 3 Cu-S

interactions in the fitting model for all the Cox19 samples, which confirms the presence of the trigonal Cu(I). However, the Debye-Waller factor of Cu-S interaction in Cox19-1mMDTT is more than 60% larger than that in other Cox19 samples. For all the Cox19 samples, fitting of the 2.7 Å peak with 2 shorter Cu···Cu interactions and one longer Cu···Cu interaction is better than that with 1 Cu···Cu interaction. However, the bond length for the shorter Cu···Cu interaction in Cox19-1mMDTT is about 0.05 Å shorter,

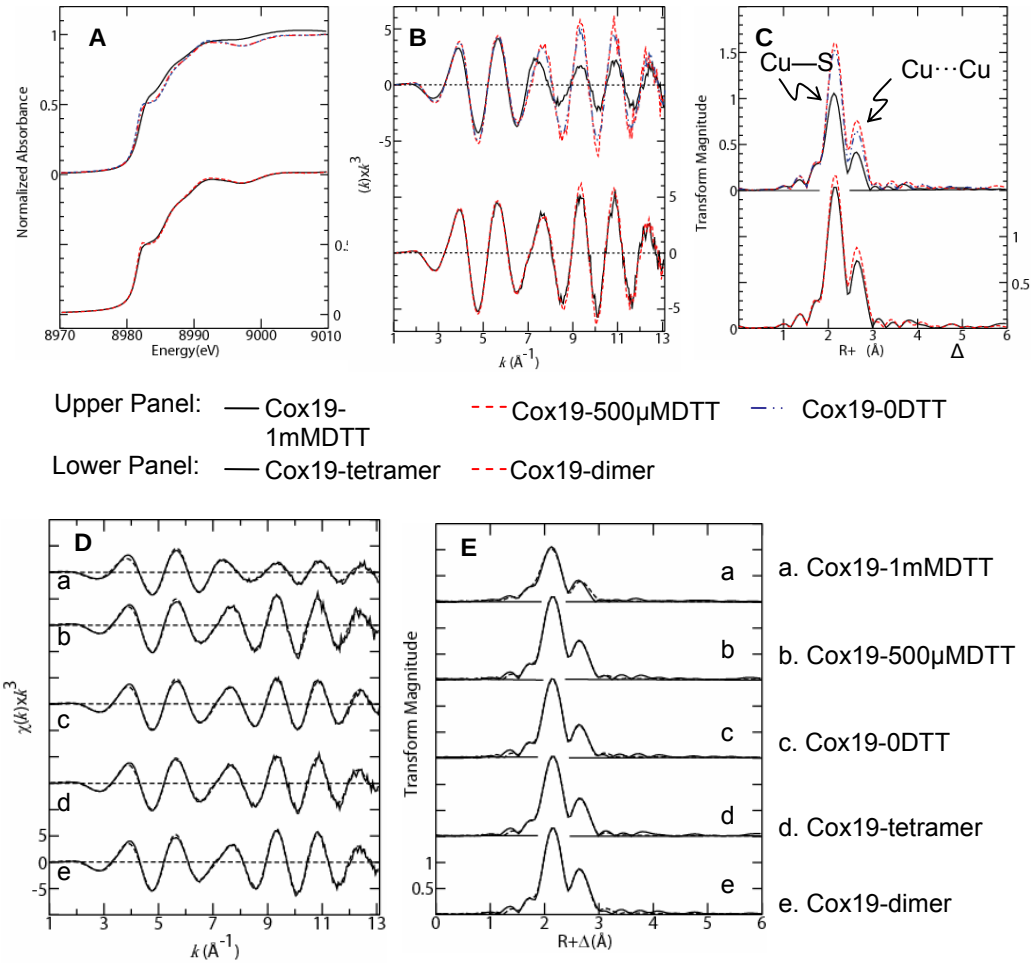

Figure 3-5. Comparison of X-ray absorption spectra of Cox19 in the presence of different concentration of DTT or in different oligomerization state. A) Cu K-edge X-ray absorption near-edge spectra, B) EXAFS and C) EXAFS Fourier transforms of CuCox19 in the presence of difference concentration of DTT as well as Cox19 dimer and tetramer separated from mother solution. D) EXAFS and E) EXAFS Fourier transforms of CuCox19 samples and its best fit obtained with parameters given in Table 3-3. All Fourier transforms are phase-corrected for Cu-S backscattering.

Table 3-3. Cu K-edge EXAFS curve-fitting parameters of Cox19 in different concentrations of DTT and oligomerization states[a].

Sample[b]	Cu-S			Cu··Cu			*F*
	N	*R*(Å)	σ^2 (Å^2)	*N*	*R*(Å)	σ^2 (Å^2)	
Cox19-1mMDTT	**3**	**2.257(2)**	**0.0079(1)**	**1**	**2.655(3)**	**0.0082(2)**	**0.169**
	3	2.261(1)	0.0077(1)	2	2.664(2)	0.0103(2)	
				1	2.861(5)	0.0112(1)	0.139
Cox19-0DTT	3	2.251(1)	0.0049(1)	1	2.700(2)	0.0061(2)	0.148
	3	**2.258(1)**	**0.0048(2)**	**2**	**2.704(2)**	**0.0082(1)**	
				1	**2.884(5)**	**0.0095(2)**	**0.115**
Cox19-500μMDTT	3	2.250(1)	0.0047(1)	1	2.708(2)	0.0048(2)	0.179
	3	**2.256(1)**	**0.0047(1)**	**2**	**2.713(2)**	**0.0072(2)**	
				1	**2.893(7)**	**0.0098(7)**	**0.153**
Cox19-dim	3	2.251(1)	0.0043(1)	1	2.706(2)	0.0042(1)	0.165
	3	**2.259(1)**	**0.0045(1)**	**2**	**2.709(1)**	**0.0065(1)**	
				1	**2.906(6)**	**0.0095(6)**	**0.120**
Cox19-tet	3	2.254(2)	0.0048(1)	1	2.706(2)	0.0051(2)	0.189
	3	**2.260(1)**	**0.0050(1)**	**2**	**2.716(2)**	**0.0074(1)**	
				1	**2.906(6)**	**0.0095(6)**	**0.143**

a. *N* represents for coordination number, *R* for interatomic distance, σ^2, the Debye-Waller factor for mean-square deviation in *R*. The fit error *F* is defined as $(\sum k^6(\chi_{exptl} - \chi_{calcd})^2/\sum k^6\chi_{exptl}^2)^{1/2}$. The values in parentheses are the estimated standard deviations (precisions) obtained from the diagonal elements of the covariance matrix. Fits shown in boldface represent the best fits obtained for the samples. *b*. The samples are listed in Table 3-1.

while the Debye-Waller factor for this interaction is about 25% larger than that of others. The EXAFS and Fourier transform of Cox19-0DTT is similar to that of Cox19-500μMDTT, although subtle differences between the two are observed. However, if DTT does attach to the copper centre, given that an initial concentration of 0.75 mM

DTT was present in the protein solution prior to its removal to make the Cox19-0DTT sample, it is possible that Cox19-0DTT might still have DTT bound. There are also subtle differences between Cox19-dim and Cox19-tet in both near edge and EXAFS, which are close to the margin detectability for XAS, but these differences are much smaller than those between Cox19-1mMDTT and those with 500 μM DTT or less.

Attempts to prepare Cox19 without any added DTT were unsuccessful. Due to limitations of the equipment available to us, the first two steps of preparation including sonication to break cells and high-speed centrifugation to remove cell debris has to be done in air, while remaining steps in the preparation can be done in an anaerobic glove box. Exposure of samples to air during the first two steps (totally less than 1 hour) resulted in predominantly tetrameric species in the purified protein (as judged by subsequent chromatography), even with final protein concentrations as low as 20 μM. Adding the mild reductant ascorbate to the purification solution at all stages did not prevent the protein from forming tetramers.

3.4.3 Comparison of the Cu-Binding Centres in Cox19 and Cox23 to Cox17

The Cu sites of Cox19, Cox17 and Cox23 were compared directly by comparison of the XAS data from each. The Cox19 sample used here is the same as the Cox19 wild type mentioned in Section 3.5.1. Cox23 was purified with 1 mM DTT in solution at 4°C under the aerobic condition, and DTT was subsequently removed by dialysis.

The preparation of Cox17 sample has been previously described (Srinivasan et al., 1998). The Cu(I) K-edge near edge spectrum of Cox19 is similar to that of Cox17 and Cox23, although subtle differences are observed (Figure 3-6). By comparison, the 1s $\rightarrow$ 4p transition peak around 8983 eV in the near edge spectrum in Cox19 shifts about 0.4 eV towards higher energy relative to that of Cox17 and Cox23.

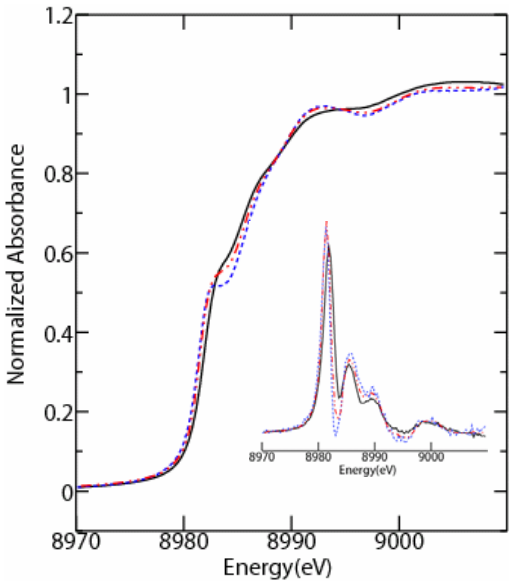

Figure 3-6. Cu K-edge X-ray absorption near-edge spectra of Cu chaperones in the cytochrome c oxidase assembly. The black solid curve represents Cox19, the blue dash curve for Cox17 and the red broken curve for Cox23. The inset is the first-derivative of the near edge spectra.

More significant differences are seen in the EXAFS and corresponding Fourier transforms. As shown in Figure 3-7, the EXAFS amplitude of Cox19 is significantly reduced in the high k range (> 7.5 $Å^{-1}$) in comparison to that observed with the other two proteins, although the EXAFS are similar at low *k*. The frequency at high *k* for Cox19 EXAFS is also shifted slightly relative to the other two. The Cox23 EXAFS spectrum is generally similar to that observed for Cox17, although the amplitude at high *k* is slightly reduced. As expected, the differences in the EXAFS spectra are reflected in the EXAFS curving fitting results (Table 3-4). The intensities of both prominent peaks in the Fourier transform of Cox19 is about 2/3 of that observed for Cox17 spectrum. In addition, the centre of the peak around 2.7 Å shifts slightly towards lower distance in the Fourier transform of Cox19. Similarly, the transform peak intensities for Cox23 are less than those observed for Cox17, although the differences are smaller than for Cox19. The nuclearity of the copper clusters in these Cu-chaperones cannot be conclusively derived from the EXAFS analysis results alone. The best fits (in bold font of Table 3-4)

are chosen by combining the EXAFS curving fitting results and current best knowledge on the Cu-binding properties of these chaperones.

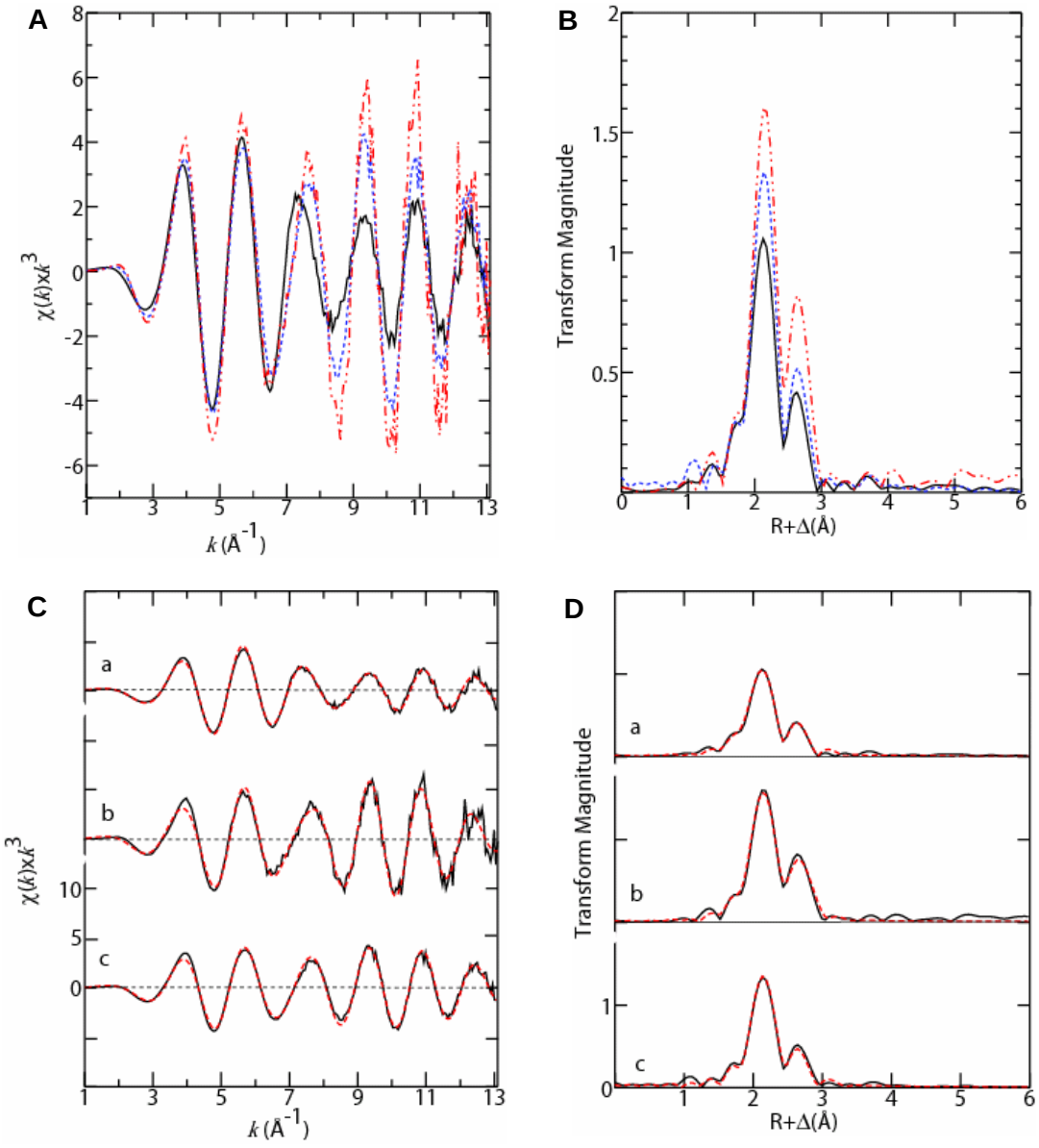

Figure 3-7. Comparison of Cu K-edge EXAFS and Fourier transform of Cox19, Cox17 and Cox23. A) and B) show the EXAFS and Fourier transforms of Cox19 (solid black curve), Cox17 (red broken curve) and Cox23 (blue dash curve), respectively. The best fits for the) the EXAFS and Fourier spectra of Cox19 (a), Cox17 (b) and Cox23(c) are shown in C) and D) respectively, with experimental data in solid curve and the best fits in red dash curve.

Table 3-4. Cu K-edge EXAFS curve-fitting parameters of Cox19, Cox17 and Cox23[a].

Sample	Cu-S			Cu-Cu			*F*
	N	*R*(Å)	σ^2 (Å^2)	*N*	*R*(Å)	σ^2 (Å^2)	
Cox19	3	2.261(1)	0.0077(1)	2	2.664(2)	0.0103(2)	0.139
				1	2.861(5)	0.0112(1)	
	3	**2.257(2)**	**0.0079(1)**	**1**	**2.655(3)**	**0.0082(2)**	**0.169**
Cox17	3	2.255(2)	0.0048(1)	2	2.715(2)	0.0067(2)	0.21
				1	2.911(7)	0.0080(2)	
	3	**2.249(2)**	**0.0049(1)**	**1**	**2.705(2)**	**0.0043(2)**	**0.22**
Cox23	**3**	**2.253(1)**	**0.0060(1)**	**2**	**2.708(2)**	**0.0091(2)**	**0.134**
				1	**2.902(5)**	**0.0097(5)**	
	3	2.248(1)	0.0060(1)	1	2.699(2)	0.0070(2)	0.17

a. *N* represents for coordination number, R for interatomic distance, σ^2, the Debye-Waller factor for mean-square deviation in *R*. The fit error *F* is defined as $(\sum k^6(\chi_{exptl} - \chi_{calcd})^2/\sum k^6\chi_{exptl}^2)^{1/2}$. The values in parentheses are the estimated standard deviations precisions) obtained from the diagonal elements of the covariance matrix. Fits shown in boldface type represent the best fits obtained for the samples.

3.5 Discussions and Future Work

3.5.1 The Copper Centre in Cox19

In this study, the EXAFS data show that Cox19 forms a multi-copper cluster with each copper trigonally coordinated by sulfur donors under the experimental conditions. Identification of cysteines involved in copper binding by site directed mutagenesis was not completely conclusive. The XAS results show that the non-functional mutant Cox19-C3062A has a very similar local Cu site structure to the wild type protein, which may rule out the change of the local metal-binding structure as an explanation for the loss of function of Cox19 in the absence of Cys30. The role of Cys30 in Cox19 during the copper transfer remains unknown. One possibility is that

Cys30 directly binds to copper in the wild type Cox19, and in the absence of Cys30 Cox19 might bind copper in a similar manner, but less efficiently thus reducing its activity in terms of copper delivery. Studies in *Winge*'s lab support this prediction by showing that the mutant showed significantly reduced affinity to Cu(I) (Rigby et al., 2007). Alternatively, it is possible that instead of directly binding to copper, Cys30 may be a key factor in stabilizing the Cu(I) binding centre, such as being involved in shielding the copper site from solvent access.

3.5.2 Effects of Protein Concentration and DTT on the Copper Centre of Cox19

The correlation between protein concentration and oligomeric state of the protein has been observed in earlier studies (Rigby et al., 2007). However, the observations to date do not prove that increased protein concentrations cause oligomerization of the protein as other factors which may also affect oligomerization are in play. In the same work, it has been observed that tetramerization (or higher level of oligomerization) of Cox19 is not reversed by dilution. Disassociation of the tetramer into dimers requires sufficiently reducing conditions (incubation of the tretramer protein with 100 mM DTT in guanidine HCl for 1 hour) that any disulfide bridges might be broken (Winge et al., personal communication). These results imply that the tetramerization of Cox19 may be associated with, if not actually caused by, oxidation. Such association of oligomerization with air exposure was also observed during the semi-anaerobic preparation of DTT-free protein samples. It is speculated here that the apparent link between the concentrations of the protein with the oligomerization may be at least partially related to oxidisation of the protein by the oxygen with less protection of DTT. As mentioned earlier, many previous studies were performed in the presence of 1 mM DTT (Rigby et al., 2007). On concentrating a protein sample, the ratio of DTT to protein decreases. Thus, if tetramerization is caused by oxidative formation of disulfide bridge(s), a feasible explanation of the observations is that Cox19 might be more likely to be oxidized and thus forms higher order of oligomer with the reduced ratio of DTT to protein. This explanation is consistent with the phenomena of DTT- and time-dependent

oligomerization observed during studies (Winge et al, personal communication), which are hard to explain by concentration change alone: Cox19 tends to start to form tetramers at lower protein concentrations in the presence of lower concentrations of DTT, compared to preparations with higher concentration of DTT. Given sufficient time, Cox19 at lower than 100 μM concentration will also form tetramers. The higher the concentration of the protein, and/or the lower the concentration of DTT is, the faster the tetramer forms. Besides the effects discussed above, the potential perturbation to the metal binding site of Cox19 by DTT is another severe concern. The EXAFS results presented here clearly show significant differences between Cox19 samples in the presence of 1mM DTT and at lower levels. These results cannot simply be explained by the protein concentration effects, or by protein tetramerization. Instead the results presented here suggest the possibility of the nonlinear dependence of the copper centre structures in Cox19 on the concentration of DTT. In order to obtain an improved understanding of the effects of DTT, the experiments reported here should be repeated under more rigorous conditions in order to avoid undesired effects on the copper centre of the protein. Firstly, Cox19 should be prepared under rigorously anaerobic conditions from start to end to control the effects of oxidation. Alternatively, other non-thiol based disulfide reducing agents, such as immobilized tris(2-carboxyethyl)phosphine, could be tested as replacements of DTT during protein preparation. Secondly, because results varied slightly in a preparation-dependent manner, protein samples from the same preparative batch should be used in tests of the effects of protein concentration and DTT on the structure of the copper centre.

3.5.3 The Nuclearity of the Copper Centre in Cox19

The nuclearity of the copper binding site in Cox19 was not resolved by EXAFS in this study, mainly due to uncertainties arising from possible EXAFS cancellation of two different types of Cu···Cu interactions. The inter-atomic distance resolution of EXAFS can be estimated as $\pi/2k$. With a 13-$Å^{-1}$ scan, the resolution will be close to 0.12 Å, and it should resolve the two different types of Cu···Cu with distance difference

around 0.18 Å by theory. However, any EXAFS cancellation in Cox19 would be complicated by the presence of two short Cu···Cu and one longer Cu···Cu interactions, where the oscillations for the two Cu···Cu types nearly completely cancel, which would make the EXAFS very similar to that from a single short Cu···Cu interaction. A high resolution EXAFS experiment with a *k* range exceeding 18 $Å^{-1}$ did not resolve the two interactions (data not shown). Furthermore, with the large Debye-Waller factors required to fit the data (>0.008 $Å^2$), the Cu···Cu EXAFS diminishes significantly at higher *k*, so that it is not possible to determine the nuclearity of the Cu cluster in the Cox chaperones by Cu K-edge EXAFS alone.

Sulfur K-edge EXAFS has been considered as an alternative to solve the puzzle of cluster nuclearity. For a two-copper cluster model, each sulfur would "see" on average 1 C and 1.5 Cu, while for a four-copper cluster each sulfur would see 1 C and 2 Cu. These differences are close to the detection limit by EXAFS. Furthermore, the resolution of S K-edge EXAFS is limited by the difficulties in preparing chloride-free samples. There are also not insignificant difficulties in conducting EXAFS measurements at the sulfur K-edge. To use Cox19 as an example, four cysteine residues are present in each monomer. If the Cox19 binds to copper in the two-copper cluster model, then two cysteines in each monomer are not bound to copper, while one free cysteine if taken a four-copper cluster model. These "free" cysteine residues need to be removed before examining the S K-edge EXAFS. It has also been considered to determine the nuclearity of the copper cluster in Cox19 by examining the sulfur K near edge spectrum of the protein. As discussed above, Cox19 possesses different number of metal-free cysteines and Cu-bound cysteines in a two-copper cluster model and a four-copper cluster model. Therefore nuclearity of the copper cluster can be defined if the number of the metal-free cysteines is determined by edge fitting. However, in order to do so, it requires to replace 6 Mets in the Cox19 by with Se-Met, and to purify the protein in the absence of DTT (due to its thiol content) under anaerobic conditions. In addition, Cu-aliphatic thiolate models are required for the S K near edge fitting. Attempts to prepare Cu-aliphatic thiolate models have encountered with difficulties in

separating single Cu-thiolate and tetracopper thiolate cluster formed simultaneously in the reaction.

Substitution of the cysteine in the copper binding site with selenocysteine could be another option, and it has been used to characterize the copper binding site in the past (Ralle et al., 2004; Barry and Blackburn, 2008; Barry et al., 2008). In a two-copper cluster model, one or two copper per Se atom would be present in the Se K-edge EXAFS depending on whether the monodentate or bidentate S has been replaced, while it is always two copper atoms per Se for the four-copper cluster model. This experiment is also expected to present difficulties, as it has been estimated that the efficiency in the substitution of cysteine with Se-cysteine in a peptide decreases rapidly with the increase in the size of the peptide.

Metal-Catalyzed Oxidation (MCO) might also be used to identify the cysteines involved in the copper binding. It has been reported that MCO reactions and Mass Spectroscopy were used for determining ligands that directly bind to the metal in the copper metalloproteins (Lim and Vachet, 2003). This method use MCO to oxidize amino acids in the metal binding site and MS to identify the amino acids that have been oxidized. These techniques might be used to help identity which cysteines are involved in the metal binding site of the copper chaperones in this study.

3.5.4 Cu Binding Centres in Copper Chaperones of the CcO Assembly Pathway

To date, the copper centres of a number of proposed copper chaperones, including Cox17, Cox19 and Cox23, have been examined by EXAFS (Heaton et al., 2001; Carr et al., 2002). All of them show a trigonally coordinated polycopper cluster with either a dimeric or tetrameric form. The Cu··Cu distance (2.7 Å) from the EXAFS indicates a typical Cu(I) cluster with μ_2 thiolate bridging sulfur ligands (Atkinson et al., 1985; Pickering et al., 1993). The results from EXAFS in this study are in conflict with the NMR analysis (Protein Bank Database ID: 1U96), which suggests a digonally coordinated copper centre of Cox17 in monomeric state (Abajian et al., 2004). However, it is noted that NMR does not directly detect metal-binding, which is instead inferred

from chemical shifts of candidate ligands. In most cases quantitative interpretation of the chemical shifts in terms of metal coordination is not possible and caution is needed when interpreting the structures around metal binding sites from NMR. The discrepancy between the EXAFS and NMR is unlikely to be related to DTT, since similar NMR is observed for Cox17 in the presence of 1 mM DTT in the protein solution (Arnesano et al., 2005a). In addition, NMR analysis is also contradicted by the UV spectrum, which suggests a solvent-shielded copper centre rather than one exposed to the solvent as suggested by NMR (Heaton et al., 2001). If the metal binding site in Cox17 is indeed exposed to the solvent as suggested by NMR, it may raise the question how the metal binding site is protected from the water or other small molecules with thiol group(s). It remains unknown whether the oligomerization of these copper chaperones observed *in vitro* is physiologically relevant. One possible role for oligomerization of the copper chaperones might be to protect the copper at the binding site during transport before delivery to the target protein.

CHAPTER 4

STRUCTURES OF CUPROUS-THIOLATE CLUSTERS IN *SACCHAROMYCES CEREVISIAE* METALLOTHIONEIN

4.1 Abstract

Copper metallothioneins are cuprous thiolate proteins that contain multi-metallic clusters and are thought to have dual functions of copper storage and copper detoxification. A combination of X-ray absorption spectroscopy and density functional theory was used to investigate the nature of copper binding to *Saccharomyces cerevisiae* metallothionein. X-ray absorption spectroscopy analyses of metallothionein prepared with a full complement of copper are quantitatively consistent with the crystal structure. Reconstitution of the apometallothionein with stoichiometric copper results in the formation of a tetracopper cluster, indicating the cooperative binding of copper ions by the metallothionein.

4.2 Introduction

Proteins containing cuprous-thiolate multimetallic clusters form a large family of biological macromolecules that includes copper metallochaparones (Rigby et al., 2007), copper transporters (Xiao et al., 2004), copper-modulated transcription factors (Brown et al., 2002) and copper buffering systems such as copper metallothioneins (Cu-MTs) (Pickering et al., 1993). These proteins play key roles in the cellular copper

homeostasis, which is critical because of copper's essentiality to the living cells and yet the toxic nature of the metal. Key to understanding the molecular mechanisms of copper homeostasis is an understanding of the molecular details of the binding of the metal ions in biological molecules. In many cases structural information from protein crystallography is lacking, although some details are available from spectroscopic techniques such as X-ray absorption spectroscopy (XAS).

The Cu-MT found in *Saccharomyces cerevisiae* consists of 12 cysteinyl residues within a 61 amino acid polypeptide (Butt et al., 1984). Cu-MT has been proposed to be involved in both copper storage and detoxicification (Hartmann et al., 1983), although its physiological role has not been fully understood. To fulfill the dual tasks, metallothionein must bind copper tightly but be ready to release copper when needed. Previous structural studies show that the protein binds Cu(I) ions with a solvent-shielded polymetallic core coordinated by only ten of the twelve cysteinyl residues (Bertini et al., 2000; Calderone et al., 2005). The nuclearity of the polymetallic core is not fixed, and structural data confirm that complexes with 7 or 8 Cu(I) ions can form (Bertini et al., 2000; Calderone et al., 2005). Cooperativity in Cu(I) binding of Cu-MT has been known for a long time (Byrd et al., 1988), but the extent of the cooperativity is not clear. Here, a combination of XAS and computational chemistry is used to examine the copper clusters in *Saccharomyces cerevisiae* Cu-MT prepared with a full complement and with stoichiometric levels of added copper.

4.3 Material and Methods

4.3.1 Sample Preparation

Cu-MT from *Saccharomyces cerevisiae* was prepared as previously described by members of *Dr. Dennis R. Winge*'s group at University of Utah (Byrd et al., 1988). The apometallothionein was reconstituted with different mole equivalents of cuprous chloride solution under anaerobic conditions (Byrd et al., 1988), and loaded into 2-mm-thick Lucite sample cuvettes closed with metal-free adhesive mylar tape.

4.3.2 X-ray Absorption Spectroscopy Data Collections

X-ray absorption spectra were collected at a temperature of 10 K as previously described (Pickering et al., 1993) using beamline 7-3 of the Stanford Synchrotron Radiation Lightsource, with the storage ring SPEAR operating at 3 GeV, ring current of 80-100 mA and a wiggler field of 1.8 Tesla. Si(220) monochromator crystals were used and harmonic rejection was achieved by slightly offsetting the angle of the second monochromator crystal to give 50% of the peak intensity. Data on low molecular weight compounds were collected in transmission mode using nitrogen-filled ionization chambers, while protein data were collected by monitoring the Cu K_α X-ray fluorescence excitation spectrum using a 13-element Ge array detector (Cramer et al., 1988).

4.3.3 X-ray Absorption Spectroscopy Data Analysis

Extended X-ray absorption fine structure (EXAFS) oscillations $\chi(k)$ were analyzed using the EXAFSPAK suite of computer programs as previously described (George et al., 1988; George et al., 1999), and employing the *ab initio* theory code FEFF (Version 8.25) to compute the amplitude and phase functions required for curve-fitting (Rehr and Albers, 2000). No smoothing, filtering, or related operations were performed on the data.

4.3.4 Computational Chemistry

Density Functional Theory (DFT) molecular modeling used the program Dmol^3 Materials Studio Version 4.1 (Delley, 1990; Delley, 2000). The Becke exchange (Becke, 1988b) and Perdew correlation (Perdew and Wang, 1992) functionals were used to calculate both the potential during the self consistent field procedure and the energy. Double numerical basis sets included polarization functions for all atoms. Calculations were spin-unrestricted and all electron core potentials were used. No symmetry constraints were applied (unless otherwise stated) and optimized geometries used energy tolerances of 2.0×10^{-5} Hartree. The effects of solvation were simulated by using

the Conductor-like Screening Model (COSMO) with a dielectric constant of 78.54 (Klamt and Schuurmann, 1993).

4.4 Results and Discussions

4.4.1 X-ray Absorption Spectroscopy

Figure 4-1 shows the Cu K near edge spectra of the Cu-MTs from *S. cerevisiae* prepared from apometallothionein reconstituted with stoichiometric copper (i.e. 1:1 Cu:protein), and from fully-loaded protein, reconstituted with eight copper ions (Calderone et al., 2005). These spectra are also compared with those of synthetic Cu(I)-thiolate clusters of stoichiometries CuS_2, Cu_4S_6, Cu_5S_6 (Pickering et al., 1993). CuS_2 contains a digonally-coordinated copper and Cu_4S_6 contains four trigonal copper, while

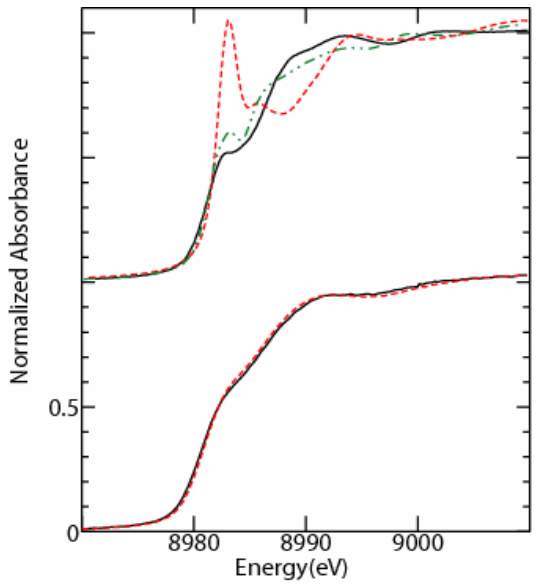

Figure 4-1. Comparison of Cu K-edge near edge spectra of Cu-loaded metallothioneins with synthetic Cu(I)-thiolate clusters. On the top panel are the trigonal cuprous thiolate cluster, $(Me_4N)_2[Cu_4(SPh)_6]$ or Cu_4S_6 (solid black curve), the mixed coordinated $(Et_4N)[Cu_5(SBu^t)_6]$ or Cu_5S_6 (green broken curve), and the digonal $[Cu(SC_{10}H_{12})_2]^{2-}$ or CuS_2 (dash red curve). The stoichiometric and fully-loaded Cu metallothionein are shown in the lower panel in solid black curve and red dash curve respectively.

Cu_5S_6 has a mixed coordination with 2 digonal copper and 3 trigonal copper (Pickering et al., 1993). These near edge spectra are broadly similar to each other except for the digonally coordinated CuS_2, particularly in the region around 8983 eV. The peak around 8983 eV in the Cu K-edge near edge spectrum was assigned as dipole-allowed 1s→4p transition and the data were rationalized from the expected degeneracy of the 4p orbital from simple ligand field arguments (Kau et al., 1987). The near edge spectra of the two Cu-MTs are essentially identical under the current experimental conditions, and they more closely resemble the spectrum of Cu_4S_6 rather than Cu_5S_6. According to the reported crystal structure, the fully loaded Cu-MT contains 25% of digonal copper (Calderone et al., 2005). The lack of increase in the intensity of the 1s→4p peak might be due to the distortion of the S-Cu-S angle (Calderone et al., 2005), This has been discussed in previous work (Kau et al., 1987).

In previous studies (Pickering et al., 1993), it has been suggested that measurement of Cu—S bond lengths by EXAFS could provide a tool for determining the coordination of copper in cuprous-thiolate systems, and this has been used to estimate that approximately 30% of the copper bound in *Saccharomyces cerevisiae* metallothionein is digonally coordinated, with the rest being trigonally coordinated. It was also observed in the same study that the Cu···Cu interaction is much diminished, which was attributed to EXAFS cancellation arising from a variety of Cu···Cu interatomic separations (Pickering et al., 1993). EXAFS cancellation occurs when the EXAFS oscillations from different absorber-backscatterer pairs are wholly or partly out of phase. This phenomenon was previously observed in systems containing tetranuclear $[Cu_4S_6]^{2-}$ clusters, and in particular the transcription factors Ace1 and Mac1 (Brown et al., 2002), and in the Ctr1 transporter of *S. cerevisiae* (Xiao et al., 2004). In these cases, the cluster is distorted so that partial cancellation occurs, and the presence of a tetranuclear cluster is only definitively indicated by small features arising from interactions with distant sulfur atoms (Pickering et al., 1993). Figure 4-2 compares the XAS data for *S. cerevisiae* metallothionein prepared from apometallothionein reconstituted with stoichiometric copper, and from fully-loaded protein, reconstituted

with eight copper ions. Interestingly, the metallothionein prepared with stoichiometric copper shows a distinct Cu···Cu peak, definitively indicating the presence of a cuprous thiolate cluster. Thus, the binding of copper to metallothionein must occur cooperatively, and EXAFS curve-fitting analysis (Table 4-1) indicates a best fit with the Cu···Cu interactions that might be expected from a distorted Cu_4S_6 cluster of the type established for other cuprous thiolate systems (i.e. Xiao et al., 2004). In general agreement with this, mass spectrometry of mammalian metallothionein indicates the presence of a tetra-metal cluster when the protein is treated with stoichiometric copper (Jensen et al., 1998). The EXAFS spectrum of metallothionein containing a full complement of copper indicates a copper cluster, but with a severely damped Cu···Cu interaction, as illustrated in the EXAFS Fourier transform (Figure 4-2). Indeed, the damping of the Cu···Cu EXAFS is so severe that, if there were no foreknowledge concerning the presence of a metal cluster, the data could easily be misinterpreted as supporting a mononuclear site.

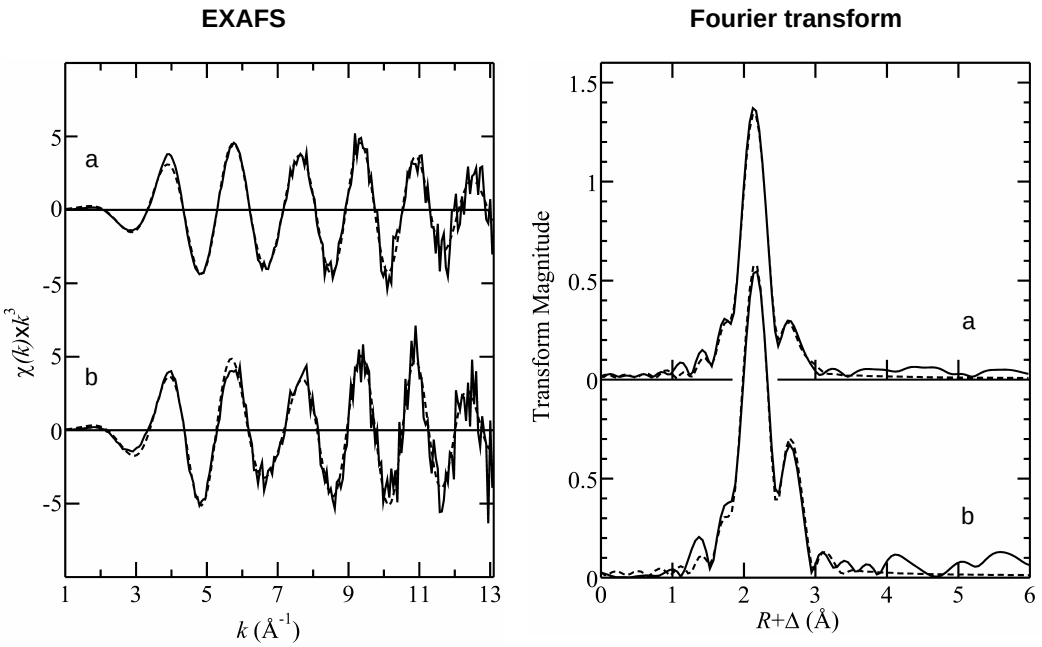

Figure 4-2. EXAFS spectra and corresponding Fourier transforms (Cu—S phase-corrected) of a) copper metallothionein prepared with a full complement of eight copper ions, and b) with stoichiometric levels of copper and protein. The solid lines show experimental data while the broken lines show the best fits.

Table 4-1. EXAFS curve-fitting parameters[a].

Sample	*Cu—S*			*Cu···Cu*		
	N	***R*(Å)**	**σ^2(Å^2)**	***N***	***R*(Å)**	**σ^2(Å^2)**
a	2.75	2.241(2)	0.0031(1)	$^1/_8$	2.623[b]	0.0073(6)[c]
				$^1/_8$	2.640	0.0073
				$^1/_8$	2.688	0.0073
				$^1/_8$	2.693	0.0073
				$^1/_8$	2.695	0.0073
				$^1/_8$	2.696	0.0073
				$^1/_8$	2.736	0.0073
				$^1/_8$	2.739	0.0073
				$^1/_8$	2.845	0.0073
				$^1/_8$	2.895	0.0073
b	3	2.256(3)	0.0049(2)	2	2.714(4)	0.0073(4)
				1	2.900(11)	0.0077(4)

a. *N* is the mean coordination number; *R,* the interatomic distance in Å; σ^2, the Debye-Waller factors (the mean square deviation in interatomic distance). The values in parentheses are the estimated standard deviations (precisions) obtained from the diagonal elements of the covariance matrix. b. Values for Cu···Cu interatomic distances are not refined, instead obtained from density functional theory. c. A common σ^2 value for the Cu···Cu interaction was refined.

4.4.2 Computational Chemistry

The crystal structure of the copper binding part of *S. cerevisiae* metallothionein has recently been solved to a resolution of 1.4 Å (Calderone et al., 2005). Protein crystal structure determinations are usually insufficiently accurate to allow translation of interatomic distances to simulate the EXAFS data. Therefore, the cluster portion of the protein crystal structure was isolated and DFT was used to refine the coordinates by energy minimization of the cluster structure, while constraining the positions of the cysteine alpha-carbon atoms to their crystallographically determined locations. Figure 4-3 shows the result, which is very similar to the structure obtained from analysis of the crystallographic data (Calderone et al., 2005). The structure shows two digonally coordinated and six trigonally coordinated copper atoms, which is in excellent agreement with the previous estimate of the digonal copper content in the fully loaded

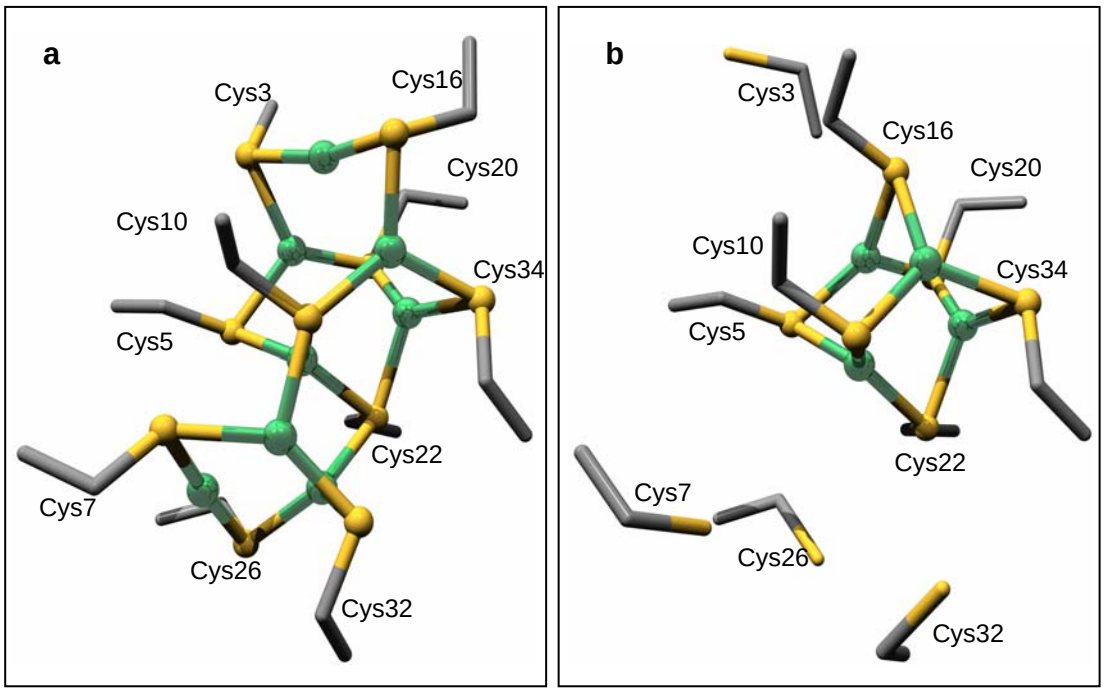

Figure 4-3. DFT energy-minimized structures for (a) copper metallothionein fully loaded with copper and (b) copper metallothionein containing a tetracopper cluster. Copper and cysteinyl sulfur atoms are indicated by green and yellow spheres, respectively. Only the alpha carbon and side-chain carbon atoms were included in the computations, and the alpha carbons were constrained at the crystallographic locations, with the exception of Cys16 in (*b*).

Cu-MT (Pickering et al., 1993). The structure shows ten Cu···Cu inter-atomic separations that are less than 3 Å, and these can be used to simulate the EXAFS, as shown in Figure 4-4, indicating that the EXAFS and the crystal structure are in good agreement. Perhaps more interesting than the structure of the cluster in fully copper-loaded protein, is the structure of the cluster that forms upon exposure to stoichiometric copper. As mentioned above, the EXAFS of this sample are best interpreted as a tetranuclear cluster. The crystal structure of fully loaded metallothionein has a fragment which shows structural resemblance to a tetranuclear cluster. It was also attempted to model the metallothionein encapsulated tetranuclear cluster using density functional theory. In order to allow the cluster to form properly, the constraints on Cys16 were lifted, and so the alpha-carbon was allowed to move away from the crystallographically

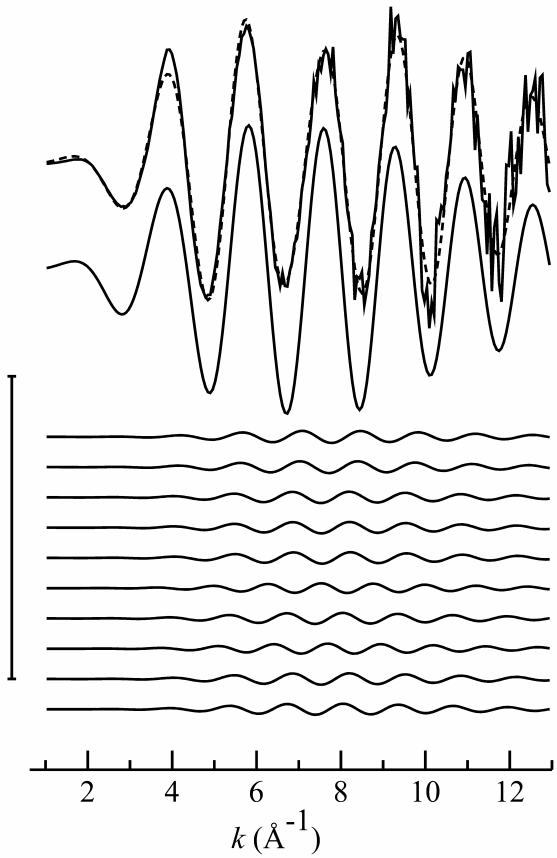

Figure 4-4. Simulation of EXAFS spectrum of copper metallothionein containing a full complement of eight copper atoms showing cancellation of Cu···Cu EXAFS. The top-most pair of traces, show the experimental data (solid line) and best fit (broken line), with the traces below indicating the Cu—S, and the ten different Cu···Cu interactions, with the latter using interatomic distances obtained from computational chemistry (Table 4-1, Figure 4-3). The overall effect is that the Cu···Cu interactions mostly cancel. The vertical bar indicates the scale for the ordinate $\chi(k)\times k^3$ of 10 Å^{-3}.

coordinates, which it did by about 4 Å (Figure 4-3). This movement of Cys16 would imply somewhat different polypeptide folding, but this is not unexpected. There may be many ways in which a tetranuclear $[Cu_4S_6]^{2-}$ cluster could form within the metallothionein polypeptide, but the modelling results shown here do indicate that the formation of such a cluster is perfectly reasonable from the chemical point of view within the crystallographically defined framework. The conclusion of the formation of a tetracopper cluster is at apparent odds with earlier work which followed the cluster

luminescence on titration of apometallothionein with copper and suggested that the cluster formed cooperatively in an all-or-nothing manner (Byrd et al., 1988). The EXAFS results reported here are, however, quite unambiguous in demonstrating that the cluster formed with stoichiometric copper, is distinct from that formed with a full complement of eight coppers (Figure 4-2). This apparent discrepancy could be explained if copper binding to MT in digonal coordination increases the solvent accessibility to the copper centre and thus the fluorescence quantum yield of the cluster decreases due to solvent quenching (Lytle, 1970; Byrd et al., 1988). This assumption is supported by the observation from the same paper (Byrd et al., 1988) that the fluorescence yield maximized at 6-mole equivalence of copper without any external ligands, while it reached maximum at 8-mole equivalence of copper with the presence of either cysteine or KCN in the protein solution.

The stability of $[Cu_4S_6]^{2-}$ clusters may have an important role in Cu-MTs. The $[Cu_4S_6]^{2-}$ structural motif is very common in the synthetic inorganic literature. A search of the Cambridge Crystal Structure Database (Allen and Kennard, 1983) gives 41 different examples with the $[Cu_4S_6]^{2-}$ core, which is by far the most common type of $[Cu_xS_y]^{z-}$ structures. The $[Cu_4S_6]^{2-}$ structural motif is observed in proteins other than the Cup1 metallothionein. The tetracopper motif exists in the Cu-activated Ace1 transcriptional activator from *S. cerevisiae* and the related factor Amt1 from *Candida glabrata* (Brown et al., 2002). The Cu-regulated transcription factor Mac1 from *S. cerevisiae* contains a related tetracopper cluster in its Cu-inactive state (Brown et al., 2002). The cytoplasmic domain of the Cu(I) donor in the mitochondrial intermembrane space Cox17 is capable of forming a tetracopper cluster, although its physiological state is more likely a mononuclear Cu(I) complex (Heaton et al., 2000; Voronova et al., 2007). As discussed above, copper is very tightly regulated. The intracellular copper concentration is therefore thought to be very low, and cooperative formation of the stable $[Cu_4S_6]^{2-}$ cluster at low copper concentrations may be important *in vivo*. As mentioned earlier, Cu-MT is thought to have the dual roles of copper storage and detoxification in the presence of high levels of copper. Previous work has shown that

some of the coppers in metallothionein are more tightly bound than others (Weser and Hartmann, 1988). In agreement with this, DFT calculations indicate that the total energy decrease on binding the first four copper ions (Figure 4-3b) is greater by 0.95 eV than the decrease on binding the next four copper ions (Figure 4-3a), to make up the full complement of eight copper ions. These energetic differences would be reflected in the copper binding constants, and different affinities have previously been proposed for dissociation of the digonally and trigonally bound coppers (Calderone et al., 2005). Thus, under physiological conditions, metallothioneins may only rarely encapsulate a full complement of copper ions. While the ability to bind up to eight copper ions (in yeast metallothionein) will be important, these results suggest that the predominant form of metallothionein may be the tetracopper cluster.

CHAPTER 5

CHARACTERIZATION OF THE METAL CENTRE OF COPPER BINDING DOMAIN IN MTF-1 FROM *DROSOPHILA*

5.1 Abstract

Drosophila melanogaster metal-responsive transcription factor-1 (dMTF-1) is a transcriptional activator that regulates gene expression responsive to various metal ions including Zn, Cd and Cu. It up-regulates the expression of *Drosophila* MtnA (encoding metallothionein) in response to excess Cu. The mechanism by which dMTF-1 senses metal stress is poorly understood. Functional studies suggest that the Cys-rich cluster in the C-terminal domain of dMTF-1, ^{547}**C**N**C**TN**C**K**C**DQTKS**C**HGGD**C**^{565}, is essential and sufficient for protection from Cu toxicity. In the current study, X-ray absorption spectroscopy was used to provide structural information on the metal centre in the Cu-dMTF-1 complex. Results from the study indicate that Cu(I) binds to dMTF-1 to form a Cu_4S_6 cluster in a cooperative manner, with each copper ion in the cluster coordinated by 3 sulfur atoms from Cys-rich domain. The conclusions from XAS are backed up by results from mass spectroscopy and NMR. The cooperativity in the Cu-binding manner in dMTF-1 has been observed previously in other Cu-responsive transcription factors and the potential biological significance of the cooperative Cu-binding to dMTF-1 is also discussed.

5.2 Introduction

Metal-responsive transcription factor-1 (MTF-1) was first identified in mouse as a metal-inducible metallothionein-I gene enhancer induced in response to Zn toxicity (Westin and Schaffner, 1988), and has been extensively studied in different organisms. Results from these studies indicate that MTF-1 is a transcription activator that regulates the expression of genes involved in cellular control of heavy meals such as zinc, cadmium and copper (Andrews, 2001; Giedroc et al., 2001; Lichtlen and Schaffner, 2001; Laity and Andrews, 2007). However, the regulation function of MTF-1 is not limited to heavy metals. Accumulating evidences suggest that MTF-1 may also regulate transcription of genes in response to oxidative stress or hypoxia (Murphy, 2004; Murphy et al., 2005; Tamura et al., 2005; Maruyama et al., 2007). Recent sequence analysis predicts that MTF-1 may also be involved in the transcriptional regulation of microRNAs, a class of endogenous small RNAs that are thought to negatively regulate protein production, and aberrant expression of which is linked to cancer and other diseases (Lee et al., 2007).

So far MTF-1 has been identified and at least partially characterized from fruit fly (Zhang et al., 2001), fish (Maur et al., 1999; Dalton et al., 2000; Chen et al., 2002; Chen et al., 2007), mouse (Muller et al., 1995; Maur et al., 2000) and human (Brugnera et al., 1994). Sequence analyses indicate MTF-1 from these species share common domains, including: a highly conserved zinc-finger domain that mediates interactions with the metal response element (MRE) (Westin and Schaffner, 1988); short sequences that mediate intracellular trafficking into and out of the nucleus (Saydam et al., 2001); and multiple domains for transcription activation including a Cys-rich cluster which is involved in metal binding (Muller et al., 1995) (Figure 5-1). Among all the homologs examined so far, *Drosophila* MTF-1 show the least similarity, with little in common with the others outside of the Zn-finger domains (Zhang et al., 2001). Six cysteines are found in a Cys-rich cluster of dMTF-1 in a $CXCX_2CXCX_5CX_4C$ (where X represents any other amino acid) pattern and this pattern is conserved in MTF-1 from other insects.

In contrast, only four cysteines are found in mammalian MTF-1 in a CXCXCXC pattern. Consistent with the structural differences, dMTF-1 is also functionally distinct from its homologs in mammals. Mammalian MTF-1 mainly responds to Zn and Cd, while dMTF-1 has been found to also strongly respond to Cu in addition to Zn and Cd (Zhang et al., 2001). In the control of Cu homeostasis, dMTF-1 responds to both Cu deficiency and Cu overload in flies by regulating the expression of both the high-affinity copper transporter for copper import and metallothioneins to protect against copper toxicity, thus effectively responding in the opposite manner to the changes in cellular copper level (Zhang et al., 2001; Selvaraj et al., 2005).

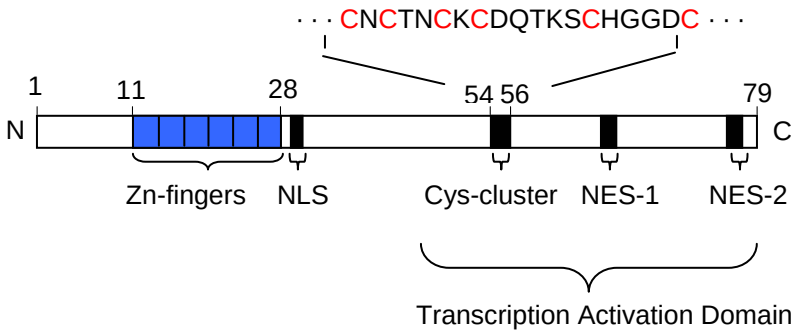

Figure 5-1. Domain structure of *Drosophila* MTF-1 with highlight of the short Cys-cluster region (residues 547-565). In addition to the zinc-finger DNA-binding domain, a putative nuclear localization signal (NLS) and two nuclear export signals (NES1 and NES2) are also indicated (*Günther et al*., unpublished results).

It remains a mystery how dMTF-1 regulates gene expression in response to Cu homeostasis. Recently, *Giedroc* and coworkers performed a series of cellular and biochemical studies in an attempt to understand the functional mechanisms of the dMTF-1 (Chen et al., 2008). Their results suggest that the 19 amino acid residues in the Cys-rich cluster of dMTF-1, ^{547}**C**N**C**TN**C**K**C**DQTKS**C**HGGD**C**^{565}, are responsible for Cu binding, and they are essential and sufficient for Cu detoxification. Transgenic flies harbouring mutant dMTF-1 proteins with alanine substitution of two or four cysteines in

the Cys-rich cluster are significantly impaired in their ability to protect flies from copper toxicity, while the mutant flies with substitution of all six cysteines fail to induce MtnA (the gene encoding *Drosophila* metallothionein) expression in response to copper overload and completely abolish their protection of the flies from copper toxicity (Chen et al., 2008). In parallel, X-ray absorption spectroscopy was used to provide structural information around the Cu-binding site of dMTF-1.

5.3 Material and Methods

5.3.1 Sample Preparations

The samples used in this study were prepared by the members of *Dr. David Giedroc's* group at Texas A&M University. A bacterial expression plasmid, pETC-dMTF_81, was constructed to express residues 499-579 of *Drosophila* MTF-1, denoted C-dMTF_81. The Recombinant C-dMTF_81 was then transformed into in *E. coli* BL21(DE3) and induced for C-dMTF_81 expression. The protein was then purified as previously described (Chen et al., 2008). The purified protein is in 95% homogeny and dissolved in MES buffer (10 mM MES pH 6.3; 100 mM NaCl). The protein concentration was determined by absorbance at 280 nm with ε_{280} = 5600 M^{-1} cm^{-1}. To construct the Cu(I)-C-dMTF_81 complex, Cu(I) was added to the protein solution to the desired metal to protein ratios under anaerobic conditions.

5.3.2 X-ray Absorption Spectroscopy Data Collections

X-ray absorption spectroscopy measurements were conducted at the Stanford Synchrotron Radiation Lightsource with the SPEAR 3 storage ring containing 80-100mA at 3.0 GeV. Copper K-edge data were collected using beamline 9-3 with a wiggler field of 2 Teslas and employing a Si(220) double-crystal monochromator. Beamline 9-3 is equipped with a rhodium-coated vertical collimating mirror upstream of the monochromator and a bent cylindrical focusing mirror (also rhodium-coated) downstream of the monochromator. Harmonic rejection was accomplished by setting the energy cut-off angle of the mirrors to 12 keV. The incident and transmitted X-ray

intensities were monitored using nitrogen-filled ionization chambers, and X-ray absorption was measured as the copper Kα fluorescence excitation spectrum using an array of 30 germanium detectors (Cramer et al., 1988). During data collection, samples were maintained at a temperature of approximately 10 K using an Oxford instruments liquid helium flow cryostat. For each sample, four 35-min scans were accumulated, and the energy was calibrated by reference to the absorption of a standard copper metal foil measured simultaneously with each scan, assuming a lowest energy inflection point of the copper foil to be 8980.3 eV.

5.3.3 X-ray Absorption Spectroscopy Data Analysis

The extended X-ray absorption fine structure (EXAFS) oscillations $\chi(k)$ were quantitatively analyzed by curve fitting using the EXAFSPAK suite of computer programs (http://ssrl.slac.stanford.edu/exafspak.html). *Ab initio* theoretical phase and amplitude functions were calculated using the program FEFF version 8.25 (Rehr and Albers, 2000). No smoothing, filtering, or related operations were performed on the data.

5.4 Results and Discussion

X-ray absorption spectroscopy was carried out to structurally characterize the copper binding properties of C-dMTF_81. Figure 5-2 (lower) shows that the Cu K-edge near-edge spectra from Cu(I)-C-dMTF_81 complex prepared with 1.0 and 3.5 mole-equiv. of Cu(I) are essentially identical. The peak centred at around 8983 eV is due to 1s→4p transition that is commonly used as a fingerprint for determining the coordination environment of Cu(I) compounds (Kau et al., 1987). As shown in Figure 5-2, the features of the peak around 8983 eV in the spectra of the Cu(I)-peptide complexes are similar to trigonally-coordinated $[Cu_4(SPh)_6]^{2-}$ and distinct from digonally-coordinated $[Cu(SC_{10}H_{12})_2]^{2-}$ (Dance, 1986; Kau et al., 1987), suggesting a trigonal coordination environment for Cu(I) bound to the peptide.

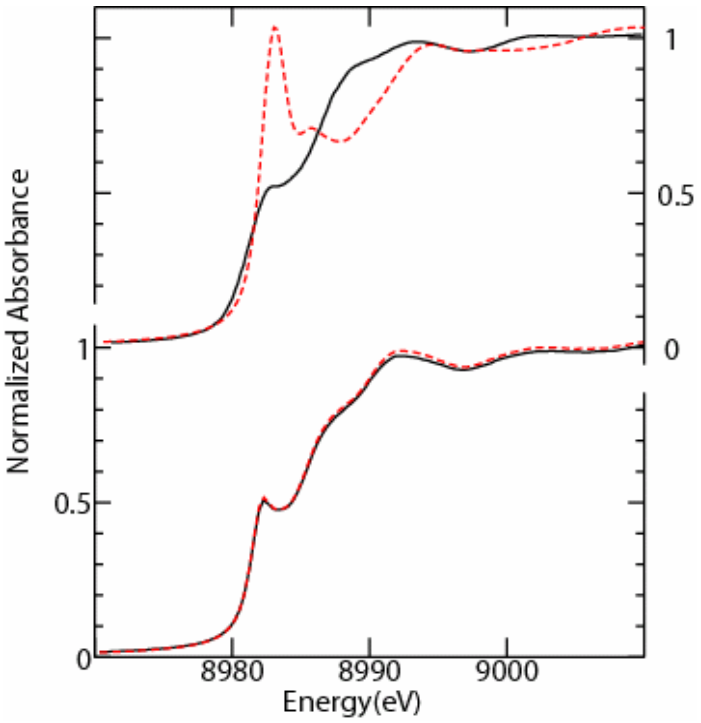

Figure 5-2. Cu K-edge near edge comparison of Cu(I)-C-dMTF_81 complexes with two Cu-thiolate model compounds. The upper panel shows the trigonal Cu(I) thiolate model $[Cu_4(SPh)_6]^{2-}$ (or $[Cu_4(SR)_6]^{2-}$, black solid line) forming a four-Cu(I) cluster, and the digonal Cu(I) thiolate model $[Cu(SC_{10}H_{12})_2]^{2-}$ (or $[Cu(SR)_2]^{2-}$, *red dash line*) which contains a single Cu(I) ion. The lower panel shows Cu(I)-C-dMTF_81 complexes with metal stoichiometries of 1.0 (black solid line) and 3.5 (red dash line), respectively.

More structural details are available from analysis of the Cu K-edge extended X-ray absorption fine structure (EXAFS) spectra. Figure 5-3A and B show the EXAFS, the corresponding Fourier transforms, as well as the best fits of the spectra of the Cu(I)-C-dMTF_81 complexes with both 1:1 and 3.5:1 Cu:peptide stoichiometries. EXAFS curve-fitting parameters are listed in Table 5-1, with the best fits highlighted in bold font. As with the near-edge spectra, the EXAFS of the two stoichiometries are essentially identical, and curve fitting analyses (discussed below) are also very similar. Two major Fourier transform peaks are observed at around 2.3 Å and 2.7 Å, and are attributable to Cu—S and Cu···Cu interactions, respectively. In agreement with the near-edge spectra (Figure 5-2), EXAFS curve fitting indicates three Cu—S interactions at

2.26 Å. Inclusion of lighter scatterers such as N or O results in unreasonably small Debye-Waller factor for Cu—S, indicating a sulfur-only $Cu(SR)_3$ coordination. The 2.7 Å Fourier transform peak is best fitted when including Cu as backscatters for 3.5:1 Cu(I):C-dMTF_81, suggesting a multiple Cu-thiolate cluster at the metal binding site. The large Debye-Waller factor (0.0082 $Å^2$) for Cu···Cu interaction in the fit with a symmetric tetrahedron copper cluster model may suggest a structural distortion in the cluster, which results in a large static Debye-Waller factor (George et al., 1999). Alternatively the 2.7 Å peak in the Fourier transform can be slightly better fitted when using a tetracopper cluster model with the edge-squashed distortion which results in two short Cu···Cu interaction at 2.71 Å and one long one at 2.84 Å, respectively. However, the improvement in the fit with this model is not significant considering the increase in the fitting parameters, and thus the distortion fashion of the copper cluster in the Cu(I)-C-dMTF_81 remains undefined.

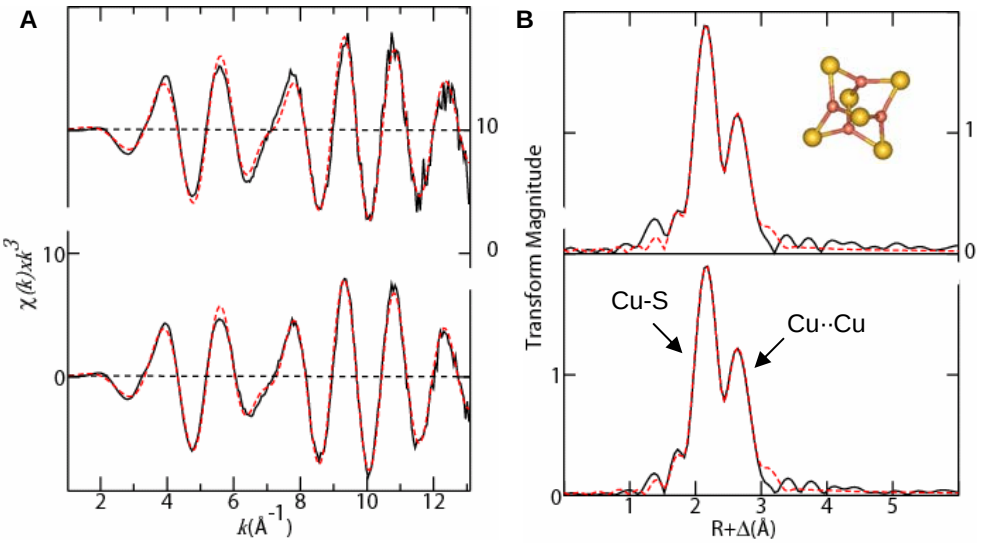

Figure 5-3. Cu K-edge EXAFS and Fourier transforms of Cu(I)-C-dMTF_81 with different mole-equiv. Cu. The EXAFS spectra are shown in Panel A and Cu-S phase-corrected EXAFS Fourier transforms are in Panel B. On the top and bottom of the both panels are the Cu(I)-C-dMTF_81 complexes mixing with 1 mole-equiv. Cu (upper panel) and 3.5 mole-equiv. Cu, respectively. Black solid curves represent the experimental data, while the red dash curves are for best fits with the parameters listed in Table 5-1. The inset shows a structural model representing the proposed metal coordination of the Cu(I)-C-dMTF_81 complex based on the XAS data. The red balls represent copper atoms, while the yellow ones are for sulfur atoms.

Table 5-1. EXAFS curve fitting parameters[a].

Cu-S			Cu-N/O			Cu···Cu			*F*
N	***R* (Å)**	**σ^2 (Å^2)**	***N***	***R* (Å)**	**σ^2(Å^2)**	***N***	***R* (Å)**	**σ^2(Å^2)**	
C-dMTF_81 with 1 mole-equiv. Cu(I)									
3	**2.259 (2)**	**0.0035 (1)**				**2**	**2.698(3)**	**0.0051(2)**	**0.214**
						1	**2.822(7)**	**0.0055(3)**	
3	2.257 (2)	0.0033 (1)				3	2.718(2)	0.0087(1)	0.224
2	2.264 (2)	0.0010 (1)	1	2.029 (9)	0.0020 (8)	3	2.721(1)	0.0093(2)	0.218
3	2.248 (2)	0.0036 (2)				1	2.707(2)	0.0028(2)	0.251
C-dMTF_81 with 3.5 mole-equiv. Cu(I)									
3	**2.260 (1)**	**0.0036 (1)**				**2**	**2.709(2)**	**0.0043(1)**	**0.133**
						1	**2.840(4)**	**0.0047(1)**	
3	2.258 (1)	0.0033 (1)				3	2.727(2)	0.0082(1)	0.16
2	2.264 (1)	0.0009 (1)	1	2.019 (6)	0.0025 (5)	3	2.730(2)	0.0087(1)	0.144
3	2.247 (2)	0.0035 (1)				1	2.714(2)	0.0023(1)	0.187

a. N represents for the coordination numbers; R, interatomic distances; σ^2, the Debye-Waller factors (the mean square deviation in interatomic distance); the fit-error function, *F*, is defined as $[\Sigma(\chi_{expt}-\chi_{calc})^2k^6/\Sigma(\chi_{expt})^2k^6]^{1/2}$, where the summations are over all data points included in the refinement; and the values in parentheses are the estimated standard deviations (precisions) obtained from the diagonal elements of the covariance matrix. The parameters highlighted in **bold** represent the best fits to each data set (see text for discussion).

Subtly different Cu···Cu interactions were found with the 1:1 Cu(I):C-dMTF_81 stoichiometry when comparing to those in 3.5:1 Cu(I):C-dMTF_81 stoichiometry, although these differences are minor and are within the expected accuracies of the technique. In such case, the results for the higher stoichiometry are expected to be quantitatively more reliable because of the better data quality for that sample. Based on the XAS results and the availability of cysteines in the C-dMTF_81 protein, a distorted Cu_4S_6 polynuclear cluster is proposed to form in Cu(I)-C-dMTF_81, as shown in inset of Figure 5-3B.

The overall similarity of the XAS for both Cu(I):C-dMTF_81 stoichiometries provides the direct evidence that C-dMTF-1 may bind to Cu(I) cooperatively in an all-or-none manner, which has been backed up by results from mass spectroscopy and NMR (Chen et al., 2008). Interestingly, similar copper binding behaviour has been observed in several other Cu-responsive transcription factors in the eukaryotes such as Amt1 and Ace1 (Graden et al., 1996; Brown et al., 2002). As previously discussed, the tetracopper cluster may relate to metal-specific response, while the highly cooperative manner in copper-binding may ensure a concentration-dependent response to copper (Graden et al., 1996). Alternatively, formation of the tetracopper cluster might be required for a conformational change to trigger activation or inhibition of gene expression. Assuming a tetracopper cluster is essential for dMTF-1 to fulfil the gene regulation function, one might expect that all of the six cysteines in the 19-residue Cys-rich cluster are required for functional dMTF-1. Surprisingly, site-directed mutagenesis shows that dMTF-1 mutants with two or four cysteines substituted by alanine retain residual protection against Cu toxicity, although far less than that exhibited in the wild type. This phenomenon appears contradictory to the above hypothesis. However, a careful examination of the sequence within the C-dMTF_81 may help to explain the apparent discrepancy. Several residues including His, Lys, Thr, Ser, or Asp are adjacent to the conserved cysteines in the Cys-rich cluster and can provide candidate ligands to Cu. Therefore, in the dMTF-1 mutants with cysteines substituted by alanine, copper may bind to N or/and O from these residues to form a tetracopper cluster with a mixture of ligands. The less effective protection from the mutants to copper toxicity might be due to either less efficient binding of copper to these ligands in the mutant, or the conformation resulting from copper binding to these ligands being less efficient in triggering the transcriptional activity. XAS studies on the copper centres in these mutants will provide valuable information to assess the validity of the above hypotheses.

CHAPTER 6

STRUCTURE-FUNCTIONAL STUDIES ON CSOR FROM MYCOBACTERIUM TUBERCULOSIS

6.1 Abstract

A novel Cu-specific repressor of a copper-sensitive operon (cso) in *M. tuberculosis*, termed CsoR, has been identified and characterized as a representative of a large, previously uncharacterized family of proteins (DUF156). Copper K-edge X-ray absorption spectroscopy (XAS) was used to provide accurate bond-length information on the copper site of Cu(I)-bound CsoR. Analysis of the extended X-ray absorption fine structure (EXAFS) indicated a three-coordinate site, with two Cu-S ligands at 2.21 Å and one oxygen or nitrogen at 2.11 Å. Mutagenesis studies, X-ray absorption analysis, and protein crystallography confirmed that the Cu(I) is coordinated by Cys36, Cys65' and His61' in a subunit bridging site. Molecular dynamics simulations of both apo- and Cu-bound CsoR reveal local conformational changes in CsoR upon copper binding, which suggest a possible mechanism of the Cu-dependent transcription regulation by CsoR.

6.2 Introduction

As previously discussed (see Chapter 1), organisms have developed a series of mechanisms to strictly control copper import, export and distribution within the cells.

One such mechanism is to regulate the components involved in these processes at the transcriptional level. In fact, transcriptional regulation is the main strategy used by prokaryotic organisms for cellular copper control (Outten et al., 2000; Rensing and Grass, 2003; Solioz and Stoyanov, 2003). Two major prokaryotic copper regulators (CopY from *Enterococcus hirae* and CueR from *Escherichia coli* and *Bacillus subtilis*) have been previously identified (Strausak and Solioz, 1997; Outten et al., 2000; Stoyanov et al., 2001; Gaballa et al., 2003), but no copper-specific regulator has been reported for most of the known bacterial species until the recent discovery of CsoR (copper-sensitive operon repressor) from *Mycobateria tuberculosis* (Liu et al., 2007).

CsoR was first observed in a gene expression profile study in *M. tuberculosis* during its infection to mice (Talaat et al., 2004). Further studies found that this gene is part of a three-gene operon, which was renamed as the *cso* operon (Liu et al., 2007). The *csoR* gene is the first gene in the operon, and the last gene *ctpV* encodes a putative P-type ATPase involved in copper transport. Interestingly, the organization of the *cso* operon structure is similar to a previously characterized metal-responsive operon - *cmt* (Cavet et al., 2003). By comparing the structural organization of these two operons, it was found that the position of *csoR* corresponds to the cadmium and lead metal-sensing repressor gene *cmtR* in the *cmt* operon, and because of this, it was predicted that *csoR* may encode a Cu-specific transcription factor. Quantitative PCR experiments and site-directed mutagenesis studies confirmed that CsoR is a copper-specific repressor which up-regulates the expression of genes in the *cso* operon in response to high cellular level of copper in both *M. tuberculosis* and *Bacillus subtilis* (Liu et al., 2007; Smaldone and Helmann, 2007). *In vitro* DNA-protein binding experiment suggested that apoCsoR specifically binds to the 79-bp fragment encompassing the putative *cso* promoter region upstream of *cso* operon, while Cu(I)-binding results in the disassociation of the DNA-CsoR complex (Liu et al., 2007). These results strongly suggest that CsoR functions as a transcriptional repressor of the *cso* operon at normal copper levels, while Cu-binding de-represses the function of CsoR upon copper overload (Figure 6-1).

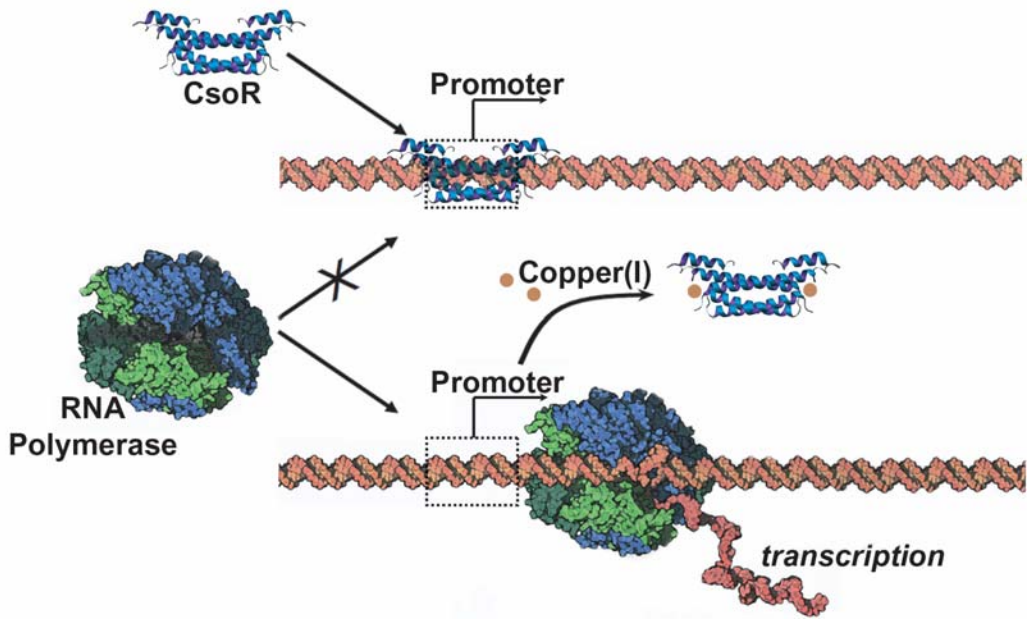

Figure 6-1. Proposed mechanism of Cu-dependent transcriptional regulation by CsoR.

Sequence analysis shows that the CsoR protein from *M. tuberculosis* contains 119-aa residues. According to BLAST analysis, CsoR homologs are present in 128 different organisms out of 191 sequenced bacterial genomes, distributed in all of the major classes of eubacteria (Liu et al., 2007). Among these 128 bacterial organisms, 82% are predicted to encode CsoR as the only known copper regulator (Liu et al., 2007) (Wheeler et al., 2000).

The crystal structure of CsoR in its Cu(I)-bound form was obtained with residues from 4 to 89 (Liu et al., 2007). According to the crystal structure, Cu-bound CsoR forms a homodimer, with each of the CsoR monomers containing three helices referred to as Helix α1 (residues 7-32), α2 (residues 36-63) and α3 (residues 75-86), respectively, and they are linked together by either a short turn (between Helix α1 and α2) or a long loop (between Helix α2 and α3) (Figure 6-2). The α1 and α2 helices are packed against their corresponding components to form an antiparallel four-helix bundle. The α3 helix is located in the C-terminus of the monomer, and is packed against the N-terminus of the α2' helix in the corresponding monomer. There are two Cu(I)

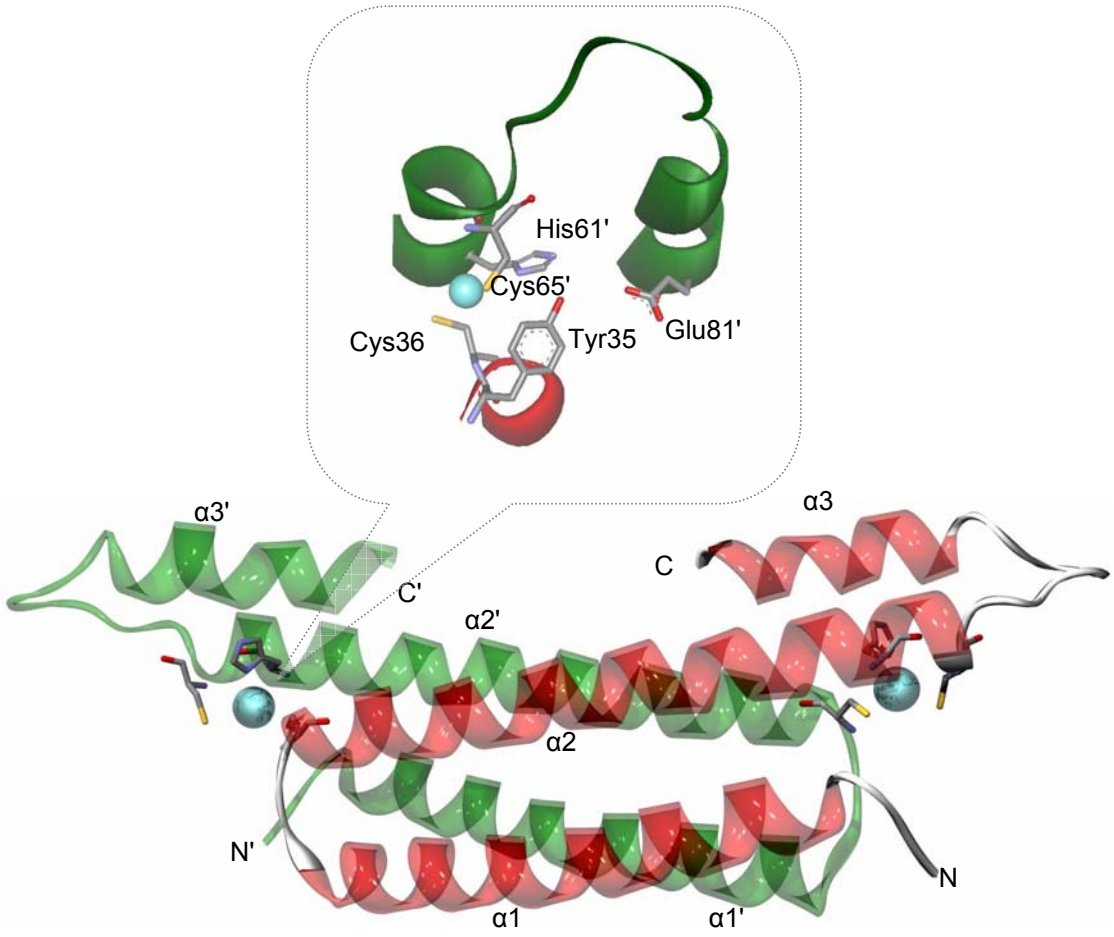

Figure 6-2. Crystallographic structure of Cu-bound CsoR from *M. tuberculosis* with residues 4-89. CsoR forms an all-helix dimmer, with each monomer (shaded in red and green, respectively) composed of three helices denoted α1, α2 and α3. The N-terminus (residue 4) and C-terminus are labelled with N (N') and C (C'), respectively. The Cu(I) (represented as a in blue sphere)-coordinating residues Cys36, His61' and Cys65', as well as two conserved residues Tyr35 and Glu81' which do not directly bind to copper are shown in stick mode. The prime designations refer to the second monomer in green.

binding sites, each located between the helix turn of α1-α2 and α2'-α3'. Three conserved residues, Cys36 from one monomer, and His61' and Cys65' from the other monomer, are present near the Cu(I) binding site and each provides a potential ligand for Cu(I) (Figure 6-2). The limited resolution (2.55 Å) of the crystallographic data means that detailed information regarding the copper binding sites is not available from this

technique alone. In this work, X-ray absorption spectroscopy (XAS) was used to determine the structure around the Cu-binding sites of the wild type CsoR as well as those in the non-functional CsoR mutants. Two conserved residues Tyr35 and Glu81, which are close to the Cu binding site, were also found to be essential for the functional CsoR (Figure 6-2) (Liu et al., 2007). The *in vitro* studies indicated that copper-binding to the CsoR mutants with absence in either of these residues fail to disassociate the mutant protein-promoter DNA complex, although the Cu(I)-binding affinity of these mutants is comparable to that of the wild type protein (*Giedroc et. al.*, personal communication). In order to understand the roles of these two residues in the function of CsoR, the Cu binding sites in CsoR with the aforementioned mutations in either of these residues were compared to wild type protein using XAS. To date no crystallographic or NMR structures of apoCsoR have been reported. In order to predict the conformational changes in CsoR upon Cu-binding, and to interpret the mechanisms of Cu-dependent transcriptional regulation, molecular dynamics (MD) simulations for both apo- and copper-bound CsoR have been performed.

6.3 Material and Methods

6.3.1 Sample Preparations for X-ray Absorption Spectroscopy

Protein expression and purification was done by members of *Dr. David R. Giedroc*'s group at Texas, A &M University. The *csoR* gene from *M. tuberculosis* was cloned and overexpressed in *E. coli* and the protein was purified as previously described (Liu et al., 2007). The protein as-isolated contains about 0.5 mol equiv. of Cu(I), and labeled as $Cu_{0.5}$CsoR. The Cu_1CsoR form was prepared by adding 0.5 mol equiv. of Cu(I) to $Cu_{0.5}$CsoR. The final concentration of the protein was about 1 mM, dissolved in 10 mM HEPES, 0.20 M NaCl, 30% v/v glycerol, pH 7.0, in an anaerobic environment. Protein samples were loaded into polycarbonate XAS cuvettes and immediately frozen in liquid nitrogen and stored under liquid nitrogen until XAS data collection.

Non-functional CsoR mutants, with one of essential residues Cys36 (CsoR-C36A), His61 (CsoR-H61A), Tyr35 (CsoR-Y35F), or Glu81 (CsoR-E81A) substituted by either Ala or Phe, were prepared as for the wild type protein. All the mutants contained 1 mol equiv. of Cu(I), except for the CsoR-C36A, which contained about 0.3 mol equiv. of Cu(I) due to the low affinity of the mutant protein to the Cu(I).

6.3.2 X-ray Absorption Spectroscopy Data Collection

The XAS data of wild-type CsoR protein as well as the CsoR-H61A mutant were collected at Stanford Synchrotron Radiation Lightsource (SSRL) on beamline 9-3. The XAS spectra for the CsoR-C36A, CsoR-Y35F and CsoR-E81A mutants were collected at the Canadian Light Source (CLS) on the HXMA beamline. The SSRL SPEAR 3 storage ring operates with 80-100mA at 3.0 GeV. Beamline 9-3 uses the synchrotron source with a wiggler field of 2 Tesla and employs a Si(220) double-crystal monochromator, a rhodium-coated vertical collimating mirror upstream of the monochromator and a bent cylindrical focusing mirror (also rhodium-coated) downstream of the monochromator. Harmonic rejection at beamline 9-3 was accomplished by setting the energy cut-off angle of the mirrors to 12 keV. The operational current in the storage ring of CLS is 200-250 mA at 2.9 GeV. The optics of the HXMA beamline at CLS is similar to that of beamline 9-3, except that at HXMA harmonic rejection was accomplished by detuning the second monochromator crystal to 50% of the maximum intensity. At both beamlines, the incident and transmitted X-ray intensities were monitored using nitrogen-filled ionization chambers, and X-ray absorption was measured as the copper Kα fluorescence excitation spectrum using an array of 30 germanium detectors (Cramer et al., 1988). During data collection, samples were maintained at a temperature of approximately 10 K using an Oxford instruments liquid helium flow cryostat. The energy was calibrated by reference to the absorption of a standard copper metal foil measured simultaneously with each scan, assuming the lowest energy inflection point of the copper foil to be 8980.3 eV.

6.3.3 *X-ray Absorption Spectroscopy Data Analysis*

The extended X-ray absorption fine structure (EXAFS) analysis was performed using EXAFSPAK (http://ssrl.slac.stanford.edu/~george/exafspak/exafs.htm), with *ab initio* phase and amplitude functions computed using the program FEFF version 8 (Rehr and Albers, 2000). No smoothing, filtering, or related operations were performed on the data.

6.3.4 *Density Functional Theory Calculation*

Geometry optimizations of the Cu(I) binding site in CuCsoR was carried out using the Gaussian03 (G03) suite of software (Frisch et al., 2004) by *Dr. Jake Pushie* in

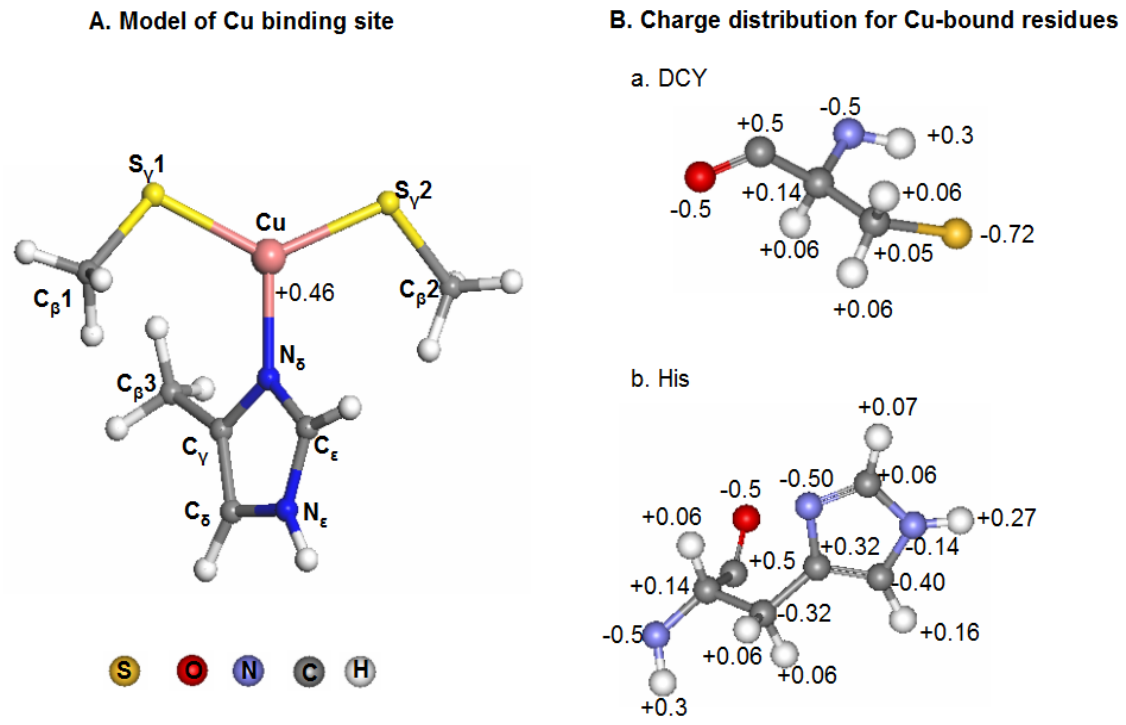

Figure 6-3. The model and OPLS force field setup of the Cu binding site in CuCsoR. Panel A represents the model for Cu binding site. The cysteines and histidine have been replaced by methylthiolate and methylimidazole, respectively, to speed up DFT calculation. DFT-calculated charge of the Cu ion is indicated in Panel A, and the charge distributions for Cu-bound, deprotonated Cys (DCY) and His are indicated in Panel B and C, respectively. The optimized potential for the bonds and angle restraints at the Cu binding sites are listed in Table 6-1.

Dr. Graham George's group. For structural calculations the Cu-bound cysteines and histidine were replaced by methylthiolate and methylimidazole, respectively, to speed up the density functional theory (DFT) calculation (Figure 6-3A). Geometry optimization was carried out at the B3LYP/6-31G(d) level of theory (Becke, 1993) without geometry or symmetry constraints, followed by a harmonic frequency calculation. The convergence criteria employed for geometry optimization required the energy change to be less than 0.3 x 10^{-3} kJ/mol per iteration. The atom-centred charges of the copper binding site were calculated using the CHELPG charge derivation method (Carlson et al., 1993), also at the B3LYP/6-31G(d) level of theory, to represent the distribution of charge density in the metal binding environment within the force field.

Table 6-1. List of parameters for OPLS setup.

	Bond length (Å)	**Harmonic potential (kJ/mol/nm^2)**
Cu-N	2.11	15925
Cu-S_γ1	2.21	43188
Cu-S_γ2	2.21	43188
	Bond angle	**Harmonic potential (kJ/mol/nm^2)**
S_γ1-Cu-S_γ2	130.89	
S_γ1-Cu-N_δ	116.28	
N_δ-Cu-S_γ2	112.28	
Cu-S_γ1-C_β1	107.76	397.48
Cu-S_γ2-C_β2	107.66	
Cu-N_δ-C_γ	126.06	
Cu-N_δ-C_ε	127.27	
	Improper Dihedral Angle	**Harmonic potential (kJ/mol/nm^2)**
{S_γ1,Cu,S_γ2,N_δ}	-178.65	33.472

6.3.5 Optimized Potentials of the Cu-Bound Site for Liquid Simulations Force Field

A new residue type, DCY, was defined within the force field for the deprotonated cysteines bound to the copper ion. The calculated charges (see Section 6.4.4) were distributed over the DCY and His side chains, as well as the Cu(I) centre

(Figure 6-3), with the exception of the charges on the backbone atoms of these residues, which remained unchanged from their parent amino acid topologies. The force constants used to represent the Cu(I)-ligand bonds in the optimized potentials for liquid simulations (OPLS) force field were determined from the output of the G03 frequency calculations (described in Section 6.3.4). The Cu-ligand bond lengths determined by EXAFS analysis were used as equilibrium bond lengths, designated r_0. Restraints used for bond lengths, angles and improper dihedral angles of the Cu coordination sites are listed in Table 6-1.

6.3.6 Molecular Dynamics Simulations

MD simulations of both the di-Cu(I)-bound (CuCsoR) and metal-free (apoCsoR) forms of the CsoR dimer were carried out using the GROMACS software, version 3.2 (Berendsen et al., 1995; Lindahl et al., 2001). The CsoR crystal structure coordinates (PDB ID: 2hh7) (Liu et al., 2007) were used as a starting point for all CsoR systems. The initial structure of apoCsoR was estimated by removing the copper ions and protonating the Cu-bound Cys residues in the crystallographic structure of CuCsoR. Each protein was then solvated with 18009 single point charge (SPC) water molecules (Berendsen et al., 1981) in a 9.0 x 9.0 x 7.0 nm box. The SPC water positions were minimized by the method of steepest descent (keyword integrator=steep) before starting the simulation. Two Na(I) counter-ions were added to the box with CuCsoR to maintain an overall charge of zero for the system.

MD simulations of both forms of CsoR were carried out using the OPLS-(AA)/L all-atom force field (Jorgensen et al., 1996). The OPLS force field setup for the Cu binding sites was described above in Section 6.4.5. Temperature (300 K) and pressure (1 bar) were kept constant during the simulation by weakly coupling the system to an external bath (τ_T = 0.1 ps for temperature and τ_P = 1.0 ps for pressure) (Berendsen et al., 1984). The particle mesh Ewald method approach was used for evaluating long-range electrostatics, and SETTLE (Miyamoto and Kollman, 1992) and LINCS (Hess et al., 1997) were used to constrain bond lengths in water and protein molecules, respectively,

during the simulations. A 2-femtosecond time step and periodic boundary conditions were employed in all the simulations. The simulations were run until the total energy, the potentials for non-bonded interactions within the protein molecule and between the protein and solvent, as well as the atom position root mean square deviation (RMSD) were stable for at least 10 ns. Results from this initial time (designated an equilibration phase) were not explicitly included in some parts of data analysis.

6.3.7 Analysis of Molecular Dynamics Simulation Results

Energy, RMSD, root mean square fluctuations (RMSF), solvent accessibilities, hydrogen bonds, and atomic distances were calculated using the tools provided in the GROMACS package. The size-dependent RMSD at a given time frame *t* was calculated with respect to the initial structure (at the time frame zero) after least-square fitting the structure to the initial structure, as defined following:

$$\sqrt{\frac{1}{M}\sum_{i=1}^{N} m_i[(r_i(t\ ) - (r_i(0)]^2}\ , \qquad (6.1)$$

where m_i is the mass of the *ith* atom; $r_i(0)$ and $r_i(t)$ are the position vectors of the *ith* atom at the time frame zero and time frame *t*, respectively; and *M* is the sum of all atom mass in the system with N atoms. The C_α atom standard deviation (RMSF) was calculated with the program g_rmsf after least-square fitting the structure to the initial structure at time zero. Analysis of the secondary structure was performed using DSSP program (Kabsch and Sander, 1983). VMD (Humphrey et al., 1996) and MOLMOL (Koradi et al., 1996) were used for molecular visualization.

6.4 Results

6.4.1 Structural Study on the Copper Binding Site by X-ray Absorption Spectroscopy

The Cu binding properties of CsoR have been reported earlier (Liu et al., 2007). According to these studies, the CsoR dimer can bind up to two Cu ions, although CsoR with only one copper ion bound is functional. Cys36, His61 and Cys65 are candidate

residues for binding the copper ion. Both Cys36 and His61 are essential for CsoR functionality, and mutation of either of these residues significantly reduces the Cu(I) binding-affinity of the protein. To probe the structure of the metal coordination complex in CsoR, the Cu_1CsoR form (containing one copper atom per monomer) and $Cu_{0.5}$CsoR form (containing one copper atom per dimer) of wild-type CsoR proteins were examined by copper K-edge X-ray absorption spectroscopy. CsoR-C36A and CsoR-H61A, the non-functional CsoR mutants with Cys36 and His61 substituted by Ala, respectively, were also included in the XAS experiments to examine the involvement of these residues in the copper binding centre.

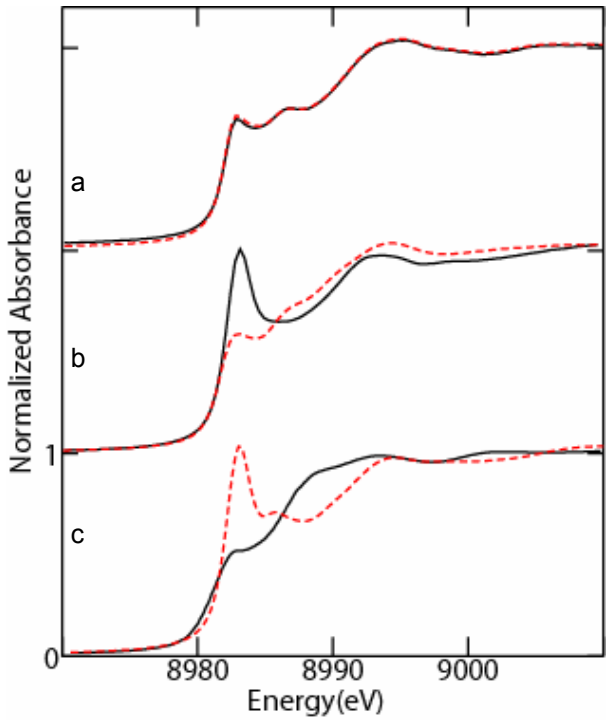

Figure 6-4. Comparison of Cu K-edge X-ray absorption near-edge spectra of CsoR proteins with Cu(I)-thiolate model compounds. a) the Cu_1CsoR form with one copper atom per monomer (solid black line) and $Cu_{0.5}$CsoR form with one copper atom per dimmer (broken red line) of wild-type protein; b) the CsoR mutants with His61 substituted by Ala (solid black line) and with Cys36 substituted by Ala (broken red line); c) the two model Cu(I) thiolate compounds – a trigonal Cu(I) complex, $[Cu_4(SR)_6]^{4-}$ ($[Cu_4(SPh)_6]^{4-}$) (solid black line), and a digonal Cu(I) complex, $[Cu(SR)_2]^{2-}$ ($[Cu(SC_{10}H_{12})_2]^{2-}$) (broken red line).

The near-edge XAS spectra of CsoR proteins are compared with three coordinate and two-coordinate model compounds in Figure 6-4. The peak at approximately 8,981.5 eV is due to a 1s→4p transition which becomes more intense for 2-coordinate species because of 4p orbital degeneracy (Figure 6-4c) (Kau et al., 1987). The 1s→4p feature in the near-edge spectra of the CuCsoR is more similar to that of three-coordinate model compounds than to that of two-coordinate species, suggesting a trigonal copper centre in CsoR wild type. The near-edge spectra of CsoR with metal stoichiometries of 0.5 and 1.0 are essentially identical, which indicates identical coordination of both Cu(I) sites in homodimeric CsoR (Figure 6-4a). Notably, CsoR-H61A shows a near-edge spectrum almost identical to that of digonal 2-coordinate Cu(I) species with thiolate donors, with an intense 1s→4p peak, while the near-edge spectrum of CsoR-C36A remains similar to the wild type CsoR and the 3-coordinated cuprous-thiolate model (Figure 6-4b).

Experimental copper K-edge EXAFS spectra of CsoR proteins are shown in Figure 6-5, together with the corresponding Fourier transform spectra and their best fits. Structural parameters derived from EXAFS curve fitting indicate the presence of two Cu-S interactions, at an averaged distance of 2.21 Å, and a single Cu-(N/O) interaction at 2.11 Å (Table 6-2). The total coordination number of three determined from the EXAFS curve fitting is consistent with the near-edge spectra. The small outer shell Fourier transform peaks at ~ 3 and 4 Å expected from the outer carbons of the histidine ring are not obvious in the data. Nevertheless, there are small features in this region that are reasonably well fitted by including the multiple scattering paths from an imidazole ring (Figure 6-5Ba) with a small improvement in the fit quality of about 5%. The data from the CsoR-H61A shows a peak shift (evident in both the *k*-space and the *R*-space) towards lower values, suggesting that the copper-centre in the mutant has a shorter metal-to-ligand distance by average (Figure 6-5 A and B). This observation is confirmed by the curve fitting results shown in the Table 6-2. The copper site of the CsoR-H61A mutant unambiguously shows a digonal coordination by two sulfurs donors with bond lengths (2.14 Å) that are characteristic of 2-coordinate sites (Chen et al.,

2003). The minor peak around 4 Å is best fitted when including multiple scattering from S-Cu-S using a linear 2-coordiate Cu-thiolate model. These XAS results provide evidences that His61 donates a ligand to the Cu(I) in wild type CsoR, which is consistent with the crystallographic structure and functional characterization of CsoR-H61A. Curve fitting results from the EXAFS data of CsoR-C36A indicate the presence of one Cu-S interaction, at a distance of 2.23 Å, and two Cu-(N/O) interactions, at an average distance of 1.98 Å. This is consistent with copper coordination by His61 and Cys65 of the same monomer, and probably a hydroxide or water ligand in CsoR-C36A. There is a minor peak at around 2.6 Å in the Fourier transform of the CsoR-C36A mutant, which might be due to the Cu···Cu interactions when CsoR-C36A forms higher order of oligomers (Giedroc, *et. al.,* personal communication).

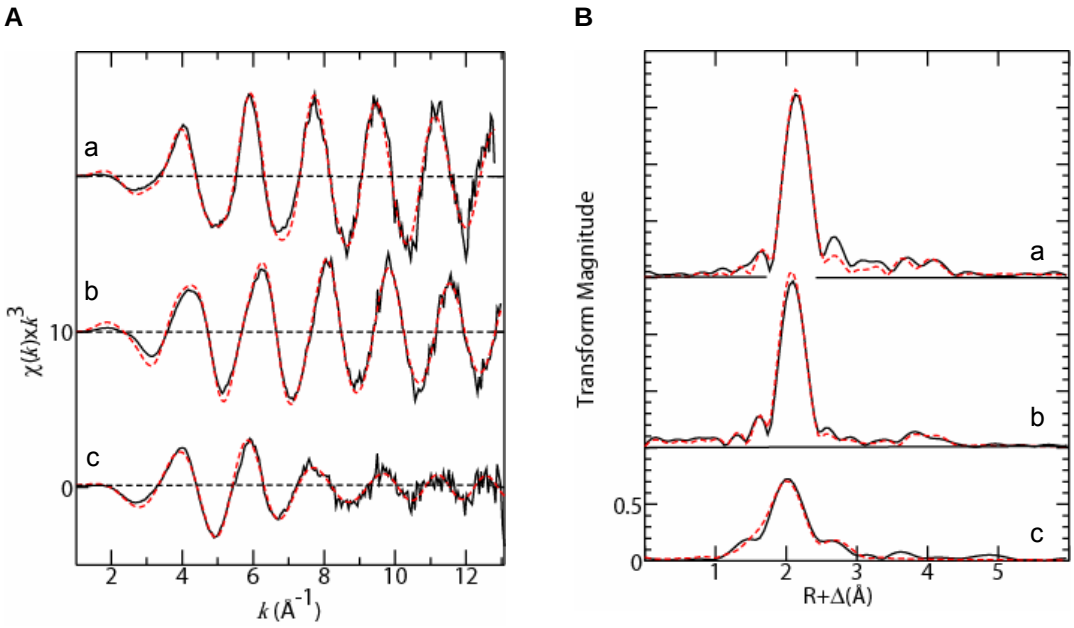

Figure 6-5. A) EXAFS and B) Fourier transforms of CsoR proteins. a) Cu_1CsoR wild type protein with one copper ion per monomer protein; b) CsoR mutant CsoR-H61A with His61 substituted by Ala; c) CsoR mutant CsoR-C36A with Cys36 substituted by Ala. Solid lines indicate experimental data and broken lines are the best fits obtained with parameters given in Table 6-2. All Fourier transforms are phase-corrected for Cu-S backscattering.

As mentioned above, residues Tyr35 and Glu81 have been shown to be essential for CsoR function. Thus, mutation of either of these residues abolishes Cu-induced disassociation of the protein-DNA complex *in vitro*, but, interestingly, does not appreciably change the Cu binding affinity of CsoR. In order to quantitatively assess whether the mutants have altered Cu binding sites, the Cu K-edge XAS of the CsoR-Y35F and CsoR-E81A mutants were collected and compared to that of the wild type protein.

Table 6-2. Summary of Cu K-edge EXAFS curve-fitting results[ab].

Sample	Cu-S			Cu-N/O			
	N	***R*(Å)**	**σ^2(Å^2)**	***N***	***R*(Å)**	**σ^2(Å^2)**	***F***
CuCsoR	**2**	**2.209(3)**	**0.0027(1)**	**1**	**2.113(7)**	**0.0028(1)**	**0.235**
	1	2.234(3)	0.0004(4)	1	2.026(4)	0.0008(4)	0.443
CsoR-H61A	**2**	**2.143(2)**	**0.0033(1)**				**0.186**
	1	2.133(1)	0.0031(3)	1	2.097(13)	0.0011(3)	0.186
CsoR-C36A	**1**	**2.227(11)**	**0.0059(12)**	**2**	**1.991(9)**	**0.0038(10)**	**0.621**
	2	2.219(8)	0.0103(11)	1	1.992(11)	0.0011(10)	0.621

a. N represents for coordination number, R for interatomic distance, σ^2, the Debye-Waller factor for mean-square deviation in *R*. The fit error *F* is defined as $[\sum k^6(\chi_{exptln}-\chi_{calcd})^2/\sum k^6\chi_{exptl}{}^2]^{1/2}$. The values in parentheses are the estimated standard deviations (precisions) obtained from the diagonal elements of the covariance matrix. Fits shown in boldface fonts represent the best fits obtained for the samples. *b*. Only first-shell EXAFS components are included in the table.

As shown in Figure 6-6A, the near edge spectra of CsoR-Y35F and CsoR-E81A mutants are essentially identical to that of the wild type protein, suggesting a very similar 3-coordinate copper centre in both cases. When overlaying the EXAFS and corresponding Fourier transform spectra of the mutant proteins with the wild type, they

are again almost identical to each other (Figure 6-6B and C). From the Fourier transforms, very slight differences are evident in the intensity of the major peak between CsoR-Y35F and the other two proteins, as well as in the position and the intensity of two minor peaks around 3.5 – 4.2 Å between the two mutants and the wild type protein. However, these differences are close to the level of the noise and significantly better data is required for a definitive result. Despite this uncertainty, the conclusion from these EXAFS data is that the Cu binding sites of CsoR-Y35F and CsoR-E81A are essentially identical to that of wild-type protein. In agreement with this, curve-fitting analysis of the EXAFS gave Cu-S and Cu-N bond-lengths that were within ±0.02 Å of those in the wild-type protein.

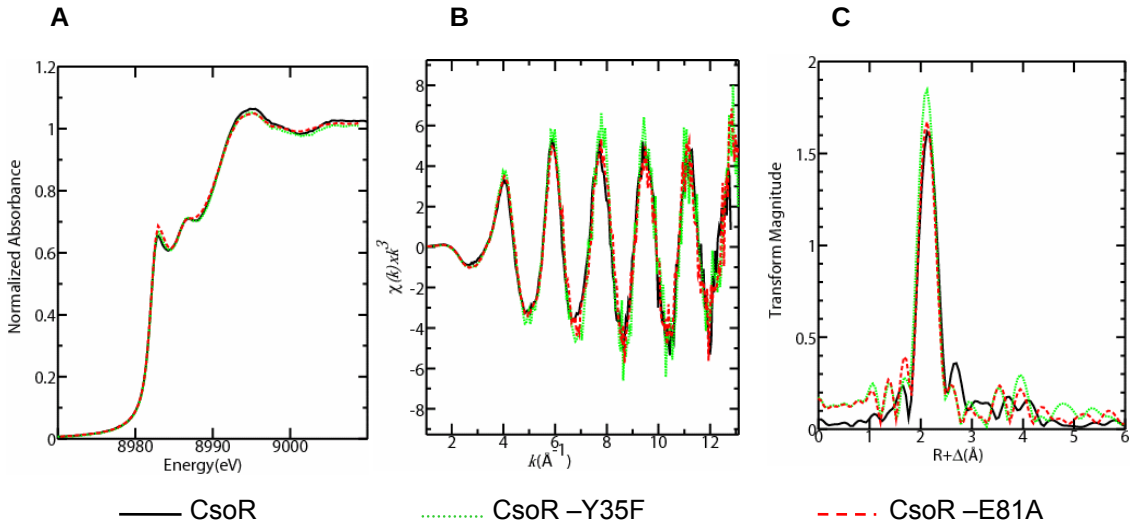

Figure 6-6. Comparison of X-ray absorption spectra of the wild type CsoR with two non-functional mutants CsoR-Y35F and CsoR-E81A. The CsoR-Y35F and CsoR-E81A are non-functional mutants with Tyr35 and Glu81 substituted by Phe and Ala, respectively. Panel A shows the near edge spectra, and EXAFS and corresponding Fourier transforms spectra in B and C, respectively.

6.4.2 Molecular Dynamics Simulations of Cu-Bound and Metal-Free Forms of CsoR

MD simulations on the solvated CsoR with and without bound Cu ions were carried out in this study, with a goal of providing information on the mechanisms of Cu-dependent disassociation of the DNA-CsoR complex. Only 85 residues (from 4 to 88) that were resolved by crystallography were included in the simulations. The first 59.8 ns of the simulation for apoCsoR and 54.1 ns for CuCsoR are included here for simulation analysis. With MD calculations it is important to assess whether the simulation has achieved what is known as the production state in which dramatic changes in structure due to equilibration are no longer occurring in the simulation (i.e. steady-state sampling has been achieved). The equilibration time required to reach the production state usually depends on how different the initial structure from the structure in its production state. Analysis of the conformational fluctuation of the system, the evolution of total energy and sub-category potentials, the atom position RMSDs and C_α RMSFs in the proteins relative to the initial structure were used to estimate the simulation time needed for the equilibration. Following that, the overall conformational changes with time were examined for both CuCsoR and apoCsoR, and the conformation of these two proteins in the production state were compared.

6.4.2.1 Equilibration Measurements

As shown in Figure 6-7A, the total energy of the system stabilizes after about 2.5 ns for both apoCsoR and CuCsoR. The total energy of CuCsoR stabilizes around 643.4±0.5 $x10^3$ kJ/mol, and about 1700 kJ/mol higher for apoCsoR. The difference here is at least partially due to the interactions between Cu and the ligands in the copper binding sites as well as the inclusion of sodium ions in the CuCsoR simulation. Given that the water molecules account for the majority of atoms in the simulation system, the potential energies excluding the interactions with water molecules are considered to be more sensitive to the conformational changes of the proteins. Figure 6-7B represents the time-dependent evolution of the non-bonded potentials, including the Coulomb potentials and van der Waals potentials among the atoms in the dimer protein and

between the protein and solvent. The non-bonded potentials reach the production state after about 20 ns of equilibration process for both systems. The difference in the non-bonded potentials between apoCsoR and CuCsoR are small, with an approximately 100 kJ/mol difference.

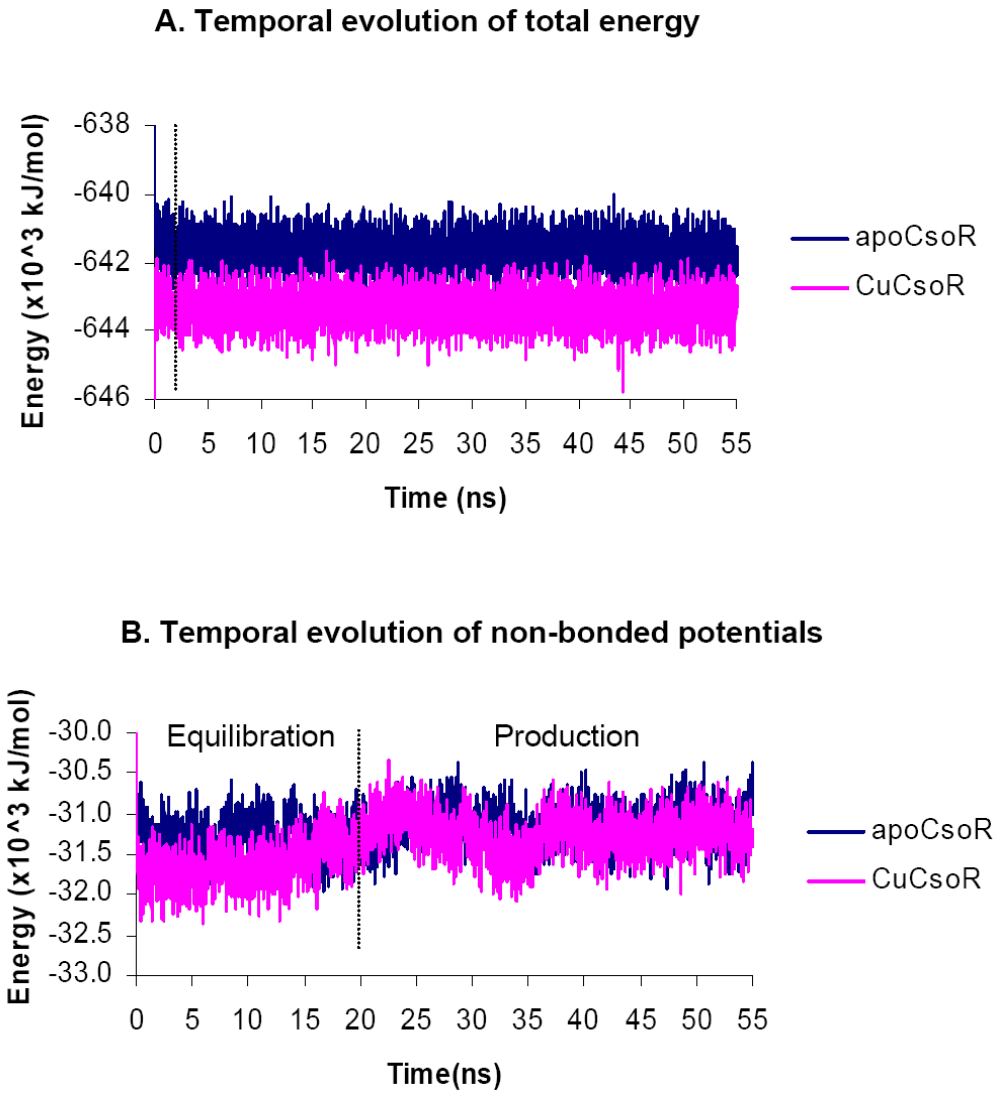

Figure 6-7. Time-dependent evolution of the total energy and non-bonded potentials for apoCsoR and CuCsoR. The non-bonded potentials include the potentials for Coulomb interactions and van der Waals interactions within the protein and between the protein and solvent molecules.

In contrast to the energy analysis, different equilibration times are required for CuCsoR and apoCsoR to reach the production state as determined by examination of the atom position RMSDs (Figure 6-8). For CuCsoR, the atomic position RMSDs of both monomers increases rapidly and continuously within the first 2.3 ns mainly due to departures from the crystallographic structure (Levitt and Sharon, 1988), and reaches

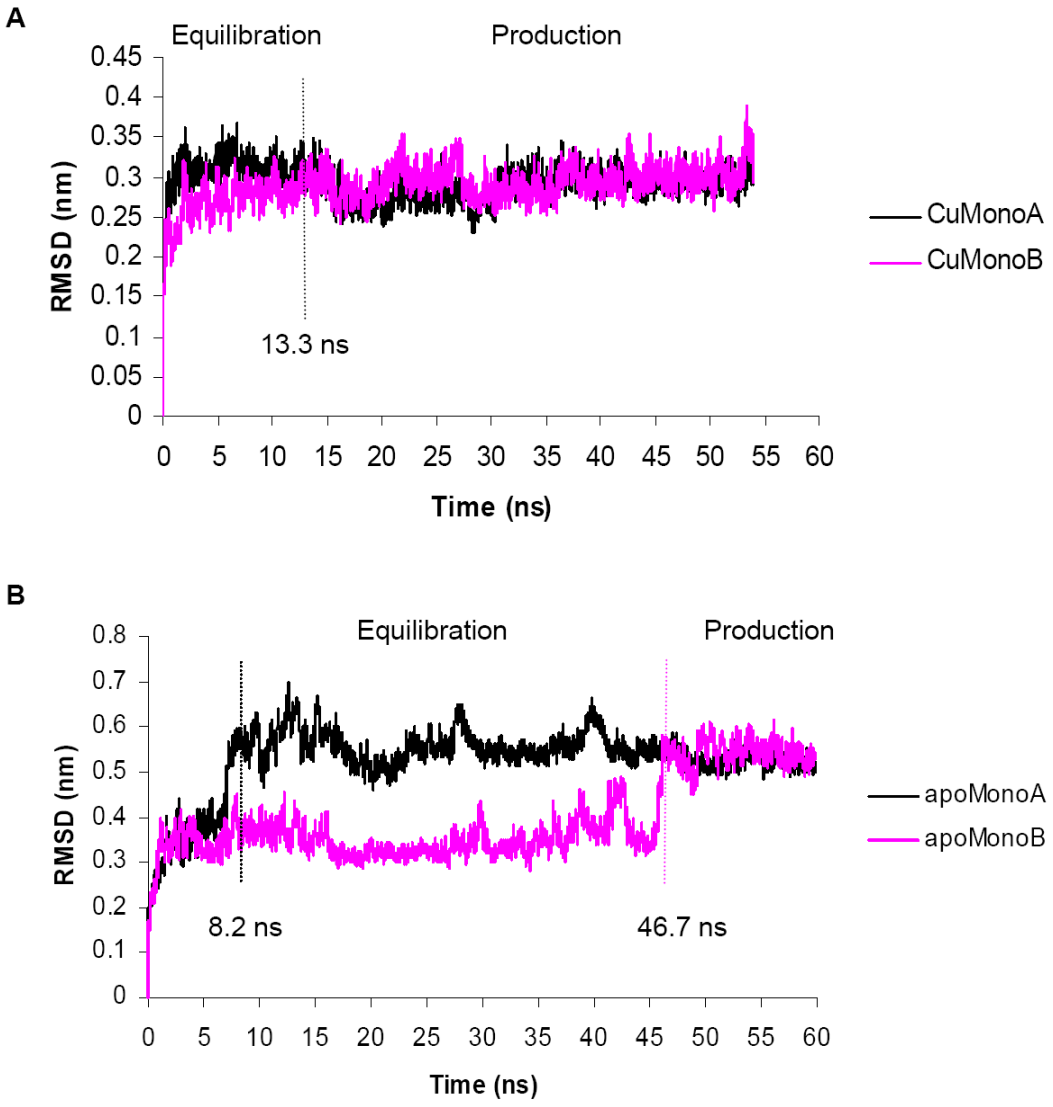

Figure 6-8. Time-evolution of the atomic position RMSDs for the CuCsoR (A) and apoCsoR (B) proteins. The RMSD at given time frame (t_1) was calculated using the program g_rms from GROMACS as described in the method section (Section 6.4.6).

production state about 13 ns after starting the simulation, thereafter fluctuating around 3 Å. Similarly, the RMSDs of the monomers in apoCsoR also show a rapid increase for the first 2.3 ns, reaching a plateau around 4 Å. However, in contrast to CuCsoR, both monomers in apoCsoR undergo a conformational turnover at 8.2 ns and 46.7 ns of the simulation, respectively, indicating by a sharp 2-Å increase in RMSD for each. The RMSDs of both apoCsoR monomers are stable at around 5.3 Å for the last 13 ns of the simulation.

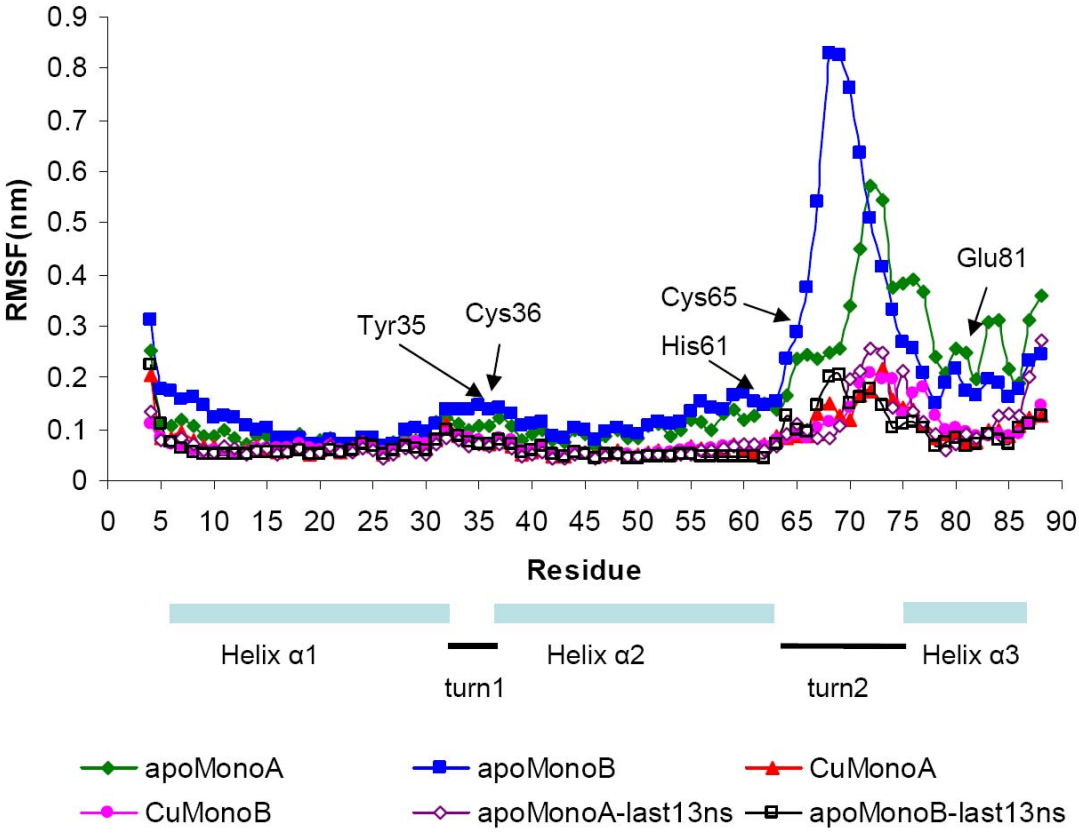

Figure 6-9. The Cα RMSFs of the monomers in CuCsoR (A) and apoCsoR (B) proteins. The RMSFs was calculated with the program g_rmf from GROMACS as described in the method section (Section 6.4.6). The C_α RMSFs of CuCsoR monomers were calculated by including the whole simulation time (~ 54 ns). For apoCsoR, the C_α RMSFs of the monomers over the entire simulation time (~ 59 ns) and during the production state (the last 13 ns) were calculated to compare the conformational changes during the simulation. The crystallographic secondary structure of the residues involved is specified underneath the plot.

The occurrence of conformational turnover in apoCsoR is further confirmed by examining the C_α atomic position RMSFs of the monomers in the protein. As shown in Figure 6-9, the C_α RMSFs of monomers in apoCsoR is overall larger than those in CuCsoR over the whole simulation, with a significant increase around residues 62-78, and three minor ones around residues 30-40, 55-62 and 79-85 (residues on both ends ignored). These conformational turnovers all occur in or close to the flexible turns that link helices based on observation from the crystal structure (Figure 6-9) (Liu et al., 2007). In addition, all the residues involved in Cu binding, as well as two confirmed essential residues, Tyr35 and Glu81, are located in these regions. To rule out the possibility that the increase in the RMSFs in these regions is due to increased flexibility (fluctuation) of the residues, the C_α RMSFs of monomers in apoCsoR over the last 13 ns of the simulation after both monomers have finished the significant turnover are compared to both that of apoCsoR and CuCsoR over the whole simulation. The results show that the C_α RMSFs of monomers in apoCsoR over the last 13 ns of the simulation are significantly reduced compared to those with the whole simulation time included, and overall resemble the variations observed in the CuCsoR simulation (Figure 6-9).

Based on above analysis, CuCsoR and apoCsoR are concluded to have reached the production state at approximately 13.2 ns and 46.8 ns after initiation of the simulations, respectively. To keep the analyses statistically comparable, the last 13 ns of the simulation for CuCsoR was used in comparing conformational differences between apoCsoR and CuCsoR in the production state.

6.4.2.2 Overall Conformational Comparison between ApoCsoR and CuCsoR

The secondary structures of CsoR proteins were analyzed using the DSSP program to examine any conformational differences between the simulated CuCsoR in solution and the reported crystal structure, as well as between the metal-free and the Cu-bound CsoR models.

As shown in Figure 6-10, the secondary structure for both forms of CsoR are dominated by α-helices, similar to but with minor differences from the structure

observed crystallographically (Liu et al., 2007). About 2 ns into the simulation the helix α1 (residues 7-32) from the crystal structure breaks into two shorter helices connected

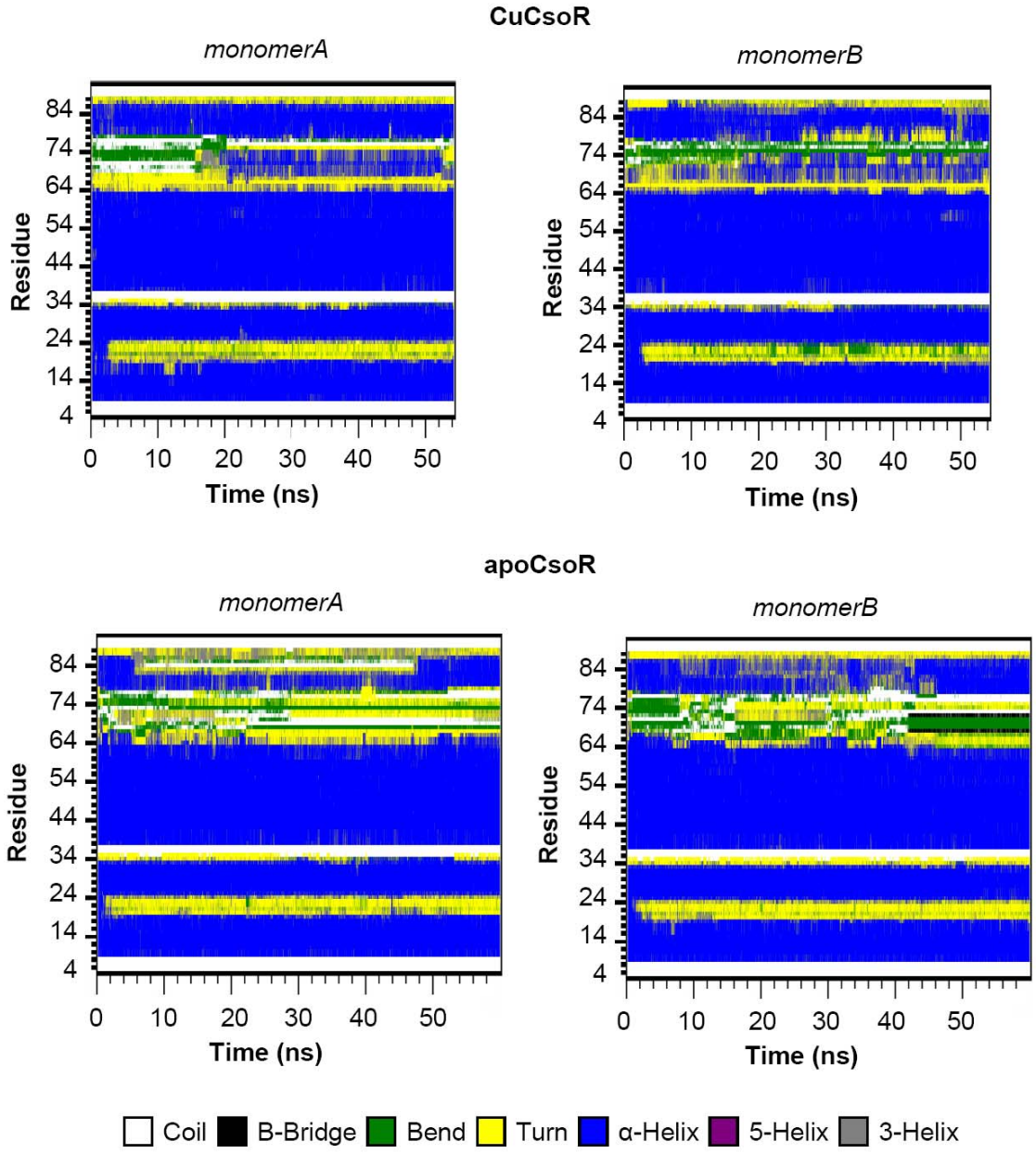

Figure 6-10. Temporal evolution of the secondary structures of monomers in both CuCsoR and apoCsoR proteins. The secondary structures of the protein were analyzed using DSSP program as described in the method section (Section 6.4.6).

by a turn spanning residues 18-22 for both CuCsoR and apoCsoR. Consistent with the RMSF analysis, the most significant differences in the secondary structures between apoCsoR and CuCsoR are found in the region around residues 66-72. The residues in this region form a better-ordered secondary structure in CuCsoR, changing from bends or turns into a short α-helix compared to apoCsoR. This short α-helix is observed for both CuCsoR monomers at approximately 20 ns after the start of the simulation, and it remains as a dominant secondary structure (*i.e.* present > 50% of the simulation time) during the remainder of the simulation (Table 6-3).

Table 6-3. Comparison of the secondary structure elements of residues 66-72 in both apoCsoR and CuCsoR from the MD simulations.

Residue No	% of α-helix during simulation time			
	apoCsoR-MonoA	apoCsoR-MonoB	CuCsoR-MonoA	CuCsoR-MonoB
	Over the entire simulation time			
66	0.00	0.01	0.38	0.53
67	0.00	0.01	0.43	0.55
68	0.00	0.00	0.43	0.56
69	0.00	0.00	0.53	0.61
70	0.00	0.00	0.44	0.36
71	0.00	0.00	0.42	0.34
72	0.00	0.00	0.41	0.33
	Over the production state			
66	0.00	0.00	0.62	0.58
67	0.00	0.00	0.71	0.61
68	0.00	0.00	0.71	0.61
69	0.00	0.00	0.77	0.75
70	0.00	0.00	0.63	0.50
71	0.00	0.00	0.59	0.48
72	0.00	0.00	0.58	0.46

The conformational fluctuations of both forms of CsoR in the production state are visualized by randomly sampling 20 structures from each form of the protein simulations. The 20 structures were sampled in the following way: both forms of CsoR

during the last 13 ns of simulation were grouped into clusters with a cutoff of the heavy atoms RMSDs of the residues 7-63 (mainly involved in helix α1-turn-helix α2) at 0.8 Å

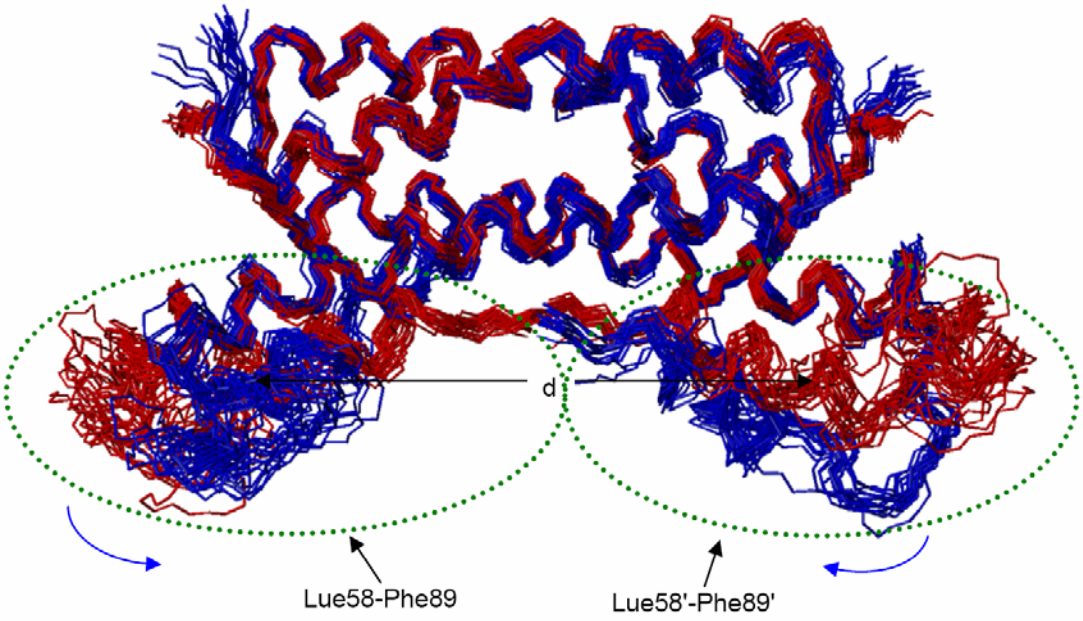

	apoCsoR	CuCsoR
d(Å)	34.9 (0.8)	40.0 (0.6)

Figure 6-11. The backbone of apoCsoR and CuCsoR structures randomly sampled from the representative clusters in the production state. The structures during the last 13-ns simulation were grouped into clusters with the backbone of the residues 7-63 equal or less than 0.8 Å for CuCsoR and 0.9 Å for apoCsoR, respectively, and the representative clusters with the cluster size larger than 65 were chosen for random sampling. 20 structures were sampled from each form of CsoR, and they are overlaid by aligning the backbones of the residues 7-63. The apoCsoR structures are drawn in the blue lines, while the CuCsoR structures are presented in red color. The blue curve arrows indicate the direction of a flexible motion of apoCsoR along the helix bundle. The average distances between residues Leu58-Phe89 and Leu58'-Phe89' (highlighted in the green circles) for both apoCsoR and CuCsoR are listed below the structures, with the standard deviation in the round brackets.

for CuCsoR and 0.9 Å for apoCsoR, respectively. The 20 structures were then randomly sampled from these clusters with size larger than 65 (account for 5% of the simulation structures) in each form of CsoRs. The backbones of the sampled structures are shown

in Figure 6-11. As indicated by the RMSF and secondary structure analyses, the structures of apoCsoR and CuCsoR are similar to each other in the region of helix α1-turn-helix-α2 (residues 7-63), while distinct differences are noticeable around the long loop (including residues 64-72) and helix α3. In contrast to CuCsoR, apoCsoR shows flexible motion along the helix bundle in the direction indicated by the blue arrow in Figure 6-11, together with a bending of the helix bundle. The degree of bending can be quantitatively described by the distance d between the centre of the residues Leu58-Phe89 and Leu58'-Phe89' (as highlighted by the green circles in Figure 6-11) which include the long loop and the short helix α3. The average distance d in the apoCsoR is about 13% shorter than that in the CuCsoR, suggesting the Cu-binding results in straightening of the helix bundles in CsoR.

6.4.2.3 Comparison of the Proposed Functional Groups in ApoCsoR and CuCsoR

Several residues have been identified by site-directed mutagenesis as essential for CsoR function. These include the residues involved in Cu-binding (Cys36, His61 and Cys65) (Liu et al., 2007) and the two conserved residues Tyr35 and Glu81 near the Cu-binding site which do not appear to be involved in copper binding (section 6.5.1) and whose function is uncertain. In addition, several positively charged residues derived from the α1 and α2 helices, including Arg15 (highly conserved), Lys8, Arg52, Arg55 and His59, are candidates for DNA binding (Liu et al., 2007). Comparison of the conformation and mobility of these residues in the simulations for apoCsoR and CuCsoR is therefore of interest in order to understand their possible roles in the Cu-dependent dissociation of the CsoR protein-DNA complex.

At Cu binding site 1 (Cys36, His61' and Cys65') of CuCsoR, the distance of Cu and His-N is around 2.3 Å and that of Cu and Cys-S is around 2.4 Å on average (Figure 6-12), and these bond lengths are inconsistent what are observed in EXAFS (see discussion in Section 6.5). Compared to apoCsoR the backbone of the Cys65' residue moves significantly (about 2.7 Å relative to the backbone of His61') towards the Cu binding site in CuCsoR. No apparent differences are observed for the backbones of

Cys36 and His61', but the side chains of both residues are rotated compared to what is found for apoCsoR so that the Cu-bound ligands (S_γ from Cys36 and N_δ from His61') are oriented closer to the metal binding site. Similar structural changes are also found at Cu binding site 2 (Cys36', His61 and Cys65) although these are more subtle.

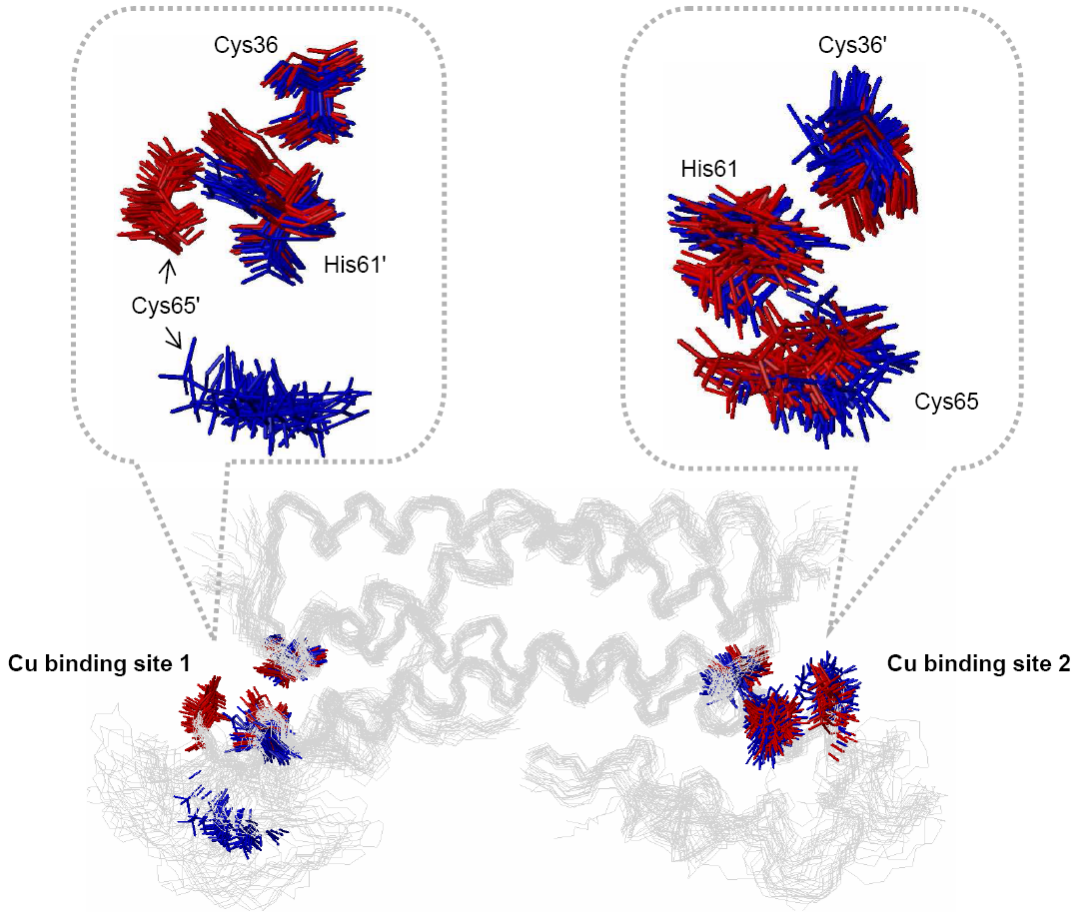

Figure 6-12. Comparison of the Cu-bound residues between apoCsoR and CuCsoR. The structures of apoCsoR and CuCsoR were sampled and aligned as described earlier in Section 6.4.2.2. The backbone structures of both forms of proteins are shaded in light grey color. The residues at the Cu binding site, Cys36, His61 and Cys65, are shown in blue for apoCsoR and in red for CuCsoR.

Significant differences between CuCsoR and apoCsoR are observed in the behaviour of the highly conserved and essential residue Glu81. As shown in Figure 6-13, the backbone atoms of Glu81 have moved significantly towards Lys41' in the α2' helix

of the corresponding monomer. This movement can be quantified by the distance between the centres of the backbone atoms of Glu81 and Lys41', which changes from

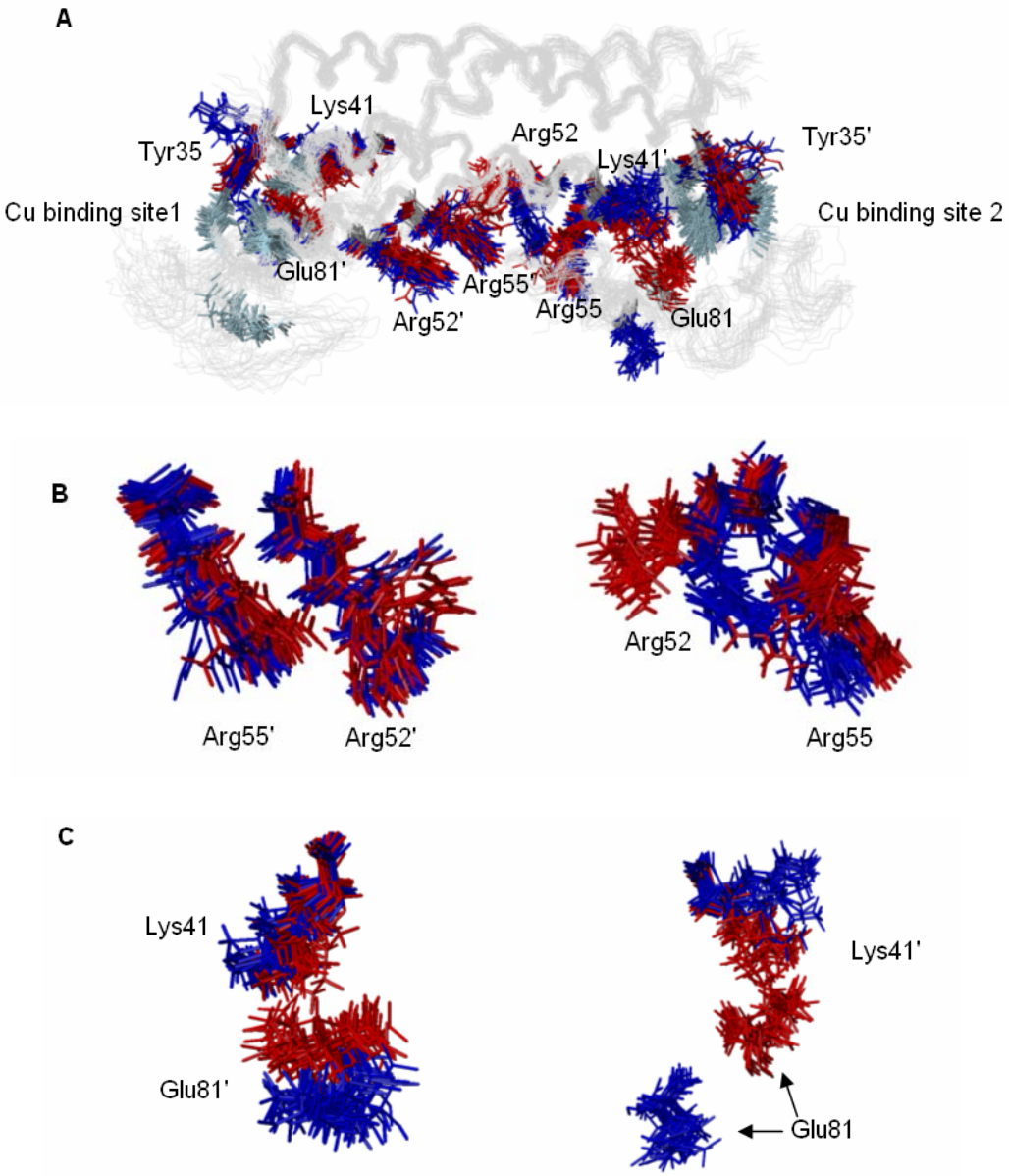

Figure 6-13. Comparison of the proposed functional groups between apoCsoR and CuCsoR. The structures of apoCsoR and CuCsoR were sampled and aligned as described earlier in Section 6.5.2.2. The backbone structures of both forms of proteins are shaded in light grey color, and the residues at the Cu binding site, Cys36, His61 and Cys65, are shown in light blue color. Other proposed functional group residues, namely Tyr35, Lys41, Glu81, Arg52 and Arg55 are shown in blue for apoCsoR and in red for CuCsoR.

Table 6-4. Comparison of the distances between the proposed functional residue pairs Lys41-Glu81 and Arg52-Arg55 in both apoCsoR and CuCsoR over the production state of the simulations.

	Distance between the backbones [a] (Å)		Distance between the side chains[b] (Å)	
	Lys41-Glu81'	**Lys41'-Glu81**	**Arg52-Arg55**	**Arg52'-Arg55'**
apoCsoR	11.7	14.2	6.0	5.8
	(0.3)	(0.6)	(0.5)	(0.8)
CuCsoR	9.3	10.0	11.8	6.1
	(0.4)	(0.4)	(1.6)	(1.2)

Note: a, the distance between the centre of the backbone atoms N, C and Cα; b, the distance between the centre of the heavy atoms $N_{\zeta 1}$-Cη-$N_{\zeta 2}$ at the end of the side chain. The number in bracket is the standard deviations of the distances over the simulation time.

14.2 Å in apoCsoR to 10.0 Å in CuCsoR (averaged over the production state simulations) (Table 6-4). Similar although smaller trends are also observed for the analogous Glu81'-Lys41 residue-pair close to Cu binding site 1. Hydrogen-bonding analyses indicate that Glu81-Lys41' and Glu81'-Lys41 form a hydrogen bond for 99% and 95% of the simulation time in two monomers of CuCsoR, respectively, while there is essentially no hydrogen bond formed between these residue pairs in apoCsoR. For the other essential residue Tyr35, the side chains change the orientation and turn away from the Cu binding sites in about 15-20% of the sampled structures of apoCsoR, in comparison to CuCsoR (Figure 6-13). No significant differences are detected for Tyr35 in terms of hydrogen bonding between apoCsoR and CuCsoR form.

Among the residues that have been proposed to be involved in DNA binding, Arg52 and Arg55 show the most significant differences between two forms of CsoR (Figure 6-13). The side chains of Arg52 and Arg55 in apoCsoR are aligned along the inner surface of the bent helix bundle and perpendicular to long axis of the helix bundle, while these residues are orientied away from each other in the CuCsoR. This change is quantized by the distance between the centres of the terminal heavy atoms in the side chains of Arg 52 and Arg55, $N_{\zeta 1}$-Cη-$N_{\zeta 2}$ which is nearly doubled upon Cu binding by increasing from 6.0 Å in apoCsoR to 11.8 Å in CuCsoR. Similar to the Glu81-Lys41

pair (discussed above), the structural changes for the Arg52-Arg55 pair are larger for the pair close to Cu site 2 (Arg52-Arg55) than for the corresponding pair in the other monomer (Arg52'-Arg55') that are close to Cu site 1.

6.5 Discussion and Future Work

In this study, XAS and MD simulations have been used to probe the functional mechanisms of the novel Cu-specific repressor CsoR from *M. tuberculosis*. The XAS results reveal that Cu(I) binds to CsoR in a trigonal coordination with one His-N at 2.11 Å and two sulfurs from the cysteine residues at 2.21 Å. The XAS results of site-directed mutants also confirm the involvement of His61 and Cys36 in binding Cu. A search of the Cambridge crystal structure database (Allen and Kennard, 1983) shows that Cu-N bond lengths in trigonal Cu(I) species typically range from 1.95 Å to 2.05 Å (1.99 Å on average) based on 66 hits with an R factor smaller than 6.0. The Cu-N bond found in CsoR is longer than those commonly observed in low-molecular weight species, but a small number of examples of such long bonds can be found in the Cambridge crystal structure database (e.g. (Lee et al., 2006b)). However, in these cases copper is found to bind in a tripodal or T-shape geometry and this observation may imply that the copper binding site in CsoR is in a distorted trigonal coordination.

The two conserved residues Tyr35 and Glu81, which are essential for CsoR function (Liu et al., 2007), are close to the Cu binding sites, and it has been proposed that Tyr35, His61' and Glu81' might form a hydrogen bonding network upon Cu binding and thus induce a conformational change. The Cu K-edge XAS spectra of site-directed mutants substituting these two residues closely resemble that of the wild type CsoR. This suggests that the dysfunction of CsoR with the absence of these two residues is not due to local structural changes in the Cu binding sites. But it is also possible that mutation of these residues modified the local structure of the copper binding site at distances that are beyond the detection limit of XAS.

In order to understand the molecular basis of Cu-induced disassociation of CsoR from its complex with DNA, molecular dynamics structures of both the metal-free and Cu-bound CsoR in solution were simulated starting with the structural information from crystallography and XAS as an initial structure. Several structural differences both in the overall conformation of the proteins and in the proposed functional residues are observed between apoCsoR and CuCsoR.

The overall structures of both apoCsoR and CuCsoR are similar to the crystal structure showing an all-helix homodimer, with three helices in each monomer connected by flexible linkers or turns. The residues involved in Cu binding are located in the turn between helix α1- α2 (Cys36), and helix α2'- α3' (His61' and Cys65') of the corresponding monomer, respectively. In the apoCsoR, the region where residues 58-89 are located (C-terminal of helix α2-turn/unstrucutured region-helix α3 structure) bends along the long axis of the helix bundle, which allows apoCsoR to adopt a clamp-like shape. This clamp-like shape may facilitate DNA binding. It is noteworthy that the side chains of the proposed DNA-binding residues Lys8, Arg15, Arg52 and Arg55 are directed outward from the inner surface of the "clamp" in the apoCsoR structure. Such orientations would make these residues valid candidates for DNA binding if the appropriate DNA fragment fits in the "clamp". In CuCsoR, the long loop between helix α2 and α3 close to the Cu binding site shows a more organized structure, and the helix bundle is straightened compared to apoCsoR. Furthermore, the backbone of residues in the crystallographically-identified long loop and helix α3 are moved towards helix α2 upon Cu binding. The essential residue Glu81, located in this long loop between helix α2 and α3, moves significantly towards helix α2, and forms a stable hydrogen bond with Lys41' in the helix α2. The formation of this hydrogen bond may facilitate turning of helix α2 and subsequently result in a modified orientation of the positively charged residues of helix α2, as the side chains of Arg52 and Arg55 in CuCsoR appear to turn away from each other relative to their orientations in the apoCsoR. This hypothesis needs to be tested further by mutagenesis studies. Evidence from sequence alignments is unfavourable to this hypothesis, as it shows that Lys41 is not conserved in CsoR

homologs, and the residue at the equivalent position to Lys41 does not have the potential to form hydrogen bonds through the side chain in 3 out of 16 CsoR homologs. While this might suggest that variation in the functional mechanisms of CsoR in other species, further work is needed to define the function of Lys41.

It has been proposed from earlier crystallographic and mutagenesis (Liu et al., 2007) that Glu81' and Tyr35 form a hydrogen bonding network with the Cu-binding residue His61', and perhaps trigger a conformational change. While a hydrogen bond between Tyr35 and Glu81' is observed during the first 2 ns of the simulations in CuCsoR, this hydrogen bond is broken at later simulations. No significant differences are found in the behaviour of Tyr35 between apoCsoR and CuCsoR. The side chain atoms of Tyr35 are turned away from the Cu binding sites in a small percentage (<20%) of the sampled apoCsoR structures, relative to those of CuCsoR. However, it is unknown whether this change is due to the random dynamic flexibility of residues in this region of apoCsoR or if this change is indicative of a conformational transition which will lead to a greater population at longer time scales. Furthermore Tyr35 is observed to form a hydrogen bond with the side chain of the Cu-bound Cys65 in the second monomer for over 30% of the simulation time in CuCsoR, but for only 18% in apoCsoR. However, this hydrogen bonding is not stabilized in the production state, and similar hydrogen bonding is not detected with Tyr35' on the other side of helix bundle. The initial apoCsoR structure was taken from the crystal structure of the Cu-bound form, and it is thus expected that a longer time for structural equilibration to production state will be required than for CuCsoR. Future work is planned to confirm the roles of Glu81 and Tyr35, by comparison of the molecular dynamics of site-directed CuCsoR mutant structures with wild type protein.

The distances between Cu and its ligands S and N from MD simulation are around 2.4 Å and 2.3 Å, respectively. These distances are shorter than those reported in the crystal structure, but they are still longer than the distances determined by EXAFS analysis, which is accurate in determining bond lengths. Changing from flat-well to

harmonic potential for the bonding interactions at Cu binding sites causes the distances between Cu and its ligands to be consistent with the EXAFS results. These changes in the local structures at the Cu binding sites did not significantly alter the conformation of CuCsoR within 5 ns of the simulation. However, longer simulations are needed to confirm this. It is also observed that the conformational changes for CuCsoR are not symmetric. This may be due that apoCsoR requires still longer times for equilibration (as mentioned above). Since there are no strong interactions between the monomers of apoCsoR, the two monomers undergo structural conversion independently. It is also possible that the two monomers function cooperatively in conformational change, as it has been proved that binding of only one Cu is sufficient for disassociation of the CsoR-DNA complex (Liu et al., 2007). This observation will also be the subject of future MD calculations.

In summary, XAS and MD simulations of this study suggest that Cu regulates the DNA binding properties of CsoR in multiple ways. According to the MD simulations, the metal-free form of CsoR has a flexible structure around its copper binding site, and the helix bundle bends to form a clamp-shape structure that might directly facilitate DNA binding (Figure 6-14A). Cu binding to CsoR seems to result in straightening of the helix bundle, and this motion may make DNA binding less favourable (Figure 6-14B). In addition, copper binding promotes the formation of a hydrogen bond between Glu81 and Lys41 from the corresponding monomer, and thus may cause the charged residues involved in DNA binding (e.g. Arg52 and Arg55) to turn away from an orientation that is favourable for DNA binding. These simulations, based on the input structural parameters from XAS and crystallography, provide mechanistic insights into the Cu-regulated DNA-binding properties of CsoR that were not available from biochemical experiments, and provide an essential guide for future research directions.

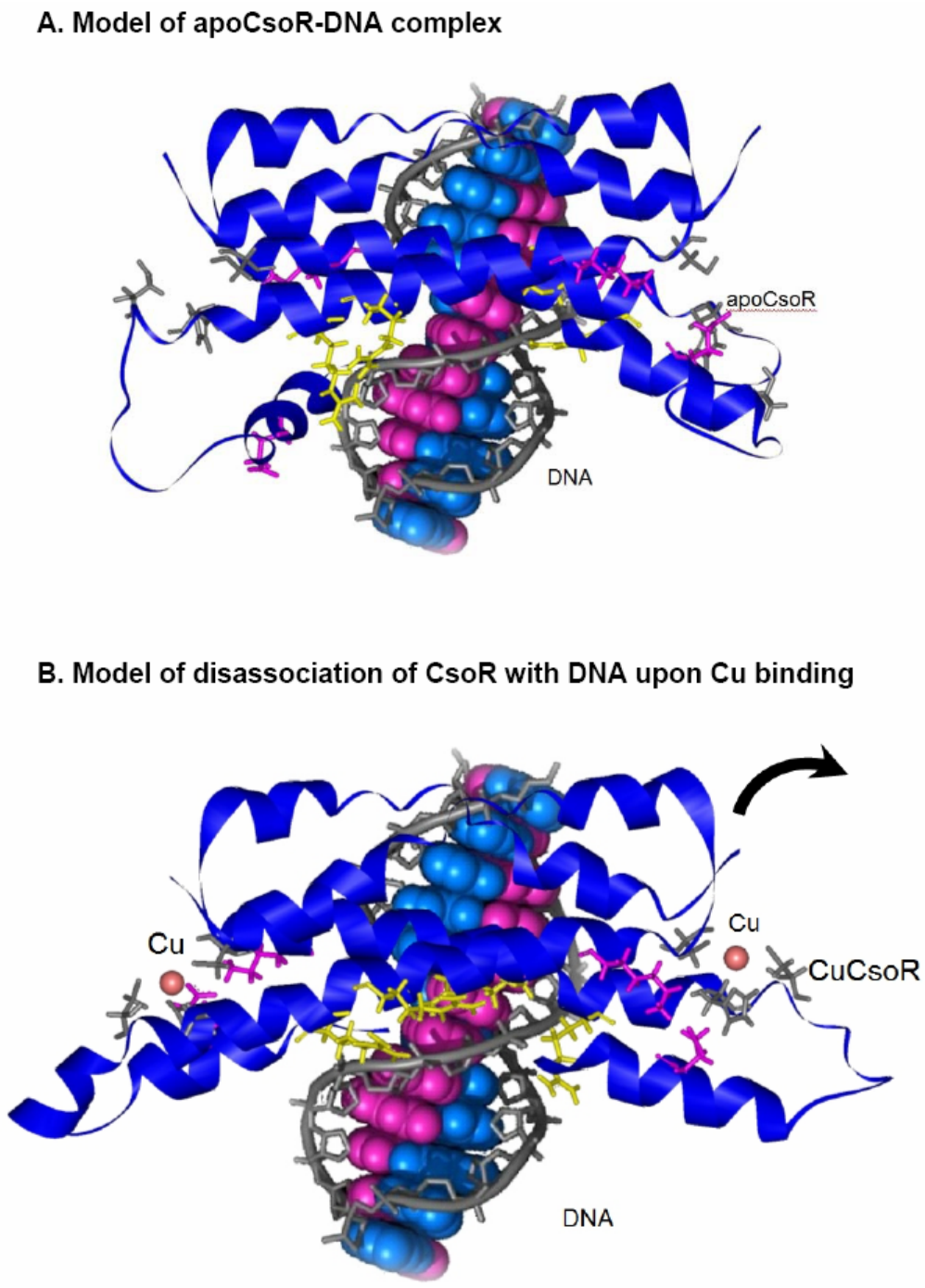

Figure 6-14. The schematic illustration of the proposed mechanisms of Cu-binding induced disassociation between CsoR and promoter DNA. The positive-charged residues are highlighted in yellow color, the residues involved in Cu binding are in dark grey and the Glu81-Lys41' pair is in pink.

CHAPTER 7

TRACING COPPER – THIOMOLYBDATE COMPLEXES IN A PROSPECTIVE TREATMENT FOR WILSON'S DISEASE

7.1 Abstract

Wilson's disease is a human genetic disorder which results in copper accumulation in liver and brain. If left untreated, it results in hepatitis, neurological complications, and death. Treatments such as copper chelation therapy or dietary supplementation with zinc have been used to ameliorate the effects of the disease. Tetrathiomolybdate has been demonstrated as a promising new copper chelator for Wilson's disease in both an animal model and in clinical trials. X-ray absorption spectroscopy measurements have suggested that tetrathiomolybdate acts as a novel copper chelator, forming a complex with accumulated copper in liver. In this study, X-ray fluorescence imaging and X-ray absorption spectroscopy were used to trace the distribution of the complex in the organs of an animal model of human Wilson's disease. This work allows new insights into metabolism of the metal complex in the diseased state.

7.2 Introduction

Wilson's disease is a human illness in which large quantities of copper accumulate in various organs, including the brain and the liver (Wilson, 1912). It is an

autosomal recessive disorder arising from a mutation in the *Atp7b* gene, which encodes a copper-transporting P-type ATPase involved in cellular copper excretion (Bull et al., 1993; Petrukhin et al., 1993; Tanzi et al., 1993; Yamaguchi et al., 1993; Roelofsen et al., 2000). The exact symptoms vary from patient to patient, and individuals can present chronic hepatitis or acute liver failure, and neurological and psychiatric symptoms (Fink et al., 1999; Loudianos and Gitlin, 2000; Walshe, 2006; Ala et al., 2007; Pfeiffer, 2007). Wilson's disease is fatal without administration of proper treatment before severe damage occurs to vital organs such as liver or brain.

Current drug treatments for Wilson's disease can be divided into two strategies, Zn^{2+} administration and copper chelation therapy. Administration of Zn^{2+} is thought to be effective by inducing intestinal metallothionein which may partially block copper absorption, and by inducing tissue metallothioneins which may serve to reduce the toxic effects of copper (Yuzbasiyangurkan et al., 1992). However, Zn can not promote the excretion of copper accumulated in the liver, and thus it is usually used for asymptomatic patients, or used as a maintenance therapy after the initial treatment with copper-chelating drugs. Chelation therapy (George et al., 2008) is thought to mobilize excess copper for excretion, and prescription approved drugs currently include D-penicillamine (drug names Cuprimine and Depen) and triethylenetetramine (Trientine). Both of these drugs are expected to effectively bind Cu^{2+} although no structurally characterized compounds have yet been prepared (Allen and Kennard, 1983). However, both drugs exhibit unwanted side effects, and long-term neurological deterioration is also observed (Brewer et al., 1987; Brewer et al., 2003). Given the shortcomings in the currently available therapies, tetrathiomolybdate (TTM, $[MoS_4]^{2-}$) was introduced as a potential alternative drug for Wilson's disease.

It has been known for a long time that molybdenum interferes with copper metabolism (Dick, 1953; Dick, 1954). As early as the 1940s, it was reported that sheep tended to suffer from copper deficiency when feeding in a pasture with high concentrations of molybdenum and sulfur (Stewart et al., 1946). Later on, the

interaction between Cu and tetrathiomolybdate (TTM) was exploited by using TTM to counteract copper toxicity in farm animals (Mason et al., 1988). Since 1991, TTM has been used in clinical trials for Wilson's disease patients with neurological symptoms (Brewer et al., 1991), and later has also been tested in animal models as a treatment for hepatic Wilson's disease (Ogra et al., 2000; George et al., 2003; Klein et al., 2004). Studies showed that TTM removes copper in Wilson's disease via novel mechanisms and it has several advantages compared to currently available Cu-chelators. When taken together with food, TTM interacts with copper in the diet and thus prevents absorption of copper into body. If taken without food, TTM is delivered to the liver through the blood system and then removes copper from the liver. TTM selectively binds to Cu(I) without significantly interfering with other essential metals in the living system, and it prefers to bind to copper with sulfur as the only type of ligand (Suzuki et al., 1993). Based on previous EXAFS results, TTM can interact with up to 6 copper to form Cu-S-Mo complexes, suggesting that TTM can remove Cu more efficiently than copper chelators in current use (Laurie, 2000; George et al., 2003). Moreover, current clinical trials suggest that TTM treatment shows fewer side effects. In both open-labelled and randomly controlled double-blind tests, TTM showed less than 5% neurological deterioration, comparing to 50% for Penicillamine and more than 20% for Trientine (Brewer et al., 2003; Brewer et al., 2006). Despite these successes, open questions still remain. In particular, although the formation of Cu-TTM complexes in purified preparations of liver lysosomes has been demonstrated (George et al., 2003), *in situ* measurements of whole tissues have not yet been reported. Furthermore, following TTM treatment Mo and Cu appear to accumulate in kidney (Komatsu et al., 2000), and the mechanisms underlying this accumulation are as yet unclear.

This chapter builds upon previous X-ray absorption spectroscopy (XAS) work by George and coworkers (George et al., 2003), in which Long Evans cinnamon (LEC) rats were employed as an animal model to understand the chelating mechanisms of TTM with repeated doses of treatment (George et al., 2003). LEC rats carry a deletion in the *Atp7b* gene and have been a widely used animal model for Wilson's disease (Li et

al., 1991; Wu et al., 1994). An alternative product known as Pineal Night-specific ATPase (PINA) is generated by an intronic promoter in the *Atp7b* gene, a putative Cu transporter expressed in pineal gland and in retina which is also defective in LEC rats (Ahmed et al., 2005). However, a recent study showed that LEC rats contain an additional defect in serotonin N-acetyltransferase (NAT), the key enzyme in melatonin production (Ahmed et al., 2005). In order to eliminate the possible complications from the NAT mutation, Ahmed et al. have obtained a new strain of rat that is defective only in the PINA/*Atp7b* locus by crossing LEC rats with normal rats (Ahmed et al., 2005). This new strain, called LPP rat, represents an improved animal model for Wilson's disease. In the study reported here, the results of a single dose of TTM to a LPP rat are examined using X-ray fluorescence imaging (XFI) to demonstrate co-localization of Cu and Mo in tissues and using X-ray absorption spectroscopy (XAS) to demonstrate the presence of multi-metallic clusters in liver and kidney, and part of the results presented here have been published recently (Zhang et al., 2009).

7.3 Material and Methods

7.3.1 Animals and Treatments

Treatment of LPP rats with TTM and following organ preparation were carried out by members of *Dr. Karl H Summer*'s group at Munich University. LPP rats with *Atp7b*(-/-) of approximately 100 days in age were observed to be jaundiced (characteristic of liver dysfunction). 10mg TTM/kg body-weight was administered as previously described (Klein et al., 2004), 4 days before sample collection. Analysis of serum aspartate aminotransferase and bilirubin was performed as previously described (Table 7-1) (Klein et al., 2004). Control animals were *Atp7b*(+/-), and appeared healthy with normal levels of serum aspartate aminotransferase bilirubin and liver copper. Animals were exsanguinated under ether anaesthesia, and samples taken. Samples were additionally taken from *Atp7b*(-/-) LPP rats but without TTM treatment.

Table 7-1. List of samples.

A. Samples for X-ray absorption spectroscopy and metal analysis

Name	Description	Serum AST (U/L)	Serum bilirubin (mg/dl)	Cu in Liver (μg/g)
LPP rat	Animal with *Atp7b* (-/-) mutation, 120 days old, in jaundiced state	2290	37.9	222.5
TTM-treated LPP rat	Animal with *Atp7b* (-/-), 133 days old, treated with 10mg/kg body weight of TTM on Day 129.	280	<0.5	149.5
Control	Animal with *Atp7b* (+/-), non-diseased, 133 days old	137	<0.5	4.1

B. Samples for X-ray absorption fluorescence imaging

Name	Description	Serum AST (U/L)	Serum bilirubin (mg/dl)	Cu in Liver (ug/g)
LPP rat	Animal with *Atp7b* (-/-) mutation, 109 days old, jaundiced	N.D.	N.D.	191.0
TTM-treated LPP rat	Animal with *Atp7b* (-/-) mutation, 98 days old, jaundiced, treated with 10mg/kg body weight TTM on Day 94.	N.D.	N.D.	181.5
Control	Animal with *Atp7b* (+/-), non-diseased, 73 days old	N.D.	N.D.	3.8

N.D. = not determined.

AST: aspartate aminotransferase

7.3.2 Sample Preparation

For the tissue section imaging, liver, kidney and brain from treated and untreated LPP rats and the control animal were fixed in 4% neutral formalin, and then embedded in 20% gelatine. The organs were then sectioned into 1-mm thickness for XFI quick raster scan, and selected sections were mounted between two sheets of a transparent

plastic file folder (ITOYA.com). This brand of file folder had been pre-tested to ensure that no metals of interest were detectable by XFI under these experimental conditions. The brain and liver were sectioned sagittally, while the kidney was sectioned longitudinally. All the sections from each brain were included in the imaging scan and two representative sections from each kidney or liver were chosen for the XFI quick raster scan. The 10-μm sections for high-resolution XFI were prepared as follows: the sections obtained as described above were equilibrated in 4% paraformaldehyde for two hours at room temperature, and then were dehydrated in a gradient series (0%, 25%, 50%, 75% and 100%) of ethanol in PBST buffer (30 mM PBS, 0.1% Tween 20) for 5 minutes each. The fixed and dehydrated sections were then re-hydrated in PBST using 5 minutes washes with the same ethanol gradient in the reverse order. The re-hydrated sections were then infiltrated for around 20 hours on a rotating stirrer at 4°C with JB-4 (Polysciences Inc., Warrington, PA, USA) catalyzed solution A (10 mL solution A: 0.125 g catalyst), with one change of the fresh infiltration solution during the process. The infiltrated samples were then placed in embedding molds filled with a mixture of JB-4 solution B and fresh infiltration solution (1 mL solution B: 25 mL infiltration solution) and left overnight at 4°C to polymerize. Sections with 10-μm thickness were prepared on a microtome using glass knives. Of two adjacent sections, one was mounted on a glass slide and stained with methylene blue for optical microscopy, while the other, intended for XFI high-resolution scan, was fixed on a Thermanox plastic coverslip (Gibco BRL) without any further processing.

For X-ray absorption spectroscopy, the fresh liver or kidney were sliced and packed into 2-mm Lucite sample holders with Mylar window and kept frozen prior and during data collection.

7.3.3 X-ray Fluorescence Imaging and Data Analysis

XFI quick raster scan (50 μm resolution) and high-resolution scan (2.5 μm x 3.5 μm resolution) were conducted at Stanford Synchrotron Radiation Lightsource (SSRL) on beamline 6-2 and 2-3, respectively. The XFI quick raster scans were carried out at

beamline 6-2 using a Si(111) monochromator and a downstream Rh-coated mirror. These scans were aimed at mapping the distribution of Cu, Zn, Fe, Mn, Se, Ca, Hg, and Ni in the liver, kidney and brain in large scale. The incident X-ray beam was set at the energy of 13 keV, and the incident beam was apertured to 50 μm using a tungsten pin hole. The sample was oriented at 45° to the incident X-ray beam, and was spatially rastered in the microbeam driven by a motorized stage. The incident and transmitted X-ray intensities were measured with a nitrogen-filled ion chamber. The fluorescence signals of the elements of interest and the intensity of the collective scatter (Compton and elastic scatters) were monitored by using a silicon-drift Vortex detector (SII NanoTechnology USA Inc.) set in the plane of the beam path at 90° to the incident beam, and 45° to the sample. Elements were mapped by windowing around the Kα fluorescence lines specific to each element in the fluorescence spectrum from the detector. The motor moved continuously during each raster while the relevant data were recorded at a defined counting time interval. The motor was set at a speed to achieve a resolution of 50 μm per pixel with a 6.7-millisecond counting time.

XFI high-resolution scans were collected on beamline 2-3, whose source is a 1.3 Tesla Bend Magnet and which uses a Si(220) double-crystal monochromator. Harmonic rejection was achieved by detuning one monochromator crystal to give 50% of the peak intensity. The beam size on the sample is around 2.5 μm provided by a Kirkpatrick-Bayez mirror pair (Xradia Inc.). The setup of the experiment is similar to what is described above. The sample was driven in two-dimension raster scan by three sets of Newport motor stages. Different from the continuous motion per raster in the quick raster scan, the motors was set to stepwise scan with a step size of 2.5 μm. The sample was scanned with a step size of around 3.5 μm in x-axial and 2.5 μm in y-axial and a counting time of 4 sec per pixel. The energy of the incident X-ray was set at 20.5 keV, right above the Mo K-edge absorption edge. Mo, Cu, Fe, Ca, Cr, Zn, as well as the total scattering intensity were monitored during the scan as described above.

The XFI imaging data were processed either using software written by the candidate or using SMAK software written by *Dr. Sam Webb* (http://www-ssrl.slac.stanford.edu/~swebb/smak.htm). Windowed Fluorescence data were corrected for scatter as previously described (Pickering et al., 2000).

7.3.4 X-ray Absorption Spectroscopy Data Collection

Cu and Mo K-edge X-ray absorption spectroscopy data were collected on beamline 7-3 at SSRL with a wiggler field of 2 teslas and employing an Si(220) double-crystal monochromator. Harmonic rejection at the Cu K-edge was accomplished by adjusting the cutoff of a Rh-coated vertical collimating mirror to 15 keV, whereas for Mo K-edge measurements the collimating mirror was removed and harmonic rejection was achieved by detuning the second monochromator crystal to 50% of peak intensity. The incident and transmitted X-ray intensities were monitored using ionization chambers filled with nitrogen for Cu XAS and argon for Mo XAS. X-ray absorption was measured as either Cu or Mo Kα fluorescence excitation spectrum using an array of 30 germanium detectors (Cramer et al., 1988). During data collection, samples were maintained at a temperature of approximately 10 K using an Oxford instruments liquid helium flow cryostat. For each sample, eight to ten 35-min scans for Cu K-edge data or four 40-min scans for Mo K-edge data were collected for averaging. Energy was calibrated by reference to the absorption of a standard metal foil measured simultaneously with each scan, assuming a lowest energy inflection point to be 8980.3 eV and 20003.9 eV for Cu and Mo foil, respectively.

7.3.5 X-ray Absorption Spectroscopy Data Analysis

The extended x-ray absorption fine structure (EXAFS) oscillations $\chi(k)$ were quantitatively analyzed by curve fitting using the EXAFSPAK suite of computer programs (http://ssrl.slac.stanford.edu/exafspak.html). *Ab initio* theoretical phase and amplitude functions were calculated using the program FEFF version 8.25 (Rehr and Albers, 2000). No smoothing, filtering, or related operations were performed on the data.

7.3.6 Metal Analysis

Metals were determined by inductively coupled plasma mass spectroscopy (ICP-MS). The liver or kidney tissues were measured by wet weight and digested with 69% nitric acid (from EMDChemicals, Cat. No.: NX0409-52) and 30% hydrogen peroxide solution (from VWR, Cat. No. VW3742-1).

7.3.7 Molecular Modelling

Density Functional Theory (DFT) molecular modeling used the program Dmol^3 Materials Studio Version 4.2 (Delley, 1990; Delley, 2000). Using this level of theory, bond-length accuracies of around 0.05 Å is expected, with good estimates of energetic trends between postulated molecular entities. The Becke exchange (Becke, 1988) and Perdew correlation functionals (Perdew and Wang, 1992) were used to calculate both the potential during the self consistent field procedure, and the energy. Double numerical basis sets included polarization functions for all atoms. Calculations were spin-unrestricted and all electron relativistic core potentials were used. No symmetry constraints were applied, and optimized geometries used energy tolerances of 2.0×10^{-5} Hartree. The effects of solvation were simulated by using the Conductor-like Screening Model (COSMO) (Klamt and Schuurmann, 1993; Delley, 2006) employing the dielectric constant of water.

7.4 Results

7.4.1 X-ray Fluorescence Imaging

As expected from previous work (Klein et al., 2004), LPP rats developed symptoms consistent with Wilson's disease, exhibiting acute hepatitis at an age of approximately 100 days. Thus, LPP rats showed elevated serum aspartate aminotransferase activity and serum bilirubin levels (Table 7-1, data obtained in *Dr. Karl Summer*'s lab). Four days after treatment with TTM, LPP rats showed serum

aspartate aminotransferase activity and serum bilirubin levels that had reduced to either normal levels, or marginally higher than normal levels.

X-ray fluorescence imaging was used in this study to map the distribution of Cu and other metals at tissue level in liver, kidney and brain upon TTM treatment. Samples were studied at two different spatial resolutions – quick raster scans provided macroscopic maps of sections of whole organs employing a pixel size of 50x50 μm^2, and microscopic maps were obtained by high resolution scans with a pixel size of 3.5 μm (h)x2.5 μm (v). For the former resolution, Mo localizations could not be included in the maps since the maximum beamline energy was below the Mo K-edge. Mo L-edge fluorescence also cannot be used because of overlap of the Mo L fluorescence lines with the intense sulfur K-edge fluorescence due to the high sulfur content of biological samples.

Figure 7-1A and B show the macroscopic maps of Cu, Fe and Zn in the livers and kidneys, respectively, from LPP rat with and without TTM-treatment, as well as the control. Consistent with what is expected, Cu is heavily loaded in the whole liver tissue of the jaundiced LPP rat, while it is barely visible in the control. In addition, Fe and Zn are also noticeably increased in the jaundiced LPP rat when comparing to the control. Treatment of the LPP rat with TTM did not make remarkable visual changes in the quick raster scan XFI maps of Cu, Fe or Zn. However, all the metal level changes described here are only a rough estimate considering the low signal to noise ratio for the XFI quick raster scan in this study. Marked accumulation of copper is observed in the cortex of the kidney, at levels that are approximately four times of that found in jaundiced LPP rats with no TTM treatment. In contrast, Cu levels in kidney medulla were comparable in LPP rats with and without TTM treatment. No significant changes in the distributions of other metals, such as Fe and Zn, were observed, apart from a slight decrease in cortex iron with both treated and untreated LPP rats.

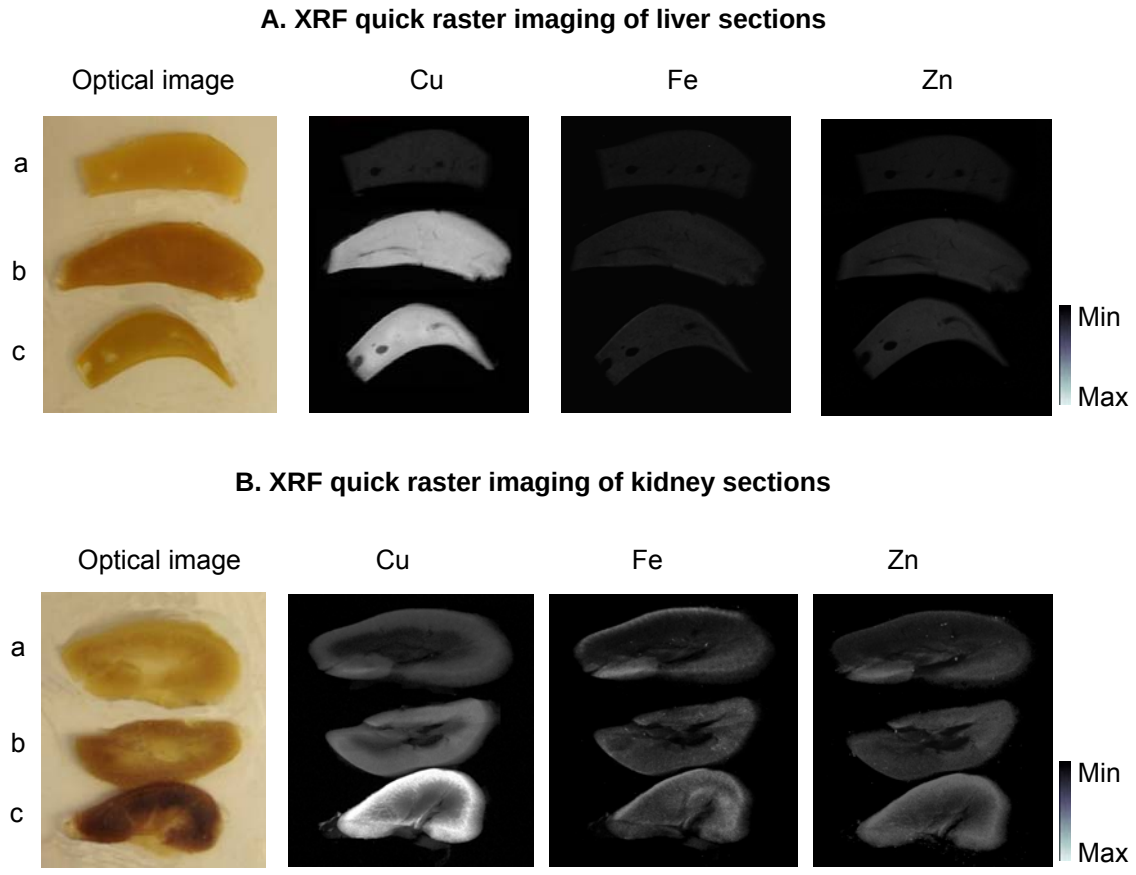

Figure 7-1. Effects of TTM treatment on metal distribution in the liver and kidney of LPP rat. The metal distribution in A) the livers and B) the kidneys of the TTM-treated LPP rat, the untreated LPP rat and the control animal by XFI quick raster scan. The sections from a) control animal, b) LPP rat without treatment, and c) TTM-treated LLP rat.

When using XFI high resolution scans to further trace the distributions of Cu and Mo at the cellular level in the liver, Cu is found to accumulate evenly within about 280 μm range around the central vein of the liver lobule (Figure 7-2). No mosaic pattern of Cu distribution are observed as previously described (Klein et al., 2004). The difference between the observation reported here and that reported by *Klein et al*. may be due to the resolution or/and sensitivity limitation of the XFI in this study. The regions of highest Cu in the histochemical imaging were around 5 x 5 μm^2, which is close to the resolution of high resolution XFI presented here (around 3.5 x 2.5 μm^2).

Also, in order to synchronize the mapping of Cu and Mo in the tissue, the incident X-ray energy was set at 20.5 keV, which has the effect of comprising by reducing the sensitivity of the imaging to the Cu concentration. In the XFI high resolution images, the Cu level in the liver of LPP rat after treatment is reduced to about 70% of the corresponding liver in absence of treatment. Due to the low concentration and the interference of the inelastic scattering, the Mo level in the liver could not be distinguished from the background in either case.

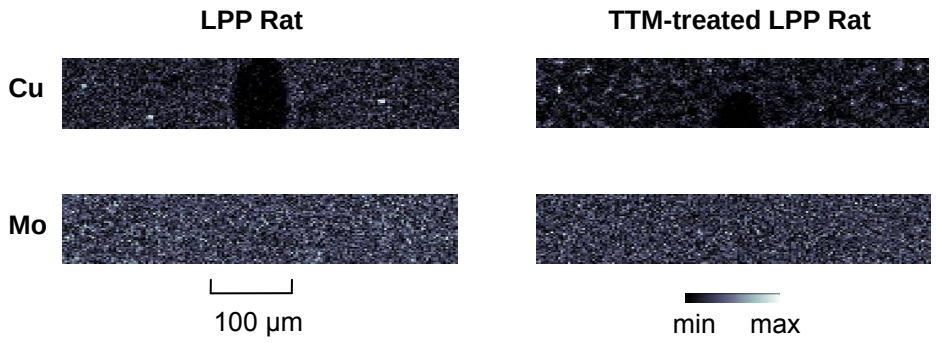

Figure 7-2. Mapping of Cu and Mo in livers from LPP rats with and without TTM treatment by X-ray fluorescence high resolution scan.

In contrast to images of the liver, XFI high resolution images of the kidney reveal highly tissue-specific maps for both Cu and Mo for the TTM-treated LPP rat. Figure 7-3 shows a representative image with X-ray fluorescence imaging maps of both Cu and Mo and an optical micrograph of the corresponding (adjacent) section stained with methylene blue. In general the Mo and Cu X-ray fluorescence intensities show a high degree of correlation (Pearson product-moment correlation coefficient = 0.86). Comparison of the optical micrograph, the well-known anatomy of the kidney nephron (Ross and Pawlina, 2006), and the XFI maps (Figure 7-3) indicates that Cu and Mo accumulate in the proximal convoluted tubules, but not in the glomeruli or in the distal convoluted tubules. This cell-specific co-localization of Cu and Mo suggests that the Cu and Mo are released from the blood into the filtrate in the glomerulus cavity, and then

re-absorbed and accumulated locally when passing through the proximal tubules. This re-absorption by the proximal tubules provides an explanation for the accumulation of Cu and Mo within the kidney cortex.

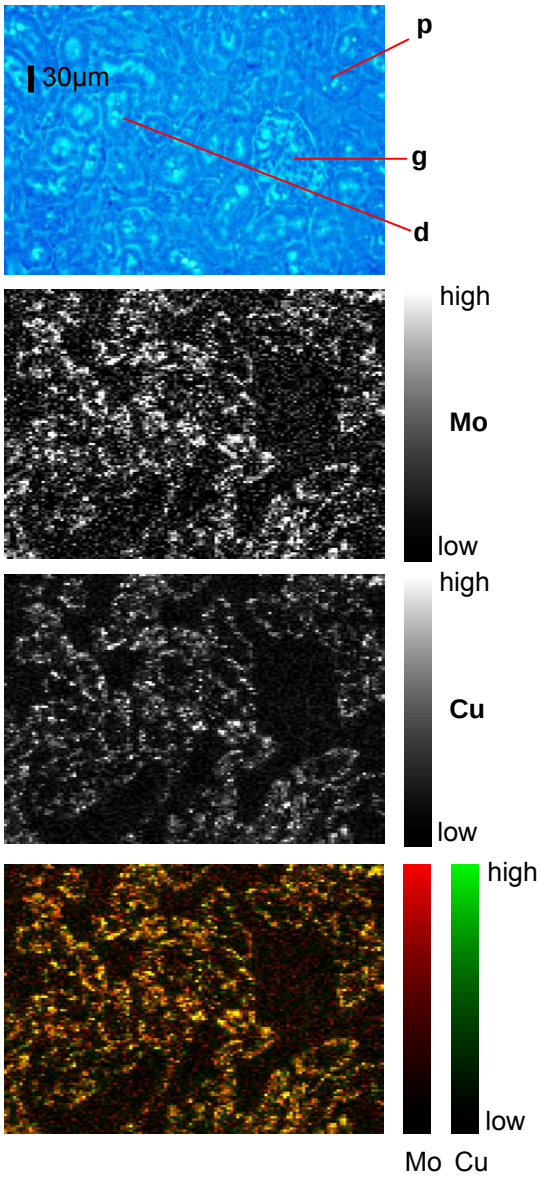

Figure 7-3. Mapping of Cu and Mo in the kidney cortex of LPP rat with TTM treatment using X-ray fluorescence high resolution scan. In the top panel, the optical micrograph shows locations of proximal convoluted tubule p, distal convoluted tubule d, and glomerulus g. The similarity of the Mo and Cu XFI maps is evident. A combined Cu and Mo map showing Cu in green and Mo in red is shown in the lower panel. The yellow color indicates the locations where Cu and Mo co-localize with high concentration.

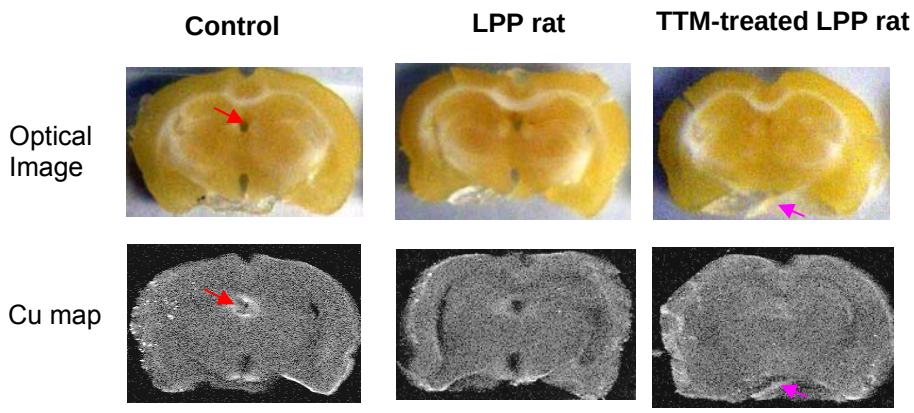

Figure 7-4. Comparison of Cu distribution in the brains of LPP rats with and without TTM treatment and of the control animal by XFI quick raster scan. A representative section from anatomically similar regions of each rat brain is shown here. High copper regions are indicated by red arrow for centre canal and pink arrow for gelatine.

Figure 7-4 shows the macroscopic maps of Cu in the brains from LPP rats with and without TTM-treatment, as well the control (only one selected representative section from anatomically similar regions of each rat brain is shown here). Similar Cu distribution patterns are observed in the brain sections of all the examined animals. High-Cu regions are observed around the centre canal of the brain in the control, and to a slightly lesser extent in the LPP rats with and without TTM treatment. However, concerns are aroused since the high-Cu regions observed in the brain sections are correlated with high Fe, Zn, as well as high scatter signals (not illustrated), which may suggest the presence of shadow effects due to imperfections in the sections. In addition, high-Cu regions were found near the periphery of the sections for each animal, and comparable levels are found within residual gelatine used to support the sample for sectioning. Therefore these results are ambiguous due to possible copper contamination. Improved background subtraction or collection of the Cu K near edge spectra in the high Cu regions would help to rule out these possibilities. Several earlier studies have reported the age-dependent and region-specific changes in Cu distribution in the brain of LEC rat, although regions and magnitude of changes varied among the studies (Sugawara et al., 1992; Saito et al., 1995). According to these studies, Cu levels in the

regions of the LEC rat brain slightly decreased in the early stages, but increased later in life. The turnover occurred at or right after 13 weeks of age, and the difference was less than 35%. The LPP rat examined in this study is between 12 and 13 weeks old, which is close to the time of turnover of the Cu level in the brain as reported. In order to identify such subtle changes in the Cu level of brain from LPP rat, it would be necessary to increase the signal to noise ratio in the XFI imaging either by using a brighter beam or by using longer counting times than those used in here (6.7 milliseconds). Similar requirements would be needed to detect changes in the Cu/Mo level in the brain upon TTM treatment if these are present.

7.4.2 X-ray Absorption Spectroscopy of Bulk Tissues

In order to examine how TTM interacts with Cu in the liver of LPP rat upon TTM treatment, and in which form the TTM-Cu complex are transported and accumulated in the kidney, X-ray absorption spectroscopy was used to probe the chemical forms of TTM-Cu complexes in the whole tissue of liver and kidney from TTM-treated LPP rat. Figure 7-5A shows the near-edge portion of the Cu K-edge X-ray absorption spectra of kidney and liver from LPP rat treated with a single dose of TTM compared with the spectra of cuprous thiolate standard compounds, the two-coordinated Cu(I) thiolate (Dance, 1986) and three-coordinated Cu(I)-thiolate cluster (Dance, 1986). A previously characterized four-coordinated Cu(I)-S-Mo complex in *Desulfovibrio gigas* orange protein (Chen et al., 2008) is also included in the comparison. None of the Cu near-edge spectra show any signs of the small 1s$\rightarrow$3d transition at ~8979.5 eV characteristic of Cu(II), confirming that copper is predominantly in the cuprous oxidation state (George et al., 2003). The feature located around 8983 eV can be assigned as a 1s$\rightarrow$4p transition, which is most intense in digonal coordination environments (Kau et al., 1987; Pickering et al., 1993). By comparing the position and intensity of this transition with the corresponding feature in model compound spectra, it is observed that the near edge spectra of copper complexes in the liver and kidney are intermediate in appearance between the three- and four-coordinate Cu(I)-thiolate

species and that the data are very similar to those reported previously for LEC rat purified liver lysosomes (George et al., 2003). Figure 7-5B shows the Mo K near edge spectra of liver and kidney from TTM-treated LPP rats. The spectrum is very similar to that of tetrathiomolybdate, suggesting a tetrahedral geometry for Mo and a full complement of four sulfur donors. As was the case for Cu, the Mo K-edge spectra are also very similar to those reported previously of purified LEC rat liver lysosomes (George et al., 2003).

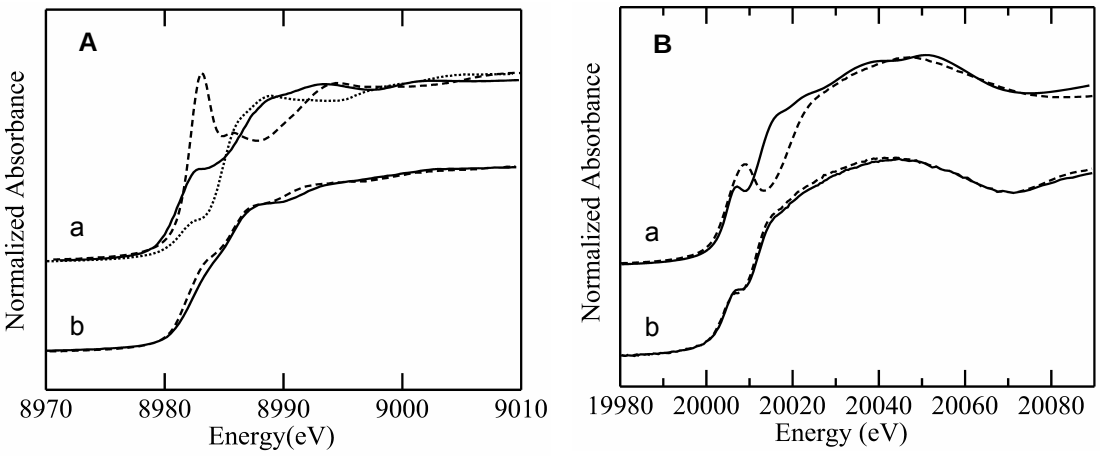

Figure 7-5. Cu (A) and Mo (B) K-edge X-ray absorption near edge spectra of whole liver and kidney from TTM-treated LPP rat in comparison with model compounds and the previously characterized Cu-Mo complex protein. A) a shows the Cu K near edge X-ray absorption spectra of model compounds with different coordination numbers: 2, (– – – –) $[Cu(SC_{10}H_{12})_2]^-$; 3, (———) $[Cu_4(SPh)_6]^{2-}$; 4, (·····) $[S_2MoS_2CuS_2MoS_2]^{3-}$ from the metal center of Desulfovibrio gigas orange protein. B) a shows Mo K near edge X-ray absorption spectra of tetrathiomolybdate (———) $[MoS_4]^{2-}$ and molybdate (– – – –) $[MoO_4]^{2-}$. The spectra in b of panels A and B compare TTM-treated LPP rat liver (– – – –) and kidney (———) for Cu and Mo, respectively.

More structural detail is available from quantitative analysis of the EXAFS portion of the spectrum. Figure 7-6 shows the Cu and Mo EXAFS and best-fits, together with the corresponding EXAFS Fourier transforms, for TTM-treated LPP rats. The EXAFS curve-fitting analysis is summarized in Table 7-2. All data sets have prominent

EXAFS from directly coordinated ligands, which are identified by curve-fitting as sulfur. EXAFS cannot readily distinguish between backscatterers of similar atomic number (cf. (George and Pickering, 2007)), thus EXAFS from S and Cl backscatterers cannot easily be distinguished, whereas S and O are normally quite straightforward to

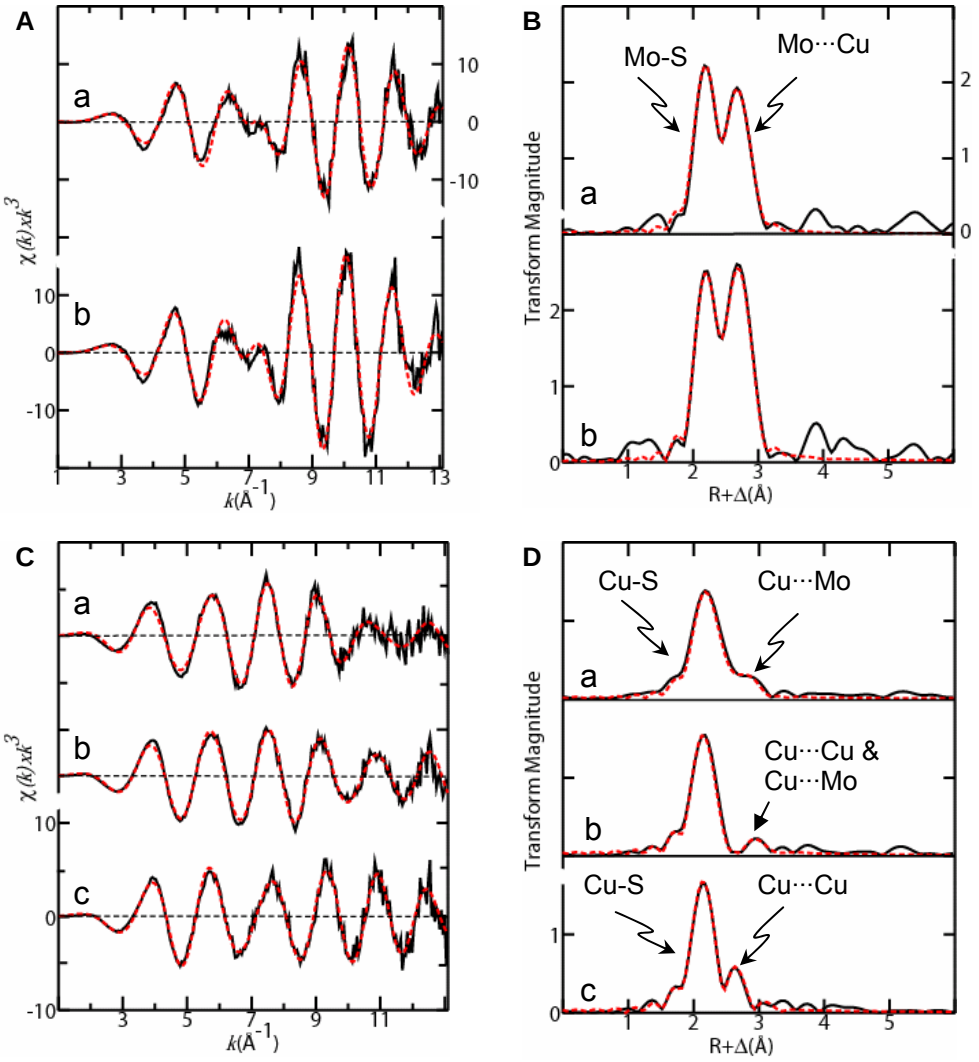

Figure 7-6. Comparison of the Cu and Mo K-edge EXAFS and the corresponding Fourier transforms of liver and kidney from LPP rat either with or without TTM treatment. On the top are the Mo K-edge EXAFS spectra A) and the Mo-S phase-corrected Fourier transforms B) of kidney (a) and liver (b) from the LPP rat with TTM treatment. On the bottom are the Cu K-edge EXAFS C) and Cu-S phase-corrected Fourier transforms D) of kidney (a) and liver (b) from TTM-treated LPP rat as mentioned above, as well as liver from the non-treated LPP rat (c). Black solid curves represent the experimental data, while the red dash curves are for best fits with the parameters listed in Table 7-2.

Table 7-2. Cu (A) and Mo (B) K-edge EXAFS curve-fitting parameters of kidney and liver from TTM-treated and untreated LPP rats.

A. Cu K-edge EXAFS curve fitting results[a].

Cu–S			Cu···Mo			Cu···Cu			*F*
N	***R*(Å)**	**σ^2(Å^2)**	***N***	***R*(Å)**	**σ^2(Å^2)**	***N***	***R*(Å)**	**σ^2(Å^2)**	
Kidney of TTM-treated LPP rat									
3	2.282 (3)	0.0060 (2)	1	2.717 (4)	0.0071 (3)				0.269
3	2.279 (2)	0.0057 (1)	0.5 (3)	2.706[b]	0.0037[b]				0.279
3.6 (1)	2.280 (3)	0.0069 (3)	0.5 (3)	2.706[b]	0.0037[b]				0.269
Liver of TTM-treated LPP rat									
3	2.265 (2)	0.0049 (1)	0.4 (1)	2.721[b]	0.0035[b]	1.2[c] (1)	2.698[d]	0.0088[d]	
						0.6[c] (1)	2.878[d]	0.0091[d]	0.227
3.0 (1)	2.265 (2)	0.0049 (1)	0.4 (1)	2.721[b]	0.0035[b]	1.2[c] (1)	2.698[d]	0.0088[d]	
						0.6[c] (1)	2.878[d]	0.0091[d]	0.227
3	2.265 (2)	0.0053 (1)							0.253
Liver of untreated LPP rat									
3	2.248(2)	0.0045 (1)				1	2.694 (4)	0.0071 (4)	0.286
3	2.253 (2)	0.0045 (1)				2	2.698 (5)	0.0088 (4)	
						1	2.878 (11)	0.0092 (4)	0.273

B. Mo K-edge EXAFS curve fitting results[a].

Mo–S			Mo···Cu			
N	***R*(Å)**	**σ^2(Å^2)**	***N***	***R*(Å)**	**σ^2(Å^2)**	***F***
Kidney of TTM-treated LPP rat						
4	2.237 (3)	0.0034 (1)	3	2.706 (3)	0.0037 (1)	0.261
4	2.241 (2)	0.0034 (2)	4	2.709 (3)	0.0051 (1)	0.267
4	2.237 (3)	0.0034 (1)	3.1(3)	2.706 (3)	0.0037 (1)	0.261
Liver of TTM-treated LPP rat						
4	2.245 (2)	0.0025 (1)	4	2.721 (2)	0.0035 (1)	0.251
4	2.240 (3)	0.0025 (2)	3	2.719 (3)	0.0021 (1)	0.262
4	2.246 (3)	0.0024 (1)	4.3(3)	2.722 (3)	0.0039 (4)	0.251

a) The parameters in the curve fitting are coordination numbers, *N*, interatomic distances *R* (Å), and Debye-Waller factors σ^2 (Å^2). Values in parentheses are the estimated standard deviations (precisions) obtained from the diagonal elements of the covariance matrix. The accuracies will be much greater than these values, and are generally accepted to be ±0.02 Å for bond-lengths and ±20% for coordination numbers and Debye-Waller factors. The fit-error function *F* is defined as $F = \sqrt{\sum k^6 \left(\chi_{calc} - \chi_{expt}\right)^2 / \sum \chi_{expt}^2}$, where the summations are over all data points included in the refinement. *b*) Value fixed to that determined from Mo K-edge EXAFS curve-fitting. *c*) The ratio of the Cu···Cu *N* values was held fixed at the 2:1 value used to model the untreated LPP rat Cu K-edge EXAFS. *d*) Value fixed at that determined from fitting untreated LPP rat Cu K-edge EXAFS (*untreated*, *liver*).

discriminate. Here the presence of sulfur donors is assumed, as these are physiologically far more likely than the alternatives (i.e. phosphorus or chlorine). Quantitative curve-fitting analysis indicates that for both liver and kidney Mo is coordinated by four sulfurs at a distance of 2.24 Å while Cu is coordinated by between 3 and 4 sulfurs at 2.27-2.28 Å (Table 7-2). This is as expected from the near-edge spectra, as discussed above.

Table 7-3. Metal concentrations in live and kidney from LPP rats with or without TTM treatment, and from the control animal.

μg/g wet weight (μmol/g wet weight)	Cu	Mo	Fe	Zn
Liver samples				
control	4.74	0.61	78.62	25.73
	(0.07)	(0.01)	(1.41)	(0.39)
TTM-treated LPP rat	127.51	17.03	269.88	44.55
	(2.01)	(0.18)	(4.83)	(0.68)
LPP rat	206.82	0.60	311.41	46.54
	(3.25)	(0.01)	(5.58)	(0.71)
Kidney samples				
control	11.81	0.31	63.72	20.88
	(0.19)	(0.00)	(1.14)	(0.32)
TTM-treated LPP rat	53.61	18.18	50.15	21.36
	(0.84)	(0.19)	(0.90)	(0.33)
LPP rat	172.20	0.30	88.72	19.53
	(2.71)	(0.00)	(1.59)	(0.30)

Note, the metal concentration values shown are the average of two independent measurements with the samples from the same animal. The concentrations in the first row for each sample are in the unit of μg per gram wet weight, and μmol per gram wet weight for the values in round bracket.

Metal-metal interactions are observed for both Cu and Mo data, but it is more pronounced for Mo which will be discussed first. Curve-fitting of the Mo EXAFS clearly indicates 3 and 4 Mo···Cu interactions at 2.71 and 2.72 Å, for kidney and liver, respectively. This is seen clearly in the EXAFS Fourier transforms as the intense peak at about 2.7 Å in the spectra from both organs. For Cu, however, only a rather low-intensity peak is observed. Similar spectra were observed earlier for purified LEC rat liver lysosomes (George et al., 2003). Chemical analysis of the samples yielded Cu:Mo molar stoichiometries of 11.2:1 and 4.4:1 for liver and kidney, respectively (Table 7-3). This indicates that liver has considerable additional copper that is not involved in a multimetallic cluster. The Cu K near edge and EXAFS of LPP rat liver in the absence of

TTM treatment were therefore examined (Figure 7-6). The data indicate a copper environment that is very similar to that of copper metallothionein (Zhang et al., 2008) with mostly trigonal Cu—S coordination (Cu—S 2.25 Å) plus a weaker Cu···Cu at about 2.7 Å. This is in agreement with previous work indicating that copper in LEC rat liver is predominantly bound by metallothioneins (George et al., 2003). The Cu···Cu interaction was modeled for simplicity with only two partially cancelling Cu···Cu components (Table 7-2), but Cu methallothionein is expected to have rather more components (*e.g.* the yeast protein has up to 10 different Cu···Cu interactions) which will interfere with each other and will partially cancel (Zhang et al., 2008). Thus, the current data of Cu in TTM-treated LPP rat liver represent the sum of the spectrum of copper that is not involved in Cu—Mo complexes with that of the Cu—Mo complexes. The ~2.7 Å Cu···Cu EXAFS effectively cancel EXAFS from Cu—Mo as EXAFS from Mo and Cu backscatterers are expected to be 180° out of phase, with Mo having higher amplitude than Cu especially at higher *k*, all other factors being equal. EXAFS cancellation has been discussed in more detail by George (George, 1997) and by Zhang et al. (Zhang et al., 2008). Because of this complexity the Cu EXAFS from TTM-treated LPP rat liver was modeled by taking the parameters (bondlengths and Debye-Waller factors) for the Cu···Cu interactions from the analysis of untreated LPP rat liver (Table 7-2, Figure 7-6), and the parameters for Cu—Mo interactions from the Mo K-edge curve-fitting analysis. Only the parameters for Cu—S interactions and the coordination numbers N for Cu···Cu and Cu—Mo interactions were allowed to be refined. If these parameters were freely floated then similar bond-lengths and Debye-Waller factors were obtained, except that very highly (undesirable) correlations between parameters were found upon examination of the covariance matrix. In contrast to the situation with liver, for kidney the elemental stoichiometry is much closer to that observed by Mo K-edge EXAFS (3:1), suggesting that much of the copper present is involved in Cu—Mo complexes. Chemical analysis shows the higher level of Cu in the kidney of the untreated LPP rat than the treated animal (Table 7-3), which is different from what are observed from XFI. This apparent discrepancy is most likely due to the differences in

age when the animals were exsanguinated. The LPP rat examined by the XAS and chemical analysis was exsanguinated at 120 days of age, comparing to 109 days for the XFI. The serum copper level increases with the age of the animal in the jaundiced state, and copper can be transferred from liver to other organs such as kidney. Variations of Cu content in the kidney from different animals may also contribute to the discrepancy observed here to a less extent.

7.4.3 Density Functional Theory Calculation

The chemistry of copper—molybdenum—sulfur clusters has been extensively investigated. A rich chemistry exists, much of which involving multi-metallic clusters where Cu and Mo are arranged in rhombs involving two bridging sulfurs. Tetrathiomolybdate tends to form species bridged to individual cuprous ions by two of

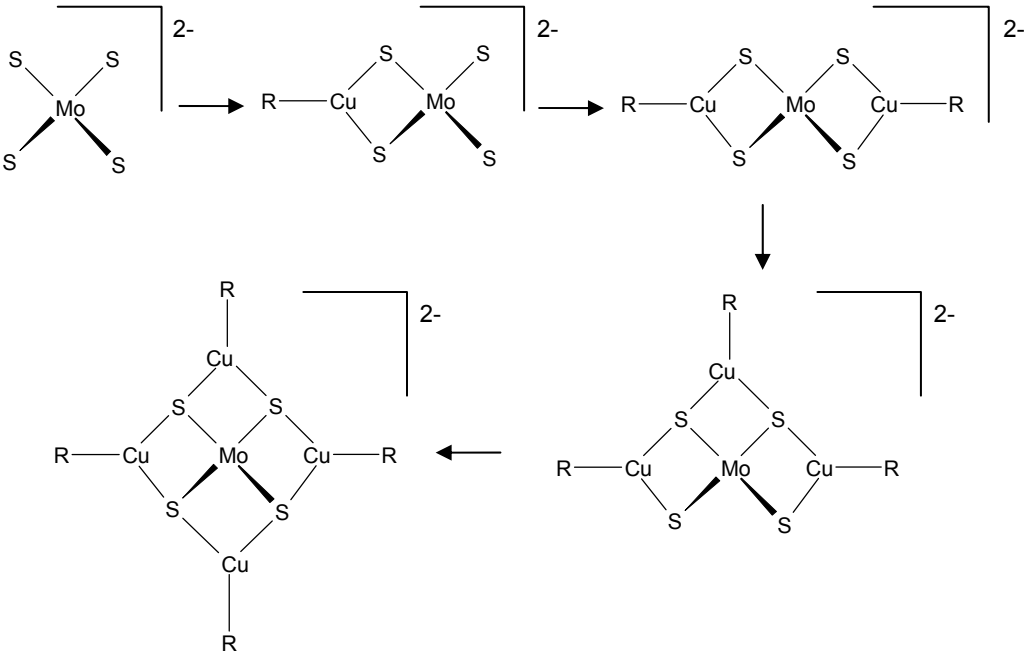

Figure 7-7. Schematic diagram of formation of polymetallic clusters by sequential addition of copper moieties to tetrathiomolybdate.

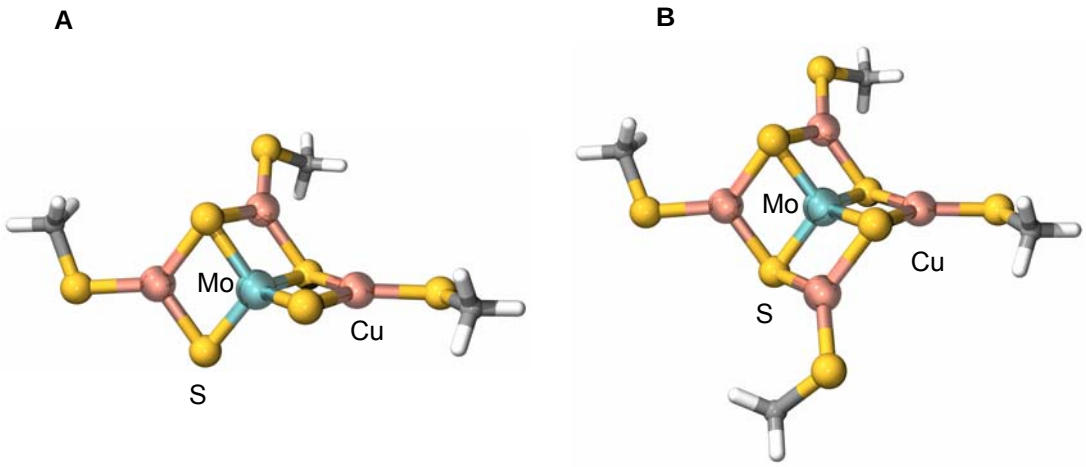

Figure 7-8. DFT energy-minimized structures for A) $[(CH_3SCu)_3MoS_4]^{2-}$ and B) $[(CH_3SCu)_4MoS_4]^{2-}$. For a selected computed average interatomic distances were Cu—SCH_3 2.217 Å, Cu—S(bridging) 2.270 Å, Mo—S 2.283 Å, Cu···Mo 2.702 Å, and Cu···Cu 3.760 Å. For b selected computed average interatomic distances are Cu—SCH_3 2.214, Cu—S(bridging) 2.291 Å, Mo—S 2.297 Å, Cu···Mo 2.703 Å, and Cu···Cu 3.821 Å.

its four sulfur ligands, so that the copper bridges across one edge of the tetrahedron of sulfur atoms. Complexes with Cu:Mo stoichiometries of one through six have been structurally characterized, with three being the most common, and four a close second (Allen and Kennard, 1983). Figure 7-7 illustrates the sequential addition of copper to tetrathiomolybdate, up to a Cu:Mo stoichiometry of four (i.e. stoichiometries 5 and 6 are not illustrated). Energy minimized structures of idealized $[(CuSR)_3MoS_4]^{2-}$ and $[(CuSR)_4MoS_4]^{2-}$ clusters are shown in Figure 7-8. The computed bond-lengths (see caption to Figure 7-8) agree well both with values from the Cambridge Crystallographic Database (Allen and Kennard, 1983) and with those obtained from EXAFS (Table 7-2). Thus, the current results are consistent with a mechanism in which copper is effectively chelated by thiomolybdate in liver (Figure 7-7), and the resulting complexes are then at least in part mobilized to kidney. The nature of the external ligands to copper is worth addressing and may be relevant to transport. The EXAFS data indicate that these are sulfur ligands, with chloride being a rather less likely alternative. Given that the copper-

molybdenum species are at least fractionally mobilized, a likely candidate for the external ligands to copper of those clusters that are mobilized is glutathione. Glutathione is the most prevalent intracellular thiol in higher eukaryotes, and its association with a Cu—Mo cluster might allow transport via one of the glutathione-linked transporters (e.g.(Lee et al., 2006a)) facilitating transport from the liver and eventual localization to kidney.

7.5 Discussions and Future Work

In this study, X-ray fluorescence imaging and X-ray absorption spectroscopy have been combined to investigate the metabolism of the Cu and Mo complex in the body upon TTM treatment. Liver, brain and kidney tissues were examined in this initial study. As expected, Cu level increases significantly in the liver of the LPP rat, according to XFI in this study. Both Cu and Mo K-edge EXAFS show that TTM interacts with Cu in the liver upon TTM treatment. The chemical form of TTM-Cu complex in the liver, determined by the EXAFS, is consistent with the model proposed previously by George and coworkers (George et al., 2003). The high co-localization of Mo and Cu in the cortex, but not in the medulla region of the kidney of the LPP rat 4 days after a single administration of TTM was clearly shown in the XFI high resolution maps. The finding here is consistent with previous reported metal analysis on the whole kidney tissue (Suzuki et al., 1993). The interaction of TTM and Cu in the kidney is further confirmed by EXAFS. Matching of the optical imaging and the XFI map indicates that Cu and Mo accumulate in the proximal convoluted tubules but not in the glomeruli or in the distal convoluted tubules. This cell-specific co-localization of Cu and Mo may suggest the Cu and Mo are released from the blood into the filtrate in the glomerulus cavity, and then re-absorbed and accumulated locally when passing through the proximal tubules.

Ogra et al. have suggested that the Cu-TTM complexes that form in liver can be divided into soluble and insoluble fractions, and that the latter might be slowly dissolved and subsequently excreted (Ogra et al., 1996). From the XAS perspective the

copper-molybdenum clusters that form in liver are structurally similar to those in kidney and the difference may simply be the nature of the external thiolate ligands to copper, as discussed above. How TTM abstracts Cu from metallothionein in the liver still remains to be clarified. In fully loaded copper metallothionein a proportion of the copper is more loosely bound with two-coordinate cuprous thiolate (Zhang et al., 2008). Preliminary DFT calculations (not illustrated) indicate that TTM should be able to sequester this copper by providing an additional sulfur ligand, and then by partially abstracting the copper from its metallothionein binding site by forming MoS_2Cu rhombs. Hepatitis is unlikely to be caused by Cu when it is actually bound to metallothionein, and perhaps it is the small fraction of free copper ions which is scavenged by TTM. In time, and with equilibration, this scavenging might result in the complexation of a significant fraction of the total copper present.

Finally, the long-term effects of TTM treatment are presently unknown. Haywood et al. (Haywood et al., 2004) have reported long-term adverse effects in a flock of copper-poisoned sheep following treatment with TTM which was successful in the short term. However, this study employed quite high oral doses of copper and it is possible that the physiological fate would differ in a Wilson's patient. Long-term experiments with LPP rat are needed to understand the effects of longer term treatments with TTM. TTM remains a highly promising candidate drug for treatment of Wilson's disease. A molecular understanding of the metallophysiology is vital to its eventual use in a clinical setting, and possible future strategies might involve both TTM and a second copper chelator, possibly customized for metal binding (George et al., 2004).

CHAPTER 8

SUMMARY AND OUTLOOK: STRUCTURE-FUNCTION RELATIONSHIPS OF MOLECULES INVOLVED IN CELLULAR COPPER CONTROL

8.1 Summary and Outlook

The existence of biomolecules that specifically regulate cellular copper has been known for a long time. However, at present, little is known about the functional mechanisms for most of these molecules. Structural studies on these molecules, and especially on the Cu binding sites, are essential in understanding the mechanisms of copper transfer from the molecules to their target proteins. The Cu ions in these copper control molecules are silent to EPR and are essentially invisible to NMR, and most attempts to crystallize these molecules with bound copper have been unsuccessful. Under these circumstances, X-ray absorption spectroscopy has been an important structural tool for probing the structures of the copper-binding sites in several families of molecules involved in cellular copper control. In this thesis species studied include the copper chaperones that deliver copper to cytochrome c oxidase in the mitochondrion, the Cu-bound metallothionein for copper storage and detoxification, and two copper-dependent transcription regulators that are responsive to the cellular copper overload. The Cu XAS and computational chemistry results presented in this thesis have provided information that is essential to the understanding of Cu homoeostasis. These results will guide future studies on cellular

Cu control and may lead to the development of new treatments for human diseases of Cu dysregulation. Furthermore, new strategies employing Cu dysregulation of bacterial pathogens could be developed to treat resistant infectious diseases. In future work, as the level of the understanding increases, the challenges will be correspondingly increased and quantitative techniques are expected to become more important.

Based on current processes (including this thesis study), the Cu control molecules share several common Cu-binding properties:

1). All copper control molecules bind to Cu(I). A low-affinity Cu(II) importer has been reported (Dix et al., 1994; Lee et al., 2002b), but no Cu(II) ions are found within cells under physiological conditions except as components of Cu-dependent redox enzymes.

2). The copper control molecules bind Cu either via all-sulphur coordination or with a mixed coordination of sulphur and nitrogen.

3). Only digonal or trigonal Cu coordination geometries are found. In the cases that S atoms provide the only ligands, Cu is either in digonal coordination state or forms multi-copper Cu-S clusters.

The question of why Cu(I) with a coordination number of 2 or 3 is preferred in the cellular copper control may be important in understanding the chemical mechanisms underlying copper regulation. Here, the coordination chemistry of Cu(I) and Cu(II) are briefly compared. Cu(I) is a soft Lewis acid, and thus prefers soft ligands such as sulfur with a coordination number of 2, 3 and 4. Four-coordinate Cu(I) is coordinatively saturated, and thus cannot bind additional ligands. Two coordinate or three coordinate Cu(I) might be transferred from a donor molecule to the target protein by forming a 3-coordinate or 4-coordinate intermediates employing an additional S donor from the target protein. In fact, a 3-coordinated intermediate has been observed in the solution structure of the Atx1-Ccc2 complex (Banci et al., 2006b). Cu(II) is a stronger Lewis acid than Cu(I) and hence favours hard N/O-donor

ligands. In addition, Cu(II) prefers higher coordination number (4, 5 or 6). The differences in the coordination chemistry between Cu(I) and Cu(II) described above may help in understanding why Cu(II) is not employed in cellular copper control. If charge compensation is adequate then the thermodynamic preference between 2-, 3- and 4- coordinate cuprous thiolates is not strong, and this flexible coordination chemistry means that cuprous ions should be much simpler to bind and to transfer from the copper control molecule to its target.

Density functional theory (DFT) (Accelrys 4.1 DMol3) calculations on the Cu-methylthiolate in different coordination states were carried out in order to estimate the thermodynamic changes during the formation of 3-coordinate and 4-coordinate Cu(I)-thiolate intermediates. The preliminary results suggest that the digonal coordination is the most stable coordination state for Cu(I). These results are consistent with previous experimental and DFT calculation results on the interactions of aqueous Cu(I) with water (Iino et al., 2007; Blumberger, 2008). By comparison, the binding energies of 3- and 4-coordinated Cu-thiolate are more than 180 kJ/mol lower than that of 2-coordinated one. However, the relative instability of 3- and 4-coordinate Cu-methylthiolate could be, at least partially, due to the increased negative charge with greater numbers of thiolate ligands bound to Cu. In small molecule chemistry, neutral S donors are found to bind 3-coordinate and 4-coordinate Cu(I) species, except when 3-coordinate Cu(I) forms a four-Cu cluster (Allen and Kennard, 1983). To help cancel out effects of increased local negative charges, neutral S ligands (such as thiol-S or thiourea) were used in DFT calculations. In this case, the binding energies of Cu-S models with different coordination number are very close to each other, which make it possible to form intermediates of higher coordination number without a prohibitive energy barrier. Previous workers have shown lower proton affinities for Cu-bound cysteines (pK_a values $\leq$6) (Zhou et al., 2008). Structural analyses suggest that in biological molecules a positively-charged residue close to the Cu(I) binding site may help to cancel the negative charge from S ligands (Banci et al., 2006b; Holt and Merz, 2007). As mentioned above, experiments have

been carried out to examine the coordination environment of aqueous Cu(I) (Iino et al., 2007; Blumberger, 2008). No similar experiments have been reported with synthesized short peptides containing cysteines, which is more relevant to the coordination environment in biological systems. In future work, it may be informative to investigate the coordination chemistry of Cu(I) bound by short synthetic peptides incorporating residues that might confer stabilization by charge compensation near the metal binding site.

REFERENCES

Abajian, C., Yatsunyk, L.A., Ramirez, B.E. and Rosenzweig, A.C. (2004) Yeast cox17 solution structure and Copper(I) binding. *Journal of Biological Chemistry*, **279**, 53584-53592.

Ahmed, S., Deng, H. and Borjigin, J. (2005) A new strain of rat for functional analysis of PINA. *Molecular Brain Research*, **137**, 63-69.

Ala, A., Walker, A.P., Ashkan, K., Dooley, J.S. and Schilsky, M.L. (2007) Wilson's disease. *Lancet*, **369**, 397-408.

Allen, F.H. and Kennard, O. (1983) The Cambridge Database of Molecular-Structures. *Perspectives in Computing*, **3**, 28-43.

Andrews, G.K. (2001) Cellular zinc sensors: MTF-1 regulation of gene expression. *Biometals*, **14**, 223-237.

Arnesano, F., Balatri, E., Banci, L., Bertini, I. and Winge, D.R. (2005a) Folding studies of Cox17 reveal an important interplay of cysteine oxidation and copper binding. *Structure*, **13**, 713-722.

Arnesano, F., Banci, L., Bertini, I., Cantini, F., Ciofi-Baffoni, S., Huffman, D.L. and O'Halloran, T.V. (2001) Characterization of the binding interface between the

copper chaperone Atx1 and the first cytosolic domain of Ccc2 ATPase. *Journal of Biological Chemistry*, **276**, 41365-41376.

Arnesano, F., Banci, L., Bertini, I. and Martinelli, M. (2005b) Ortholog search of proteins involved in copper delivery to cytochrorne c oxidase and functional analysis of paralogs and gene neighbors by genomic context. *Journal of Proteome Research*, **4**, 63-70.

Atkinson, E.R., Raper, E.S., Gardiner, D.J., Dawes, H.M., Walker, N.P.C. and Jackson, A.R.W. (1985) Tetrakis-[1-Methylimidazoline-2(3h)-Thione]-μ_2-[1-Methylimidazoline-2(3h)-Thione]-Di-Copper(I) Sulfate Trihydrate - Preparation, Thermal-Analysis and Crystal-Structure. *Inorganica Chimica Acta-Articles and Letters*, **100**, 285-291.

Bagai, I., Liu, W., Rensing, C., Blackburn, N.J. and McEvoy, M.M. (2007) Substrate-linked conformational change in the periplasmic component of a Cu(I)/Ag(I) efflux system. *Journal of Biological Chemistry*, **282**, 35695-35702.

Balamurugan, K. and Schaffner, W. (2006) Copper homeostasis in eukaryotes: Teetering on a tightrope. *Biochimica et Biophysica Acta-Molecular Cell Research*, **1763**, 737-746.

Balatri, E., Banci, L., Bertini, I., Cantini, F. and Ciofi-Baffoni, S. (2003) Solution structure of Sco1: a thioredoxin-like protein Involved in cytochrome c oxidase assembly. *Structure*, **11**, 1431-1443.

Banci, L. (2003) Molecular dynamics simulations of metalloproteins. *Current Opinion in Chemical Biology*, **7**, 143-149.

Banci, L., Bertini, I., Calderone, V., Ciofi-Baffoni, S., Mangani, S., Martinelli, M., Palumaa, P. and Wang, S. (2006a) A hint for the function of human Sco1 from

different structures. *Proceedings of the National Academy of Sciences of the United States of America*, **103**, 8595-8600.

Banci, L., Bertini, I., Cantini, F., Ciofi-Baffoni, S., Gonnelli, L. and Mangani, S. (2004) Solution structure of Cox11, a novel type of beta-immunoglobulin-like fold involved in CuB site formation of cytochrome c oxidase. *Journal of Biological Chemistry*, **279**, 34833-34839.

Banci, L., Bertini, I., Cantini, F., Felli, I.C., Gonnelli, L., Hadjiliadis, N., Pierattelli, R., Rosato, A. and Voulgaris, P. (2006b) The Atx1-Ccc2 complex is a metal-mediated protein-protein interaction. *Nature Chemical Biology*, **2**, 367-368.

Banci, L., Bertini, I., Ciofi-Baffoni, S., Janicka, A., Martinelli, M., Kozlowski, H. and Palumaa, P. (2008) A structural-dynamical characterization of human cox17. *Journal of Biological Chemistry*, **283**, 7912-7920.

Barros, M.H., Johnson, A. and Tzagoloff, A. (2004) COX23, a homologue of COX17, is required for cytochrome oxidase assembly. *Journal of Biological Chemistry*, **279**, 31943-31947.

Barry, A.N. and Blackburn, N.J. (2008) A selenocysteine variant of the human copper chaperone for superoxide dismutase. A Se-XAS probe of cluster composition at the domain 3 - domain 3 dimer interface. *Biochemistry*, **47**, 4916-4928.

Barry, A.N., Clark, K.M., Otoikhian, A., van der Donk, W.A. and Blackburn, N.J. (2008) Selenocysteine Positional Variants Reveal Contributions to Copper Binding from Cysteine Residues in Domains 2 and 3 of Human Copper Chaperone for Superoxide Dismutase. *Biochemistry*, **47**, 13074-13083.

Becke, A.D. (1988a) Density-Functional Exchange-Energy Approximation with Correct Asymptotic-Behavior. *Physical Review A*, **38**, 3098-3100.

Becke, A.D. (1988b) A Multicenter Numerical-Integration Scheme for Polyatomic-Molecules. *Journal of Chemical Physics*, **88**, 2547-2553.

Becke, A.D. (1989) Density Functional Theories in Quantum-Chemistry - Beyond the Local Density Approximation. *ACS Symposium Series*, **394**, 165-179.

Becke, A.D. (1993) Density-Functional Thermochemistry .3. the Role of Exact Exchange. *Journal of Chemical Physics*, **98**, 5648-5652.

Beers, J., Glerum, D.M. and Tzagoloff, A. (2002) Purification and characterization of yeast Sco1p, a mitochondrial copper protein. *Journal of Biological Chemistry*, **277**, 22185-22190.

Beinert, H. (1995) Crystals and structures of cytochrome c oxidases--the end of an arduous road. *Chemistry & Biology*, **2**, 781-785.

Berendsen, H.J.C., Postma, J.P.M., van Gunsteren, W.F. and Hermans, J. (1981) Interaction models for water in relation to protein hydration. In *Intermolecular Forces*. D. Reidel Publishing Company (Pullman, B. *ed.*), pp. 331-342.

Berendsen, H.J.C., Postma, J.P.M., Vangunsteren, W.F., Dinola, A. and Haak, J.R. (1984) Molecular-Dynamics with Coupling to an External Bath. *Journal of Chemical Physics*, **81**, 3684-3690.

Berendsen, H.J.C., Vanderspoel, D. and Vandrunen, R. (1995) Gromacs - a Message-Passing Parallel Molecular-Dynamics Implementation. *Computer Physics Communications*, **91**, 43-56.

Bertinato, J. and L'Abbe, M.R. (2004) Maintaining copper homeostasis: regulation of copper-trafficking proteins in response to copper deficiency or overload. *Journal of Nutritional Biochemistry*, **15**, 316-322.

Bertini, I. and Cavallaro, G. (2008) Metals in the "omics" world: copper homeostasis and cytochrome c oxidase assembly in a new light. *Journal of Biological Inorganic Chemistry*, **13**, 3-14.

Bertini, I., Hartmann, H.J., Klein, T., Liu, G., Luchinat, C. and Weser, U. (2000) High resolution solution structure of the protein part of Cu7 metallothionein. *European Journal of Biochemistry*, **267**, 1008-1018.

Bertsch, P.M. and Hunter, D.B. (2001) Applications of synchrotron-based X-ray microprobes. *Chemical Reviews*, **101**, 1809-1842.

Blumberger, J. (2008) Cu-aq^{+}/Cu-aq^{2+} Redox Reaction Exhibits Strong Nonlinear Solvent Response Due to Change in Coordination Number. *Journal of the American Chemical Society*, **130**, 16065-16068.

Bowmaker, G.A., Clark, G.R., Seadon, J.K. and Dance, I.G. (1984) The Formation and Structural Chemistry of the Hexa(Mu-Tert-Butylthiolato) Pentacuprate(I) Cage Anion with Triethylammonium and Tetraethylammonium Cations. *Polyhedron*, **3**, 535-544.

Brewer, G.J., Askari, F., Lorincz, M.T., Carlson, M., Schilsky, M., Kluin, K.J., Hedera, P., Moretti, P., Fink, J.K., Tankanow, R., Dick, R.B. and Sitterly, J. (2006) Treatment of Wilson disease with ammonium tetrathiomolybdate: IV. Comparison of tetrathiomolybdate and trientine in a double-blind study of treatment of the neurologic presentation of Wilson disease. *Archives of Neurology*, **63**, 521-527.

Brewer, G.J., Dick, R.D., Yuzbasiyangurkin, V., Tankanow, R., Young, A.B. and Kluin, K.J. (1991) Initial Therapy of Patients with Wilsons-Disease with Tetrathiomolybdate. *Archives of Neurology*, **48**, 42-47.

Brewer, G.J., Hedera, P., Kluin, K.J., Carlson, M., Askari, F., Dick, R.B., Sitterly, J. and Fink, J.K. (2003) Treatment of Wilson disease with ammonium tetrathiomolybdate: III. Initial therapy in a total of 55 neurologically affected patients and follow-up with zinc therapy. *Archives of Neurology*, **60**, 379-385.

Brewer, G.J., Terry, C.A., Aisen, A.M. and Hill, G.M. (1987) Worsening of Neurologic Syndrome in Patients with Wilsons-Disease with Initial Penicillamine Therapy. *Archives of Neurology*, **44**, 490-493.

Brown, K.R., Keller, G.L., Pickering, I.J., Harris, H.H., George, G.N. and Winge, D.R. (2002) Structures of the cuprous-thiolate clusters of the Mac1 and Ace1 transcriptional activators. *Biochemistry*, **41**, 6469-6476.

Brugnera, E., Georgiev, O., Radtke, F., Heuchel, R., Baker, E., Sutherland, G.R. and Schaffner, W. (1994) Cloning, Chromosomal Mapping and Characterization of the Human Metal-Regulatory Transcription Factor Mtf-1. *Nucleic Acids Research*, **22**, 3167-3173.

Brunger, A.T. and Adams, P.D. (2002) Molecular dynamics applied to X-ray structure refinement. *Accounts of Chemical Research*, **35**, 404-412.

Bull, P.C., Thomas, G.R., Rommens, J.M., Forbes, J.R. and Cox, D.W. (1993) The Wilson Disease Gene Is a Putative Copper Transporting P-Type Atpase Similar to the Menkes Gene. *Nature Genetics*, **5**, 327-337.

Butt, T.R., Sternberg, E.J., Gorman, J.A., Clark, P., Hamer, D., Rosenberg, M. and Crooke, S.T. (1984) Copper Metallothionein of Yeast, Structure of the Gene, and Regulation of Expression. *Proceedings of the National Academy of Sciences of the United States of America-Biological Sciences*, **81**, 3332-3336.

Byrd, J., Berger, R.M., McMillin, D.R., Wright, C.F., Hamer, D. and Winge, D.R. (1988) Characterization of the copper-thiolate cluster in yeast metallothionein and two truncated mutants. *Journal of Biological Chemistry*, **263**, 6688-6694.

Calderone, V., Dolderer, B., Hartmann, H.J., Echner, H., Luchinat, C., Del Bianco, C., Mangani, S. and Weser, U. (2005) The crystal structure of yeast copper thionein: The solution of a long-lasting enigma. *Proceedings of the National Academy of Sciences of the United States of America*, **102**, 51-56.

Camakaris, J., Voskoboinik, I. and Mercer, J.F. (1999) Molecular mechanisms of copper homeostasis. *Biochemical and Biophysical Research Communications*, **261**, 225-232.

Capaldi, R.A. (1990) Structure and Assembly of Cytochrome-C-Oxidase. *Archives of Biochemistry and Biophysics*, **280**, 252-262.

Capaldi, R.A., Malatesta, F. and Darleyusmar, V.M. (1983) Structure of Cytochrome-C Oxidase. *Biochim Biophys Acta*, **726**, 135-148.

Carlson, H.A., Nguyen, T.B., Orozco, M. and Jorgensen, W.L. (1993) Accuracy of Free-Energies of Hydration for Organic-Molecules from 6-31g-Asterisk-Derived Partial Charges. *Journal of Computational Chemistry*, **14**, 1240-1249.

Carr, H.S., George, G.N. and Winge, D.R. (2002) Yeast Cox11, a protein essential for cytochrome c oxidase assembly, is a Cu(I)-binding protein. *Journal of Biological Chemistry*, **277**, 31237-31242.

Carr, H.S. and Winge, D.R. (2003) Assembly of cytochrome c oxidase within the mitochondrion. *Accounts of Chemical Research*, **36**, 309-316.

Cavet, J.S., Graham, A.I., Meng, W. and Robinson, N.J. (2003) A cadmium-lead-sensing ArsR-SmtB repressor with novel sensory sites. Complementary metal

discrimination by NmtR AND CmtR in a common cytosol. *Journal of Biological Chemistry*, **278**, 44560-44566.

Changela, A., Chen, K., Xue, Y., Holschen, J., Outten, C.E., O'Halloran, T.V. and Mondragon, A. (2003) Molecular basis of metal-ion selectivity and zeptomolar sensitivity by CueR. *Science*, **301**, 1383-1387.

Cheatham, T.E. and Young, M.A. (2000) Molecular dynamics simulation of nucleic acids: Successes, limitations, and promise. *Biopolymers*, **56**, 232-256.

Chelly, J., Tumer, Z., Tonnesen, T., Petterson, A., Ishikawa-Brush, Y., Tommerup, N., Horn, N. and Monaco, A.P. (1993) Isolation of a candidate gene for Menkes disease that encodes a potential heavy metal binding protein. *Nature Genetics*, **3**, 14-19.

Chen, K., Yuldasheva, S., Penner-Hahn, J.E. and O'Halloran, T.V. (2003) An atypical linear Cu(I)-S_2 center constitutes the high-affinity metal-sensing site in the CueR metalloregulatory protein. *Journal of the American Chemical Society*, **125**, 12088-12089.

Chen, W.Y., John, J.A.C., Lin, C.H. and Chang, C.Y. (2002) Molecular cloning and developmental expression of zinc finger transcription factor MTF-1 gene in zebrafish, Danio rerio. *Biochemical and Biophysical Research Communications*, **291**, 798-805.

Chen, W.Y., John, J.A.C., Lin, C.H. and Chang, C.Y. (2007) Expression pattern of metallothionein, MTF-1 nuclear translocation, and its DNA-binding activity in zebrafish (Danio rerio) induced by zinc and cadmium. *Environmental Toxicology and Chemistry*, **26**, 110-117.

Chen, X.H., Hua, H.Q., Balamurugan, K., Kong, X.M., Zhang, L.M., George, G.N., Georgiev, O., Schaffner, W. and Giedroc, D.P. (2008) Copper sensing function

of Drosophila metal-responsive transcription factor-1 is mediated by a tetranuclear Cu(I) cluster. *Nucleic Acids Research*, **36**, 3128-3138.

Chinenov, Y.V. (2000) Cytochrome c oxidase assembly factors with a thioredoxin fold are conserved among prokaryotes and eukaryotes. *Journal of Molecular Medicine-Jmm*, **78**, 239-242.

Christodoulou, J., Danks, D.M., Sarkar, B., Baerlocher, K.E., Casey, R., Horn, N., Tumer, Z. and Clarke, J.T. (1998) Early treatment of Menkes disease with parenteral copper-histidine: long-term follow-up of four treated patients. *American Journal of Medical Genetics*, **76**, 154-164.

Cleland, W.W. (1964) Dithiothreitol, a New Protective Reagent for SH Groups. *Biochemistry*, **3**, 480-482.

Cobine, P.A., George, G.N., Jones, C.E., Wickramasinghe, W.A., Solioz, M. and Dameron, C.T. (2002) Copper transfer from the Cu(I) chaperone, CopZ, to the repressor, Zn(II)CopY: metal coordination environments and protein interactions. *Biochemistry*, **41**, 5822-5829.

Cobine, P.A., Ojeda, L.D., Rigby, K.M. and Winge, D.R. (2004) Yeast contain a non-proteinaceous pool of copper in the mitochondrial matrix. *Journal of Biological Chemistry*, **279**, 14447-14455.

Cobine, P.A., Pieffel, F. and Winge, D.R. (2006) Copper trafficking to the mitochondrion and assembly of copper metalloenzymes. *Biochimica et Biophysica Acta-Molecular Cell Research*, **1763**, 759-772.

Cornell, N.W. and Crivaro, K.E. (1972) Stability constant for the zinc-dithiothreitol complex. *Analytical Biochemistry*, **47**, 203-208.

Cramer, S.P., Tench, O., Yocum, M. and George, G.N. (1988) A 13-Element Ge Detector for Fluorescence EXAFS. *Nuclear Instruments & Methods in Physics Research Section a-Accelerators Spectrometers Detectors and Associated Equipment*, **266**, 586-591.

Dalton, T.P., Solis, W.A., Nebert, D.W. and Carvan, M.J. (2000) Characterization of the MTF-1 transcription factor from zebrafish and trout cells. *Comparative Biochemistry and Physiology B-Biochemistry & Molecular Biology*, **126**, 325-335.

Dance, I.G. (1986) The Structural Chemistry of Metal Thiolate Complexes. *Polyhedron*, **5**, 1037-1104.

Delley, B. (1990) An All-Electron Numerical-Method for Solving the Local Density Functional for Polyatomic-Molecules. *Journal of Chemical Physics*, **92**, 508-517.

Delley, B. (2000) From molecules to solids with the $DMol^3$ approach. *Journal of Chemical Physics*, **113**, 7756-7764.

Delley, B. (2006) The conductor-like screening model for polymers and surfaces. *Molecular Simulation*, **32**, 117-123.

De Feo, C.J., Aller, S.G., Siluvai, G.S., Blackburn, N.J. and Unger, V.M. (2009) Three-dimensional structure of the human copper transporter hCTR1. *Proceedings of the National Academy of Sciences of the United States of America*, **106**, 4237-4242.

De Feo, C.J., Aller, S.G. and Unger, V.M. (2007) A structural perspective on copper uptake in eukaryotes. *Biometals*, **20**, 705-716.

Dick, A.T. (1953) Influence of Inorganic Sulphate on the Copper-Molybdenum Interrelationship in Sheep. *Nature*, **172**, 637-638.

Dick, A.T. (1954) Studies on the Assimilation and Storage of Copper in Crossbred Sheep. *Australian Journal of Agricultural Research*, **5**, 511-544.

Dickinson, E.K., Adams, D.L., Schon, E.A. and Glerum, D.M. (2000) A human SCO2 mutation helps define the role of Sco1p in the cytochrome oxidase assembly pathway. *Journal of Biological Chemistry*, **275**, 26780-26785.

DiDonato, M., Hsu, H.F., Narindrasorasak, S., Que, L., Jr. and Sarkar, B. (2000) Copper-induced conformational changes in the N-terminal domain of the Wilson disease copper-transporting ATPase. *Biochemistry*, **39**, 1890-1896.

Dix, D.R., Bridgham, J.T., Broderius, M.A., Byersdorfer, C.A. and Eide, D.J. (1994) The FET4 gene encodes the low affinity Fe(II) transport protein of Saccharomyces cerevisiae. *Journal of Biological Chemistry*, **269**, 26092-26099.

Dumay, Q.C., Debut, A.J., Mansour, N.M. and Saier, M.H. (2006) The copper transporter (Ctr) family of Cu+ uptake systems. *Journal of Molecular Microbiology and Biotechnology*, **11**, 10-19.

Elder, F.R., Gurewitsch, A.M., Langmuir, R.V. and Pollock, H.C. (1947) Radiation from Electrons in a Synchrotron. *Physical Review*, **71**, 829-830.

Fan, B., Grass, G., Rensing, C. and Rosen, B.P. (2001) Escherichia coli CopA N-terminal CysX2Cys motifs are not required for copper resistance or transport. *Biochemical and Biophysical Research Communications*, **286**, 414-418.

Ferguson-Miller, S. and Babcock, G.T. (1996) Heme/Copper Terminal Oxidases. *Chemical Reviews*, **96**, 2889-2908.

Field, L.S., Furukawa, Y., O'Halloran, T.V. and Culotta, V.C. (2003) Factors controlling the uptake of yeast copper/zinc superoxide dismutase into mitochondria. *Journal of Biological Chemistry*, **278**, 28052-28059.

Fink, J.K., Hedera, P. and Brewer, G.J. (1999) Hepatolenticular degeneration (Wilson's disease). *Neurologist*, **5**, 171-185.

Franke, S., Grass, G., Rensing, C. and Nies, D.H. (2003) Molecular analysis of the copper-transporting efflux system CusCFBA of Escherichia coli. *Journal of Bacteriology*, **185**, 3804-3812.

Frisch, M.J., Trucks, G.W., Schlegel, H.B., Scuseria, G.E., Robb, M.A., Cheeseman, J.R., Montgomery, J., J. A., Vreven, T.K., K. N., Burant, J.C., Millam, J.M., Iyengar, S.S., Tomasi, J., Barone, V., Mennucci, B., Cossi, M., Scalmani, G., Rega, N., Petersson, G.A., Nakatsuji, H., Hada, M., Ehara, M., Toyota, K., Fukuda, R., Hasegawa, J., Ishida, M., Nakajima, T., Honda, Y., Kitao, O., Nakai, H., Klene, M., Li, X., Knox, J.E., Hratchian, H.P., Cross, J.B., Bakken, V., Adamo, C., Jaramillo, J., Gomperts, R., Stratmann, R.E., Yazyev, O., Austin, A.J., Cammi, R., Pomelli, C., Ochterski, J.W., Ayala, P.Y., Morokuma, K., Voth, G.A., Salvador, P., Dannenberg, J.J., Zakrzewski, V.G., Dapprich, S., Daniels, A.D., Strain, M.C., Farkas, O., Malick, D.K., Rabuck, A.D., Raghavachari, K., Foresman, J.B., Ortiz, J.V., Cui, Q., Baboul, A.G., Clifford, S., Cioslowski, J., Stefanov, B.B., Liu, G., Liashenko, A., Piskorz, P., Komaromi, I., Martin, R.L., Fox, D.J., Keith, T., Al-Laham, M.A., Peng, C.Y., Nanayakkara, A., Challacombe, M., Gill, P.M.W., Johnson, B., Chen, W., Wong, M.W., Gonzalez, C. and and Pople, J.A. (2004) *Gaussian 03, Revision C.02*. Gaussian Inc., Wallingford, CT.

Gaballa, A., Cao, M. and Helmann, J.D. (2003) Two MerR homologues that affect copper induction of the Bacillus subtilis copZA operon. *Microbiology*, **149**, 3413-3421.

Georgatsou, E., Mavrogiannis, L.A., Fragiadakis, G.S. and Alexandraki, D. (1997) The yeast Fre1p/Fre2p cupric reductases facilitate copper uptake and are regulated

by the copper-modulated Mac1p activator. *Journal of Biological Chemistry*, **272**, 13786-13792.

George, G.N. (1997) X-ray absorption spectroscopy of molybdenum enzymes. *Journal of Biological Inorganic Chemistry*, **2**, 790-796.

George, G.N., Byrd, J. and Winge, D.R. (1988) X-Ray Absorption Studies of Yeast Copper Metallothionein. *Journal of Biological Chemistry*, **263**, 8199-8203.

George, G.N., Hilton, J., Temple, C., Prince, R.C. and Rajagopalan, K.V. (1999) Structure of the molybdenum site of dimethyl sulfoxide reductase. *Journal of the American Chemical Society*, **121**, 1256-1266.

George, G.N. and Pickering, I.J. (2007) X-RAY Absorption Spectroscopy in Biology and Chemistry In *NATO Security through Science Series: Brilliant Light in Life and Material Sciences* (Tsakanov, V. and Wiedemann, H. *eds*.). Springer Netherlands, pp. 97-119.

George, G.N., Pickering, I.J., Doonan, C.J., Korbas, M., Singh, S.P. and Hoffmeyer, R. (2008) Inorganic molecular toxicology and chelation therapy of heavy metals and metalloids. *Advances in Molecular Toxicology*, **2**, 125-155.

George, G.N., Pickering, I.J., Harris, H.H., Gailer, J., Klein, D., Lichtmannegger, J. and Summer, K.H. (2003) Tetrathiomolybdate causes formation of hepatic copper-molybdenum clusters in an animal model of Wilson's disease. *Journal of the American Chemical Society*, **125**, 1704-1705.

George, G.N., Prince, R.C., Gailer, J., Buttigieg, G.A., Denton, M.B., Harris, H.H. and Pickering, I.J. (2004) Mercury binding to the chelation therapy agents DMSA and DMPS and the rational design of custom chelators for mercury. *Chemical Tesearch in Toxicology*, **17**, 999-1006.

Giedroc, D.P., Chen, X.H. and Apuy, J.L. (2001) Metal response element (MRE)-binding transcription factor-1 (MTF-1): Structure, function, and regulation. *Antioxidants & Redox Signaling*, **3**, 577-596.

Glerum, D.M., Shtanko, A. and Tzagoloff, A. (1996a) Characterization of COX17, a yeast gene involved in copper metabolism and assembly of cytochrome oxidase. *Journal of Biological Chemistry*, **271**, 14504-14509.

Glerum, D.M., Shtanko, A. and Tzagoloff, A. (1996b) SCO1 and SCO2 act as high copy suppressors of a mitochondrial copper recruitment defect Saccharomyces cerevisiae. *Journal of Biological Chemistry*, **271**, 20531-20535.

Gnonlonfoun, N., Filella, M. and Berthon, G. (1991) Lead (II)-dithiothreitol equilibria and their potential influence on lead inhibition of 5-aminolevulinic acid dehydratase in in vitro assays. *Journal of Inorganic Biochemistry*, **42**, 207-215.

Graden, J.A., Posewitz, M.C., Simon, J.R., George, G.N., Pickering, I.J. and Winge, D.R. (1996) Presence of a copper(I)-thiolate regulatory domain in the copper-activated transcription factor Amt1. *Biochemistry*, **35**, 14583-14589.

Gralla, E.B., Thiele, D.J., Silar, P. and Valentine, J.S. (1991) ACE1, a copper-dependent transcription factor, activates expression of the yeast copper, zinc superoxide dismutase gene. *Proceedings of the National Academy of Sciences of the United States of America*, **88**, 8558-8562.

Grass, G. and Rensing, C. (2001) CueO is a multi-copper oxidase that confers copper tolerance in *Escherichia coli*. *Biochemical and Biophysical Research Communications*, **286**, 902-908.

Grassetti, D.R. and Murray, J.F. (1967) Determination of Sulfhydryl Groups with 2,2'- or 4,4'-Dithiodipyridine. *Archives of Biochemistry and Biophysics*, **119**, 41-49.

Grotz, N. and Guerinot, M.L. (2006) Molecular aspects of Cu, Fe and Zn homeostasis in plants. *Biochimica et Biophysica Acta*, **1763**, 595-608.

Gunnarsson, O. and Lundqvist, B.I. (1976) Exchange and Correlation in Atoms, Molecules, and Solids by Spin-Density Functional Formalism. *Physical Review B*, **13**, 4274-4298.

Halliwell, B. and Gutteridge, J.M.C. (1992) Biologically Relevant Metal Ion-Dependent Hydroxyl Radical Generation - an Update. *FEBS Letters*, **307**, 108-112.

Hamza, I. and Gitlin, J.D. (2002) Copper chaperones for cytochrome c oxidase and human disease. *Journal of Bioenergetics and Biomembranes*, **34**, 381-388.

Harris, H.H., George, G.N. and Rajagopalan, K.V. (2006) High-resolution EXAFS of the active site of human sulfite oxidase: Comparison with density functional theory and X-ray crystallographic results. *Inorganic Chemistry*, **45**, 493-495.

Harrison, M.D. and Dameron, C.T. (1999) Molecular mechanisms of copper metabolism and the role of the Menkes disease protein. *Journal of Biochemical and Molecular Toxicology*, **13**, 93-106.

Harrison, M.D., Jones, C.E., Solioz, M. and Dameron, C.T. (2000) Intracellular copper routing: the role of copper chaperones. *Trends in biochemical Sciences*, **25**, 29-32.

Hartmann, H.J., Morpurgo, L., Desideri, A., Rotilio, G. and Weser, U. (1983) Reconstitution of Stellacyanin as a Case of Direct Cu(I) Transfer between Yeast Copper Thionein and Blue Copper Apoprotein. *FEBS Letters*, **152**, 94-96.

Hassett, R., Dix, D.R., Eide, D.J. and Kosman, D.J. (2000) The Fe(II) permease Fet4p functions as a low affinity copper transporter and supports normal copper

trafficking in Saccharomyces cerevisiae. *Biochemical Journal*, **351 Pt 2**, 477-484.

Hassett, R. and Kosman, D.J. (1995) Evidence for Cu(II) reduction as a component of copper uptake by *Saccharomyces cerevisiae*. *Journal of Biological Chemistry*, **270**, 128-134.

Haywood, S., Dincer, Z., Jasani, B. and Loughran, M.J. (2004) Molybdenum-associated pituitary endocrinopathy in sheep treated with ammonium tetrathiomolybdate. *Journal of Comparative Pathology*, **130**, 21-31.

Heaton, D., Nittis, T., Srinivasan, C. and Winge, D.R. (2000) Mutational analysis of the mitochondrial copper metallochaperone Cox17. *Journal of Biological Chemistry*, **275**, 37582-37587.

Heaton, D.N., George, G.N., Garrison, G. and Winge, D.R. (2001) The mitochondrial copper metallochaperone Cox17 exists as an oligomeric, polycopper complex. *Biochemistry*, **40**, 743-751.

Hess, B., Bekker, H., Berendsen, H.J.C. and Fraaije, J. (1997) LINCS: A linear constraint solver for molecular simulations. *Journal of Computational Chemistry*, **18**, 1463-1472.

Hiser, L., Di Valentin, M., Hamer, A.G. and Hosler, J.P. (2000) Cox11p is required for stable formation of the Cu(B) and magnesium centers of cytochrome c oxidase. *Journal of Biological Chemistry*, **275**, 619-623.

Hohenberg, P. and Kohn, W. (1964) Inhomogeneous Electron Gas. *Physical Review B*, **136**, B864-B871.

Holt, B.T.O. and Merz, K.M. (2007) Insights into Cu(I) exchange in HAH1 using quantum mechanical and molecular simulations. *Biochemistry*, **46**, 8816-8826.

Horng, Y.C., Cobine, P.A., Maxfield, A.B., Carr, H.S. and Winge, D.R. (2004) Specific copper transfer from the Cox17 metallochaperone to both Sco1 and Cox11 in the assembly of yeast cytochrome c oxidase. *Journal of Biological Chemistry*, **279**, 35334-35340.

Horng, Y.C., Leary, S.C., Cobine, P.A., Young, F.B., George, G.N., Shoubridge, E.A. and Winge, D.R. (2005) Human Sco1 and Sco2 function as copper-binding proteins. *Journal of Biological chemistry*, **280**, 34113-34122.

Humphrey, W., Dalke, A. and Schulten, K. (1996) VMD: Visual molecular dynamics. *Journal of Molecular Graphics*, **14**, 33-38.

Iino, T., Ohashi, K., Inoue, K., Judai, K., Nishi, N. and Sekiya, H. (2007) Infrared spectroscopy of $Cu^{+}(H2O)_{n}$ and $Ag^{+}(H2O)_{n}$: Coordination and solvation of noble-metal ions. *Journal of Chemical Physics*, **126**.

Jensen, L.T., Peltier, J.M. and Winge, D.R. (1998) Identification of a four copper folding intermediate in mammalian copper metallothionein by electrospray ionization mass spectrometry. *Journal of Biological Inorganic Chemistry*, **3**, 627-631.

Jensen, L.T. and Winge, D.R. (1998) Identification of a copper-induced intramolecular interaction in the transcription factor Mac1 from Saccharomyces cerevisiae. *EMBO Journal*, **17**, 5400-5408.

Jiang, D.T., Chen, N. and Sheng, W. (2007) CLS 06ID-1: A Wiggler-based Hard X-ray Spectroscopy Beamline. In *SYNCHROTRON RADIATION INSTRUMENTATION: Ninth International Conference on Synchrotron Radiation Instrumentation* (Choi, J.Y. and Rah, S. *eds.*), Daegu, Korea, Vol. 879, pp. 800-803.

Jorgensen, W.L., Maxwell, D.S. and TiradoRives, J. (1996) Development and testing of the OPLS all-atom force field on conformational energetics and properties of organic liquids. *Journal of the American Chemical Society*, **118**, 11225-11236.

Kabsch, W. and Sander, C. (1983) Dictionary of Protein Secondary Structure - Pattern-Recognition of Hydrogen-Bonded and Geometrical Features. *Biopolymers*, **22**, 2577-2637.

Kadenbach, B. and Merle, P. (1981) On the Function of Multiple Subunits of Cytochrome-C Oxidase from Higher Eukaryotes. *FEBS Letters*, **135**, 1-11.

Kagi, J.H. (1991) Overview of metallothionein. *Methods in Enzymology*, **205**, 613-626.

Kaminski, G., Duffy, E.M., Matsui, T. and Jorgensen, W.L. (1994) Free-Energies of Hydration and Pure Liquid Properties of Hydrocarbons from the Opls All-Atom Model. *Journal of Physical Chemistry*, **98**, 13077-13082.

Karplus, M. and McCammon, J.A. (2002) Molecular dynamics simulations of biomolecules. *Nature Structural Biology*, **9**, 646-652.

Kau, L.S., Spirasolomon, D.J., Pennerhahn, J.E., Hodgson, K.O. and Solomon, E.I. (1987) X-Ray Absorption-Edge Determination of the Oxidation-State and Coordination-Number of Copper - Application to the Type-3 Site in Rhus-Vernicifera Laccase and Its Reaction with Oxygen. *Journal of the American Chemical Society*, **109**, 6433-6442.

Khalimonchuk, O., Ostermann, K. and Rodel, G. (2005) Evidence for the association of yeast mitochondrial ribosomes with Cox11p, a protein required for the Cu(B) site formation of cytochrome c oxidase. *Current Genetics*, **47**, 223-233.

Klamt, A. and Schuurmann, G. (1993) Cosmo - a New Approach to Dielectric Screening in Solvents with Explicit Expressions for the Screening Energy and Its Gradient. *Journal of the Chemical Society-Perkin Transactions 2*, 799-805.

Klein, D., Arora, U., Lichtmannegger, J., Finckh, M., Heinzmann, U. and Summer, K.H. (2004) Tetrathiomolybdate in the treatment of acute hepatitis in an animal model for Wilson disease. *Journal of Hepatology*, **40**, 409-416.

Kohn, W. and Sham, L.J. (1965) Self-Consistent Equations Including Exchange and Correlation Effects. *Physical Review*, **140**, A1133-A1138.

Komatsu, Y., Sadakata, I., Ogra, Y. and Suzuki, K.T. (2000) Excretion of copper complexed with thiomolybdate into the bile and blood in LEC rats. *Chemico-Biological Interactions*, **124**, 217-231.

Koradi, R., Billeter, M. and Wuthrich, K. (1996) MOLMOL: A program for display and analysis of macromolecular structures. *Journal of Molecular Graphics*, **14**, 51-55.

Krezel, A., Lesniak, W., Jezowska-Bojczuk, M., Mlynarz, P., Brasun, J., Kozlowski, H. and Bal, W. (2001) Coordination of heavy metals by dithiothreitol, a commonly used thiol group protectant. *Journal of Inorganic Biochemistry*, **84**, 77-88.

Kuper, J., Llamas, A., Hecht, H.J., Mendel, R.R. and Schwarz, G. (2004) Structure of the molybdopterin-bound Cnx1G domain links molybdenum and copper metabolism. *Nature*, **430**, 803-806.

Laity, J.H. and Andrews, G.K. (2007) Understanding the mechanisms of zinc-sensing by metal-response element binding transcription factor-1 (MTF-1). *Archives of Biochemistry and Biophysics*, **463**, 201-210.

Lamb, A.L., Torres, A.S., O'Halloran, T.V. and Rosenzweig, A.C. (2000) Heterodimer formation between superoxide dismutase and its copper chaperone. *Biochemistry*, **39**, 14720-14727.

Lamb, A.L., Torres, A.S., O'Halloran, T.V. and Rosenzweig, A.C. (2001) Heterodimeric structure of superoxide dismutase in complex with its metallochaperone. *Nature Structural Biology*, **8**, 751-755.

Lang, N.D. and Williams, A.R. (1978) Theory of Atomic Chemisorption on Simple Metals. *Physical Review B*, **18**, 616-636.

Laurie, S.H. (2000) Thiomolybdates - Simple but very versatile reagents. *European Journal of Inorganic Chemistry*, 2443-2450.

Leary, S.C., Kaufman, B.A., Pellecchia, G., Guercin, G.H., Mattman, A., Jaksch, M. and Shoubridge, E.A. (2004) Human SCO1 and SCO2 have independent, cooperative functions in copper delivery to cytochrome c oxidase. *Human Molecular Genetics*, **13**, 1839-1848.

Lee, J., Li, Z.H., Brower-Sinning, R. and John, B. (2007) Regulatory circuit of human microRNA biogenesis. *Plos Computational Biology*, **3**, 721-732.

Lee, J., Pena, M.M.O., Nose, Y. and Thiele, D.J. (2002a) Biochemical characterization of the human copper transporter Ctr1. *Journal of Biological Chemistry*, **277**, 4380-4387.

Lee, J., Petris, M.J. and Thiele, D.J. (2002b) Characterization of mouse embryonic cells deficient in the ctr1 high affinity copper transporter. Identification of a Ctr1-independent copper transport system. *Journal of Biological Chemistry*, **277**, 40253-40259.

Lee, P.A. and Beni, G. (1977) New Method for Calculation of Atomic Phase-Shifts - Application to Extended X-Ray Absorption Fine-Structure (Exafs) in Molecules and Crystals. *Physical Review B*, **15**, 2862-2883.

Lee, P.A., Citrin, P.H., Eisenberger, P. and Kincaid, B.M. (1981) Extended X-Ray Absorption Fine-Structure - Its Strengths and Limitations as a Structural Tool. *Reviews of Modern Physics*, **53**, 769-806.

Lee, T.C., Ho, I.C., Lu, W.J. and Huang, J.D. (2006a) Enhanced expression of multidrug resistance-associated protein 2 and reduced expression of aquaglyceroporin 3 in an arsenic-resistant human cell line. *Journal of Biological Chemistry*, **281**, 18401-18407.

Lee, Y., Sarjeant, A.A.N. and Karlin, K.D. (2006b) A molecular pinwheel multicopper(I) cluster, $[L^{S-})_6Cu^{I}_{13}(S^{2-})_2]^{3+}$ with m_4-sulfido, m_3-thiolato and nitrogen ligands. *Chemical Communications*, 621-623.

Levitt, M. and Sharon, R. (1988) Accurate Simulation of Protein Dynamics in Solution. *Proceedings of the National Academy of Sciences of the United States of America*, **85**, 7557-7561.

Li, Y., Togashi, Y., Sato, S., Emoto, T., Kang, J.H., Takeichi, N., Kobayashi, H., Kojima, Y., Une, Y. and Uchino, J. (1991) Spontaneous hepatic copper accumulation in Long-Evans Cinnamon rats with hereditary hepatitis. A model of Wilson's disease. *Journal of Clinical Investigation*, **87**, 1858-1861.

Lichtlen, P. and Schaffner, W. (2001) Putting its fingers on stressful situations: the heavy metal-regulatory transcription factor MTF-1. *Bioessays*, **23**, 1010-1017.

Lim, J. and Vachet, R.W. (2003) Development of a methodology based on metal-catalyzed oxidation reactions and mass spectrometry to determine the metal binding sites in copper metalloproteins. *Analytical Chemistry*, **75**, 1164-1172.

Lin, S.J. and Culotta, V.C. (1995) The Atx1 Gene of Saccharomyces-Cerevisiae Encodes a Small Metal Homeostasis Factor That Protects Cells against Reactive Oxygen-Toxicity. *Proceedings of the National Academy of Sciences of the United States of America*, **92**, 3784-3788.

Lindahl, E., Hess, B. and van der Spoel, D. (2001) GROMACS 3.0: a package for molecular simulation and trajectory analysis. *Journal of Molecular Modeling*, **7**, 306-317.

Lipkowitz, K.B. and Boyd, D.B. (2000). Reviews in Computational Chemistry. Wiley-Vch, Inc, New York.

Liu, T., Ramesh, A., Ma, Z., Ward, S.K., Zhang, L.M., George, G.N., Talaat, A.M., Sacchettini, J.C. and Giedroc, D.P. (2007) CsoR is a novel Mycobacterium tuberculosis copper-sensing transcriptional regulator. *Nature Chemical Biology*, **3**, 60-68.

Loftin, I.R., Franke, S., Blackburn, N.J. and McEvoy, M.M. (2007) Unusual Cu(I)/Ag(I) coordination of Escherichia coli CusF as revealed by atomic resolution crystallography and X-ray absorption spectroscopy. *Protein Science*, **16**, 2287-2293.

Loudianos, G. and Gitlin, J.D. (2000) Wilson's disease. *Seminars in Liver Disease*, **20**, 353-364.

Lubben, M., Portmann, R., Kock, G., Stoll, R., Young, M.M. and Solioz, M. (2009) Structural model of the CopA copper ATPase of Enterococcus hirae based on chemical cross-linking. *Biometals*, **22**, 363-375.

Lutkenhaus, J.F. (1977) Role of a major outer membrane protein in Escherichia coli. *Journal of Bacteriology*, **131**, 631-637.

Lutsenko, S., Barnes, N.L., Bartee, M.Y. and Dmitriev, O.Y. (2007) Function and regulation of human copper-transporting ATPases. *Physiological Reviews*, **87**, 1011-1046.

Lutsenko, S., Petrukhin, K., Cooper, M.J., Gilliam, C.T. and Kaplan, J.H. (1997) N-terminal domains of human copper-transporting adenosine triphosphatases (the Wilson's and Menkes disease proteins) bind copper selectively in vivo and in vitro with stoichiometry of one copper per metal-binding repeat. *Journal of Biological Chemistry*, **272**, 18939-18944.

Lytle, F.E. (1970) Solution Luminescence of Metal Complexes. *Applied Spectroscopy*, **24**, 319-326.

Macgillavry, C.H. and Rieck, G.D. (1962) International Tables for X-Ray Crystallography,Vol.III: Physical and Chemical Tables. The Kynoch Press, Birmingham,England.

Mandal, A.K., Cheung, W.D. and Arguello, J.M. (2002) Characterization of a thermophilic P-type Ag^{+}/Cu^{+}-ATPase from the extremophile Archaeoglobus fulgidus. *Journal of Biological Chemistry*, **277**, 7201-7208.

Maruyama, M., Yamamoto, T., Kohara, Y., Katsuragi, Y., Mishima, Y., Aoyagi, Y. and Kominami, R. (2007) Mtf-1 lymphoma-susceptibility locus affects retention of large thymocytes with high ROS levels in mice after gamma-irradiation. *Biochemical and Biophysical Research Communications*, **354**, 209-215.

Mason, J., Lamand, M., Tressol, J.C. and Mulryan, G. (1988) Studies of the Changes in Systemic Copper-Metabolism and Excretion Produced by the Intravenous Administration of Trithiomolybdate in Sheep. *British Journal of Nutrition*, **59**, 289-300.

Maur, A.A.D., Belser, T., Elgar, G., Georgiev, O. and Schaffner, W. (1999) Characterization of the transcription factor MTF-1 from the Japanese pufferfish (Fugu rubripes) reveals evolutionary conservation of heavy metal stress response. *Biological Chemistry*, **380**, 175-185.

Maur, A.A.D., Belser, T., Wang, Y., Gunes, C., Lichtlen, P., Georgiev, O. and Schaffner, W. (2000) Characterization of the mouse gene for the heavy metal-responsive transcription factor MTF-1. *Cell Stress & Chaperones*, **5**, 196-206.

Maxfield, A.B., Heaton, D.N. and Winge, D.R. (2004) Cox17 is functional when tethered to the mitochondrial inner membrane. *Journal of Biological Chemistry*, **279**, 5072-5080.

McCammon, J.A., Gelin, B.R. and Karplus, M. (1977) Dynamics of folded proteins. *Nature*, **267**, 585-590.

McWeeny, R. (1960) Some Recent Advances in Density Matrix Theory. *Reviews of Modern Physics*, **32**, 335-369.

Melchers, K., Weitzenegger, T., Buhmann, A., Steinhilber, W., Sachs, G. and Schafer, K.P. (1996) Cloning and membrane topology of a P type ATPase from Helicobacter pylori. *Journal of Biological Chemistry*, **271**, 446-457.

Mercer, J.F., Livingston, J., Hall, B., Paynter, J.A., Begy, C., Chandrasekharappa, S., Lockhart, P., Grimes, A., Bhave, M., Siemieniak, D. and et al. (1993) Isolation of a partial candidate gene for Menkes disease by positional cloning. *Nature Genetics*, **3**, 20-25.

Mercer, J.F.B. (2001) The molecular basis of copper-transport diseases. *Trends in Molecular Medicine*, **7**, 64-69.

Miyamoto, S. and Kollman, P.A. (1992) Settle - an Analytical Version of the Shake and Rattle Algorithm for Rigid Water Models. *Journal of Computational Chemistry*, **13**, 952-962.

Muller, H.P., Brugnera, E., Georgiev, O., Badzong, M., Muller, K.H. and Schaffner, W. (1995) Analysis of the heavy metal-responsive transcription factor MTF-1 from human and mouse. *Somatic Cell and Molecular Genetics*, **21**, 289-297.

Munson, G.P., Lam, D.L., Outten, F.W. and O'Halloran, T.V. (2000) Identification of a copper-responsive two-component system on the chromosome of Escherichia coli K-12. *Journal of Bacteriology*, **182**, 5864-5871.

Murphy, B.J. (2004) Regulation of malignant progression by the hypoxia-sensitive transcription factors HIF-1 alpha and MTF-1. *Comparative Biochemistry and Physiology B-Biochemistry & Molecular Biology*, **139**, 495-507.

Murphy, B.J., Sato, B.G., Dalton, T.P. and Laderoute, K.R. (2005) The metal-responsive transcription factor-1 contributes to HIF-1 activation during hypoxic stress. *Biochemical and Biophysical Research Communications*, **337**, 860-867.

Nittis, T., George, G.N. and Winge, D.R. (2001) Yeast Sco1, a protein essential for cytochrome c oxidase function is a Cu(I)-binding protein. *Journal of Biological Chemistry*, **276**, 42520-42526.

Nobrega, M.P., Bandeira, S.C., Beers, J. and Tzagoloff, A. (2002) Characterization of COX19, a widely distributed gene required for expression of mitochondrial cytochrome oxidase. *Journal of Biological Chemistry*, **277**, 40206-40211.

O'Halloran, T.V. and Culotta, V.C. (2000) Metallochaperones, an intracellular shuttle service for metal ions. *Journal of Biological Chemistry*, **275**, 25057-25060.

Odermatt, A., Krapf, R. and Solioz, M. (1994) Induction of the putative copper ATPases, CopA and CopB, of Enterococcus hirae by Ag+ and Cu2+, and Ag+ extrusion by CopB. *Biochemical and Biophysical Research Communications*, **202**, 44-48.

Odermatt, A., Suter, H., Krapf, R. and Solioz, M. (1993) Primary structure of two P-type ATPases involved in copper homeostasis in Enterococcus hirae. *Journal of Biological Chemistry*, **268**, 12775-12779.

Ogra, Y., Chikusa, H. and Suzuki, K.T. (2000) Metabolic fate of the insoluble copper/tetrathiomolybdate complex formed in the liver of LEC rats with excess tetrathiomolybdate. *Journal of Inorganic Biochemistry*, **78**, 123-128.

Ogra, Y., Ohmichi, M. and Suzuki, K.T. (1996) Mechanisms of selective copper removal by tetrathiomolybdate from metallothionein in LEC rats. *Toxicology*, **106**, 75-83.

Ooi, C.E., Rabinovich, E., Dancis, A., Bonifacino, J.S. and Klausner, R.D. (1996) Copper-dependent degradation of the Saccharomyces cerevisiae plasma membrane copper transporter Ctr1p in the apparent absence of endocytosis. *EMBO Journal*, **15**, 3515-3523.

Outten, F.W., Huffman, D.L., Hale, J.A. and O'Halloran, T.V. (2001) The independent cue and cus systems confer copper tolerance during aerobic and anaerobic growth in Escherichia coli. *Journal of Biological Chemistry*, **276**, 30670-30677.

Outten, F.W., Outten, C.E., Hale, J. and O'Halloran, T.V. (2000) Transcriptional activation of an Escherichia coli copper efflux regulon by the chromosomal MerR homologue, cueR. *Journal of Biological Chemistry*, **275**, 31024-31029.

Palmer, A.G. (2001) NMR probes of molecular dynamics: Overview and comparison with other techniques. *Annual Review of Biophysics and Biomolecular Structure*, **30**, 129-155.

Palmiter, R.D. (1998) The elusive function of metallothioneins. *Proceedings of the National Academy of Sciences of the United States of America*, **95**, 8428-8430.

Palumaa, P., Kangur, L., Voronova, A. and Sillard, R. (2004) Metal-binding mechanism of Cox17, a copper chaperone for cytochrome c oxidase. *Biochemical Journal*, **382**, 307-314.

Perdew, J.P. and Wang, Y. (1992) Accurate and Simple Analytic Representation of the Electron-Gas Correlation-Energy. *Physical Review B*, **45**, 13244-13249.

Petris, M.J. (2004) The SLC31 (Ctr) copper transporter family. *Pflugers Archiv-European Journal of Physiology*, **447**, 752-755.

Petris, M.J., Mercer, J.F., Culvenor, J.G., Lockhart, P., Gleeson, P.A. and Camakaris, J. (1996) Ligand-regulated transport of the Menkes copper P-type ATPase efflux pump from the Golgi apparatus to the plasma membrane: a novel mechanism of regulated trafficking. *EMBO Journal*, **15**, 6084-6095.

Petris, M.J., Smith, K., Lee, J. and Thiele, D.J. (2003) Copper-stimulated endocytosis and degradation of the human copper transporter, hCtr1. *Journal of Biological Chemistry*, **278**, 9639-9646.

Petrukhin, K., Fischer, S.G., Pirastu, M., Tanzi, R.E., Chernov, I., Devoto, M., Brzustowicz, L.M., Cayanis, E., Vitale, E., Russo, J.J., Matseoane, D., Boukhgalter, B., Wasco, W., Figus, A.L., Loudianos, J., Cao, A., Sternlieb, I., Evgrafov, O., Parano, E., Pavone, L., Warburton, D., Ott, J., Penchaszadeh, G.K., Scheinberg, I.H. and Gilliam, T.C. (1993) Mapping, Cloning and Genetic-

Characterization of the Region Containing the Wilson Disease Gene. *Nature Genetics*, **5**, 338-343.

Pfeiffer, R.F. (2007) Wilson's disease. *Seminars in Neurology*, **27**, 123-132.

Pickering, I.J. and George, G.N. (2007) X-Ray Absorption Spectroscopy Imaging of Biological Tissues. In *AIP Conference Proceedings* (*X-RAY ABSORPTION FINE STRUCTURE - XAFS13: 13th International Conference*), Vol. 882, pp. 311-315.

Pickering, I.J., George, G.N., Dameron, C.T., Kurz, B., Winge, D.R. and Dance, I.G. (1993) X-Ray-Absorption Spectroscopy of Cuprous Thiolate Clusters in Proteins and Model Systems. *Journal of the American Chemical Society*, **115**, 9498-9505.

Pickering, I.J., Prince, R.C., Salt, D.E. and George, G.N. (2000) Quantitative, chemically specific imaging of selenium transformation in plants. *Proceedings of the National Academy of Sciences of the United States of America*, **97**, 10717-10722.

Po, H.N., Legg, K.D. and Kuwahara, S.S. (1973) Characterization of Some Metal-Ion Dithiothreitolates and Dithioerythriotolates. *Analytical Letters*, **6**, 659-665.

Poger, D., Fuchs, J.F., Nedev, H., Ferrand, M. and Crouzy, S. (2005) Molecular dynamics study of the metallochaperone Hah1 in its apo and Cu(I)-loaded states: Role of the conserved residue M10. *FEBS Letters*, **579**, 5287-5292.

Portnoy, M.E., Schmidt, P.J., Rogers, R.S. and Culotta, V.C. (2001) Metal transporters that contribute copper to metallochaperones in *Saccharomyces cerevisiae*. *Molecular Genetics and Genomics*, **265**, 873-882.

Prohaska, J.R. and Gybina, A.A. (2004) Intracellular copper transport in mammals. *Journal of Nutrition*, **134**, 1003-1006.

Pufahl, R.A., Singer, C.P., Peariso, K.L., Lin, S.J., Schmidt, P.J., Fahrni, C.J., Culotta, V.C., PennerHahn, J.E. and Ohalloran, T.V. (1997) Metal ion chaperone function of the soluble Cu(I) receptor Atx1. *Science*, **278**, 853-856.

Puig, S., Lee, J., Lau, M. and Thiele, D.J. (2002) Biochemical and genetic analyses of yeast and human high affinity copper transporters suggest a conserved mechanism for copper uptake. *Journal of Biological Chemistry*, **277**, 26021-26030.

Rae, T.D., Schmidt, P.J., Pufahl, R.A., Culotta, V.C. and O'Halloran, T.V. (1999) Undetectable intracellular free copper: The requirement of a copper chaperone for superoxide dismutase. *Science*, **284**, 805-808.

Ralle, M., Berry, S.M., Nilges, M.J., Gieselman, M.D., van der Donk, W.A., Lu, Y. and Blackburn, N.J. (2004) The selenocysteine-substituted blue copper center: spectroscopic investigations of Cys112SeCys Pseudomonas aeruginosa azurin. *Journal of the American Chemical Society*, **126**, 7244-7256.

Ralle, M., Lutsenko, S. and Blackburn, N.J. (2003) X-ray absorption spectroscopy of the copper chaperone HAH1 reveals a linear two-coordinate Cu(I) center capable of adduct formation with exogenous thiols and phosphines. *Journal of Biological Chemistry*, **278**, 23163-23170.

Rees, E.M., Lee, J. and Thiele, D.J. (2004) Mobilization of intracellular copper stores by the ctr2 vacuolar copper transporter. *Journal of Biological Chemistry*, **279**, 54221-54229.

Rees, E.M. and Thiele, D.J. (2004) From aging to virulence: forging connections through the study of copper homeostasis in eukaryotic microorganisms. *Current Opinion in Microbiology*, **7**, 175-184.

Rehr, J.J. and Albers, R.C. (2000) Theoretical approaches to x-ray absorption fine structure. *Reviews of Modern Physics*, **72**, 621-654.

Rehr, J.J., Deleon, J.M., Zabinsky, S.I. and Albers, R.C. (1991) Theoretical X-Ray Absorption Fine-Structure Standards. *Journal of the American Chemical Society*, **113**, 5135-5140.

Rensing, C., Fan, B., Sharma, R., Mitra, B. and Rosen, B.P. (2000) CopA: An Escherichia coli Cu(I)-translocating P-type ATPase. *Proceedings of the National Academy of Sciences of the United States of America*, **97**, 652-656.

Rensing, C., Ghosh, M. and Rosen, B.P. (1999) Families of soft-metal-ion-transporting ATPases. *Journal of Bacteriology*, **181**, 5891-5897.

Rensing, C. and Grass, G. (2003) Escherichia coli mechanisms of copper homeostasis in a changing environment. *FEMS Microbiology Reviews*, **27**, 197-213.

Rentzsch, A., Krummeck-Weiss, G., Hofer, A., Bartuschka, A., Ostermann, K. and Rodel, G. (1999) Mitochondrial copper metabolism in yeast: mutational analysis of Sco1p involved in the biogenesis of cytochrome c oxidase. *Current Genetics*, **35**, 103-108.

Rigby, K., Cobine, P.A., Khalimonchuk, O. and Winge, D.R. (2008) Mapping the functional interaction of Sco1 and Cox2 in cytochrome oxidase biogenesis. *Journal of Biological Chemistry*, **283**, 15015-15022.

Rigby, K., Zhang, L.M., Cobine, P.A., George, G.N. and Winge, D.R. (2007) Characterization of the cytochrome c oxidase assembly factor Cox19 of Saccharomyces cerevisiae. *Journal of Biological Chemistry*, **282**, 10233-10242.

Rodriguez-Granillo, A. and Wittung-Stafshede, P. (2009) Differential Roles of Met10, Thr11, and Lys60 in Structural Dynamics of Human Copper Chaperone Atox1. *Biochemistry*, **48**, 960-972

Roelofsen, H., Wolters, H., Van Luyn, M.J.A., Miura, N., Kuipers, F. and Vonk, R.J. (2000) Copper-induced apical trafficking of ATP7B in polarized hepatoma cells provides a mechanism for biliary copper excretion. *Gastroenterology*, **119**, 782-793.

Ross, M.H. and Pawlina, W. (2006) Urinary System. In *Histology: a text and atlas with correlated cell and molecular biology* (Ajello, J.P. *ed.*,). Lippincott Williams & Wilkins, pp. 646-685.

Saito, T., Itoh, T., Fujimura, M. and Saito, K. (1995) Age-dependent and region-specific differences in the distribution of trace elements in 7 brain regions of Long-Evans Cinnamon (LEC) rats with hereditary abnormal copper metabolism. *Brain Research*, **695**, 240-244.

Saveanu, C., Fromont-Racine, M., Harington, A., Ricard, F., Namane, A. and Jacquier, A. (2001) Identification of 12 new yeast mitochondrial ribosomal proteins including 6 that have no prokaryotic homologues. *Journal of Biological Chemistry*, **276**, 15861-15867.

Sax, A.F. (2008) Computational chemistry techniques: covering orders of magnitude in space, time, and accuracy. *Monatshefte für Chemie*, **139**, 299-308.

Saydam, N., Georgiev, O., Nakano, M.Y., Greber, U.F. and Schaffner, W. (2001) Nucleo-cytoplasmic trafficking of metal-regulatory transcription factor 1 is

regulated by diverse stress signals. *Journal of Biological Chemistry*, **276**, 25487-25495.

Sayers, D.E., Stern, E.A. and Lytle, F.W. (1971) New Technique for Investigating Noncrystalline Structures: Fourier Analysis of the Extended X-Ray — Absorption Fine Structure. *Physical Review Letters*, **27**, 1204.

Schaefer, M., Hopkins, R.G., Failla, M.L. and Gitlin, J.D. (1999) Hepatocyte-specific localization and copper-dependent trafficking of the Wilson's disease protein in the liver. *American Journal of Physiology*, **276**, G639-646.

Schmidt, P.J., Kunst, C. and Culotta, V.C. (2000) Copper activation of superoxide dismutase 1 (SOD1) in vivo. Role for protein-protein interactions with the copper chaperone for SOD1. *Journal of Biological Chemistry*, **275**, 33771-33776.

Schmidt, P.J., Ramos-Gomez, M. and Culotta, V.C. (1999) A gain of superoxide dismutase (SOD) activity obtained with CCS, the copper metallochaperone for SOD1. *Journal of Biological Chemistry*, **274**, 36952-36956.

Selvaraj, A., Balamurugan, K., Yepiskoposyan, H., Zhou, H., Egli, D., Georgiev, O., Thiele, D.J. and Schaffner, W. (2005) Metal-responsive transcription factor (MTF-1) handles both extremes, copper load and copper starvation, by activating different genes. *Genes & Development*, **19**, 891-896.

Singleton, C. and Le Brun, N.E. (2009) The N-terminal soluble domains of Bacillus subtilis CopA exhibit a high affinity and capacity for Cu(I) ions. *Dalton Transactions*, 688-696.

Smaldone, G.T. and Helmann, J.D. (2007) CsoR regulates the copper efflux operon copZA in Bacillus subtilis. *Microbiology-Sgm*, **153**, 4123-4128.

Solioz, M. and Odermatt, A. (1995) Copper and silver transport by CopB-ATPase in membrane vesicles of Enterococcus hirae. *Journal of Biological Chemistry*, **270**, 9217-9221.

Solioz, M. and Stoyanov, J.V. (2003) Copper homeostasis in Enterococcus hirae. *FEMS Microbiology Reviews*, **27**, 183-195.

Somogyi, R. and Greller, L.D. (2001) The dynamics of molecular networks: applications to therapeutic discovery. *Drug Discovery Today*, **6**, 1267-1277.

Srinivasan, C., Posewitz, M.C., George, G.N. and Winge, D.R. (1998) Characterization of the copper chaperone Cox17 of Saccharomyces cerevisiae. *Biochemistry*, **37**, 7572-7577.

Stasser, J.P., Eisses, J.F., Barry, A.N., Kaplan, J.H. and Blackburn, N.J. (2005) Cysteine-to-serine mutants of the human copper chaperone for superoxide dismutase reveal a copper cluster at a domain III dimer interface. *Biochemistry*, **44**, 3143-3152.

Stasser, J.P., Siluvai, G.S., Barry, A.N. and Blackburn, N.J. (2007) A multinuclear copper(I) cluster forms the dimerization interface in copper-loaded human copper chaperone for superoxide dismutase. *Biochemistry*, **46**, 11845-11856.

Stern, E.A. and Heald, S.M. (1983) Basic Principles and Applications of EXAFS. In Koch, E.E. (ed.), *Handbook of Synchrotron Radiation*. North-Holland Publishing Co., Vol. 1, pp. 995-1014.

Stewart, J., Farmer, V.C. and Mitchell, R.L. (1946) Molybdenum and Copper Metabolism of Farm Animals. *Nature*, **157**, 442-442.

Stiburek, L., Hansikova, H., Tesarova, M., Cerna, L. and Zeman, J. (2006) Biogenesis of eukaryotic cytochrome c oxidase. *Physiological Research*, **55**, S27-S41.

Stoyanov, J.V., Hobman, J.L. and Brown, N.L. (2001) CueR (YbbI) of Escherichia coli is a MerR family regulator controlling expression of the copper exporter CopA. *Molecular Microbiology*, **39**, 502-511.

Strausak, D. and Solioz, M. (1997) CopY is a copper-inducible repressor of the Enterococcus hirae copper ATPases. *Journal of Biological Chemistry*, **272**, 8932-8936.

Sugawara, N., Ikeda, T., Sugawara, C., Kohgo, Y., Kato, J. and Takeichi, N. (1992) Regional Distribution of Copper, Zinc and Iron in the Brain in Long-Evans Cinnamon (LEC) Rats with a New Mutation Causing Hereditary Hepatitis. *Brain Research*, **588**, 287-290.

Suzuki, K.T., Yamamoto, K., Kanno, S., Aoki, Y. and Takeichi, N. (1993) Selective Removal of Copper Bound to Metallothionein in the Liver of Lec Rats by Tetrathiomolybdate. *Toxicology*, **83**, 149-158.

Talaat, A.M., Lyons, R., Howard, S.T. and Johnston, S.A. (2004) The temporal expression profile of Mycobacterium tuberculosis infection in mice. *Proceedings of the National Academy of Sciences of the United States of America*, **101**, 4602-4607.

Tamura, Y., Maruyama, M., Mishima, Y., Fujisawa, H., Obata, M., Kodama, Y., Yoshikai, Y., Aoyagi, Y., Niwa, O., Schaffner, W. and Kominami, R. (2005) Predisposition to mouse thymic lymphomas in response to ionizing radiation depends on variant alleles encoding metal-responsive transcription factor-1 (Mtf-1). *Oncogene*, **24**, 399-406.

Tanzi, R.E., Petrukhin, K., Chernov, I., Pellequer, J.L., Wasco, W., Ross, B., Romano, D.M., Parano, E., Pavone, L., Brzustowicz, L.M., Devoto, M., Peppercorn, J., Bush, A.I., Sternlieb, I., Pirastu, M., Gusella, J.F., Evgrafov, O., Penchaszadeh, G.K., Honig, B., Edelman, I.S., Soares, M.B., Scheinberg, I.H. and Gilliam, T.C.

(1993) The Wilson Disease Gene Is a Copper Transporting Atpase with Homology to the Menkes Disease Gene. *Nature Genetics*, **5**, 344-350.

Tapiero, H., Townsend, D.M. and Tew, K.D. (2003) Trace elements in human physiology and pathology. Copper. *Biomedicine & Pharmacotherapy*, **57**, 386-398.

Teo, B.K. (1986) *EXAFS: basic principles and data analysis*. Springer-Verlag: New York.

Thiele, D.J. (1988) ACE1 regulates expression of the *Saccharomyces cerevisiae* metallothionein gene. *Molecular and Cellular Biology*, **8**, 2745-2752.

Tottey, S., Rondet, S.A., Borrelly, G.P., Robinson, P.J., Rich, P.R. and Robinson, N.J. (2002) A copper metallochaperone for photosynthesis and respiration reveals metal-specific targets, interaction with an importer, and alternative sites for copper acquisition. *Journal of Biological Chemistry*, **277**, 5490-5497.

Tsukihara, T., Aoyama, H., Yamashita, E., Tomizaki, T., Yamaguchi, H., Shinzawa-Itoh, K., Nakashima, R., Yaono, R. and Yoshikawa, S. (1995) Structures of metal sites of oxidized bovine heart cytochrome c oxidase at 2.8 A. *Science*, **269**, 1069-1074.

Tsukihara, T., Aoyama, H., Yamashita, E., Tomizaki, T., Yamaguchi, H., Shinzawa-Itoh, K., Nakashima, R., Yaono, R. and Yoshikawa, S. (1996) The whole structure of the 13-subunit oxidized cytochrome c oxidase at 2.8 A. *Science*, **272**, 1136-1144.

Tzagoloff, A., Nobrega, M., Gorman, N. and Sinclair, P. (1993) On the functions of the yeast COX10 and COX11 gene products. *Biochemistry and Molecular Biology International*, **31**, 593-598.

Valko, M., Morris, H. and Cronin, M.T.D. (2005) Metals, toxicity and oxidative stress. *Current Medicinal Chemistry*, **12**, 1161-1208.

Van der Spoel, D., Lindahl, E., Hess, B., Groenhof, G., Mark, A.E. and Berendsen, H.J.C. (2005) GROMACS: Fast, flexible, and free. *Journal of Computational Chemistry*, **26**, 1701-1718.

Van der Spoel, D., vanBuuren, A.R., Tieleman, D.P. and Berendsen, H.J.C. (1996) Molecular dynamics simulations of peptides from BPTI: A closer look at amide-aromatic interactions. *Journal of Biomolecular NMR*, **8**, 229-238.

Van Ho, A., Ward, D.M. and Kaplan, J. (2002) Transition metal transport in yeast. *Annual Review of Microbiology*, **56**, 237-261.

Voronova, A., Meyer-Klaucke, W., Meyer, T., Rompel, A., Krebs, B., Kazantseva, J., Sillard, R. and Palumaa, P. (2007) Oxidative switches in functioning of mammalian copper chaperone Cox17. *Biochemical Journal*, **408**, 139-148.

Vulpe, C., Levinson, B., Whitney, S., Packman, S. and Gitschier, J. (1993) Isolation of a candidate gene for Menkes disease and evidence that it encodes a copper-transporting ATPase. *Nature Genetics*, **3**, 7-13.

Walshe, J.A. (2006) History of Wilson's disease: 1912 to 2000. *Movement Disorders*, **21**, 142-147.

Warshel, A. (2002) Molecular dynamics simulations of biological reactions. *Accounts of Chemical Research*, **35**, 385-395.

Weser, U. and Hartmann, H.J. (1988) Differently Bound Copper(I) in Yeast Cu-8-Thionein. *Biochimica et Biophysica Acta*, **953**, 1-5.

Westin, G. and Schaffner, W. (1988) A Zinc-Responsive Factor Interacts with a Metal-Regulated Enhancer Element (MRE) of the Mouse Metallothionein-I Gene. *EMBO Journal*, **7**, 3763-3770.

Wheeler, D.L., Chappey, C., Lash, A.E., Leipe, D.D., Madden, T.L., Schuler, G.D., Tatusova, T.A. and Rapp, B.A. (2000) Database resources of the National Center for Biotechnology Information. *Nucleic Acids Research*, **28**, 10-14.

Wilson, S.A.K. (1912) Progressive lenticular degeneration. A familial nervous disease associated with cirrhosis of the liver. *Lancet*, **1**, 1115-1119.

Wu, J., Forbes, J.R., Chen, H.S. and Cox, D.W. (1994) The LEC rat has a deletion in the copper transporting ATPase gene homologous to the Wilson disease gene. *Nature Genetics*, **7**, 541-545.

Xiao, Z., Loughlin, F., George, G.N., Howlett, G.J. and Wedd, A.G. (2004) C-terminal domain of the membrane copper transporter Ctr1 from Saccharomyces cerevisiae binds four Cu(I) ions as a cuprous-thiolate polynuclear cluster: sub-femtomolar Cu(I) affinity of three proteins involved in copper trafficking. *Journal of the American Chemical Society*, **126**, 3081-3090.

Xiao, Z. and Wedd, A.G. (2002) A C-terminal domain of the membrane copper pump Ctr1 exchanges copper(I) with the copper chaperone Atx1. *Chemical Communications*, 588-589.

Yamaguchi, Y., Heiny, M.E. and Gitlin, J.D. (1993) Isolation and Characterization of a Human Liver Cdna as a Candidate Gene for Wilson Disease. *Biochemical and Biophysical Research Communications*, **197**, 271-277.

Yonkovich, J., McKenndry, R., Shi, X. and Zhu, Z. (2002) Copper ion-sensing transcription factor Mac1p post-translationally controls the degradation of its target gene product Ctr1p. *Journal of Biological Chemistry*, **277**, 23981-23984.

Yuzbasiyangurkan, V., Grider, A., Nostrant, T., Cousins, R.J. and Brewer, G.J. (1992) Treatment of Wilsons-Disease with Zinc .10. Intestinal Metallothionein Induction. *Journal of Laboratory and Clinical Medicine*, **120**, 380-386.

Zhang, B., Egli, D., Georgiev, O. and Schaffner, W. (2001) The Drosophila homolog of mammalian zinc finger factor MTF-1 activates transcription in response to heavy metals. *Molecular and Cellular Biology*, **21**, 4505-4514.

Zhang, L., Pickering, I.J., Winge, D.R. and George, G.N. (2008) X-ray absorption spectroscopy of cuprous-thiolate clusters in Saccharomyces cerevisiae metallothionein. *Chemistry and Biodiversity*, **5**, 2042-2049.

Zhang, L.M., Lichtmannegger, J., Summer, K.H., Webb, S., Pickering, I.J. and George, G.N. (2009) Tracing Copper-Thiomolybdate Complexes in a Prospective Treatment for Wilson's Disease. *Biochemistry*, **48**, 891-897.

Zhou, L., Singleton, C. and Le Brun, N.E. (2008) High Cu(I) and low proton affinities of the CXXC motif of Bacillus subtilis CopZ. *Biochemical Journal*, **413**, 459-465.

APPENDICES

As part of the Ph.D. training, the candidate has been involved in a number of research projects and scientific activities that are either directly or indirectly related to the main theme of the thesis project. These projects/activities (with publications if there are any) are listed in the following sections.

A.1 Thesis-related Publications

A.1.1 Structural Studies on the Metal Binding Site in Cox19 of Saccharomyces cerevisiae

In this work, Cox19, the import accessory protein in the assembly of cytochrome c oxidase, was characterized structurally and functionally (See Chapter 3 for details).

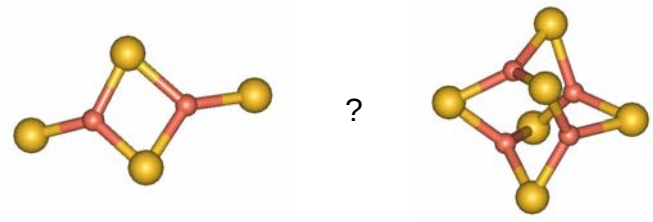

Publication:

- Rigby, K., **Zhang, L.M**., Cobine, P.A., George, G.N. and Winge, D.R. (2007) Characterization of the cytochrome c oxidase assembly factor Cox19 of Saccharomyces cerevisiae. *Journal of Biological Chemistry*, **282**, 10233-10242

Contributions from the candidate:

- Collect and analyze X-ray absorption spectra
- Write the XAS-related sections of the paper

A.1.2 Structural and Functional Studies on a Novel Mycobacterium tuberculosis Copper-sensing Transcriptional Regulator CsoR

In this work, a novel copper-responsive repressor CsoR was identified as a key factor in copper homeostasis in *M. tuberculosis*, and multiple lines of evidences were provided in understanding the molecular mechanisms of this regulator (See Chapter 6 for details).

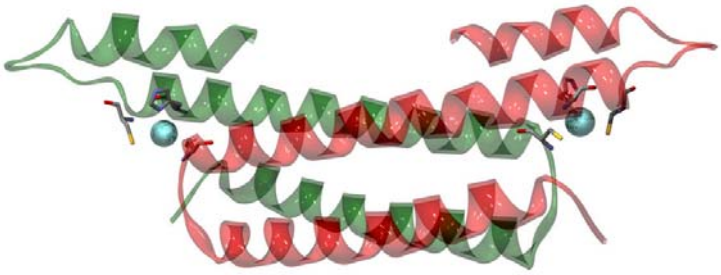

Publication:

- Liu, T., Ramesh, A., Ma, Z., Ward, S.K., **Zhang, L.M.**, George, G.N., Talaat, A.M., Sacchettini, J.C. and Giedroc, D.P. (2007) CsoR is a novel Mycobacterium tuberculosis copper-sensing transcriptional regulator. *Nature Chemical Biology*, **3**, 60-68.

Contributions from the candidate:

- Collect and analyze X-ray absorption spectra

A.1.3 Characterization of Drosophila Metal-responsive Transcription Factor-1

In this work, a novel cysteine-rich domain which is crucial for sensing excess cellular copper by *Drosophila* metal-responsive transcription factor-1 was characterized and the copper binding properties of this domain were examined using X-ray absorption spectroscopy and NMR (See Chapter 5 for details).

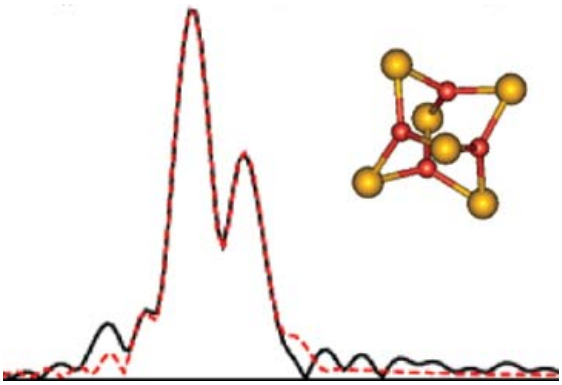

Publication:

- Chen, X.H., Hua, H.Q., Balamurugan, K., Kong, X.M., **Zhang, L.M.**, George, G.N., Georgiev, O., Schaffner, W. and Giedroc, D.P. (2008) Copper sensing function of *Drosophila* metal-responsive transcription factor-1 is mediated by a tetranuclear Cu(I) cluster. *Nucleic Acids Research*, **36**, 3128-3138.

Contributions from the candidate:

- Collect and analyze X-ray absorption spectra
- Write the XAS-related sections of the paper

A.1.4 Structure of Cuprous-Thiolate Clusters in Saccharomyces cerevisiae Metallothionein

In this work, a combination of X-ray absorption spectroscopy and density functional theory were used to investigate the nature of copper binding to *Saccharomyces cerevisiae* metallothionein (See Chapter 4 for details).

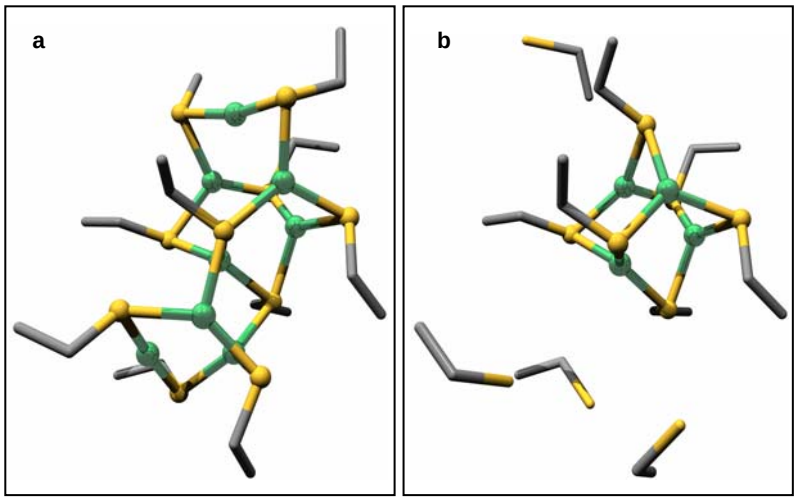

Publication:

- **Zhang, L.M.**, Pickering, I.J., Winge, D.R. and George, G.N. (2008) X-Ray Absorption Spectroscopy of Cuprous-Thiolate Clusters in Saccharomyces cerevisiae Metallothionein. *Chemistry & Biodiversity*, **5**, 2042-2049.

Contributions from the candidate:

- Analyze X-ray absorption spectra
- Write the draft of the paper

A.1.5 Copper-Thiomolybdate Complexes in the Animal Model of Wilson's Disease

X-ray absorption spectroscopy and X-ray fluorescence imaging were used in this study to trace the molecular form and distribution of the complex in liver and kidney of an animal model of human Wilson's disease (See Chapter 7 for details).

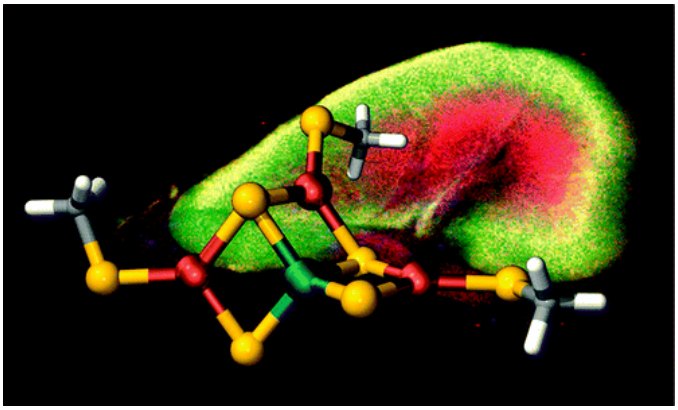

Publication:

- **Zhang, L.M.**, Lichtmannegger, J., Summer, K.H., Webb, S., Pickering, I.J. and George, G.N. (2009) Tracing Copper-Thiomolybdate Complexes in a Prospective Treatment for Wilson's Disease. *Biochemistry*, **48**, 891-897.

Contributions from the candidate:

- Section organ samples and prepare samples for X-ray absorption spectroscopy
- Collect and analyze X-ray absorption spectra and X-ray fluorescence imaging
- Carry out metal analysis
- Write draft of the paper

A.2 Other Research Projects

A.2.1 High-resolution X-ray Emission Spectroscopy of Molybdenum Compounds

High-resolution molybdenum K-edge X-ray emission spectroscopy (XES) was used to characterize the Kβ_4 and Kβ'' valence-to-core transition bands in the oxo-Mo compounds K_2MoO_4, $MoO(S_2\text{-}CNEt_2)_2$, and $MoO_2(S_2CNEt_2)_2$.

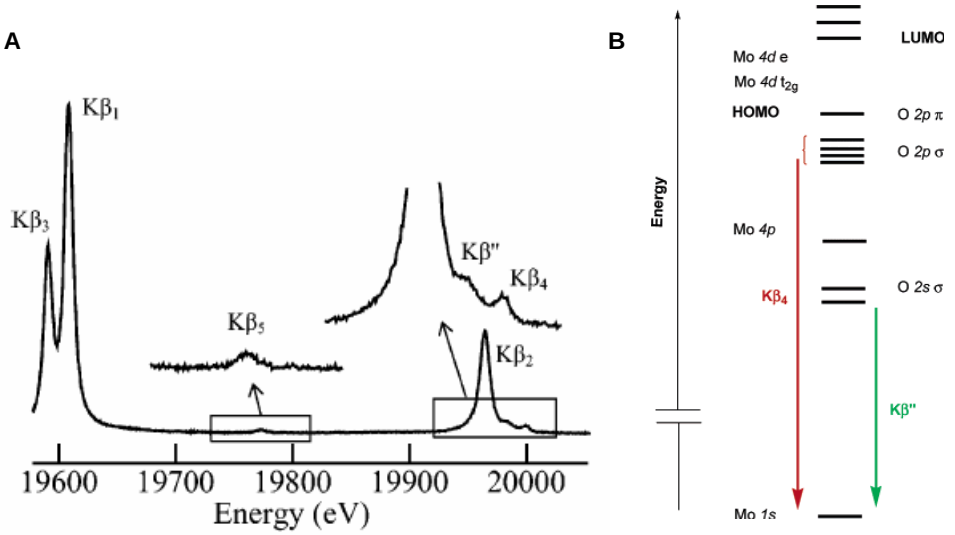

Related publication:

- Doonan, C.J., **Zhang, L.M.**, Young, C.G., George, S.J., Deb, A., Bergmann, U., George, G.N. and Cramer, S.P. (2005) High-resolution X-ray emission spectroscopy of molybdenum compounds. *Inorganic Chemistry*, **44**, 2579-2581.

Contributions from the candidate:

- Write program for data processing
- Involved in data analysis discussion

A.2.2 Characterization and Role of Zinc Binding in Yeast Cox4

In this work, the Zn binding properties of yeast Cox4, a Zn-binding subunit of cytochrome *c* oxidase in the mitochondrial inner membrane, were examined and the potential functions of this matrix-facing subunit were proposed.

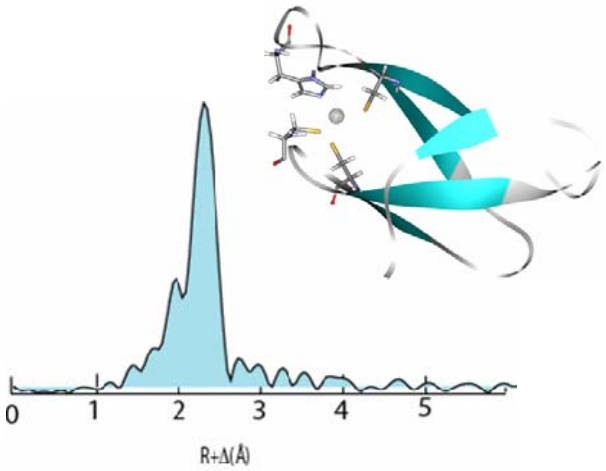

Related publication:

- Coyne, H.J., Ciofi-Baffoni, S., Banci, L., Bertini, I., **Zhang, L.M.**, George, G.N. and Winge, D.R. (2007) The characterization and role of zinc binding in yeast Cox4. *Journal of Biological Chemistry*, **282**, 8926-8934.

Contributions from the candidate:

- Analyze the EXAFS data
- Write the EXAFS-related sections of the paper

A.2.3 Structure of Molybdenum Centre in the Trimethylamine N-oxide Reductase from E. coli

In this project, molybdenum K-edge X-ray absorption spectroscopy and density functional theory calculation were used to characterize the local structure surrounding the molybdenum site of recombinant *Escherichia coli* Trimethylamine N-oxide (TMAO) reductase.

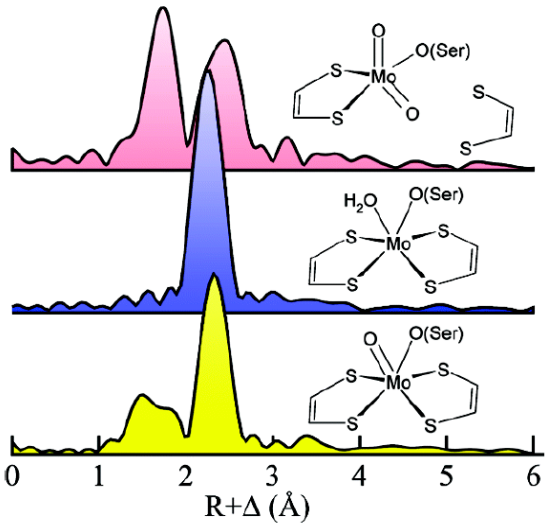

Related publication:

- **Zhang, L**., Nelson, K.J., Rajagopalan, K.V. and George, G.N. (2008) Structure of the molybdenum site of Escherichia coli trimethylamine N-oxide reductase. *Inorganic Chemistry*, **47**, 1074-1078.

Contributions from the candidate:

- Analyze the X-ray absorption spectroscopy data
- Model the Mo sites in the TMAO reductase using density functional theory
- Write the draft of the paper

A.2.4 Development of a Combined Imaging System for Small Animals Using K-Edge Subtraction and Fluorescence Subtraction

This project was involved in developing a novel combined imaging system for small animals with dilute concentrations of iodine as a contrast agent using K-edge subtraction and fluorescence subtraction imaging.

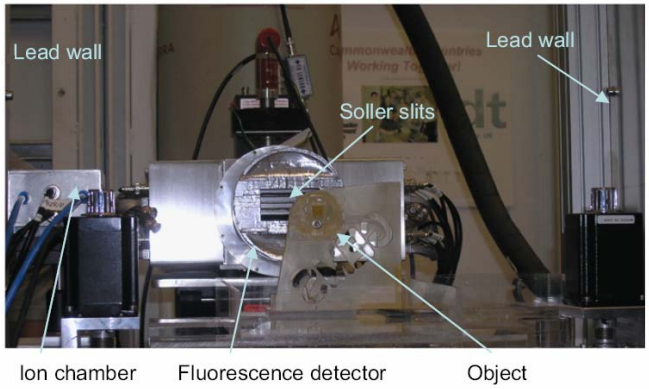

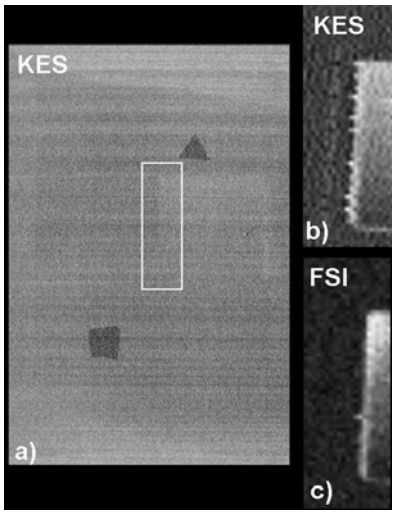

Related publications:

- Bewer, B., Zhang, H.L., Zhu, Y., **Zhang, L.M.**, George, G.N., Pickering, I.J. and Chapman, D. (2008) Development of a combined K-edge subtraction and fluorescence subtraction imaging system for small animals. *Review of Scientific Instruments*, **79**, 3.
- Zhang, H., Zhu, Y., Bewer, B., **Zhang, L.,** Korbas, M., Pickering, I.J., George, G.N., Gupta, M. and Chapman, D. (2008a) Comparison of iodine K-edge subtraction and fluorescence subtraction imaging in an animal system. *Nuclear Instruments & Methods in Physics Research*

Section a-Accelerators Spectrometers Detectors and Associated Equipment, **594**, 283-291.

Contributions from the candidate:

- Develop motor control and data acquisition software for the FSI-related experiment.
- Involved in FSI imaging measurement and data analysis.

A.3 Canadian Light Source HXMA beamline Commissioning

Canadian Light Source (CLS) Hard X-ray Micro-Analysis Beamline (HXMA, 06ID-1) is a hard X-ray spectroscopy beamline. The source of the beamline is a superconducting wiggler covering 5 to 40 keV. The primary optics include a cryogenically cooled double crystal monochromator (Si 111 and 220), white beam vertical collimating and toroidal focusing mirrors. End station experimental capabilities include XAFS (Ge solid state detectors), microprobe (Kirkpatrick-Baez mirrors, Ge solid state detector and image plate area detector), and diffraction (Huber psi-8 and powder diffraction setups, with diamond anvil cell high pressure sample environment).

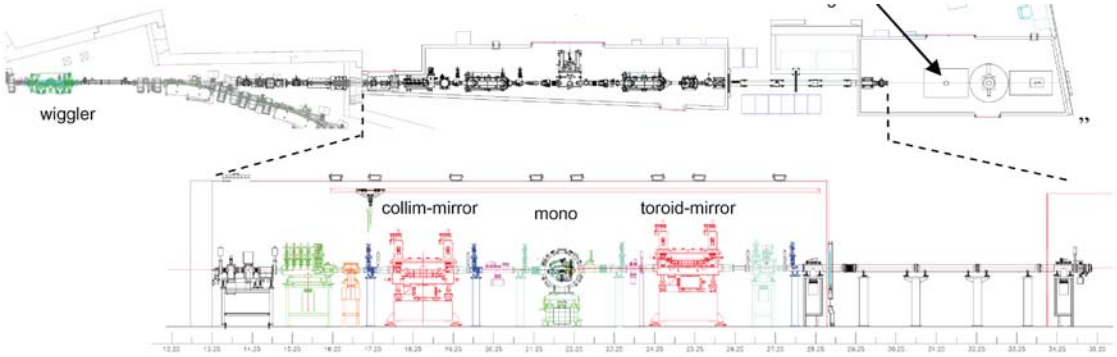

Summary of the activities:

During Sept. 2004 to Sept. 2007, the candidate has been actively involved in the commissioning for the new HXMA (Hard X-ray Micro Analysis) beamline at CLS. Projects include monochromator and optics installation, beam positioning survey and 4 out of 5 commissioning runs. The following is the list of some specific HXMA projects:

i). Sept. 2004 Kohzu CMJ-1 Monochromator Installation

- Observed the entire monochromator installation and acceptance testing process, including the autocollimator data acquisition and the crystal mounting procedures.
- Observed the first commissioning of the monochromator liquid nitrogen cooler.
- Observed and participated the initial monochromator vacuum preparation.

ii). Jan. & March 2005 IDT Beamline Optics Installation

- In charge of the vacuum preparation of the beamline graphite filter films: ultrasonic bath cleaning and pre-baking in a temperature controlled lab oven.
- Assisted with the diagnosis and an attempted repairing of the beamline X-ray beam position monitor (BPM) #1 and #2.
- Assisted with fabrication of the P31 (ZnS: Cu) coating-monochromator fluorescence screen.
- Assisted with installation of RGA in the mirror tank.

iii). Apr. 2005 2nd HXMA Commissioning Run

- In charge of operating system and software installation.

- In charge of fabrication of the temporary slit in the experimental hutch and calibration of motor control for scanning the temporary slit.
- Assisted with ion chamber setup and alignment with the X-ray beam in the experimental hutch.
- Assisted in manual acquisition and processing of the first XAS spectra at HXMA.

iv). Jul. 2005 3rd HXMA Commissioning Run/GEMS Experiment

- In charge of processing the initial Cu K-edge data using the commissioned Si(111) monochromator crystals.
- Observed the entire process of monochromator Si(220) crystal pair commissioning.
- Prepared NaI sample and processed the NaI XANES data for the beamline staff.
- Participated in optimizing beam conditions and controlling motor scans for the GEMS experiment.

v). Sept. 2005 4th HXMA Commissioning Run/GEMS Experiment

- Software development for motor control.
- Software installation and testing for quick scan.

vi). Nov. 2005 4th HXMA Commissioning Run /Expert meeting run

- Acted as beamline scientist to help users for experiment setup, alignment, data collection and data display during the absence of beamline scientist.

vii). Jan. 2006 5th HXMA Commissioning Run

- Calibration on the mirror motors.
- Involved in the strategy design for mirror commissioning.

viii). Aug. 2006 6th HXMA Commissioning Run

- In charge of hardware installation for commissioning of 32-element Ge detector and DXP devices.
- In charge of software installation and testing for 32-element Ge detector.
- In charge of initial testing on 32-element detector.
- Involved in the detector configuration and optimization.

ix). Sept. 2006 in CLS

- Help new users (Prof. Deborah Zamble's group) for data acquisition and data analysis.

x). Mar. 2007. HXMA 32-element detector commissioning run

- In charge of 32-ele detector configuration and optimization.
- Cooperate with beamline scientist (Sam Webb) at SSRL for the installation, testing and debugging of XAS data collection software (v1).

xi). Sept. 2007. HXMA biological XAS and microprobe commissioning run

- In charge of 32-ele detector configuration and optimization.
- Cooperate with beamline scientist (Sam Webb) at SSRL for the installation, testing and debugging of XAS data collection software (v2).
- Participate in microprobe commissioning run.

Related publication:

- Jiang, D.T., Chen, N., **Zhang, L.M.**, Malgorzata, K., Wright, G., Igarashi, R., Beauregard, D., Kirkham, M. and McKibben, M. (2007) XAFS at the Canadian Light Source. *American Institute of Physics Conference Proceedings* (*XAFS13*) **882**, 893-895

A.4 Development of Computer Programs

During the thesis studies, it is often required to develop computer software for data acquisition and data analysis. The main softwares developed during the period are briefly described below.

A.4.1 Data Acquisition Software

These softwares were developed in C program for the X-ray fluorescence subtraction imaging (See Apendix A.2.4). They were used to control the motors which drive the sample stages. Software package were also developed to communicate and synchronize with motor control, signal retrieving and data recording.

A.4.2 X-Ray Absorption and Emission Data Analysis Software

Computer software (mainly in FORTRAN) were developed that can execute channel by channel background subtraction for data analysis on the Cu K-edge EXAFS spectra of Cox19-related protein (See Chapter 3). This was needed to remove contaminating signals from the protein data, and has been incorporated into the EXAFSPAK program suite.

The software program was also developed in Java for data reduction of high-resolution X-ray emission spectra (See Appendix A.2.1).

A.4.3 Software for X-Ray Fluorescence Quick Raster Imaging Analysis

The X-ray fluorescence quick raster imaging data are normally in very large size, and therefore it is not practical to analyze these data using the existing software package (See Chapter 7). Software programs were developed in PERL and PHP for data chopping, data normalization and data conversion into image format.

A.4.4 Software for Molecular Dynamics Simulation Analysis

A number of PERL-based softwares were developed for analysis on the molecular dynamics simulations (See Chapter 6). These softwares were mainly used for randomly sampling representative structures and statistic analysis on the MD simulations, which are either not available or not convenient to use in the GROMACS package.